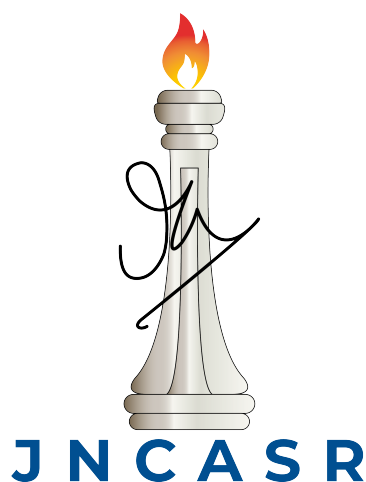


# Exploring Magnetic Frustration and Quantum Spin Liquid in Various Spin Lattices

A Thesis  
Submitted for the Degree of  
**Doctor of Philosophy**

By  
**Rahul Kumar**



**Chemistry and Physics of Materials Unit**  
**Jawaharlal Nehru Centre for Advanced Scientific Research**  
(A Deemed University)  
Bangalore 560064

**July 2024**

# Dedication

This thesis is dedicated to those who have been my pillars of support and inspiration throughout my academic journey.

To **Sh. Ramautar**, my school teacher, whose early encouragement and belief in my potential laid the foundation for my academic pursuits.

To my parents, Sh. Parmod Kumar and Smt. Kailash Devi, whose unwavering love and support have been my greatest source of strength, and my brother, Mr. Rohit Kumar, whose companionship and encouragement have been invaluable.

To my grandmother, **Late Smt. Sumarati Devi**, whose blessings and wisdom continue to guide me every day.

To my maternal uncle, Mr. Sandeep Gunwal, for his unwavering support and belief in my dreams.

To my school friend, Rahul Baghotia, whose friendship and support have been a constant source of joy and motivation.

To my college friends, Sudhakar, Yohesh Pachori, and Rahul Lamba, for their camaraderie, laughter, and support throughout my academic journey.

Thank you all for being an integral part of my life and for contributing to this achievement.



# Abstract

In condensed matter physics, the study of magnetic frustration and quantum spin liquids (QSLs) is driven by both fundamental curiosity and potential applications. Magnetic frustration occurs when spin-lattice geometries prevent spins from aligning in low-energy configurations, leading to highly degenerate ground states and exotic phenomena. This thesis aims to uncover the principles governing magnetic frustration and QSLs in various spin lattices through both experimental and theoretical methods.

We explore  $\text{NaYbTe}_2\text{O}_7$ , a compound featuring quasi-one-dimensional magnetic chains of  $\text{Yb}^{3+}$  ions, which shows no long-range magnetic ordering down to 0.285 K yet displays strong magnetic correlations indicative of a potential QSL state. Similarly, our study on  $\text{Yb}_2\text{Te}_5\text{O}_{13}$ , a  $\text{Yb}^{3+}$  dimer-based compound, reveals the absence of long-range magnetic ordering down to 44 mK and the presence of dynamic spin correlations which are stable even in the presence of 3200 Oe magnetic field, suggesting a QSL state within its dimer lattice.

Additionally, we examine the two-dimensional rhombus spin-lattice in  $\text{LiYbSiO}_4$ , which exhibits no long-range magnetic ordering down to 44 mK but  $\mu\text{SR}$  measurements unveil dynamic state below 0.5 K, supported by theoretical calculations indicating a QSL state. The doubly ordered perovskite  $\text{NaYbZnWO}_6$ , with its two-dimensional distorted square lattice, also shows spin frustration and potential QSL behavior based on experimental and theoretical analyses.

Furthermore, the triangular lattice-based compound  $\text{Sr}_3\text{CoNb}_2\text{O}_9$  demonstrates broad antiferromagnetic anomalies and magnetization plateaus, with a dynamic state from 1.3 K to 10 K. Theoretical studies suggest it as a potential Kitaev candidate due to its spin-orbit entangled  $J_{\text{eff}} = 1/2$  moments completing Jackeli Khalilun criteria for a "parallel-edge" sharing geometry. Lastly, the hyperhoneycomb lattice-based magnet  $\text{NaYbW}_2\text{O}_8$  shows a disordered magnetic state with no long-range ordering and indications of a dynamic magnetic state from combined experimental and theoretical studies.

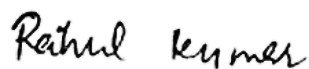
Overall, our investigations across various lattice geometries and materials highlight the intricate nature of magnetic frustration and the promising potential of these compounds as quantum spin liquids, opening exciting avenues for future research in quantum magnetism and information processing.

# Declaration

I hereby declare that the matter embodied in the thesis entitled “**Exploring Magnetic Frustration and Quantum Spin Liquid in Various Spin Lattices**” is the result of investigations carried out by me at the Chemistry and Physics of Materials Unit, Jawaharlal Nehru Centre for Advanced Scientific Research, Bangalore, India under the supervision of Prof. A. Sundaresan and it has not been submitted elsewhere for the award of any degree or diploma.

In keeping with the general practice of reporting scientific observations, due acknowledgments have been made whenever the work described is based on the findings of other investigators. Any omission that might have occurred due to oversight or error in judgment is regretted.

Place: Bangalore  
Date: 25 July, 2024



---

Rahul Kumar

# Certificate

I hereby certify that the matter embodied in this thesis entitled “**Exploring Magnetic Frustration and Quantum Spin Liquid in Various Spin Lattices**” has been carried out by Mr. Rahul Kumar at the Chemistry and Physics of Materials Unit, Jawaharlal Nehru Centre for Advanced Scientific Research, Bangalore, India under my supervision and it has not been submitted elsewhere for the award of any degree or diploma.



---

**Prof. A. Sundaresan**  
(Research Supervisor)

# Acknowledgements

Embarking on a journey towards a PhD is akin to traversing uncharted territories, and I am deeply grateful for the support, guidance, and encouragement I have received along the way. This thesis would not have been possible without the contributions of many individuals and institutions.

First and foremost, I would like to express my sincere gratitude to my advisor, **Prof. A. Sundaresan**, for his unwavering support, insightful guidance, and continuous encouragement throughout my research in a completely new field of frustrated magnetism and quantum spin liquids. His profound knowledge and meticulous approach have been instrumental in shaping this work, and his patience and understanding have been a source of great strength.

My sincere thanks go to Prof. C. N. R. Rao, FRS, for providing access to numerous experimental facilities and for being a continual source of inspiration.

I am grateful to the International Centre for Materials Science (ICMS) and Sheikh Saqr Laboratory (SSL) at JNCASR for their provision of various experimental facilities.

I extend my appreciation to Prof. A. Sundaresan, Prof. Vidhyadhiraja N. S., and Prof. Bivas Saha for their enlightening coursework.

I am delighted to acknowledge my collaborators. I am sincerely thankful to Dr. Rhea Stewart and Dr. Peter Baker from ISIS, RAL, UK, for their assistance in  $\mu$ SR data analysis. My gratitude also extends to Prof. Vidhyadhiraja N. S. and Prof. Swapan K. Pati for their profound theoretical discussions. Special thanks to Dr. Hyun-Joo Koo, Prof. Myung Whangbo, Prof. Umesh Waghmare, Ms. Anita Gemmy Francis, and Mr. Arijit Sinha for their theoretical collaboration. I am grateful to Dr. Fabio Orlandi and Dr. Pascal Manuel from WISH, RAL, UK, for their help with neutron diffraction experiments. My appreciation goes to Dr. Ralf Feyerherm, Prof. Bella Lake, Kiwan Nam, Seong-Hoon Kim, and Prof. Kee Hoon Kim for their assistance with milli-Kelvin heat capacity measurements.

I am thankful to the technical staff, namely Mrs. Usha, Mrs. Krithi, Mr. Balaraju, Mr. Srinath, Mr. Anil, Mr. Vasu, Mr. Mahesh, Mr. Arun, Mr. Sreehari, and Mrs. Radha, for their support in various research and academic endeavors.

I am grateful to Dr. Navneet Pandey from Quantum Design, India, for imparting his extensive knowledge about SQUID, PPMS, and iHe3 instruments.

I acknowledge the Council of Scientific and Industrial Research (CSIR) for providing the fellowship during my Ph.D. tenure. Additionally, I am thankful to JNCASR, the

DST-RAL project, and the DST-DESY project for their financial support, which enabled me to attend conferences, visit RAL in the UK to conduct muon and neutron diffraction experiments, and visit DESY in Germany for high-pressure and high-temperature synthesis experiments.

I express my gratitude to the complab, the library, academics, administration, Dhantari, Housekeeping, garden, dining hall, and hostel staff for providing and maintaining various facilities.

I extend my thanks to all my past and present lab mates: Dr. Abhijit, Dr. Prem, Dr. Ravi, Dr. Pavitra, Dr. Swarna, Dr. Panda, Souvik, Sudip, Shoubhik, Nishit, Dr. Anshu, Kanishka, Dr. Smruthi, Somsuvra, Anwesha, Dr. Rajesh, Dr. Anzar, Dr. Kartik, Cisha, Annal, Dr. Vijaykumar More, Anubhav, and Joshi, for their assistance, valuable discussions, and for fostering a friendly atmosphere in the lab.

A special note of thanks goes to my friends at JNCASR: Amit, for being a great roommate and always standing by my side; Devesh, for his “scientific” jokes that brought light moments; Vandana, for our cherished gossip sessions; Suryadev, for weather updates and fireside discussions; Chinmay, for taking me to the best food places and sharing culinary adventures; Diksha, for her sisterly love and support; Hariharan, for our exhilarating badminton matches; Swarnima, for our cute fights that added spice to everyday life; and Alice, for the “wonderful” secret Santa memory. Each of you has made this journey memorable in your unique way, and I am deeply grateful for your friendship. I also thank Yashwini, Suhas, Ivy, Arif, Ankita, Nazia, Aditi, Arijit, Anita, Animesh, Anupam, Arindam, Rohan, Satyajee, and Devender for making my journey memorable.

Lastly, I would like to thank all my sports friends from badminton and volleyball, particularly Anomitra, Punith, Uttam, Mayank, Momin, Rohit, Ankit, Bhupesh, Shubham, Rahul, and SBD.

# Publications

## Included in Thesis

1. **R. Kumar**, K. Nam, S.-H. Kim, K. H. Kim, and A. Sundaresan, “Exploring potential quantum spin liquid state in a quasi-one-dimensional magnetic chain,” [Phys. Rev. B](#), vol. 109, p. 224 429, 2024.
2. **R. Kumar**, Anita Gemmy Francis, Rhea Stewart, Peter J. Baker, Ralf Feyerherm, Devesh Chandra Binwal, Bella Lake, Swapan K Pati, and A. Sundaresan, “Dynamic Magnetic Ground State in a Dimer-Based Compound  $\text{Yb}_2\text{Te}_5\text{O}_{13}$ ” (Manuscript Under Preparation).
3. **R. Kumar**, Arijit Sinha, Rhea Stewart, Peter J. Baker, Premakumar Yanda, Fabio Orlandi, Pascal Manuel, Umesh V. Waghmare and A. Sundaresan, “Quantum Spin-Liquid State in a Two-Dimensional Rhombus Lattice” (Manuscript Under Preparation).
4. **R. Kumar**, S. Bhat, H.-J. Koo, M.-H. Whangbo, and A. Sundaresan, “Spin frustration in a distorted square lattice of  $\text{NaYbZnWO}_6$  prepared under high pressure,” *Physical Review B* (Under Review).
5. **R. Kumar**, Rhea Stewart, Peter J. Baker, Hyun-Joo Koo, Myung-Hwan Whangbo, Ralf Feyerherm, Bella Lake and A. Sundaresan, “ $\text{Sr}_3\text{CoNb}_2\text{O}_9$ : A New Triangular Lattice-Based Kitaev Model Candidate” (Manuscript Under Preparation).
6. **R. Kumar**, Anita Gemmy Francis, Rhea Stewart, Peter J. Baker, Swapan K Pati, and A. Sundaresan, “Magnetic Frustration in a Hyperhoneycomb Compound  $\text{NaYbW}_2\text{O}_8$ ” (Manuscript Under Preparation).

## Not Included in Thesis

7. P. K. Yadav, R. Upadhyay, **R. Kumar**, P. Nukala, and C. Upadhyay, “Influence of local defects in the generation of memory effect in  $\text{Dy}_2\text{Ti}_2\text{O}_7$  compound: Fe-doped study,” [Physica Scripta](#), vol. 99, no. 8, p. 085 941, 2024.

8. **R. Kumar** and A. Sundaresan, “Unveiling a hidden multiferroic state under magnetic fields in BaHoFeO<sub>4</sub>,” *Physical Review B*, vol. 107, no. 18, p. 184 420, 2023.
9. **R. Kumar** and A. Sundaresan, “Role of dipole relaxation in measuring electric polarization in type-II multiferroics,” *Zeitschrift für anorganische und allgemeine Chemie*, vol. 649, no. 14, e202300074, 2023.
10. K. Manna, **R. Kumar**, A. Sundaresan, and S. Natarajan, “Fixing CO<sub>2</sub> under atmospheric conditions and dual functional heterogeneous catalysis employing Cu mofs: Polymorphism, single-crystal-to-single-crystal (scsc) transformation and magnetic studies,” *Inorganic Chemistry*, vol. 62, no. 34, pp. 13 738–13 756, 2023.
11. P. K. Yadav, R. Upadhyay, **R. Kumar**, P. Nukala, and C. Upadhyay, “Emergence of field-induced memory effect in spin ices,” *Journal of Physics: Condensed Matter*, vol. 35, no. 49, p. 495 601, 2023.
12. **R. Kumar** and A. Sundaresan, “Antisite disorder driven cluster glass state and colossal magnetoresistance in MnSb<sub>2</sub>Se<sub>4</sub>,” *Physical Review B*, vol. 106, no. 13, p. 134 423, 2022.
13. **R. Kumar** and A. Sundaresan, “Multiferroicity in a quasi-one-dimensional magnet MnSb<sub>2</sub>Se<sub>4</sub>,” *Materials Research Bulletin*, vol. 145, p. 111 569, 2022.
14. **R. Kumar** and A. Sundaresan, “Spin-glass behavior in Li<sub>3</sub>NiCuBiO<sub>6</sub>: A two-dimensional distorted honeycomb-lattice,” *Journal of Physics: Condensed Matter*, vol. 34, no. 41, p. 415 803, 2022.
15. **R. Kumar**, P. Yanda, and A. Sundaresan, “Cluster-glass behavior in the two-dimensional triangular lattice Ising-spin compound Li<sub>2</sub>Mn<sub>3</sub>O<sub>7</sub>,” *Physical Review B*, vol. 103, no. 21, p. 214 427, 2021.

# List of Tables

Table	Page
2.1 Comparison of Muons, Electrons, and Protons . . . . .	43
3.1 Crystallographic parameters along with occupancy and isotropic displacement parameters obtained from the Rietveld refinement of the powder XRD data. Space group: $P2_1/n$ , $a = 6.7041(1)$ Å, $b = 7.4820(1)$ Å, $c = 11.8521(2)$ Å, $\beta = 100.184(1)^\circ$ , $V = 585.14(1)$ Å <sup>3</sup> , $\chi^2 = 2.44$ %, Bragg $R$ factor = 7.56 %, $R_f = 5.06$ % . . . . .	54
3.2 Observed and expected weight and atomic percentage value of different elements . . . . .	54
3.3 Magnetic field dependence of $a$ and $\alpha$ parameter . . . . .	62
4.1 Crystallographic parameters along with occupancy and average isotropic displacement parameters obtained from the Rietveld refinement of the powder XRD data. Space group: $P\bar{1}$ , $V = 599.02(1)$ Å <sup>3</sup> , $\chi^2 = 2.29$ %, Bragg $R$ factor = 3.00 %, $R_f = 2.07$ % . . . . .	75
4.2 The optimised lattice parameters. . . . .	86
4.3 The nearest, next nearest, third nearest neighbor exchange couplings and the zero-field splitting parameters calculated from first principles calculations. . . . .	86
5.1 Crystallographic parameters along with occupancy and isotropic displacement parameters obtained from the Rietveld refinement of the room temperature powder XRD data. Space group: $Pnma$ , $a = 10.7558(1)$ Å, $b = 6.2530(1)$ Å, $c = 4.9022(1)$ Å, $V = 329.70(2)$ Å <sup>3</sup> , $\chi^2 = 5.76$ %, Bragg $R$ factor = 9.95 %, $R_f = 13.87$ % . . . . .	98



5.2	Crystallographic parameters along with occupancy and isotropic displacement parameters obtained from the Rietveld refinement of the neutron diffraction data. Space group: $Pnma$ , $a = 10.7166(1) \text{ \AA}$ , $b = 6.2417(1) \text{ \AA}$ , $c = 4.8846(1) \text{ \AA}$ , $V = 326.71(1) \text{ \AA}^3$ , $\chi^2 = 3.92 \%$ , Bragg $R$ factor = $5.39 \%$ , $R_f = 6.92 \%$ .	99
5.3	Crystallographic parameters along with occupancy and isotropic displacement parameters obtained from the Rietveld refinement of the neutron diffraction data. Space group: $Pnma$ , $a = 10.7172(1) \text{ \AA}$ , $b = 6.2420(1) \text{ \AA}$ , $c = 4.8849(1) \text{ \AA}$ , $V = 326.77(1) \text{ \AA}^3$ , $\chi^2 = 3.10 \%$ , Bragg $R$ factor = $5.49 \%$ , $R_f = 6.94 \%$ .	100
5.4	Magnetic field dependence of $a$ and $\alpha$ parameter . . . . .	108
5.5	Table compares the relative energies of the various orders of the spins in the L1 and L2 layers of the $1 \times \sqrt{2} \times \sqrt{2}$ supercell of LYSO. It reveals the the lowest energy configuration of spins is AFM3 . . . . .	117
5.6	Estimated exchange couplings show that the in-plane couplings $J_1$ and $J_2$ are 384 and 205 times, respectively w.r.t. $J_3$ coupling. . . . .	120
6.1	Crystallographic parameters along with occupancy and isotropic displacement parameters obtained from the Rietveld refinement of the powder XRD data. Space group: $P2_1$ , $V = 228.91(1) \text{ \AA}^3$ , $\chi^2 = 2.97 \%$ , Bragg $R$ factor = $7.86 \%$ , $R_f = 6.70 \%$ . . . . .	132
6.2	Comparison of $\Delta$ value obtained from two-level and three-level fit. . . . .	139
6.3	The fractional coordinates of the atoms in the optimized structure of $\text{NaYbZnWO}_6$	141
6.4	Values of the spin exchanges $J_1$ – $J_4$ in K determined by DFT+ $U$ and DFT+ $U$ +SOC calculations with $U_{eff} = 5 \text{ eV}$ . The numbers in the parenthesis are the relative values. . . . .	142
6.5	Values of the spin exchanges $J_1$ – $J_4$ in K determined by DFT+ $U$ and DFT+ $U$ +SOC calculations with $U_{eff} = 5 \text{ eV}$ . The numbers in the parenthesis are the relative values. . . . .	143
7.1	Crystallographic parameters along with occupancy and isotropic displacement parameters obtained from the Rietveld refinement of the powder XRD data. Space group: $P2_1/c$ , $V = 767.71(2) \text{ \AA}^3$ , $\chi^2 = 2.97 \%$ , Bragg $R$ factor = $3.6 \%$ , $R_f = 4.86 \%$ . . . . .	154
7.2	Comparison of the Co-O bond distances (in $\text{\AA}$ ) from the XRD and DFT calculations. . . . .	167
7.3	Relative energies (meV/formula unit) obtained from DFT+ $U$ calculations. .	167
7.4	Values of $J_1$ - $J_3$ (in K) obtained from DFT+ $U$ calculations. . . . .	169

8.1	Atomic coordinates, occupancy and isotropic thermal parameters obtained from the Rietveld refinement, Space group: $I4_1/a$ , $V = 299.75(1) \text{ \AA}^3$ , $\chi^2 = 1.56 \%$ , $R_p = 10.7 \%$ , $R_{wp} = 12.2 \%$ . . . . .	183
8.2	The nearest, next nearest exchange couplings from first principles calculations for lattice A and lattice B . . . . .	189
8.3	The ordering vector $Q$ of the ground state for lattice A, in units of $2\pi$ , obtained from the peak of the equal time structure factor obtained from Iterative Minimisation (IM). . . . .	191

# List of Figures

Figure	Page
1.1 (a) Arrangement of oxygen (in blue color) and hydrogen (in red color) atom in a tetrahedron environment. The right side tetrahedron illustrates the equivalent spins for each O-H bond (adapted from [2], reproduced with permission from Springer Nature). (b) Change in residual entropy when hydrogen disorder changes (adapted from [3], reproduced with permission from Royal Society of Chemistry). . . . .	3
1.2 Rugged energy landscape of protein folding dynamics (adapted from [6]) . .	4
1.3 Arrangement of atoms in a amorphous solid (adapted from [8]). . . . .	5
1.4 Illustration of the nematic phase of the liquid crystals (adapted from [14]). .	6
1.5 Antiferromagnetically coupled triangular lattice in which all the exchange interactions can not be satisfied simultaneously. . . . .	7
1.6 (a) Triangular Lattice, (b) Kagome Lattice, and (c) Pyrochlore Lattice. (adapted from [20], reproduced with permission from Springer Nature) . . .	8
1.7 Nearest neighbor and next neighbor interactions are shown in (a) one-dimensional lattice and (b) square lattice. . . . .	9
1.8 Various magnetic phases predicted from $J_1$ - $J_2$ model calculation for (a) a one-dimensional lattice [32], (b) a square lattice (adapted from [38], reproduced with permission from Elsevier). . . . .	10
1.9 Kitaev model on a honeycomb lattice (adapted from [45]) . . . . .	11

1.10	(a) Different incommensurate magnetic structures: sinusoidal spin density wave (upper one), cycloidal spiral (middle one), and proper screw structure (lower one), adapted from [46]. (b) Breathing pyrochlore magnetic sublattice of $\text{LiFeCr}_4\text{O}_8$ , adapted from [49] and reproduced with permission from American Physical Society. (c) A snapshot of the spins frozen in random directions. (d) Pyrochlore lattice, (adapted from [20], reproduced with permission from Springer Nature) (e) Fluctuating singlets in a quantum spin liquid, adapted from [50]. . . . .	13
1.11	(a) An illustration of the quantum entangled state, adapted from [61]. (b) Fractionalization of electron into spinon and chargon. . . . .	15
1.12	(a) A quantum processor attached to a dilution refrigerator, adapted from [67]. (b) An illustration of secured quantum communication, adapted from [68]. . . . .	17
1.13	Typical splitting of (a) $\text{Co}^{3+}$ and (b) $\text{Yb}^{3+}$ ions, resulting in $J_{eff} = \frac{1}{2}$ ground state. . . . .	19
2.1	(a) 6-ram Large Volume Press Aster-15 at P61B beamline, DESY. (b) Sample assembly used for synthesis. (c) Sample placed inside the press before starting an HPHT reaction. . . . .	32
2.2	(a) Illustration of the process happening during an X-ray diffraction (Google Image). (b) Reflection of the incident beam of X-rays by atomic planes, adapted from [5]. . . . .	34
2.3	(a) A file photo of quantum design make MPMS (Quantum Design Website). (b) iHE3 addition to MPMS. (c) MPMS3 SQUID system diagram showing important elements, including the relative location of the sample, gradiometer, and magnet (adapted from [11]). (d) Schematic diagram of VSM (adapted from [11]). . . . .	38
2.4	(a) ACMS insert in which sample is mounted (adapted from [12]). (b) Location of the sample during the measurement. . . . .	41
2.5	(a) Thermal connections to sample and sample Platform in PPMS heat capacity option (adapted from [14]). (b) The graph displays a plot of fit and measured temperature versus time. . . . .	42
2.6	(a) Thermal connections to sample and sample platform in PPMS thermal transport option (adapted from [15]). (b) Sample being mounted on the puck. (c) The time dependence of the sample data, along with the fitted curves. The heater pulse is shown schematically as a yellow square wave (adapted from [15]). . . . .	43

2.7	(a) MuSR spectrometer at RAL, UK. (b) Longitudinal field (LF) and Zero field (ZF) geometry of a $\mu$ SR measurement. B and F stand for backward and forward detectors. (c) Transverse field (TF) geometry of a $\mu$ SR measurement. U and D denoted up and down detectors. (d) Typical $\mu$ SR spectra of a ZF measurement. (e) Typical $\mu$ SR spectra of a TF measurement. . . . .	45
2.8	A comparison of various spectroscopic techniques, adapted from STFC website [16]. . . . .	46
3.1	(a) Rietveld refinement of $\text{NaYbTe}_2\text{O}_7$ . (b) The unit cell of $\text{NaYbTe}_2\text{O}_7$ viewed along the $a$ axis. (c) Projection of the one-dimensional Yb-chains along $b$ -axis. (d) Possible exchange pathways between nearest magnetic ions. . . . .	53
3.2	Elemental mapping of $\text{NaYbTe}_2\text{O}_7$ sample with the help of FE-SEM. Various elements have been shown in different colors. . . . .	54
3.3	Elemental mapping spectra of the $\text{NaYbTe}_2\text{O}_7$ sample. . . . .	55
3.4	(a) Temperature dependence of dc magnetic susceptibility performed under ZFC and FC protocol down to 2 K. Inset shows the variation down to 0.4 K. (b) Isothermal magnetization curves measured at different temperatures along with the Brillouin fits represented by solid lines. The black dashed line accounts for the Van Vleck contribution. Inset shows the zoomed version of the fitting in low-field region. . . . .	55
3.5	(a) Fitting of low-temperature and high-temperature linear region of the inverse susceptibility data by using the Curie-Weiss model. (b) Fitting of the inverse susceptibility data with the help of the modified Curie-Weiss model. . . . .	56
3.6	Variation of frequency-dependent ac susceptibilities with temperature. . . . .	57
3.7	(a) Fitting of the heat capacity data measured in the absence of the magnetic field with the Debye-Einstein model. (b) Temperature dependence of heat capacity below 1 K and fitting with power law. (c) Temperature dependence of heat capacity data measured under different magnetic fields. The inset shows the variation in low-temperature regions. (d) Entropy calculated from magnetic heat capacity down to 0.285 K. Inset shows the temperature dependence of magnetic entropy calculated down to 2 K in the presence of different magnetic fields. . . . .	59
3.8	(a) Variation of Schottky contribution with temperature and its fitting with the two-level model equation. (b) Linear fitting of $\Delta$ (left axis) values calculated from the CEF fitting and variation of $n$ values with the magnetic fields . . . . .	60

3.9	(a) Temperature dependence of the thermal conductivity divided by temperature measured under different magnetic fields. (b) Fitting of $\kappa/T$ measured under 0 T with the equation described in the text. . . . .	62
3.10	Fitting of $\kappa/T$ versus $T$ data measured under different magnetic fields. . . .	63
4.1	(a) A crystal centered on the sample holder of a single crystal diffractometer. (b) Reciprocal lattice observed along the $c$ -axis. . . . .	73
4.2	A comparison between simulated pattern from single crystal data and powder x-ray diffraction data. . . . .	74
4.3	Observed and refined powder x-ray diffraction pattern of $\text{Yb}_2\text{Te}_5\text{O}_{13}$ . Bragg positions are shown in green color and the difference between experimental and calculated intensities is represented by the bottom solid blue line. . . .	74
4.4	(a) Single unit cell of $\text{Yb}_2\text{Te}_5\text{O}_{13}$ . (b) Stacking of the Yb-based two types of polyhedra in the $bc$ plane. (c) Stacking of Yb1-Yb2 dimers along the $a$ -axis. . . .	76
4.5	(a) Temperature dependence of dc magnetic susceptibility performed under ZFC and FC protocol down to 0.4 K. Inset shows the fitting of the inverse susceptibility data with the modified Curie-Weiss model. (b) Isothermal magnetization curves measured at different temperatures and the black dashed line account for the Van Vleck contribution. . . . .	77
4.6	(a) The fitting of high-temperature susceptibility data with the Curie-Weiss law. Inset shows the deviation from the linear regime below 125 K (b) Variation of effective moment $\mu_{eff} = [(3k_B/N_A\mu_B^2)\chi T]^{1/2} \sim 2.828\sqrt{\chi T}$ versus $T$ . Inset shows the variation below 1.8 K. . . . .	78
4.7	(a) Temperature dependence of the heat capacity in the absence of an applied magnetic field. The asterisk indicates an anomaly corresponding to $\text{Yb}_2\text{O}_3$ ( $T_N = 2.3$ K). Inset: Fitting of zero field heat capacity data using the Debye-Einstein model. (b) Temperature dependence of the magnetic entropy, derived from the heat capacity data, is depicted for different magnetic fields. . . . .	80
4.8	(a) Magnetic field dependence of the Schottky anomaly. Inset: Linear fitting of the $\Delta$ values from CEF fitting (right axis) and the variation of the $n$ values with magnetic field are presented. (b) The plot demonstrates the variation of the Schottky contribution with temperature, fitted with the two-level model equation. . . . .	81

4.9	(a) Zero field muon spin relaxation data measured at different temperatures. The solid lines show fits to the data using equation 4.3. (b) The temperature dependence of the relaxation rates obtained from the asymmetry fitting. The solid line depicts their fitting with the Orbach process (equation 4.4). (c) Longitudinal Field measurements are carried out at 70 mK in the presence of the different applied fields. (d) Field dependence of both the relaxation rates.	83
4.10	(a) The band structure and (b) the atom projected Density of States for $\text{Yb}_2\text{Te}_5\text{O}_{13}$ . From (b), it is clear that the bands in the gap are formed by the $f$ orbitals of Yb with significant contribution of O $p$ and Te $p$ orbitals near the Fermi level.	85
4.11	Spin exchange paths; $J_1$ shown in (a) and $J_2, J_3$ are shown in (b).	86
4.12	(a) The Structure Factor along the $c$ -axis in at 100 K and 30 K(inset) (b) the static structure factor at 50 K.	88
4.13	(a) and (b) depicts the $S_{qx}$ and $S_{qy}$ respectively at $T = 30$ K, while (c) and (d) denote the static structure factor along $a$ -axis and $b$ -axis for $T = 100$ K.	88
5.1	Rietveld refinement of the XRD data collected at 300 K. Experimental pattern, simulated pattern, difference, and Bragg position are shown by red open circles, black solid line, blue solid line, and green bars, respectively.	99
5.2	Rietveld refinement of the time of flight neutron diffraction data of $\text{LiYbSiO}_4$ . Red open circles indicate experimental data, the black solid line represents a simulated pattern, and blue solid lines represent the difference. Green bars indicate Bragg peaks of $\text{LiYbSiO}_4$ , while Maroon bars denote Bragg peaks of $\text{Yb}_2\text{O}_3$ . Star indicates a small peak coming from $\text{Yb}_2\text{O}_3$ .	100
5.3	(a) Single unit cell of $\text{LiYbSiO}_4$ . (b) Top view of the magnetic Yb sub-lattice in the $bc$ plane.	101
5.4	(a) Temperature dependence of dc magnetic susceptibility measured under ZFC and FC protocols down to 0.4 K. Inset shows fitting of the inverse susceptibility with the modified Curie-Weiss model. (b) Isothermal magnetization measured at different temperatures along with the Brillouin fits represented by solid lines. Black dashed line represents the Van Vleck contribution. Inset shows the zoomed version of the fitting in the low-field region.	102
5.5	(a) Temperature dependence of the susceptibility measured in the presence of three different magnetic fields by following the ZFC and FC protocol. (b) Variation of effective moment $\mu_{eff} = [(3k_B/N_A\mu_B^2)\chi T]^{1/2} \sim 2.828\sqrt{\chi T}$ versus $T$ . Inset shows the variation below 8 K.	103

5.6	(a) Isothermal magnetization curves collected at various temperatures. (b) AC susceptibility measurements variation on applying a small ac magnetic field of 10 Oe at various frequencies. . . . .	104
5.7	(a) Fitting of the heat capacity data measured in the absence of the magnetic field with the Debye-Einstein model. (b) Entropy calculated from magnetic heat capacity. To better observe the residual magnetic entropy, the $S_{mag}(T)$ curve is shifted vertically so that its maxima coincide with the $S_{mag}(T \rightarrow \infty)$ . Inset shows the temperature dependence of magnetic entropy in the presence of different magnetic fields. (c) Variation of Schottky contribution with temperature and its fitting with the two-level model equation. (d) Linear fitting of $\Delta$ (left axis) values calculated from the CEF fitting and variation of $n$ values with the magnetic fields. . . . .	106
5.8	Magnetic field dependence of Specific Heat from 2 to 100 K. Inset shows the variation below 30 K. . . . .	107
5.9	(a) Variation of thermal conductivity with temperature measured in the presence of various applied magnetic fields. (b) Magnetothermal conductivity measured at four different temperatures. . . . .	108
5.10	(a) Zero field $\mu$ SR spectra collected at different temperatures. Solid lines represent fits with simple exponential function. (b) Longitudinal field $\mu$ SR spectra collected in the presence of a 40 Oe magnetic field at various temperatures and solid lines represent their fitting with the dynamic Kubo-Toyabe function. (c) Evolution of the relaxation rate ( $\lambda$ ) (left axis) and parameter $\Delta$ (right axis) with temperature. . . . .	109
5.11	(a) Longitudinal $\mu$ SR spectra measured at 70 mK by varying the longitudinal fields from 0 to 400 Oe. The solid lines depict fitting with the dynamic Kubo-Toyabe function. (b) Field dependence of $\Delta$ . . . . .	111
5.12	(a) Time dependence of $\mu^+$ asymmetry in a weak transverse magnetic field 20 Oe at three different temperatures. The solid line depicts a fitting with equation 7.5. (b) Change in the relaxation rate with temperature. . . . .	112
5.13	(a) Crystal structure of orthorhombic ( $Pnma$ ) $\text{LiYbSiO}_4$ , (b) shows Brillouin zone and high-symmetry path. (c) and (d) show the arrangement of Yb atoms in the structure from the side and top directions, respectively. Note that the Yb atoms form a 2D square network, stacked along $a$ direction. Yb atoms from different layers are shown in different colors and all the other atoms are removed in (c)–(d) for clarity. . . . .	114



5.14	(a) The electronic structure and orbital projected density of states (PDOS) of $\text{LiYbSiO}_4$ (LYSO), which reveals LYSO is a metal. (c) shows the same in a zoomed view, which reveals that states at the Fermi level are dominated by Yb-4 <i>f</i> and O-2 <i>p</i> orbitals. (b) displays the same with spin-orbit coupling, which opens a band gap of 0.45 eV. The zoomed view in (d) reveals that the states near the valence band are primarily dominated by O-2 <i>p</i> orbitals. In contrast, those near flat conduction bands are constituted by highly localized 4 <i>f</i> orbitals of Yb atoms. . . . .	115
5.15	Bottom and top layers of three antiferromagnetic ordering considered for exchange coupling calculations (a) Neel antiferromagnet, (b) A-type antiferromagnet, and (c) Columnar antiferromagnet. . . . .	116
5.16	Visualization of the spin density of the AFM3 configuration of LYSO reveals that the magnetization is concentrated on Yb sites and O (nearby Yb) atoms also carry significant moment. This indicates the magnetic exchange interaction is happening through oxygen <i>p</i> -orbitals. The yellow color denotes positive magnetization, and cyan denotes negative. . . . .	118
5.17	(a) Exchange interactions in the Yb atomic sub-lattice in the <i>bc</i> plane, $J_1$ , and $J_2$ representing nearest and next nearest coupling and (b) out-of-the plane exchange interaction $J_3$ along <i>a</i> -axis. . . . .	119
6.1	(a) Pressure-dependent evolution of energy-dispersive x-ray diffraction (EDXRD) profiles at room temperature. (b) Change in EDXRD pattern at a constant pressure of 9 GPa. (c) Indexed EDXRD profile after quenching the temperature and removing the pressure. The fluorescence peaks of Yb, W, and Pb are also indexed. . . . .	131
6.2	Rietveld refinement of the room temperature angle dispersive x-ray diffraction pattern. Experimental pattern, simulated pattern, difference, and Bragg positions are depicted by red open circles, black solid line, blue solid line, and green bars, respectively. . . . .	132
6.3	The crystal structure of $\text{NaYbZnWO}_6$ viewed along the (a) <i>c</i> - and (b) <i>b</i> -directions. The six-coordinate $\text{Zn}^{2+}$ and $\text{W}^{6+}$ cations form an ordered perovskite framework, while the $\text{Na}^+$ and $\text{Yb}^{3+}$ cations form layers parallel to the <i>ab</i> plane, which alternate along the <i>c</i> -direction. (c) The distorted square lattice of $\text{Yb}^{3+}$ cations. . . . .	133

6.4	(a) Temperature dependence of dc magnetic susceptibility performed under ZFC and FC protocol down to 0.4 K. Inset shows the fitting of inverse susceptibility data with modified Curie-Weiss law. (b) Isothermal magnetization curves measured at different temperatures along with the Brillouin fits represented by solid lines. The black dashed line accounts for the Van Vleck contribution. The inset shows a zoomed-in view of the fitting at lower fields. The $\chi^2$ values for the fitting for 0.4, 1, and 1.5 K are 0.9696, 0.9901, and 0.9972, respectively. . . . .	134
6.5	Variation of frequency-dependent ac susceptibilities with temperature. . . .	135
6.6	(a) Fitting of the specific heat data measured in the absence of the magnetic field with the Debye-Einstein model. (b) Entropy calculated from magnetic specific heat. To better observe the residual magnetic entropy, the $S_{mag}(T)$ curve is shifted vertically so that its maxima coincide with the $S_{mag}(T \rightarrow \infty)$ . Inset shows the temperature dependence of magnetic entropy in the presence of different magnetic fields. (c) Variation of Schottky contribution with temperature and its fitting with the two-level model equation. (d) Linear fitting of $\Delta$ (left axis) values calculated from the CEF fitting and variation of $n$ values with the magnetic fields. . . . .	136
6.7	(a) Temperature dependence of specific heat data measured under different magnetic fields. The inset shows the variation in low-temperature regions. (b) Fitting of the Schottky contribution using the three-level model. . . . .	138
6.8	(a) Four spin exchange paths $J_1$ – $J_4$ defined for a distorted square of four $\text{Yb}^{3+}$ ions in a kite arrangement. The red labels 1–4 represent the spin exchange paths $J_1$ – $J_4$ , respectively. The black label 1–4 represents the Yb...Yb distances in the spin exchange paths $J_1$ – $J_4$ , respectively. (b) The $\text{WO}_6$ octahedra surround a distorted square of $\text{Yb}^{3+}$ ions. They provide the Yb–O... $\text{W}^{6+}$ ...O–Yb exchange paths. (c) The relative spin exchanges $R_i = J_i/J_1$ ( $i = 1$ –4) obtained from DFT+ $U$ and DFT+ $U$ +SOC calculations. . . . .	140
7.1	Rietveld refinement of the X-ray diffraction pattern collected at $T = 300$ K. Experimental pattern, simulated pattern, difference, and Bragg peaks are represented by red open circles, solid black line, blue solid line, and green color, respectively. . . . .	153

7.2	(a) Atomic arrangement of different ions in the unit cell. Co1 and Co2 octahedra are shown in blue color. (b) Top view of the magnetic lattice in the $ab$ plane. (c) Sides of an isosceles triangle of $\text{Co}^{2+}$ ions. (d) Co1 octahedra are perfectly parallel to each other along the $b$ axis. . . . .	155
7.3	(a) Temperature dependence of dc magnetic susceptibility performed under ZFC down to 0.4 K. Inset shows zoomed version from 0.4 to 20 K. (b) Solid lines of blue and red color represent fitting of low-temperature and high-temperature linear region of the inverse susceptibility data by using the Curie-Weiss model, while yellow dotted line represents fitting of the inverse susceptibility data with the help of the modified Curie-Weiss model. . . . .	155
7.4	(a) Variation of the frequency-dependent real part of ac susceptibilities with temperature. (b) Temperature dependence of imaginary part of the ac susceptibilities at different frequencies. . . . .	157
7.5	(a) Field dependence of the magnetization under isothermal conditions at 0.4 and 0.8 K. (b) First order derivative of magnetization showing anomalies at $1/3$ and $2/3$ of $M_S$ . . . . .	158
7.6	(a) Heat capacity data measured in the temperature range from 370 mK to 100 K and its fitting with the Debye-Einstein model equation 7.2. (b) Temperature dependence of the magnetic entropy calculated from magnetic heat capacity. Inset shows the variation of magnetic heat capacity calculated from the total heat capacity measured in the presence of various magnetic fields from 0 to 14 T. . . . .	158
7.7	Change in the exponent of the power law with respect to the applied magnetic fields. . . . .	160
7.8	(a) Temperature dependence of the zero field MuSR measurements and solid lines represent fitting with a combination of two exponential functions. Temperature dependence of the relaxation rates, $\lambda_1$ and $\lambda_2$ is shown in (b) and (c), respectively. . . . .	161
7.9	(a) Field dependence of MuSR spectra measured at 100 mK. (b) and (c) show field dependence of relaxation rates and their fitting with the Redfield equation. . . . .	163
7.10	$\mu\text{SR}$ spectra collected at three different temperatures in the presence of a weak transverse magnetic field. The solid line represents its fit with eq. 7.5. . . . .	164
7.11	(a) Temperature dependence of thermal conductivity in the presence of different applied magnetic fields. (b) Variation of $a$ and $\alpha$ parameters with magnetic field. . . . .	165

7.12	Four ordered spin states: (a) ferromagnet (FM), (b) antiferromagnet (AFM)1, (c) AFM2, and (d) AFM3 state. The orange circles indicate the down spin $\text{Co}^{2+}$ ion sites. . . . .	168
7.13	Various exchange interactions present in the triangular lattice. . . . .	169
7.14	(a) Single layer of $\text{CoO}_6$ octahedra viewed along the $c$ direction. (b) A single layer of $\text{CoO}_4$ square planes, which result when the elongated Co-O bonds are removed. . . . .	170
8.1	(a) Observed and refined powder x-ray diffraction pattern of $\text{NaYbW}_2\text{O}_8$ . The Bragg positions are marked in green. The bottom solid blue line represents the difference between experimental and calculated intensities. (b) Arrangement of the atoms in the $ac$ plane viewed along the $b$ axis. (c) Hyper-Honeycomb magnetic lattice formed by Na/Yb ions. . . . .	182
8.2	(a) Temperature dependence of the magnetic susceptibility measured under ZFC and FC protocol down to 0.4 K. Inset shows the fitting of the inverse susceptibility data with two-level Curie-Weiss model. (b) Field-dependent isothermal magnetization curves at 0.4, 1, and 1.5 K. The dashed line shows a linear fit to higher field data. . . . .	184
8.3	(a) Heat Capacity measured from 2 to 100 K in the absence of the magnetic field and its fitting with the Debye Einstein model. (b) Entropy calculated from magnetic heat capacity. Inset shows the temperature dependence of magnetic entropy in the presence of different magnetic fields. (c) Heat capacity measured under different magnetic fields up to 9 T, and the inset shows the variation of the heat capacity at low temperatures. (d) Temperature dependence of the Schottky contribution and its fitting with the two-level Schottky equation 8.8.	186
8.4	Linear fitting of $\Delta/k_B$ (left axis) values calculated from the CEF fitting and variation of $f$ values with the magnetic fields. . . . .	187
8.5	(a) Temperature dependence of thermal conductivity measured in the presence of different applied fields. (b) Change in thermal conductivity with field at two different temperatures, 2 and 10 K. . . . .	187
8.6	(a) Fitting of the ZF $\mu\text{SR}$ spectra collected at various temperatures with single exponential function. (b) Temperature variation of the relaxation rate ( $\lambda$ ) and its fitting with Orbach equation. . . . .	188

8.7	(a) and (b) shows a schematic representation of the nearest and next nearest neighbors in lattice A. (c) and (d) The nearest and next nearest pairs in lattice B. It is clear that lattice A is geometrically frustrated and that such geometric frustration is absent in lattice B. Lattice A has two nearest neighbors and four nearest neighbors as compared to lattice B, which has four nearest neighbors and eight nearest neighbors. . . . .	190
8.8	The energy per spin, $e$ , for various linear system sizes $L$ (a) for lattice A and (b) lattice B. The energy per spin remains almost the same for varying $L$ . . .	191
8.9	(a) The equal time structure factor of lattice A from Iterative Minimisation for $L = 10$ at 1 K. The peaks in this case occur at $(\frac{\pm 1}{2}, \frac{\pm 3}{10}, \frac{\pm 3}{10})$ . (b) The equal time structure factor at 5 K ( $T > T_C$ ). The peaks are diffused about the peaks in (a). . . . .	192
8.10	(a) The equal time structure factor of lattice B from Iterative Minimisation for $L = 16$ at $T = 0.1$ K (b) The equal time structure factor at 1 K ( $T > T_C$ ). The peaks are broad and diffused about the peaks in (a) . . . . .	193

# Table of Contents

<b>Dedication</b>	<b>i</b>
<b>Abstract</b>	<b>ii</b>
<b>Declaration</b>	<b>iii</b>
<b>Certificate</b>	<b>iv</b>
<b>Acknowledgements</b>	<b>v</b>
<b>Publications</b>	<b>vii</b>
<b>List of Tables</b>	<b>ix</b>
<b>List of Figures</b>	<b>xii</b>
<b>1 Magnetic Frustration and Quantum Spin Liquid</b>	<b>1</b>
1.1 Frustration . . . . .	2
1.1.1 Residual Entropy of Ice . . . . .	2
1.1.2 Protein Folding Dynamics . . . . .	3
1.1.3 Amorphous Solids . . . . .	5
1.1.4 Liquid Crystals . . . . .	6
1.1.5 Frustration in Magnetism . . . . .	7
1.2 Origin of Frustration in Magnets . . . . .	8
1.2.1 Geometrical Frustration . . . . .	8
1.2.2 Competing Exchange Interactions . . . . .	9
1.2.3 Bond-dependent Exchange Interaction . . . . .	10
1.3 Consequences of Magnetic Frustration . . . . .	12

1.3.1	Incommensurate Magnetic Structure . . . . .	12
1.3.2	Magnetostructural Transition . . . . .	12
1.3.3	Spin Glass . . . . .	12
1.3.4	Spin Ice . . . . .	13
1.3.5	Spin Liquid . . . . .	13
1.4	Quantum Spin Liquid . . . . .	14
1.4.1	Long-Range Quantum Entanglement . . . . .	15
1.4.2	Fractionalized Excitations . . . . .	15
1.4.3	Potential Applications of a QSL . . . . .	16
1.4.4	Challenges and Opportunities . . . . .	17
1.4.5	Primary Ingredients of a QSL . . . . .	18
1.5	Aim of the Thesis . . . . .	20
<b>Bibliography</b>		<b>22</b>
<b>2 Experimental Techniques</b>		<b>29</b>
2.1	Sample Synthesis . . . . .	30
2.1.1	Solid-State Synthesis . . . . .	30
2.1.2	High-Pressure and High-Temperature Synthesis Technique . . . . .	31
2.2	Structural Characterization . . . . .	33
2.2.1	X-ray and Neutron Diffraction . . . . .	33
2.2.2	Rietveld Refinement . . . . .	34
2.3	Physical Properties Measuremetns . . . . .	37
2.3.1	DC Magnetization . . . . .	37
2.3.2	AC Magnetization Measurements . . . . .	40
2.3.3	Heat Capacity Measurement . . . . .	41
2.3.4	Thermal Conductivity Measurements . . . . .	42
2.3.5	Muon Spin Relaxation Measurements . . . . .	43
<b>Bibliography</b>		<b>48</b>
<b>3 Exploring Potential Quantum Spin Liquid State in a Quasi-One Dimensional Magnetic Chain</b>		<b>50</b>
3.1	Introduction . . . . .	51
3.2	Experiment . . . . .	52
3.3	Results and Discussion . . . . .	52
3.3.1	Crystal Structure . . . . .	52

3.3.2	DC Magnetization . . . . .	53
3.3.3	Heat Capacity . . . . .	58
3.3.4	Thermal Conductivity . . . . .	61
3.4	Conclusion . . . . .	63
<b>Bibliography</b>		<b>65</b>
<b>4 Dynamic Magnetic Ground State in a Dimer Based Compound</b>		
<b>Yb<sub>2</sub>Te<sub>5</sub>O<sub>13</sub></b>		<b>71</b>
4.1	Introduction . . . . .	72
4.2	Experimental . . . . .	72
4.2.1	Single Crystal Synthesis and Refinement . . . . .	72
4.2.2	Polycrystalline Sample Synthesis and Refinement . . . . .	73
4.2.3	Characterization . . . . .	75
4.3	Results and Discussion . . . . .	76
4.3.1	Crystal Structure . . . . .	76
4.3.2	DC Magnetization . . . . .	77
4.3.3	Heat Capacity . . . . .	79
4.3.4	Muon Spin Relaxation Measurements . . . . .	82
4.3.5	Theoretical Calculation . . . . .	84
4.4	Conclusion . . . . .	89
<b>Bibliography</b>		<b>90</b>
<b>5 Quantum Spin-Liquid in a Two-Dimensional Magnetic Rhombus</b>		
<b>Lattice: An Exploration</b>		<b>96</b>
5.1	Introduction . . . . .	97
5.2	Experiment . . . . .	97
5.3	Results and Discussion . . . . .	98
5.3.1	Crystal Structure . . . . .	98
5.3.2	DC Magnetization . . . . .	102
5.3.3	Heat Capacity . . . . .	104
5.3.4	Thermal Conductivity . . . . .	108
5.3.5	Muon Spin Relaxation ( $\mu$ SR) Measurements . . . . .	109
5.3.6	Theoretical Calculation . . . . .	113
5.3.7	Origin of Dynamic State . . . . .	119
5.4	Conclusion . . . . .	120



<b>Bibliography</b>	<b>121</b>
<b>6 Spin Frustration in a Distorted Square Lattice of NaYbZnWO<sub>6</sub> Prepared Under High Pressure</b>	<b>128</b>
6.1 Introduction . . . . .	129
6.2 Experiment . . . . .	129
6.3 Results and Discussion . . . . .	130
6.3.1 Crystal Structure . . . . .	130
6.3.2 DC Magnetization . . . . .	133
6.3.3 Heat Capacity . . . . .	136
6.3.4 Theoretical Calculation . . . . .	139
6.3.5 Origin of Frustration . . . . .	143
6.4 Conclusion . . . . .	144
<b>Bibliography</b>	<b>145</b>
<b>7 Sr<sub>3</sub>CoNb<sub>2</sub>O<sub>9</sub>: A New Triangular Lattice-Based Kitaev Model Candidate</b>	<b>150</b>
7.1 Introduction . . . . .	151
7.2 Experimental . . . . .	152
7.3 Results . . . . .	153
7.3.1 Crystal Structure . . . . .	153
7.3.2 DC Magnetization . . . . .	156
7.3.3 Heat Capacity . . . . .	157
7.3.4 Muon Spin Relaxation Measurements . . . . .	159
7.3.5 Thermal Conductivity Measurements . . . . .	165
7.3.6 Energy Mapping Analysis . . . . .	166
7.3.7 Fundamental Question To Resolve . . . . .	169
7.4 Conclusion . . . . .	170
<b>Bibliography</b>	<b>172</b>
<b>8 Magnetic Frustration in a Hyperhoneycomb Compound NaYbW<sub>2</sub>O<sub>8</sub></b>	<b>177</b>
8.1 Introduction . . . . .	178
8.2 Experimental . . . . .	179
8.3 Computational Methods . . . . .	179
8.4 Results and Discussion . . . . .	181
8.4.1 Crystal Structure . . . . .	181

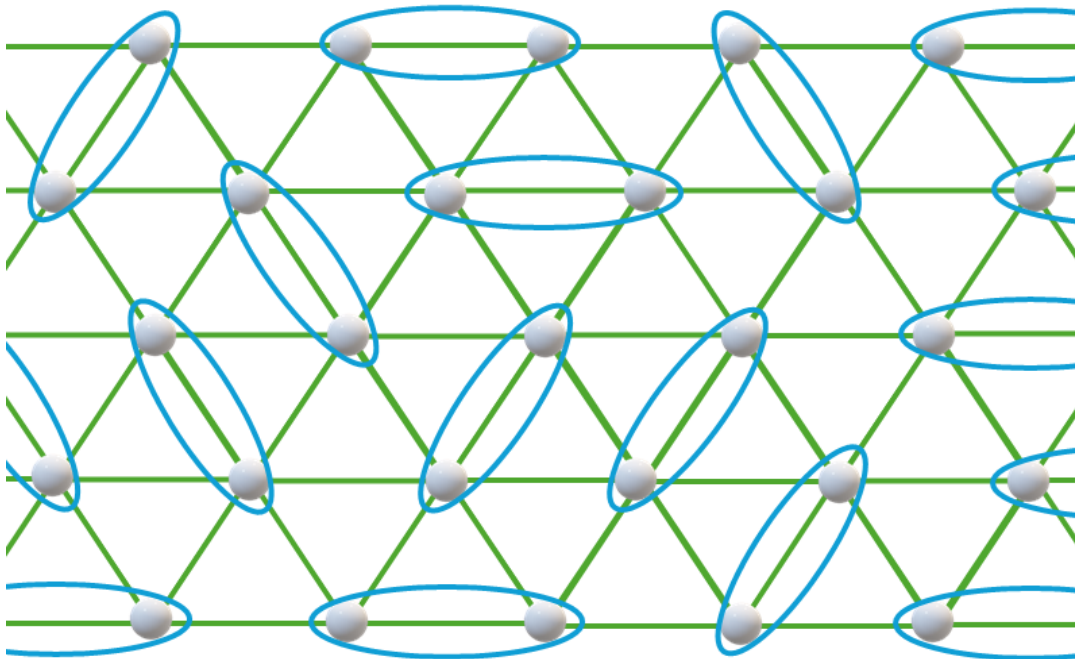
8.4.2	DC magnetization . . . . .	182
8.4.3	Heat Capacity . . . . .	184
8.4.4	Thermal Conductivity Measurements . . . . .	187
8.4.5	Muon Spin Relaxation Measurements . . . . .	188
8.4.6	Spin Exchange Interaction Calculation . . . . .	189
8.5	Conclusion . . . . .	193
<b>Bibliography</b>		<b>195</b>

# Chapter 1

## Magnetic Frustration and Quantum Spin Liquid

*“People need trouble - a little frustration to sharpen the spirit on, toughen it. Artists do; I don’t mean you need to live in a rat hole or gutter, but you have to learn fortitude, endurance. Only vegetables are happy.”*

— William Faulkner, Nobel Prize Winner in Literature, 1949.



## 1.1 Frustration

Frustration, in a broad sense, can be thought of as the experience of facing obstacles or challenges that prevent things from easily falling into place. This concept is not just limited to human emotions but is also found in nature. For instance, imagine trying to fit a group of friends around a small, round table where everyone wants to sit directly across from someone else; it's impossible to satisfy everyone's preference at the same time. Similarly, in nature, frustration can be observed in the interactions of certain systems such as magnets, plants, and animal groups. These systems often face competing forces that stop them from achieving a perfectly organized state. Instead, they find a balance that is a bit more complex but allows for unique and diverse patterns. This kind of natural frustration helps create the rich variety and adaptability we see in the world around us. A few examples of frustration in nature, ranging from microscopic to macroscopic scale, are described below.

### 1.1.1 Residual Entropy of Ice

Residual entropy in water ice is a fascinating phenomenon that highlights the complex interplay between order and disorder in nature. As water freezes into ice, its molecules arrange themselves into a tetrahedral lattice, where each oxygen atom forms hydrogen bonds with four neighboring oxygen atoms. However, the positions of the hydrogen atoms are not fixed; they can occupy multiple configurations while still adhering to the “ice rules” (each oxygen has two hydrogen atoms close to it and two far away).

This flexibility leads to a situation known as geometric frustration, where all the hydrogen bonds cannot be simultaneously satisfied in a perfectly ordered manner. As a result, even at temperatures approaching absolute zero, water ice retains a significant degree of disorder in the positioning of its hydrogen atoms. This persistent disorder is quantified as residual entropy.

First proposed by Linus Pauling in 1935 [1], residual entropy reflects the multitude of possible configurations for the hydrogen atoms in the ice lattice. Pauling estimated that the residual entropy of ice is  $Nk_B \ln(3/2)$ , where  $N$  is the number of water molecules and  $k_B$  is the Boltzmann constant. Experimental measurements have confirmed this theoretical prediction, showing that the entropy of ice does not reach zero as temperature decreases but instead levels off to the finite value.

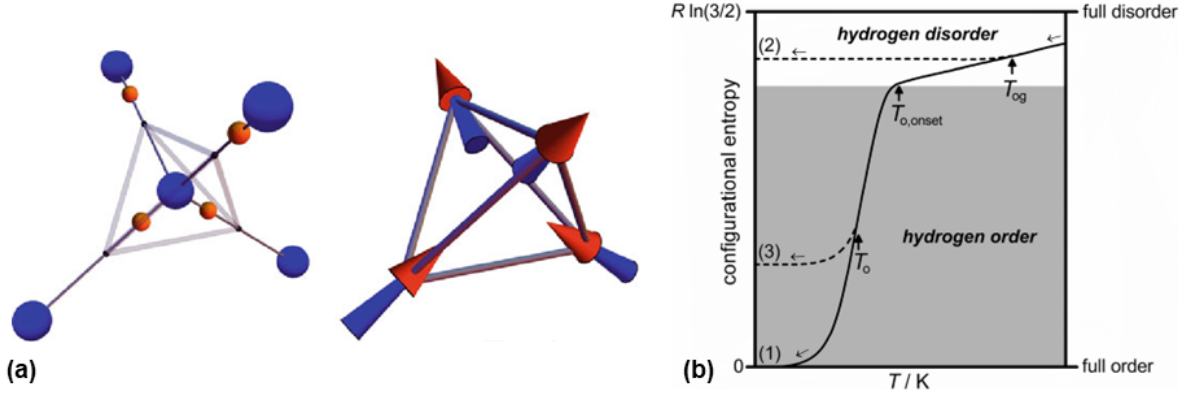


Figure 1.1: (a) Arrangement of oxygen (in blue color) and hydrogen (in red color) atom in a tetrahedron environment. The right side tetrahedron illustrates the equivalent spins for each O-H bond (adapted from [2], reproduced with permission from Springer Nature). (b) Change in residual entropy when hydrogen disorder changes (adapted from [3], reproduced with permission from Royal Society of Chemistry).

### 1.1.2 Protein Folding Dynamics

Frustration in protein folding dynamics is a crucial concept that sheds light on the complex behavior of proteins as they achieve their functional three-dimensional structures [4, 5]. Proteins are made up of long chains of amino acids that must fold into specific shapes to perform their biological roles effectively. The process of protein folding is driven by various interactions, including hydrogen bonding, hydrophobic effects, van der Waals forces, and electrostatic interactions.

Frustration in this context arises because not all interactions can be simultaneously optimized. In a protein molecule, certain regions might prefer to fold in a way that maximizes hydrogen bonding, while other regions might prioritize hydrophobic interactions. These competing demands create a “frustrated” energy landscape, where the protein has to navigate through many local energy minima before finding its most stable, functional configuration.

This frustrated energy landscape is characterized by a multitude of intermediate states and folding pathways, leading to a highly dynamic and complex folding process, as depicted in Fig. 1.2. Rather than a smooth descent to the lowest energy state, the protein’s journey involves overcoming energy barriers and sometimes even misfolding, where it gets trapped in non-functional shapes.

Despite this complexity, proteins are remarkably efficient at folding, often within

## Protein Folding Dynamics

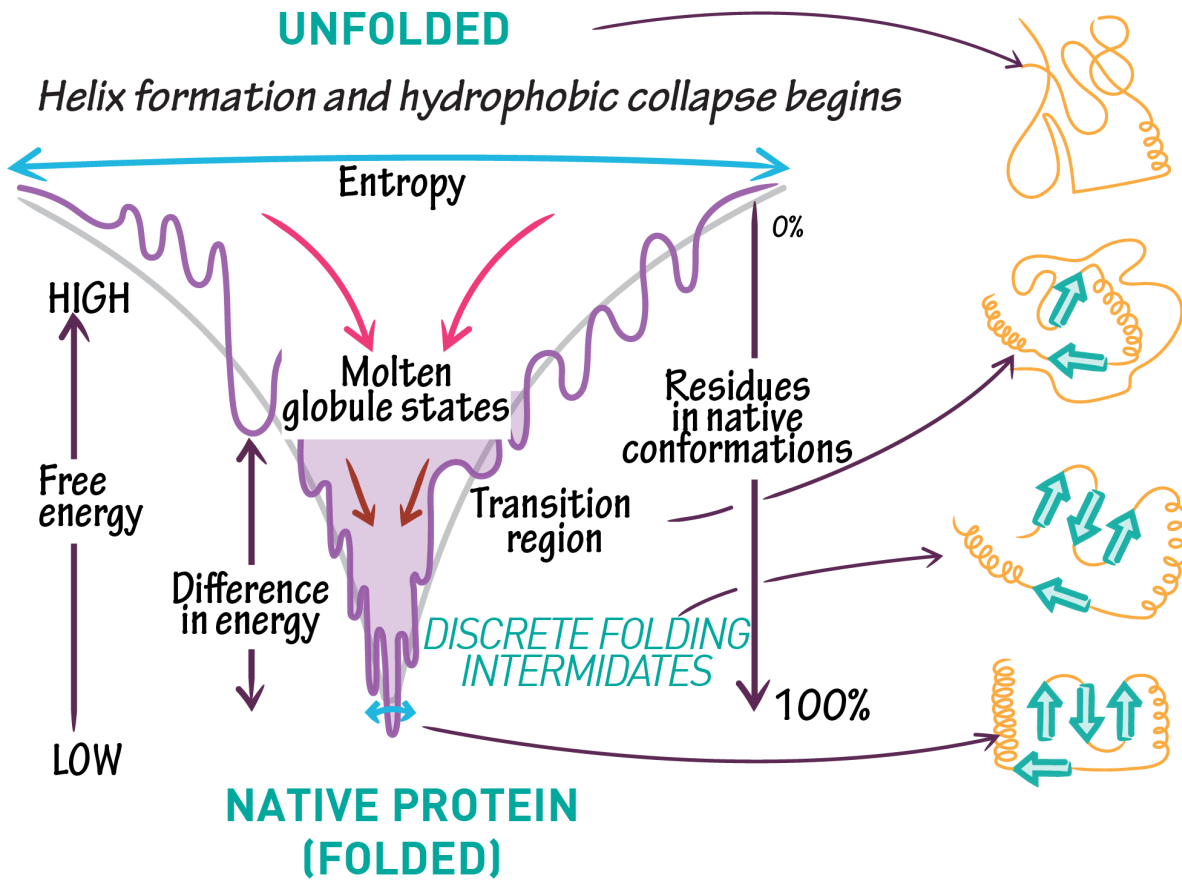


Figure 1.2: Rugged energy landscape of protein folding dynamics (adapted from [6])

milliseconds to seconds. Molecular chaperones and the cellular environment play a significant role in guiding proteins toward their correct conformations, minimizing the effects of frustration.

Understanding frustration in protein folding dynamics is essential for insights into various biological processes and diseases. Misfolded proteins are associated with numerous health conditions, including Alzheimer's, Parkinson's, and prion diseases [7]. By studying how frustration influences folding, researchers can develop strategies to prevent or correct

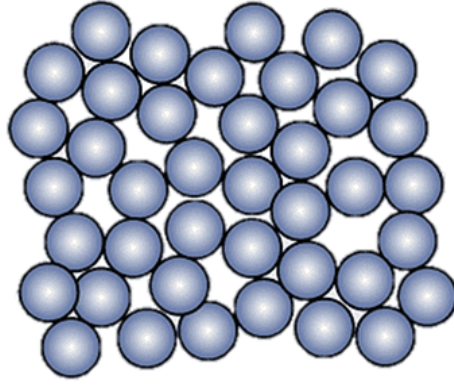


Figure 1.3: Arrangement of atoms in a amorphous solid (adapted from [8]).

misfolding, leading to potential therapeutic advancements.

### 1.1.3 Amorphous Solids

Frustration in amorphous solids, such as glasses and certain polymers, plays a crucial role in determining their unique structural and dynamic properties. Unlike crystalline solids, where atoms are arranged in an orderly and repeating pattern, amorphous solids lack long-range order [9], as shown in Fig. 1.3. This disordered arrangement is a direct result of geometric frustration, where the local interactions between atoms or molecules prevent the formation of a regular lattice.

In amorphous solids, frustration arises because the local atomic arrangements attempt to satisfy multiple competing constraints simultaneously, much like in a glass. For instance, in metallic glasses, atoms try to pack densely to minimize free volume, but they also need to accommodate varying atomic sizes and bonding preferences [10, 11]. This leads to a complex, disordered structure with a high degree of local ordering that does not extend uniformly throughout the material.

The frustration in amorphous solids has significant implications for their physical properties. One key characteristic is the presence of a broad range of energy states, leading to a complex energy landscape with many local minima. This results in slow dynamics and non-exponential relaxation processes, as the system can become trapped in various metastable states. Such behavior is observed in the glass transition, where the material transitions from a supercooled liquid to a rigid but disordered solid [12].

Additionally, the mechanical properties of amorphous solids are strongly influenced

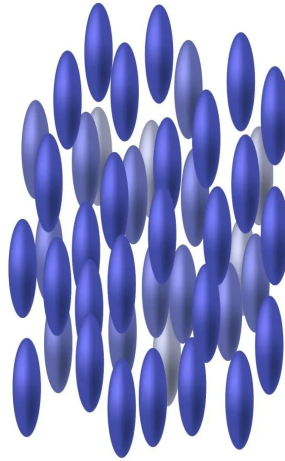


Figure 1.4: Illustration of the nematic phase of the liquid crystals (adapted from [14]).

by frustration. These materials often exhibit unique behaviors such as high strength and toughness, which are attributed to their ability to distribute stress more evenly compared to crystalline counterparts [13]. The absence of long-range order also contributes to their distinctive thermal and electrical properties.

#### 1.1.4 Liquid Crystals

Frustration in liquid crystals is a phenomenon that significantly influences their unique properties and behaviors. Liquid crystals are materials that exhibit phases with properties intermediate between those of conventional liquids and solid crystals [15]. They possess a degree of long-range order that distinguishes them from ordinary liquids but lack the complete three-dimensional periodicity of solid crystals.

Frustration in liquid crystals arises from competing interactions and geometric constraints within their molecular arrangements. Liquid crystal molecules typically have anisotropic shapes, such as rod-like or disk-like structures, which tend to align with each other to minimize free energy. However, when confined to certain geometries or subjected to external fields, these molecules experience competing alignments that cannot be simultaneously satisfied. This competition leads to frustration, where the system cannot achieve a perfectly ordered state.

One notable example of frustration in liquid crystals is found in the nematic phase [15, 16], as shown in Fig. 1.4, where molecules are oriented along a common axis but do



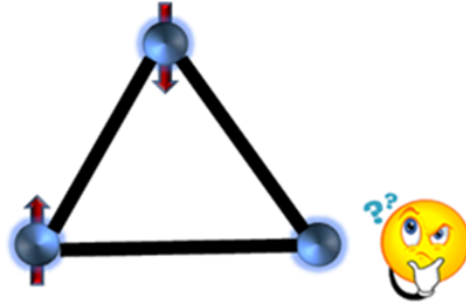


Figure 1.5: Antiferromagnetically coupled triangular lattice in which all the exchange interactions can not be satisfied simultaneously.

not possess positional order. When nematic liquid crystals are confined in geometrically constrained environments, such as within droplets or between substrates with different anchoring conditions, the molecules experience frustration. The boundary conditions force the liquid crystal molecules to adopt configurations that balance the competing alignments imposed by the constraints, leading to complex and sometimes intricate defect structures.

Frustration in liquid crystals is crucial for understanding their diverse applications, including displays, sensors, and tunable photonic devices [17, 18]. By manipulating the conditions that lead to frustration, scientists can design liquid crystal systems with tailored properties for specific technological uses.

### 1.1.5 Frustration in Magnetism

Magnetic frustration occurs when competing interactions between magnetic moments in a material prevent the system from achieving a single, well-ordered ground state. This leads to highly degenerate ground states and complex magnetic behaviors [19–21]. In simple terms, frustration arises from competing interactions among spins, such as in antiferromagnetic materials on triangular (as depicted in Fig. 1.5), or tetrahedral lattices, where it is impossible for all neighboring spins to align antiparallelly without conflicting with each other.

Frustration leads to exotic magnetic phenomena such as spin liquids, where spins remain disordered down to very low temperatures, and emergent quasiparticles, like magnetic monopoles in spin ice. These frustrated systems have potential applications in quantum computing and novel magnetic storage technologies due to their unique properties.

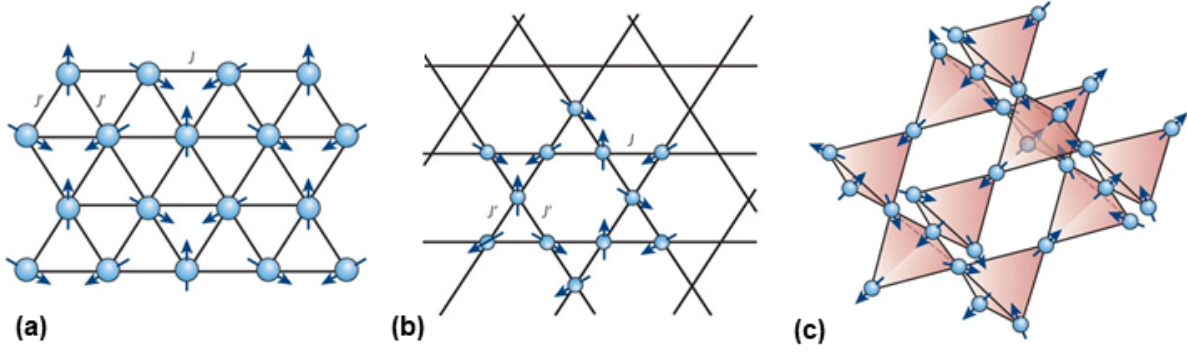


Figure 1.6: (a) Triangular Lattice, (b) Kagome Lattice, and (c) Pyrochlore Lattice. (adapted from [20], reproduced with permission from Springer Nature)

## 1.2 Origin of Frustration in Magnets

In magnetic systems, frustration can occur due to three primary reasons: the geometry of the magnetic lattice, competing exchange interactions, and bond-dependent interactions. These scenarios are pivotal in understanding complex magnetic behaviors, and they are described in detail below.

### 1.2.1 Geometrical Frustration

Geometrical frustration in magnetic systems arises when the spatial arrangement of spins prevents them from achieving a state where all interactions are minimized. This is notably observed in triangular, kagome, and pyrochlore lattices.

#### Triangular Lattice

In the triangular lattice, each spin is surrounded by three neighbors. Antiferromagnetic interactions on this lattice create a scenario where not all spins can align antiparallel to their neighbors, leading to a high degree of frustration. This type of lattice, as depicted in Fig. 1.6(a), is present in materials like  $\text{YbMgGaO}_4$  [22] and  $\text{NaYbO}_2$  [23], which exhibit complex magnetic behaviors due to this frustration.

#### Kagome Lattice

The kagome lattice, composed of corner-sharing triangles, enhances the frustration experienced by spins due to its unique connectivity, as depicted in Fig. 1.6(b). Similar to the triangular lattice, each spin in the kagome lattice is frustrated because it can-

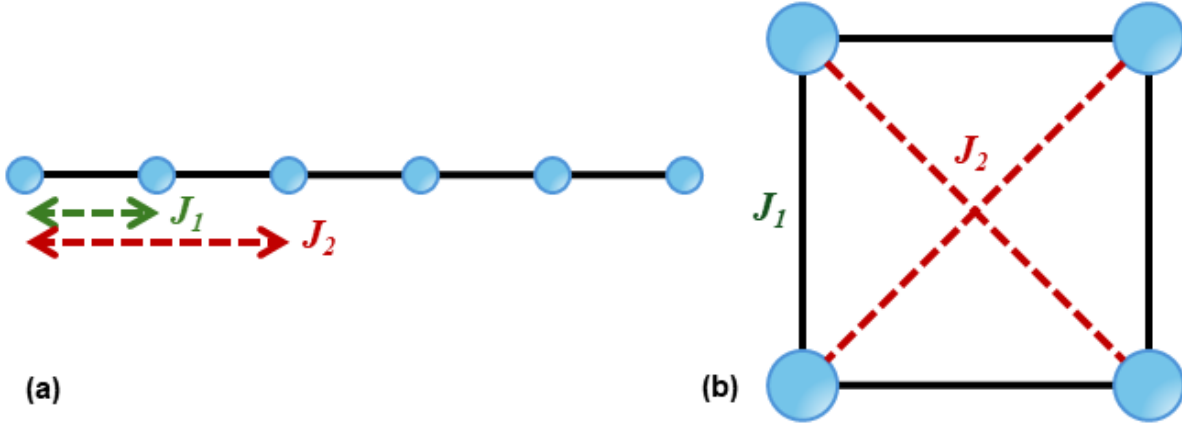


Figure 1.7: Nearest neighbor and next neighbor interactions are shown in (a) one-dimensional lattice and (b) square lattice.

not simultaneously satisfy all antiferromagnetic interactions. This results in a highly degenerate ground state and can lead to exotic magnetic phases such as spin liquids. Herbertsmithite [24, 25] is a well-known material that demonstrates the kagome lattice structure and its associated magnetic properties.

### Pyrochlore Lattice

The pyrochlore lattice, consisting of corner-sharing tetrahedra, as illustrated in Fig. 1.6(c), exhibits three-dimensional frustration. In antiferromagnetic pyrochlore materials, spins adhere to “ice rules,” where each tetrahedron has two spins pointing in and two pointing out. This rule creates a macroscopically degenerate ground state, leading to interesting phenomena such as magnetic monopoles. Examples of materials with pyrochlore lattices include  $\text{Dy}_2\text{Ti}_2\text{O}_7$  and  $\text{Ho}_2\text{Ti}_2\text{O}_7$  [26, 27].

### 1.2.2 Competing Exchange Interactions

In magnetic systems, frustration can also arise from competing exchange interactions, where different magnetic interactions vie to align spins in opposing ways. This competition can occur between nearest-neighbor (NN) and next-nearest-neighbor (NNN) spins or between different types of magnetic ordering, such as ferromagnetic and antiferromagnetic interactions. This type of frustration has been observed in one-dimensional (1D) and square magnetic lattices.

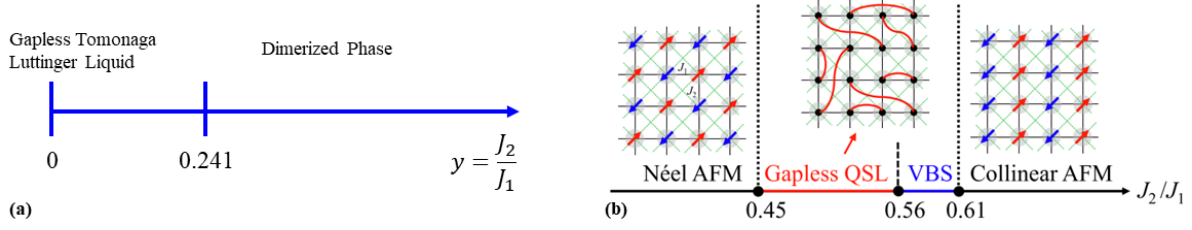


Figure 1.8: Various magnetic phases predicted from  $J_1$ - $J_2$  model calculation for (a) a one-dimensional lattice [32], (b) a square lattice (adapted from [38], reproduced with permission from Elsevier).

### One-dimensional Lattice

In 1D spin chains, frustration typically arises from competing NN and NNN antiferromagnetic interactions, often described by the  $J_1$ - $J_2$  model [28–30]. When the NNN interaction ( $J_2$ ) is strong relative to the NN interaction ( $J_1$ ), the system cannot achieve a straightforward antiferromagnetic order [31]. Instead, it can form complex ground states, such as a dimerized or a helical phase. For  $J_2 = 0$ , the chain behaves like a gapless Heisenberg antiferromagnet, but as  $J_2$  increases such that  $J_2/J_1 \approx 0.241$ , the system transitions to a gapped dimerized state, as depicted in Fig. 1.8(a). At the specific Majumdar-Ghosh point,  $J_2/J_1 = 0.5$ , the ground state consists of alternating singlet bonds along the chain. This model demonstrates how frustration in one-dimensional spin systems can lead to a transition from gapless behavior to a gapped, disordered phase [32].

### Square Lattice

In a square lattice, frustration can result from the competition between NN and NNN interactions. For example, in a classical antiferromagnet with NN interactions, each spin prefers to align antiparallel to its neighbors. However, introducing a significant NNN interaction can disrupt this simple ordering. When these interactions are of comparable strength, the system struggles to find a configuration that satisfies both types of interactions simultaneously [33–37]. This can lead to a rich variety of ground states, as shown in Fig. 1.8(b), including collinear and spiral spin structures and, in some cases, spin liquids [38].

### 1.2.3 Bond-dependent Exchange Interaction

Frustration in magnetic systems can also stem from bond-dependent exchange interactions, where the preferred alignment of spins depends on the direction or nature of the bonds

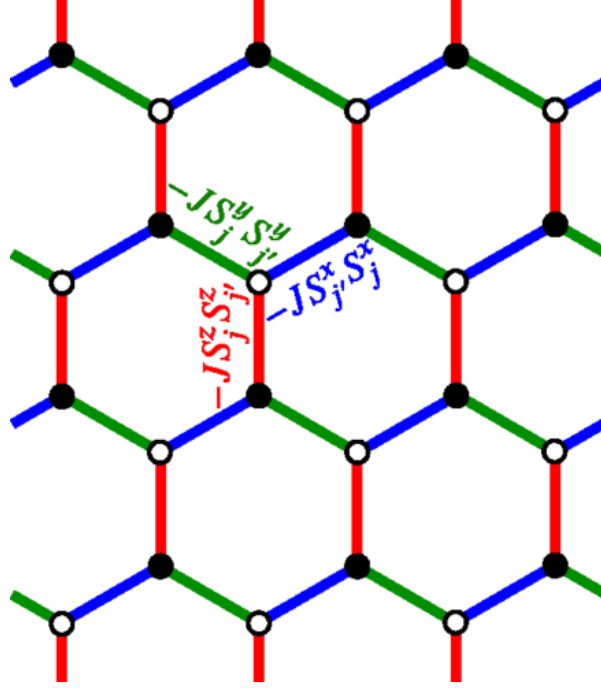


Figure 1.9: Kitaev model on a honeycomb lattice (adapted from [45])

connecting magnetic ions. This type of frustration is particularly prevalent in systems with strong spin-orbit coupling, such as in certain transition metal oxides and rare-earth compounds [39].

In bond-dependent exchange interactions, the anisotropy of the interaction means that the energy of the system depends on the relative orientation of spins and the spatial direction of the bonds. This anisotropy can arise from the underlying crystal field effects and spin-orbit coupling, leading to interactions that vary with bond direction. An example of such interactions is the Kitaev model on a honeycomb lattice [40], where the interaction between spins depends on the bond's orientation ( $x$ ,  $y$ , or  $z$  direction), as presented in Fig. 1.9. This dependence creates a highly frustrated system because the spins cannot simultaneously satisfy all bond-dependent interactions, leading to a macroscopic degeneracy of the ground state. As a result, the frustration can give rise to a quantum spin liquid state in Kitaev materials [41], where spins are highly entangled and do not order even at absolute zero temperature.  $\alpha$ - $\text{RuCl}_3$  [42, 43] and  $\text{Na}_2\text{IrO}_3$  [44] are two prominent examples that exhibit frustration due to bond-dependent interactions.

## 1.3 Consequences of Magnetic Frustration

Magnetic frustration leads to a variety of exotic magnetic structures and behaviors, each with unique physical properties and potential applications. Below are the main consequences of magnetic frustration:

### 1.3.1 Incommensurate Magnetic Structure

Incommensurate magnetic structures are structures in which the periodicity of the magnetic order does not match the underlying crystal lattice. This often results from competing interactions that cannot be simultaneously satisfied. These structures are characterized by a modulation of the spin configuration that varies in a non-integral manner relative to the lattice. Three such magnetic structures, sinusoidal spin density wave, cycloidal spiral, and proper screw structure, are shown in Fig. 1.10(a). Such systems can exhibit complex magnetic behaviors and have implications for understanding electronic properties in materials [47, 48].

### 1.3.2 Magnetostructural Transition

Magnetic frustration can induce structural transitions in materials as the system tries to relieve the frustration by distorting the lattice. These structural changes can significantly alter the material's properties, including its electronic, magnetic, and mechanical behaviors. For example,  $\text{LiFeCr}_4\text{O}_8$  undergoes a structural transition from cubic to the tetragonal structure below 23 K as a result of frustrated breathing pyrochlore lattice, as shown in Fig. 1.10(b) [49]. Such transitions are important for designing materials with tunable properties for various technological applications.

### 1.3.3 Spin Glass

A spin glass is a disordered magnetic state characterized by frozen random orientations of magnetic moments, as depicted in Fig. 1.10(c). In spin glasses, the frustration is typically due to competing ferromagnetic and antiferromagnetic interactions [51] or geometrical frustration [52], leading to a highly disordered ground state where spins are frozen in random directions. Spin glasses exhibit unique properties such as slow relaxation, aging, and memory effects, making them useful for studying complex systems and applications in neural networks and optimization problems.

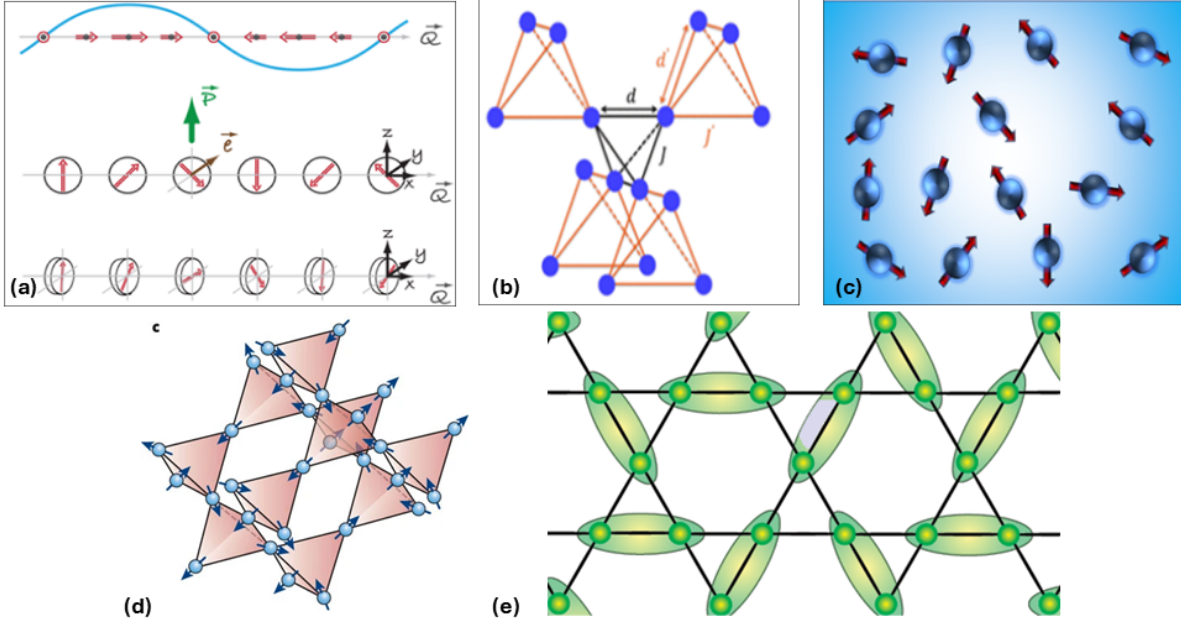


Figure 1.10: (a) Different incommensurate magnetic structures: sinusoidal spin density wave (upper one), cycloidal spiral (middle one), and proper screw structure (lower one), adapted from [46]. (b) Breathing pyrochlore magnetic sublattice of  $\text{LiFeCr}_4\text{O}_8$ , adapted from [49] and reproduced with permission from American Physical Society. (c) A snapshot of the spins frozen in random directions. (d) Pyrochlore lattice, (adapted from [20], reproduced with permission from Springer Nature) (e) Fluctuating singlets in a quantum spin liquid, adapted from [50].

### 1.3.4 Spin Ice

Spin ice is a type of frustrated magnet where the magnetic moments obey a local “ice rule,” similar to the proton disorder in water ice. This rule leads to a highly degenerate ground state with residual entropy. Spin ices, like those found in pyrochlore lattices (refer to Fig. 1.10(d)), can exhibit emergent magnetic monopole excitations and interesting thermodynamic properties [53]. These materials are important for understanding frustration in three-dimensional systems and potential applications in magnetic monopole research.

### 1.3.5 Spin Liquid

Spin liquids are highly entangled quantum states that do not exhibit long-range magnetic order even at absolute zero temperature. It can be considered as a superposition of many singlets, as shown in Fig. 1.10(e). In these systems, the frustration prevents the spins from freezing into a regular pattern, resulting in a fluid-like state of magnetic moments. Spin

liquids can have fractionalized excitations and topological order, making them candidates for robust quantum computing platforms [20]. Their study provides deep insights into quantum many-body physics.

After this point, the chapter will focus exclusively on quantum spin liquids, exploring the challenges of experimentally realizing this elusive state. Additionally, it will outline an alternative approach to accelerate the search for quantum spin liquids.

## 1.4 Quantum Spin Liquid

Half a century ago, Philip W. Anderson posed an intriguing question [54]: **could the ground state of a spin  $S = \frac{1}{2}$  quantum antiferromagnet on a triangular lattice exist without any broken symmetry?** He introduced a new state, named the “resonating valence bond” (RVB) state, which could potentially represent the true ground state of the  $S = \frac{1}{2}$  antiferromagnetic Heisenberg model on a triangular lattice. A valence bond can be understood as a nonmagnetic ( $S = 0$ ) or singlet state resulting from antiferromagnetically coupled magnetic moments, and the spins present in the valence bond are maximally entangled. The RVB model is one of the earliest theoretical proposals of a quantum spin liquid (QSL) state. A QSL state can be defined as a unique magnetic state that does not exhibit a conventional magnetic phase transition and hence no spontaneous symmetry breaking down to  $T = 0$  K despite having strong exchange interactions [55].

After the discovery of high-temperature superconductivity in cuprates in 1986 [56], Anderson extended the RVB theory to explain the superconducting state in these materials [57]. He suggested that the pairing of electrons (Cooper pairs) observed in superconductors arises from the same quantum entanglement that characterizes QSLs [58]. The parent compounds of high-temperature superconductors are typically Mott insulators, which exhibit antiferromagnetic order. Upon doping, these materials lose their magnetic order and transition into a superconducting state [59]. In this intermediate doping range, there is evidence of spin liquid behavior, where the spins remain disordered yet highly entangled. This study suggested that the cuprates might host a QSL state under certain conditions. An ideal quantum spin liquid is defined by its two distinctive characteristics: long-range quantum entanglement and the presence of fractionalized excitations.



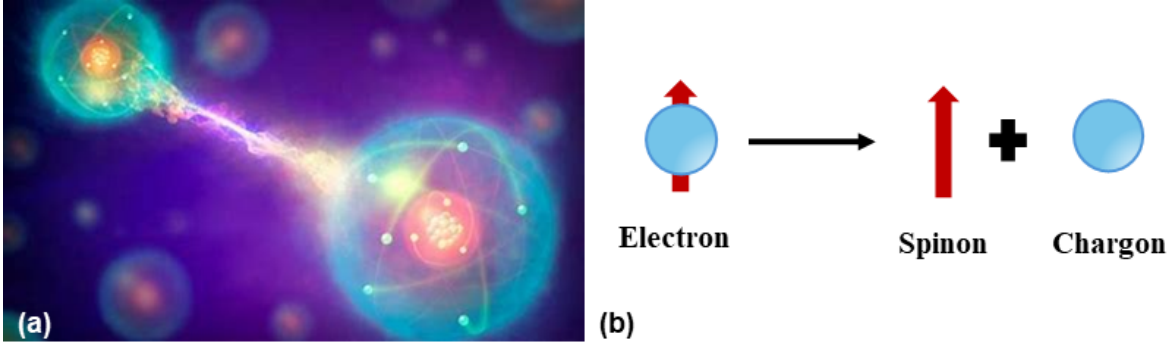


Figure 1.11: (a) An illustration of the quantum entangled state, adapted from [61]. (b) Fractionalization of electron into spinon and chargon.

### 1.4.1 Long-Range Quantum Entanglement

Quantum entanglement is a fundamental phenomenon in quantum mechanics where two or more particles become linked in such a way that the state of one particle instantaneously influences the state of the other, regardless of the distance separating them, as depicted in Fig. 1.11(a). Albert Einstein famously referred to this phenomenon as “*spooky action at a distance*” due to its counterintuitive nature. Before measurement, quantum particles exist in a superposition of all possible states. For example, an electron can be in a superposition of spin-up and spin-down states simultaneously. When particles become entangled, their combined state is described by a single wavefunction, meaning the individual states of the particles cannot be described independently of one another. If two particles are entangled, measuring the state of one particle immediately determines the state of the other, no matter the distance between them [60].

### 1.4.2 Fractionalized Excitations

One of the most intriguing aspects of QSLs is the presence of fractionalized excitations [62]. Unlike conventional magnets, where excitations involve the flipping of entire spins, QSLs exhibit excitations that carry fractions of the original spin quantum number. These fractionalized excitations arise due to the highly entangled nature of the QSL ground state and have significant implications for both fundamental physics and potential applications in quantum technologies. In QSLs, the elementary excitations can be spinons and holons. Spinons carry spin-1/2 but no charge, whereas holons carry charge but no spin, as exhibited in Fig. 1.11(b). This is in contrast to conventional magnets, where magnons carry both spin and charge, which are basic excitations. The separation of spin and charge into distinct excitations is a hallmark of the fractionalization phenomenon in

QSLs.

Furthermore, the entangled ground state of QSLs can give rise to emergent gauge fields, which mediate interactions between fractionalized excitations [63]. These emergent fields are not present in the original Hamiltonian but arise due to the collective behavior of the spins. The presence of these gauge fields can lead to a variety of exotic phenomena, such as anyonic statistics, where the excitations obey neither fermionic nor bosonic statistics. Many QSLs exhibit topological order, a form of order that is characterized by global properties of the ground state rather than local symmetry breaking [40]. Topological order can protect the fractionalized excitations and make them robust against local perturbations. This robustness is crucial for potential applications in quantum computing, where topologically protected states can serve as qubits that are resistant to decoherence.

### 1.4.3 Potential Applications of a QSL

Owing to their unique properties, QSLs have garnered significant interest in the realm of quantum computing and quantum communications. The entangled nature of QSLs and their fractionalized excitations offer promising avenues for developing advanced quantum technologies.

#### Quantum Computing

Anyons are the fractional excitations that can emerge in certain QSLs and can be used to encode quantum information. Anyons can braid around each other, and their braiding operations can perform quantum gates, leading to robust quantum computation [64]. Furthermore, the topological nature of the states in QSLs provides inherent protection against local noise and decoherence, making topological quantum computing highly fault-tolerant [65].

#### Quantum Communication

QSLs can significantly enhance quantum key distribution (QKD) protocols. The long-range entanglement in QSLs ensures that entangled states remain intact over large distances, improving the reliability and security of QKD systems [66]. Additionally, quantum repeaters, which extend the range of quantum communication, can leverage the topological properties of QSLs to create and maintain entangled states, thereby mitigating transmission loss over long distances [64]. Moreover, QSLs' topological order facilitates the

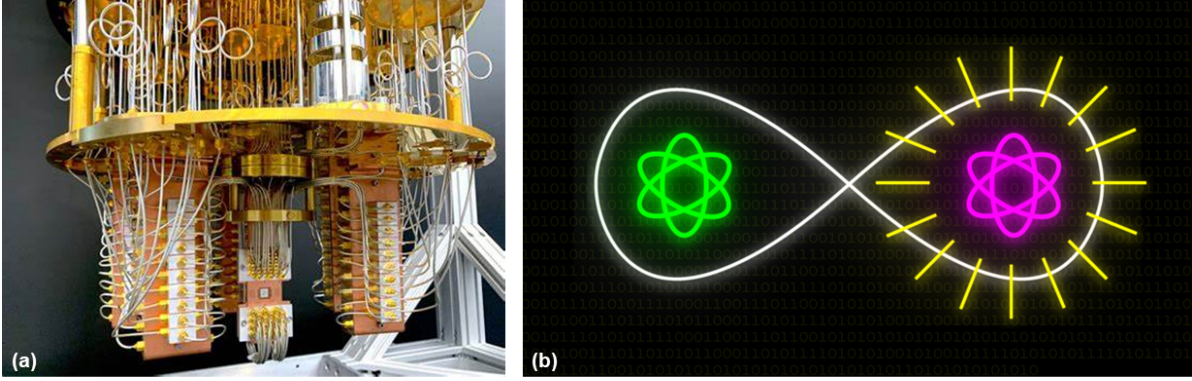


Figure 1.12: (a) A quantum processor attached to a dilution refrigerator, adapted from [67]. (b) An illustration of secured quantum communication, adapted from [68].

creation of fault-tolerant codes for error correction in quantum communication systems, ensuring robust and reliable transmission of quantum information even in the presence of noise and disturbances [65].

#### 1.4.4 Challenges and Opportunities

Since the initial proposal of the Resonating Valence Bond (RVB) state, the theory of Quantum Spin Liquids (QSLs) has undergone significant evolution. Various QSLs have been theoretically identified and characterized by different models showcasing these exotic phases. These models can be broadly classified into gapped and gapless QSLs, depending on whether there is a finite energy gap above the ground state. For example, a nearest-neighbor RVB-type model represents a gapped QSL, where breaking the valence bonds incurs an energy cost, leading to unique quasiparticle excitations [20].

Experimentally, identifying and synthesizing QSLs remains challenging, despite the increasing number of promising candidate materials. This gap between theory and experiment presents numerous opportunities for materials research. The main questions include how to use theoretical models to guide the synthesis of QSL materials, how to reliably and reproducibly create these materials in the lab, and how to characterize them convincingly. Moreover, understanding how real materials deviate from theoretical models can provide deeper insights into QSL physics. The following section focuses on the primary requirements for finding a new QSL candidate material.

### 1.4.5 Primary Ingredients of a QSL

Following theoretical predictions, identifying the chemical design aspects necessary for QSLs in real materials is essential. Essential ingredients common across various QSL models are **quantum fluctuations, low dimensionality, and magnetic frustration**, which prevent long-range magnetic order in a material. The precise combination of these ingredients in a candidate material may lead to diverse possible ground states [41, 69].

#### Quantum Fluctuations

Quantum fluctuations are a critical factor in the realization of a QSL. These fluctuations originate from spin degrees of freedom associated with the unpaired electrons and can persist even at absolute zero temperature, preventing the establishment of long-range magnetic order. This effect is most pronounced in the magnets, which have the smallest possible spin, i.e.,  $S = \frac{1}{2}$ . For magnets based on first-row transition metal ions, the contribution of orbitals to the atomic magnetic moment is suppressed due to the strong interaction between the  $3d$  orbitals and the surrounding crystal field, leading to a spin-only magnetic moment. The magnitude of this moment is decided by the unpaired electrons present in the crystal field-split manifold of orbital states. For instance,  $\text{Cu}^{2+}$  in an octahedral crystal field with a  $3d^9$   $S = \frac{1}{2}$  configuration is commonly used in the search for QSL ground states [70]. There are also examples of materials containing  $\text{Ti}^{3+}$  [71] and  $\text{V}^{4+}$  [72], both with a  $3d^1$   $S = \frac{1}{2}$  configuration, which have been investigated for QSL properties.

However, quantum fluctuations are not limited to  $S = \frac{1}{2}$  systems made up of transition metal ions. Moving towards heavier atoms and ions (down the periodic table) for which relativistic spin-orbit coupling interactions become increasingly significant [73]. For  $4d/5d$  transition metal ions or lanthanide (rare-earth) ions-based magnets, both spin and orbital contributions are present, and the total magnetic moment is defined by the total angular momentum quantum number,  $J$ . In certain ions, the combination of the local crystal field environment and spin-orbit coupling can result in  $J_{\text{eff}} = \frac{1}{2}$  or  $S_{\text{eff}} = \frac{1}{2}$  ground states which have enhanced quantum fluctuations. Notable examples include transition metal ions, such as  $\text{Co}^{3+}$  [74],  $\text{Ir}^{4+}$  [44] and  $\text{Ru}^{3+}$  [75] within kitaev lattice, and rare-earth ions;  $\text{Yb}^{3+}$  [22] and  $\text{Ce}^{3+}$  [76]. Typical splitting of  $\text{Co}^{3+}$  and  $\text{Yb}^{3+}$  is illustrated in Fig. 1.13(a) and Fig. 1.13(b), respectively.

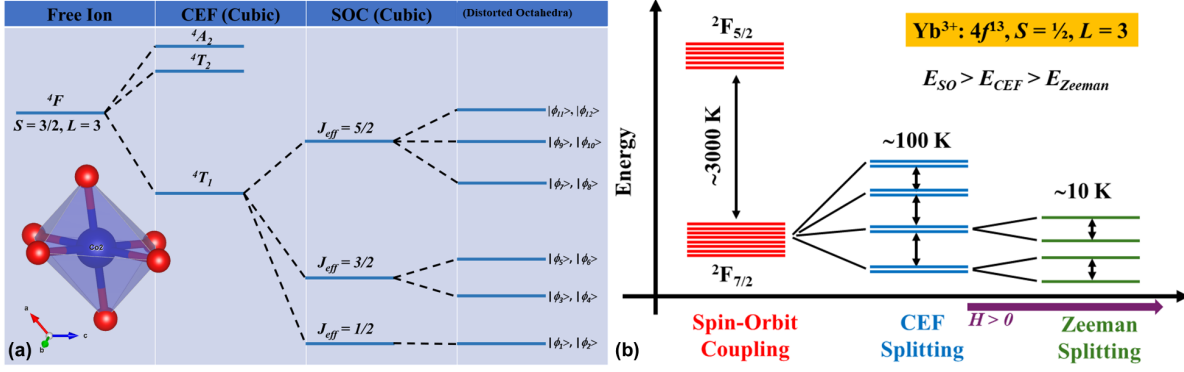


Figure 1.13: Typical splitting of (a)  $\text{Co}^{3+}$  and (b)  $\text{Yb}^{3+}$  ions, resulting in  $J_{\text{eff}} = \frac{1}{2}$  ground state.

## Low Dimensionality

A magnetic material can be considered low-dimensional if exchange interactions are restricted to one or two dimensions. For QSLs, low-dimensional magnetic materials are interesting because they are analytically tractable [77, 78] and, in some cases, exactly solvable [40]. Low dimensionality helps suppress long-range magnetic order, making quantum fluctuations more pronounced. With fewer exchange pathways in low-dimensional systems, quantum fluctuations can more easily destroy magnetic order [79]. A well-studied model in the pursuit of QSLs is the one-dimensional chain of antiferromagnetically coupled isotropic  $S = \frac{1}{2}$  moments [80]. The Bethe-Ansatz solution of this model demonstrated the emergence of a QSL ground state. Experimental evidence for this one-dimensional QSL state in  $\text{KCuF}_3$  [81] and  $\text{CuSO}_4 \cdot 5\text{D}_2\text{O}$  [82] has been confirmed by the presence of magnetic excitations.

## Frustration

Beyond one-dimensional QSL states in  $S = \frac{1}{2}$  Heisenberg antiferromagnetic spin chains, it is possible theoretically to have higher-dimensional QSL states but challenging to realize in materials [83]. A wise approach to higher-dimensional QSL candidates is magnetic frustration. In frustrated magnets, the presence of competing interactions prevents all interactions from being satisfied at the same time, which inhibits the formation of long-range magnetic order. When combined with strong quantum fluctuations, a QSL state can be realized in both two and three dimensions.

Geometrical frustration, resulting from the spatial arrangement of magnetic ions, is a key factor in many QSL candidates. For example, in two dimensions, a network

of edge-sharing triangles, as shown in Fig. 1.6(a), with antiferromagnetically coupled moments was the foundation of the original Resonating Valence Bond (RVB) model [54]. Quantum fluctuations are more significant in the  $S = \frac{1}{2}$  kagomé antiferromagnet, which is a two-dimensional corner-sharing network of triangular plaquettes, as depicted in Fig. 1.6(b). This framework has been extensively studied, with materials like herbertsmithite  $[\text{ZnCu}_3(\text{OH})_6\text{Cl}_2]$  [70], barlowite  $[\text{Cu}_4(\text{OH})_6\text{FBr}]$  [84], and volborthite  $[\text{Cu}_3\text{V}_2\text{O}_7(\text{OH})_2 \cdot 2\text{H}_2\text{O}]$  [85] showing evidence of QSL ground states. In three dimensions, the pyrochlore antiferromagnet (refer to Fig. 1.6(c)), with the general formula  $\text{A}_2\text{B}_2\text{O}_7$ , is a well-known example of a frustrated magnet. In these systems, rare-earth ions typically occupy the A-site, while transition metal ions occupy the B-site [27]. This structure, composed of interpenetrating networks of corner-sharing tetrahedra, leads to a manifold of degenerate configurations and unconventional dynamics for both classical and quantum spins.

An alternate approach to magnetic frustration is through exchange anisotropy, as illustrated by Kitaev's QSL model [40]. In this model, each site on a honeycomb network experiences ferromagnetic anisotropic Ising-like exchange interactions that prefer a spin arrangement orthogonal to each bond, as illustrated in Fig. 1.9. This leads to frustration and a topological QSL ground state. This model is exactly solvable and provides a framework for QSL realization beyond the RVB state [41]. Extending Kitaev's theoretical predictions to real materials requires anisotropic contributions to the exchange mechanism, which can be achieved through spin-orbit coupling interactions in spin-orbit-assisted Mott insulators with  $4d^5$  and  $5d^5$  electronic configurations [86]. Jackeli and Khaliullin's work outlined the necessary electronic and structural criteria, emphasizing the importance of an edge-sharing geometry to inhibit isotropic Heisenberg interactions and promote Kitaev-type exchange [39]. Material candidates like iridate and rhodate honeycomb-based systems ( $\text{A}_2\text{MO}_3$ , where  $\text{A} = \text{Li}^+, \text{Na}^+$ ;  $\text{M} = \text{Ir}^{4+}$  [44], and  $\alpha\text{-RuCl}_3$  [42] have been extensively studied. Recent efforts have expanded the search to  $d^7$  ions [87] and  $f$ -electron systems [88], exploring new possibilities for Kitaev-type physics.

## 1.5 Aim of the Thesis

This thesis aims to explore the nature of magnetic frustration and potential QSL states across various spin lattices, including spin-chains and dimers (1D), triangular, rhombus, kite, and honeycomb lattices (2D), as well as hyper-honeycomb lattices (3D). These

lattices offer diverse environments for studying the interplay between lattice geometry, spin interactions, and quantum fluctuations, each contributing uniquely to the realization and stability of QSL states.

A significant focus of this research is on Yb-based novel quantum magnets, addressing the limited exploration of these systems despite meeting all necessary criteria. Yb compounds offer unique opportunities due to their strong spin-orbit coupling and potential to exhibit QSL behavior. These materials, featuring different lattice geometries, provide fertile ground for discovering new QSL states and understanding their underlying mechanisms. Moreover, the thesis examines a  $\text{Co}^{3+}$ -based Kitaev candidate, featuring Co octahedra arranged in a “parallel-edge” sharing geometry.

In summary, this thesis seeks to advance the understanding of magnetic frustration and QSLs in low-dimensional magnetism, focusing on Yb-based compounds. By investigating these materials’ unique properties and behaviors, this research aims to contribute to the broader quest for novel quantum states and their potential applications in future technologies.

# Bibliography

- [1] L. Pauling, The structure and entropy of ice and of other crystals with some randomness of atomic arrangement, *J. Am. Chem. Soc.* **57**, 2680 (1935).
- [2] C. Castelnovo, R. Moessner, S. L. Sondhi, Magnetic monopoles in spin ice, *Nature* **451**, 42 (2008).
- [3] C. G. Salzmann, P. G. Radaelli, B. Slater, and J. L. Finney, The polymorphism of ice: Five unresolved questions, *Phys. Chem. Chem. Phys.* **13**, 18468 (2011).
- [4] C. M. Dobson, Protein Folding and Misfolding, *Nature* **426**, 884 (2003).
- [5] D. J. Selkoe, Folding proteins in fatal ways, *Nature* **426**, 900 (2003).
- [6] <https://ditki.com/course/biochemistry/proteins/protein-structure/937/protein-folding-dynamics>
- [7] C. Soto, Unfolding the role of protein misfolding in neurodegenerative diseases, *Nature Reviews Neuroscience* **4**, 49 (2003).
- [8] <https://www.pngegg.com/en/png-yxfng>
- [9] C. A. Angell, Formation of glasses from liquids and biopolymers, *Science* **267**, 1924 (1995).
- [10] A. L. Greer, Metallic Glasses, *Science* **267**, 1947 (1995).
- [11] M. Kleman and O. D. Lavrentovich, *Soft matter physics: an introduction*, Springer (2003).
- [12] P. G. Debenedetti and F. H. Stillinger, Supercooled liquids and the glass transition, *Nature* **410**, 259 (2001).
- [13] M. D. Ediger and P. Harrowell, Perspective: Supercooled liquids and glasses, *The Journal of Chemical Physics* **137** (2012).
- [14] <https://www.smartglassworld.net/what-is-a-liquid-crystal>



- 
- [15] PG De Gennes and J Prost, *The Physics of Liquid Crystals*, Oxford University Press (1993).
  - [16] P. J. Collings, *Liquid Crystals: Nature's Delicate Phase of Matter* (Princeton University Press, Princeton, NJ, 2001).
  - [17] M Schadt, Liquid crystal materials and liquid crystal displays, *Annual review of materials science* **27**, 305 (1997).
  - [18] H.-W. Chen, J.-H. Lee, B.-Y. Lin, S. Chen and S.-T. Wu, Liquid crystal display and organic light-emitting diode display: present status and future perspectives, *Light: Science & Applications* **7**, 17168 (2018).
  - [19] R. Moessner and A. P. Ramirez, Geometrical frustration. *Physics Today*, **59**, 24 (2006).
  - [20] L. Balents, Spin liquids in frustrated magnets, *Nature* **464**, 199 (2010).
  - [21] A. P. Ramirez, Strongly geometrically frustrated magnets, *Annual Review of Materials Science* **24**, 453 (1994).
  - [22] Y. Li, G. Chen, W. Tong, L. Pi, J. Liu, Z. Yang, X. Wang, and Q. Zhang, Rare-Earth Triangular Lattice Spin Liquid: A Single-Crystal Study of  $\text{YbMgGaO}_4$ , *Phys. Rev. Lett.* **115**, 167203 (2015).
  - [23] L. Ding, P. Manuel, S. Bachus, F. Grussler, P. Gegenwart, J. Singleton, R. D. Johnson, H. C. Walker, D. T. Adroja, A. D. Hillier, and A. A. Tsirlin, Gapless spin-liquid state in the structurally disorder-free triangular antiferromagnet  $\text{NaYbO}_2$ , *Phys. Rev. B* **100**, 144432 (2019).
  - [24] J. S. Helton, K. Matan, M. P. Shores, E. A. Nytko, B. M. Bartlett, Y. Yoshida, Y. Takano, A. Suslov, Y. Qiu, J.-H. Chung, D. G. Nocera, and Y. S. Lee, *Phys. Rev. Lett.* **98**, 107204 (2007).
  - [25] T. Imai, E. A. Nytko, B. M. Bartlett, M. P. Shores, and D. G. Nocera,  $^{63}\text{Cu}$ ,  $^{35}\text{Cl}$ , and  $^1\text{H}$  NMR in the  $S = \frac{1}{2}$  Kagome Lattice  $\text{ZnCu}_3(\text{OH})_6\text{Cl}_2$ , *Phys. Rev. Lett.* **100**, 077203 (2008).
  - [26] M. J. Harris, S. T. Bramwell, D. F. McMorrow, T. H. Zeiske and K. W. Godfrey, Geometrical Frustration in the Ferromagnetic Pyrochlore  $\text{Ho}_2\text{Ti}_2\text{O}_7$ , *Phys. Rev. Lett.* **79**, 2554 (1997).
  - [27] J. S. Gardner, M. J. P. Gingras and J. E. Greedan, Magnetic pyrochlore oxides, *Review of Modern Physics* **82**, 53 (2010).

- 
- [28] S.-L. Drechsler, J. Richter, A.A. Gippius, A. Vasiliev, A. A. Bush, A. S. Moskvina, J. Mañle, Y. Prots, W. Schnelle, and H. Rosner, Helical ground state and weak ferromagnetism in the edge-shared chain cuprate  $\text{NaCu}_2\text{O}_2$ , *Europhys. Lett.* **73**, 83 (2006).
  - [29] M. Hartel, J. Richter, D. Ihle, and S.-L. Drechsler, Thermodynamics of a one-dimensional frustrated spin-1/2 Heisenberg ferromagnet, *Phys. Rev. B* **78**, 174412 (2008).
  - [30] H. T. Lu, Y. J. Wang, S. Qin, and T. Xiang, Zigzag spin chains with antiferromagnetic-ferromagnetic interactions: Transfer-matrix renormalization group study, *Phys. Rev. B* **74**, 134425 (2006).
  - [31] S. E. Dutton, M. Kumar, M. Mourigal, Z. G. Soos, J.-J. Wen, C. L. Broholm, N. H. Andersen, Q. Huang, M. Zbiri, R. Toft-Petersen, and R. J. Cava, Quantum Spin Liquid in Frustrated One-Dimensional  $\text{LiCuSbO}_4$ , *Phys. Rev. Lett.* **108**, 187206 (2012).
  - [32] C. K. Mazumdar, and D. K. Ghosh, On Next-Nearest-Neighbor Interaction in Linear Chain. I, *J. Math. Phys.* **10**, 1388 (1969).
  - [33] G. Shirane, Y. Endoh, R. J. Birgeneau, M. A. Kastner, Y. Hidaka, M. Oda, M. Suzuki, and T. Murakami, Two-dimensional antiferromagnetic quantum spin-fluid state in  $\text{La}_2\text{CuO}_4$ , *Phys. Rev. Lett.* **59**, 1613 (1987).
  - [34] J. D. Reger and A. P. Young, Monte Carlo simulations of the spin-(1/2 Heisenberg antiferromagnet on a square lattice, *Phys. Rev. B* **37**, 5978 (1988).
  - [35] R. J. Birgeneau, M. Greven, M. A. Kastner, Y. S. Lee, B. O. Wells, Y. Endoh, K. Yamada, and G. Shirane, Instantaneous spin correlations in  $\text{La}_2\text{CuO}_4$ , *Phys. Rev. B* **59**, 13788 (1999).
  - [36] R. Coldea, S. M. Hayden, G. Aeppli, T. G. Perring, C. D. Frost, T. E. Mason, S.-W. Cheong, and Z. Fisk, Spin Waves and Electronic Interactions in  $\text{La}_2\text{CuO}_4$ , *Phys. Rev. Lett.* **86**, 5377 (2001).
  - [37] C. Lacroix, P. Mendels, and F. Mila, eds., *Introduction to Frustrated Magnetism: Materials, Experiments, Theory* (Springer Series in Solid-State Sciences), 2011th ed. (Springer, 2011).
  - [38] W. Y. Liu, S. S. Gong, Y. B. Li, D. Poilblanc, W. Q. Chen, and Z. C. Gu, Gapless quantum spin liquid and global phase diagram of the spin-1/2  $J_1$ - $J_2$  square antiferromagnetic Heisenberg model, *Science Bulletin* **67**, 1034 (2022).

- 
- [39] G. Jackeli and G. Khaliullin, Mott insulators in the strong spin-orbit coupling limit: From Heisenberg to a quantum compass and Kitaev models, *Phys. Rev. Lett.* **102**, 017205 (2009).
  - [40] A. Kitaev, Anyons in an exactly solved model and beyond. *Ann. Phys.-New York* **321**, 2 (2006).
  - [41] H. Takagi, T. Takayama, G. Jackeli, G. Khaliullin, and S. E. Nagler, Concept and realization of Kitaev quantum spin liquids. *Nat. Rev. Phys.* **1**, 264 (2019).
  - [42] A. Banerjee, C. A. Bridges, J.-Q. Yan, A. A. Aczel, L. Li, M. B. Stone, G. E. Granroth, M. D. Lumsden, Y. Yiu, J. Knolle *et al.*, Proximate Kitaev quantum spin liquid behaviour in a honeycomb magnet, *Nature Materials* **15**, 733 (2016).
  - [43] K. W. Plumb, J. P. Clancy, L. J. Sandilands, V. V. Shankar, Y. F. Hu, K. S. Burch, H.-Y. Kee, and Y.-J. Kim,  $\alpha$ - $\text{RuCl}_3$ : A spin-orbit assisted Mott insulator on a honeycomb lattice *Phys. Rev. B* **90**, 041112(R) (2014).
  - [44] J. Chaloupka, G. Jackeli, and G. Khaliullin, Kitaev-Heisenberg Model on a Honeycomb Lattice: Possible Exotic Phases in Iridium Oxides  $\text{A}_2\text{IrO}_3$ , *Phys. Rev. Lett.* **105**, 027204 (2010).
  - [45] J. Nasu and Y. Motome, Nonequilibrium Majorana dynamics by quenching a magnetic field in Kitaev spin liquids, *Phys. Rev. Res.* **1**, 033007 (2019).
  - [46] D. Khomskii, Classifying multiferroics: Mechanisms and effects, *Physics* **2**, 20 (2009).
  - [47] P. Yanda, I. V. Golosovsky, I. Mirebeau, N. V. Ter-Oganessian, J. R.-Carvajal, and A. Sundaresan, Interplay of  $4f$ - $3d$  interactions and spin-induced ferroelectricity in the green phase  $\text{Gd}_2\text{BaCuO}_5$ , *Phys. Rev. Res.* **2**, 023271 (2020).
  - [48] R. Shankar P. N., F. Orlandi, P. Manuel, W. Zhang, P. S. Halasyamani, and A. Sundaresan, A-Site and B-Site Cation Ordering Induces Polar and Multiferroic Behavior in the Perovskite  $\text{NaLnNiWO}_6$  ( $\text{Ln} = \text{Y}, \text{Dy}, \text{Ho}, \text{and Yb}$ ), *Chem. Mater.* **32**, 5641 (2020).
  - [49] R. Saha, R. Dhanya, C. Bellin, K. Béneut, A. Bhattacharyya, A. Shukla, C. Narayana, E. Suard, J. Rodriguez-Carvajal, and A. Sundaresan, Magnetostructural coupling and magnetodielectric effects in the A-site cation-ordered spinel  $\text{LiFeCr}_4\text{O}_8$ , *Phys. Rev. B* **96**, 214439 (2017).
  - [50] L. Clark, Pool of Candidate Spin Liquids Grows, *Physics* **6**, s71 (2013).
  - [51] R. Kumar and A. Sundaresan, Antisite disorder driven cluster glass state and colossal magnetoresistance in  $\text{MnSb}_2\text{Se}_4$ , *Phys. Rev. B* **106**, 134423 (2022).

- 
- [52] R. Kumar, P. Yanda, and A. Sundaresan, Cluster-glass behavior in the two-dimensional triangular lattice Ising-spin compound  $\text{Li}_2\text{Mn}_3\text{O}_7$ , *Phys. Rev. B* **103**, 214427 (2021).
  - [53] Y. Tokiwa, T. Yamashita, M. Udagawa, S. Kittaka, T. Sakakibara, D. Terazawa, Y. Shimoyama, T. Terashima, Y. Yasui, T. Shibauchi and Y. Matsuda, Possible observation of highly itinerant quantum magnetic monopoles in the frustrated pyrochlore  $\text{Yb}_2\text{Ti}_2\text{O}_7$ , *Nat. Comm.* **7**, 10807 (2016).
  - [54] P. W. Anderson, Resonating valence bonds: A new kind of insulator? *Mater. Res. Bull.* **8**, 153 (1973).
  - [55] L. Clark, A. H. Abdeldaim, Quantum Spin Liquids from a Materials Perspective, *Annual Review of Material Research* **51**, 1 (2021).
  - [56] J. G. Bednorz and K. A. Muller, Possible high  $T_C$  superconductivity in the Ba-La-cu-O system, *Z. Phys. B-Condensed Matter* **64**, 189 (1986).
  - [57] P. W. Anderson, The Resonating Valence Bond State in  $\text{La}_2\text{CuO}_4$  and Superconductivity. *Science*, **235**, 1196 (1987).
  - [58] G. Baskaran, Z. Zou, and P. W. Anderson, The resonating valence bond state and high- $T_c$  superconductivity: A mean field theory. *Solid State Communications*, **63**, 973 (1987).
  - [59] P. A. Lee, N. Nagaosa, and X. G. Wen, Doping a Mott insulator: Physics of high-temperature superconductivity. *Reviews of Modern Physics*, **78**, 17 (2006).
  - [60] What is quantum entanglement? A physicist explains the science of Einstein’s ‘spooky action at a distance’ (2022, October 7) retrieved 16 July 2024 from <https://phys.org/news/2022-10-quantum-entanglement-physicist-science-einstein.html>
  - [61] Science photo library/ Alamy Stock Photo
  - [62] T. H. Han, J. S. Helton, S. Chu, D. G. Nocera, J. A. Rodriguez-Rivera, C. Broholm, C., and Y. S. Lee, Fractionalized excitations in the spin-liquid state of a Kagome-lattice antiferromagnet. *Nature* **492**, 406 (2012).
  - [63] X. G. Wen, Quantum Field Theory of Many-Body Systems: From the Origin of Sound to an Origin of Light and Electrons, *Oxford University Press* (2004).
  - [64] C. Chamon, D. Green, and Z.-C. Yang, Constructing Quantum Spin Liquids Using Combinatorial Gauge Symmetry, *Phys. Rev. Lett.* **125**, 067203 (2020).

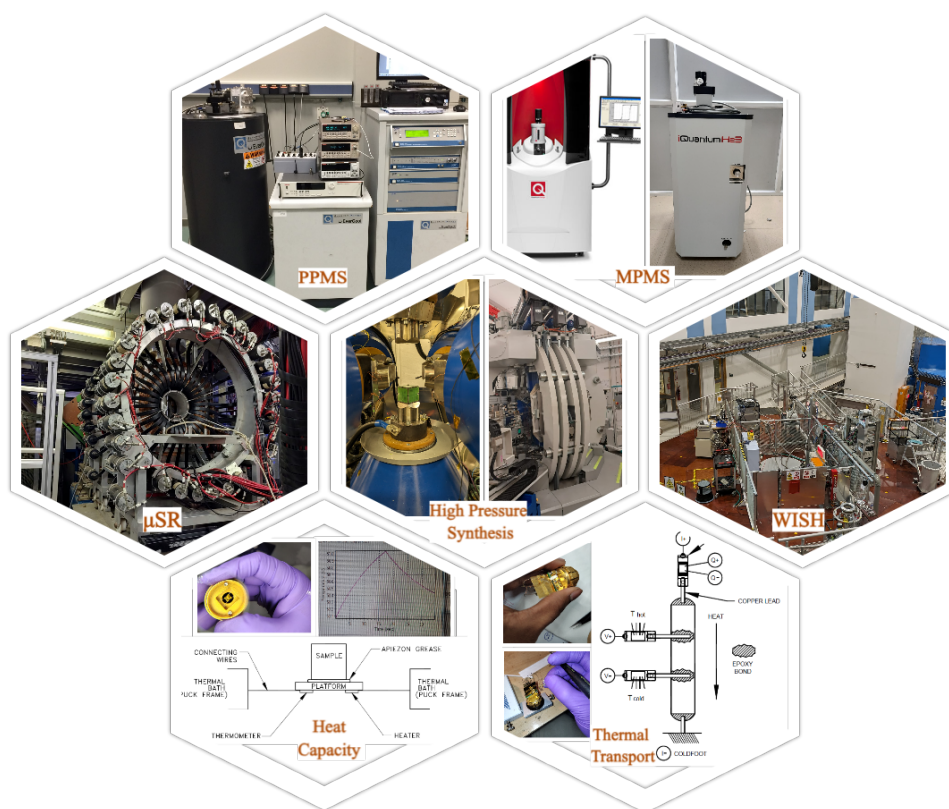
- 
- [65] G. B. Halasz, Gate-Controlled Anyon Generation and Detection in Kitaev Spin Liquids, *Phys. Rev. Lett.* **132**, 206501 (2024).
- [66] Y. Liu, K. Slagle, K. S. Burch, and J. Alicea, Dynamical Anyon Generation in Kitaev Honeycomb Non-Abelian Spin Liquids, *Phys. Rev. Lett.* **129**, 037201 (2022).
- [67] <https://www.popsoci.com/technology/in-photos-journey-to-the-center-of-a-quantum-computer/>
- [68] <https://www.technologyreview.com/2019/02/14/103409/what-is-quantum-communications/>
- [69] L. Savary, L. Balents, Quantum spin liquids: a review. *Rep. Prog. Phys.* **80**, 16502 (2016).
- [70] M. A. de Vries, J. R. Stewart, P. P. Deen, J. O. Piatek, G. J. Nilsen, H. M. Rønnow, and A. Harrison, Scale-free antiferromagnetic fluctuations in the  $s = 1/2$  kagome antiferromagnet herbertsmithite, *Phys. Rev. Lett.* **103**, 237201 (2009).
- [71] G. J. Nilsen, A. Raja, A. A. Tsirlin, H. Mutka, D. Kasinathan, C. Ritter, and H. M. Rønnow, One-dimensional quantum magnetism in the anhydrous alum  $\text{KTi}(\text{SO}_4)_2$ , *New J. Phys.* **17**, 113035 (2015).
- [72] L. Clark, J. C. Orain, F. Bert, M. A. De Vries, F. H. Aidoudi, R. E. Morris, P. Lightfoot, J. S. Lord, M. T. F. Telling, P. Bonville, J. P. Attfield, P. Mendels, and A. Harrison, Gapless Spin Liquid Ground State in the  $S = 1/2$  Vanadium Oxyfluoride Kagome Antiferromagnet  $[\text{NH}_4]_2[\text{C}_7\text{H}_{14}\text{N}][\text{V}_7\text{O}_6\text{F}_{18}]$ , *Phys. Rev. Lett.* **110**, 207208 (2013).
- [73] J. G. Rau, E. K. H. Lee, and H. Y. Kee, Spin-orbit physics giving rise to novel phases in correlated systems: iridates and related materials, *Annu. Rev. Condens. Matter Phys.* **7**, 195 (2016).
- [74] S. Zhang, S. Lee, A. J. Woods, W. K. Peria, S. M. Thomas, R. Movshovich, E. Brosha, Q. Huang, H. Zhou, V. S. Zapf, and M. Lee, Electronic and magnetic phase diagrams of the Kitaev quantum spin liquid candidate  $\text{Na}_2\text{Co}_2\text{TeO}_6$ , *Phys. Rev. B* **108**, 064421 (2023).
- [75] A. Banerjee, J. Yan, J. Knolle, C. A. Bridges, M. B. Stone, M. D. Lumsden, D. G. Mandrus, D. A. Tennant, R. Moessner, and S. Nagler, Neutron scattering in the proximate quantum spin liquid  $\alpha\text{-RuCl}_3$ , *Science* **356**, 1055 (2017).

- 
- [76] R. Sibille, E. Lhotel, V. Pomjakushin, C. Baines, T. Fennell, and M. Kenzelmann, Candidate quantum spin liquid in the  $\text{Ce}^{3+}$  pyrochlore stannate  $\text{Ce}_2\text{Sn}_2\text{O}_7$ , Phys. Rev. Lett. **115**, 097202 (2015).
  - [77] S. S. Gong, W. Zhu, K. Yang, O. A. Starykh, D. N. Sheng, and L. Balents, Emergent quasi-one-dimensionality in a kagome magnet: A simple route to complexity, Phys. Rev. B **94**, 35154 (2016).
  - [78] Y. Iqbal, W. J. Hu, R. Thomale, D. Poilblanc, and F. Becca, Spin liquid nature in the Heisenberg  $J_1$ - $J_2$  triangular antiferromagnet, Phys. Rev. B **93**, 144411 (2016).
  - [79] R. J. Birgeneau and G. Shirane, Magnetism in one dimension, Physics Today **31**, 32 (1978).
  - [80] H. Bethe, Zur Theorie der Metalle, Z. Phys. **71**, 205 (1931).
  - [81] D. A. Tennant, T. G. Perring, R. A. Cowley, and S. E. Nagler, Unbound spinons in the  $S=1/2$  antiferromagnetic chain  $\text{KCuF}_3$ , Phys. Rev. Lett. **70**, 4003 (1993).
  - [82] M. Mourigal, M. Enderle, A. Klopfferpieper, J. S. Caux, A. Stunault, and H. M. Ronnow, Fractional spinon excitations in the quantum Heisenberg antiferromagnetic chain, Nat. Phys. **9**, 435 (2013).
  - [83] M. R. Norman, *Colloquium: Herbertsmithite and the search for the quantum spin liquid*, Rev. Mod. Phys. **88**, 41002 (2016).
  - [84] K. Tustain, B. Ward-O' Brien, F. Bert, T. Han, H. Luetkens, T. Lancaster, B. M. Huddart, P. J. Baker, and L. Clark, From magnetic order to quantum disorder in the Zn-barlowite series of  $s=1/2$  kagome antiferromagnets, npj Quantum Mater. **5**, 74 (2020).
  - [85] H. Ishikawa, M. Yoshida, K. Nawa, M. Jeong, S. Kramer, M. Horvatic, C. Berthier, M. Takigawa, M. Akaki, A. Miyake, M. Tokunaga, K. Kindo, J. Yamaura, Y. Okamoto, and Z. Hiroi, One-third magnetization plateau with a preceding novel phase in volborthite, Phys. Rev. Lett. **114**, 227202 (2015).
  - [86] T. Moriya, Anisotropic superexchange interaction and weak ferromagnetism, Phys. Rev. **120**, 91 (1960).
  - [87] H. Liu and G. Khaliullin, Pseudospin exchange interactions in  $d^7$  cobalt compounds: Possible realization of the Kitaev model, Phys. Rev. B **97**, 014407 (2018).
  - [88] S.-H. Jang, R. Sano, Y. Kato, and Y. Motome, Antiferromagnetic Kitaev interaction in  $f$ -electron based honeycomb magnets, Phys. Rev. B **99**, 241106(R) (2019).

# Chapter 2

## Experimental Techniques

This chapter provides an overview and explains the operating principles of the synthesis and characterization techniques employed in this thesis.



## 2.1 Sample Synthesis

### 2.1.1 Solid-State Synthesis

The solid-state reaction method is a widely employed technique in materials science and solid-state chemistry for preparing polycrystalline samples. This method involves a series of steps, beginning with the selection of appropriate starting materials, often metal oxides, carbonates, nitrates, or pure elements, based on the desired final compound. Accurate weighing of the reactants in stoichiometric proportions is followed by thorough mixing, ensuring a homogeneous distribution. This mixing process, often performed using a mortar and pestle or a ball mill, is critical for achieving a uniform reaction.

The mixture may undergo a preliminary heat treatment to decompose certain reactants or remove volatile components. This is followed by grinding to increase the surface area and ensure intimate contact between reactant particles, thereby enhancing the reaction rate and uniformity of the product. In some cases, the ground mixture is pressed into pellets to improve density and uniformity.

The process can be better understood by considering the role of diffusion, described by Fick's laws, and the impact of temperature, highlighted by Tamman's Rule. Fick's laws describe the movement of particles through a medium, with the diffusion rate influenced by the concentration gradient and the diffusion coefficient. Fick's First Law is expressed as [1]:

$$J = -D \frac{dC}{dx}$$

where  $J$  is the diffusion flux (amount of substance per unit area per unit time),  $D$  is the diffusion coefficient (dependent on temperature and the nature of the material), and  $\frac{dC}{dx}$  is the concentration gradient (change in concentration with respect to distance). Fick's Second Law, which describes how the concentration of diffusing species changes with time, is expressed as [1]:

$$\frac{\partial C}{\partial t} = D \frac{\partial^2 C}{\partial x^2}$$

In a solid-state reaction, reactant particles must diffuse through the solid matrix



to interact and react. The diffusion process is crucial for the reaction to progress, as reactants must come into contact at the atomic level.

Tamman’s Rule states that for significant diffusion to occur, the temperature of the reaction should be at least half of the melting point (in Kelvin) of the reactants. This rule can be expressed as [2]:

$$T_{\text{reaction}} \geq 0.5 \times T_{\text{melting}}$$

This ensures that the temperature is sufficient to facilitate the necessary diffusion rates for the reaction to proceed efficiently. By following Tamman’s Rule, higher temperatures enhance atomic mobility, thereby increasing the diffusion coefficient and promoting faster diffusion of reactant particles.

All samples except NaYbZnWO<sub>6</sub> used in this thesis are polycrystalline in nature and were prepared using the solid-state reaction method. The synthesis was conducted in commercial muffle furnaces available in our laboratory. Detailed descriptions of the procedures for each sample are provided in the subsequent chapters.

### 2.1.2 High-Pressure and High-Temperature Synthesis Technique

The high-pressure and high-temperature (HPHT) technique is a sophisticated method used to synthesize new materials, particularly those that require conditions not achievable under normal atmospheric pressures and temperatures. In the HPHT technique, pressures can range from a few gigapascals (GPa) to several hundred gigapascals, and temperatures can reach thousands of degrees Celsius. These extreme conditions are achieved using specialized equipment such as diamond anvil cells or large-volume presses. The combination of high pressure and high temperature induces reactions that are not possible under standard conditions, allowing the formation of new phases and compounds with unique crystal structures and properties.

To prepare NaYbZnWO<sub>6</sub>, we used the 6-ram Large Volume Press Aster-15 installed at the P61B beamline at Deutsches Elektronen-Synchrotron (DESY), Germany [3]. The detailed process has been described in Chapter 6. This beamline enables researchers to subject materials to extreme pressures and temperatures while simultaneously performing

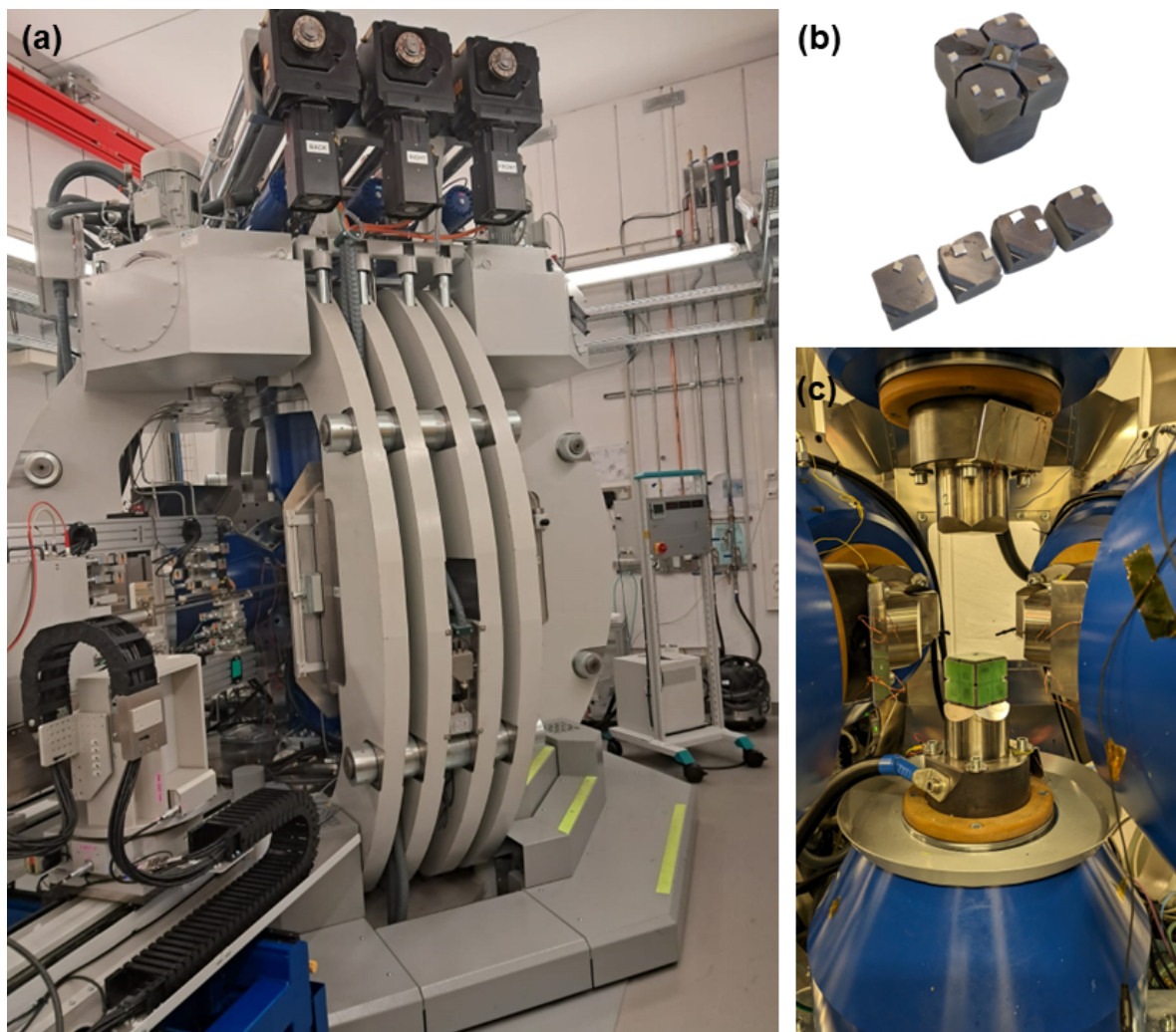


Figure 2.1: (a) 6-ram Large Volume Press Aster-15 at P61B beamline, DESY. (b) Sample assembly used for synthesis. (c) Sample placed inside the press before starting an HPHT reaction.

in situ analysis using high-energy X-rays. The P61B beamline provides unique opportunities for observing the formation and transformation of materials under HPHT conditions in real time, allowing for precise control and monitoring of the synthesis process. By leveraging the high-resolution diffraction and imaging capabilities of the beamline, one can gain invaluable insights into the structural and chemical changes occurring during the synthesis, leading to the discovery of novel materials with enhanced properties.

## 2.2 Structural Characterization

### 2.2.1 X-ray and Neutron Diffraction

X-ray diffraction (XRD) is a crucial method for determining the structural characteristics of a sample. For the samples prepared in this thesis, XRD measurements were carried out using a PANalytical Empyrean Alpha-1 diffractometer, which utilizes a monochromatic Cu  $K\alpha_1$  radiation and XRD patterns were further processed for detailed crystal structure analysis.

An X-ray diffractometer typically consists of an X-ray tube, a sample holder, and a detector. A typical illustration of what happens during an XRD measurement is shown in Fig. 2.2(a). When X-rays are directed at the powdered sample, they are scattered at various levels. Some of the X-rays are scattered by the atoms in the first layer (as depicted in Fig. 2.2(b)), while the remainder pass through and are scattered by subsequent layers. This scattering happens due to the random orientations of the grains in the sample. For effective scattering, the distance between the crystallographic planes must be comparable to the wavelength of the X-rays.

A peak in the XRD pattern is observed only when constructive interference occurs, meaning the phases of the scattered rays from different planes are the same. According to Bragg's law, constructive interference occurs if [4]:

$$2d \sin \theta = n\lambda \quad (2.1)$$

where  $d$  is the spacing between consecutive planes,  $n$  is the order of reflection,  $\lambda$  is the wavelength of the incident X-rays, and  $\theta$  is the angle of incidence (refer to Fig. 2.2(b)). When Bragg's law is satisfied by sets of planes in the sample, peaks appear at specific  $2\theta$  positions. Consequently, the XRD pattern, which plots intensity versus  $2\theta$ , is unique to different materials. The  $2\theta$  values are dependent on the plane distance  $d$ , which is determined by the lattice parameters. By indexing the diffraction pattern, the lattice parameters of the samples can be identified.

Furthermore, powder XRD data can be analyzed using various techniques to derive the complete crystal structure. The phase purity of a compound can be verified by comparing its XRD data with reference patterns in databases such as the Inorganic

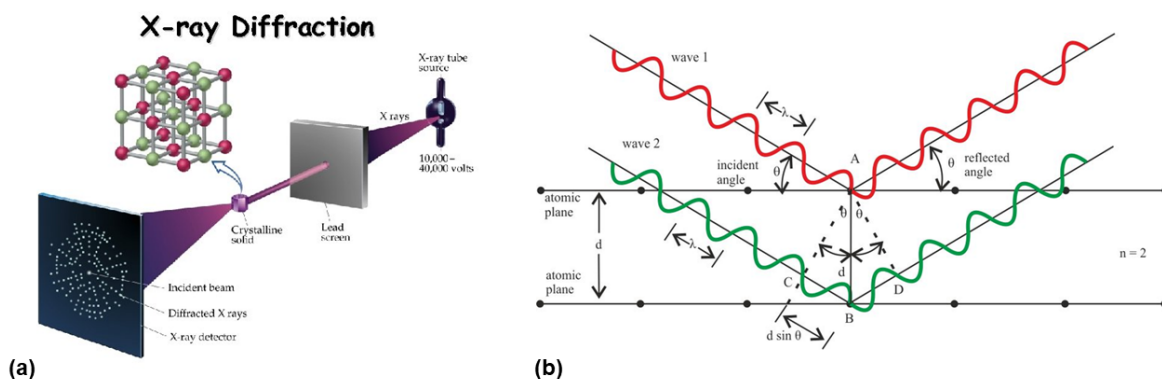


Figure 2.2: (a) Illustration of the process happening during an X-ray diffraction (Google Image). (b) Reflection of the incident beam of X-rays by atomic planes, adapted from [5].

Crystal Structure Database (ICSD) and the International Centre for Diffraction Data (ICDD). Impurity phases can also be detected using similar comparisons.

In many cases, compounds include light elements such as oxygen, carbon, and hydrogen. Since X-rays have limited sensitivity to these lighter elements, neutron diffraction experiments are essential for accurately determining the crystal structure and obtaining precise positional parameters. Neutrons interact with the atomic nuclei, allowing for a more accurate determination of the positions of lighter elements. Additionally, neutrons have an intrinsic magnetic moment that can interact with the magnetic moments of atoms within the compound, enabling the determination of the magnetic structure of the materials. Neutron diffraction experiments on the samples studied in this thesis were conducted using the WISH diffractometer [6] at the Rutherford Appleton Laboratory (RAL) in Didcot, UK.

### 2.2.2 Rietveld Refinement

Rietveld refinement is a highly effective technique for conducting comprehensive structural analysis of materials using X-ray and neutron diffraction data. This method employs a least-squares approach to iteratively simulate the theoretical profile until it agrees with the experimental diffraction pattern. In the refinement process, the observed intensity at each data point ( $y_{io}$ ) is compared with the calculated intensity ( $y_{ic}$ ) from the model. The goal is to minimize a residual function  $S$  through the least-squares method, which is expressed as [7]:

$$S = \sum w_i |y_{io} - y_{ic}|^2 \quad (2.2)$$

where  $w_i$  is a weight factor that depends on the standard deviation of the peak and background intensity. The calculated intensity at a point is given by:

$$y_{ic} = s \sum m_k L_k |F_k|^2 G(\Delta\theta_{ik}) + y_{ib} \quad (2.3)$$

In this equation,  $s$  represents the scale factor,  $m_k$  is the multiplicity factor,  $L_k$  is the Lorentz polarization factor for reflection  $k$ , and  $F_k$  is the structure factor. The term  $G(\Delta\theta_{ik})$  is the reflection profile function where  $\Delta\theta_{ik} = 2\theta_i - 2\theta_k$ , and  $2\theta_k$  is the calculated position of the Bragg peak, with  $y_{ib}$  being the background intensity.

The structure factor ( $F_k$ ) and the reflection profile function  $G(\Delta\theta_{ik})$  are crucial parameters in diffraction analysis. The structure factor  $F_{hkl}$  (equivalent to  $F_k$  for the  $k$ th reflection) is defined as:

$$F_{hkl} = \sum_j f_j e^{2\pi i(hx_j + ky_j + lz_j)} \quad (2.4)$$

$$|f|^2 = e^{-B \sin^2 \theta / \lambda^2} \quad (2.5)$$

where  $f$  represents the atomic form factor and  $B$  is the Debye-Waller temperature factor. The reflection profile function, which defines the peak shape, depends on several factors including the radiation source, detector, and wavelength distribution. Various forms can be used for the peak shape function, with the pseudo-Voigt (pV) function being the most commonly utilized. The pV function is expressed as:

$$pV = \eta L + (1 - \eta)G; \quad \text{with} \quad 0 \leq \eta \leq 1 \quad (2.6)$$

where  $L$  and  $G$  are the Lorentzian and Gaussian functions, respectively. These functions are defined as follows:

$$L = \frac{\sqrt{C_1}}{\pi H_k} \left[ 1 + C_1 \left( \frac{\Delta\theta_{ik}}{H_k} \right)^2 \right]^{-1} \quad (2.7)$$

$$G = \frac{C_0}{\sqrt{\pi H_k}} e^{-C_0(\Delta\theta_{ik}/H_k)^2} \quad (2.8)$$

where  $C_0$  and  $C_1$  are constants and  $H_k$  represents the full width at half maximum (FWHM) of the  $k$ th reflection. The FWHM for Gaussian and Lorentzian peak shapes are given by:

$$H_k^G = \sqrt{U \tan^2 \theta + V \tan \theta - W} \quad (2.9)$$

$$H_k^L = X \tan \theta + \frac{Y}{\cos \theta} \quad (2.10)$$

The parameters  $U$ ,  $V$ ,  $W$ ,  $X$ , and  $Y$  can be refined during the pattern-fitting process of the diffraction data. Additionally, the background can be manually selected or modeled as a polynomial function of  $2\theta$ , given by:

$$y_{ib} = \sum a_n (2\theta_i)^n \quad (2.11)$$

This background function must be refined by adjusting the coefficients  $a_n$  during pattern fitting.

At the final stage of the refinement process, the quality is assessed using the following  $R$  parameters [7]:

$$R_p(\text{profile}) = \frac{\sum |y_{io} - y_{ic}|}{\sum y_{io}} \quad (2.12)$$

$$R_{wp}(\text{Weighted profile}) = \left( \frac{\sum w_i (y_{io} - y_{ic})^2}{\sum w_i y_{io}^2} \right)^{1/2} \quad (2.13)$$

$$R_{pE}(\text{expected}) = \left( \frac{N - P}{\sum w_i y_{io}^2} \right)^{1/2} \quad (2.14)$$

$$\chi^2(\text{Goodness of fit}) = \left( \frac{R_{wp}}{R_E} \right)^2 = \frac{\sum w_i (y_{io} - y_{ic})^2}{N - P} \quad (2.15)$$

Here,  $N$  is the total number of profile points, and  $P$  represents the number of refined parameters. The  $\chi^2$  parameter indicates the accuracy of the fit, with a good fit typically having  $\chi^2$  approaching 1. However, reliance solely on these parameters is not advisable. It is crucial to also evaluate the fit between the observed and calculated patterns and consider the chemical plausibility of the structural model.

Rietveld refinement is executed in three steps using specific software packages. Initially, the lattice parameters and FWHM parameters ( $U$ ,  $V$ ,  $W$ , and/or  $X$ ,  $Y$ , and asymmetry parameters) are refined to achieve pattern fit, followed by the refinement of the background. Subsequently, a likely structural model is incorporated to refine the atomic positions and scale factor, ensuring good agreement with the experimental data. Finally, bond lengths and bond angles are estimated from the crystal structure. For the present work, crystal structure refinements were carried out using the Fullprof software package [8] and the JANA crystallographic software [9] and then visualized using VESTA software [10].

## 2.3 Physical Properties Measurements

### 2.3.1 DC Magnetization

The DC magnetization measurements described in this thesis were performed using a Superconducting Quantum Interference Device (SQUID) integrated into a Magnetic Property Measurement System (MPMS3), shown in Fig. 2.3(a), which is equipped with  $^3\text{He}$  (iHelium3, Quantum Design Japan) attachment, depicted in Fig. 2.3(b) and can measure down to 0.4 K. The fundamental principle underlying these measurements is based on Faraday's law of induction, which states that the induced voltage in a closed circuit is proportional to the rate of change of magnetic flux through the circuit. The magnetic flux ( $\phi$ ) through a coil with  $n$  turns and a cross-sectional area  $A$  is given by:  $\phi = A \cdot B$  where  $B$  is the magnetic field. Consequently, the induced voltage ( $V$ ) in the coil is expressed as:



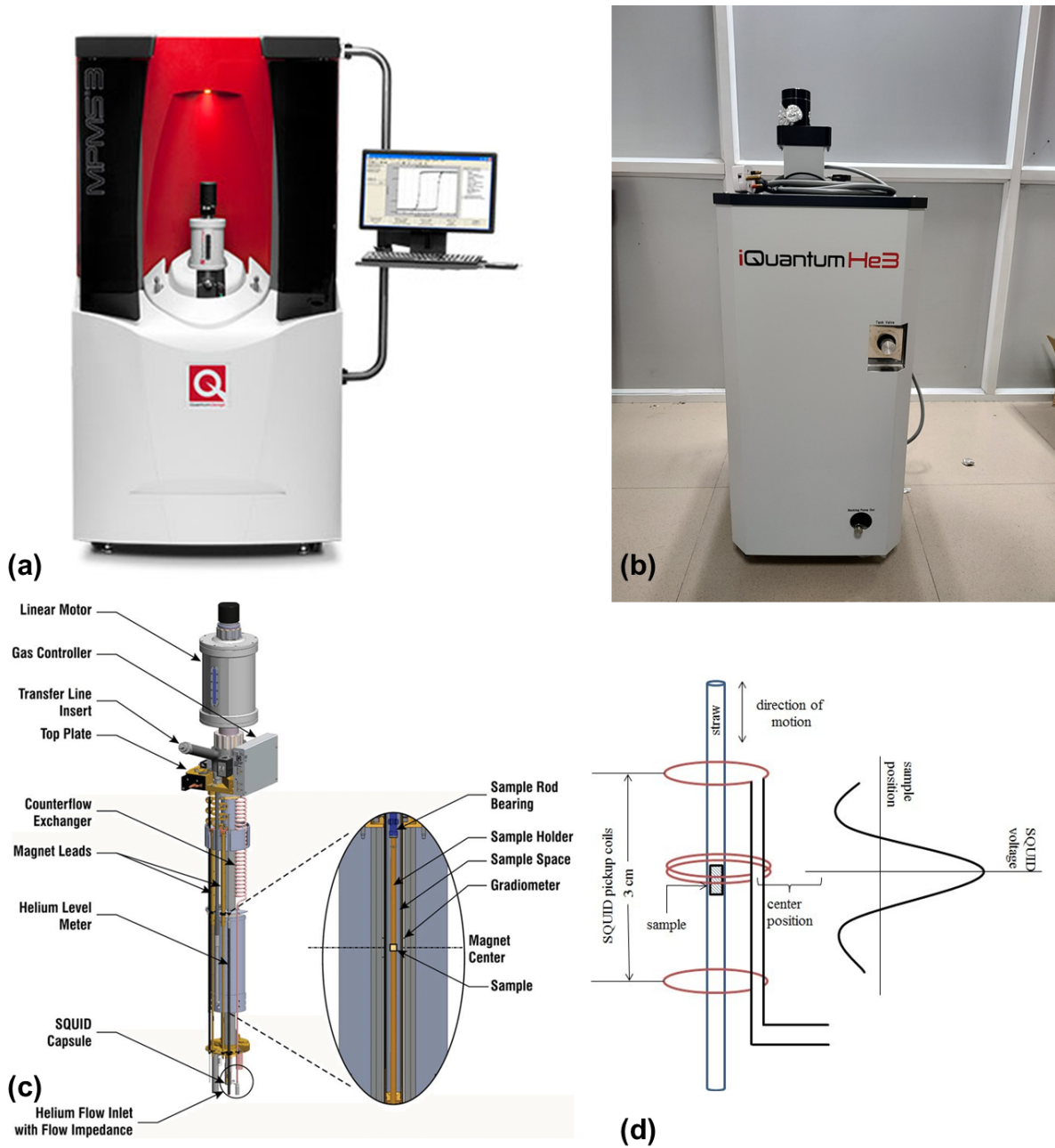


Figure 2.3: (a) A file photo of quantum design make MPMS (Quantum Design Website). (b) iHE3 addition to MPMS. (c) MPMS3 SQUID system diagram showing important elements, including the relative location of the sample, gradiometer, and magnet (adapted from [11]). (d) Schematic diagram of VSM (adapted from [11]).



$$V = -n \frac{d\phi}{dt} = -nA \frac{dB}{dt} \quad (2.16)$$

This induced voltage arises from the oscillation of the sample within the coil, which in turn induces a change in the magnetic field  $B$ .

### 2.3.1.1 SQUID

The SQUID is an extremely sensitive magnetometer used to measure very subtle magnetic fields. It consists of two superconductors separated by thin insulating layers, forming two parallel Josephson junctions. During measurements, a constant bias current is applied to the device while the measured voltage oscillates due to phase changes at the junctions. These phase changes are influenced by variations in magnetic flux caused by the oscillation of the sample, allowing for the determination of the sample's magnetic moment. From this, both DC magnetization and magnetic susceptibility can be derived.

There are two modes for magnetization measurements: the Vibrating Sample Magnetometer (VSM) mode and the DC scan mode. In VSM mode, shown in Fig. 2.3(c), the sample vibrates sinusoidally with a high frequency. In contrast, the DC scan mode involves moving the sample up and down uniformly rather than oscillating, making it preferred for obtaining high-quality data.

Measurements are conducted over a temperature range from 1.8 K to 400 K, with an applied magnetic field varying between 0 and 7 T. The required magnetic fields are generated using a superconducting magnet, which is a solenoid composed of superconducting wires. Both the superconducting magnet and the sample chamber are housed in a Dewar and cooled with liquid helium.

The superconducting detection coil is a single piece of superconducting wire configured as a two-level gradiometer, as shown in Fig. 2.3(d). This coil is placed within the uniform magnetic field produced by the superconducting magnet. Together with the SQUID circuit, which includes a signal-to-flux converter, flux-to-voltage converter, and other electronics, the system measures the magnetic moment.

### 2.3.1.2 $^3\text{He}$ Attachment

The integration of an iHelium-3 ( $^3\text{He}$ ) attachment with the SQUID MPMS3 system enables magnetic measurements from 1.8 K to 0.4 K.  $^3\text{He}$ , an isotope with a lower boiling

point than  $^4\text{He}$ , allows for lower temperatures due to its unique cryogenic properties.  $^3\text{He}$  has a boiling point of 3.2 K, significantly lower than the 4.2 K boiling point of  $^4\text{He}$ . A  $^3\text{He}$  cryostat is integrated into the MPMS3 system. The  $^3\text{He}$  gas is condensed into a liquid and then pumped to lower pressures, achieving temperatures down to 0.4 K. Precise control of the temperature is maintained through a combination of pumping and controlled heating.

### 2.3.2 AC Magnetization Measurements

AC susceptibility measurements are utilized to investigate the magnetization dynamics. Unlike DC magnetization, which remains constant in time and therefore cannot capture the dynamics of magnetization in certain scenarios, such as spin glasses, AC susceptibility is particularly useful. In cases where magnetization decays over time below the spin-glass transition, AC susceptibility measurements offer valuable insights.

The AC susceptibility measurements discussed in this thesis were conducted using the ACMS option of the PPMS system [12]. The sample is kept in the ACMS insert, which is shown in Fig. 2.4(a). During the measurement, the sample oscillates inside a gradiometer, where one coil carries current in the clockwise direction and the other in the counterclockwise direction, as illustrated in Fig. 2.4(b). According to Faraday's law of electromagnetic induction, the induced voltage in the coil,  $V_{\text{coil}}$ , is given by [13]:

$$V_{\text{coil}} = -\frac{d\phi}{dt} = -\left(\frac{d\phi}{dz}\right)\left(\frac{dz}{dt}\right) = CmA\omega \sin(\omega t) \quad (2.17)$$

Here,  $\phi$  is the magnetic flux,  $C$  is a constant,  $m$  is the magnetic moment of the sample,  $A$  is the cross-sectional area of the coil,  $\omega$  is the angular frequency of oscillation, and  $t$  is time.

The measurements were conducted using the five-point bottom-top-bottom-center-center (BTBCC) procedure in the PPMS system [12]. Initially, signals from the detection coil are captured and amplified and then digitized by an analog-to-digital (A/D) converter, collecting the data as a response waveform. Subsequently, the real and imaginary components of each response waveform are derived by fitting the data and comparing it with the driving signal. Finally, calibration readings are used to determine the real and imaginary parts of the AC susceptibility of the sample.

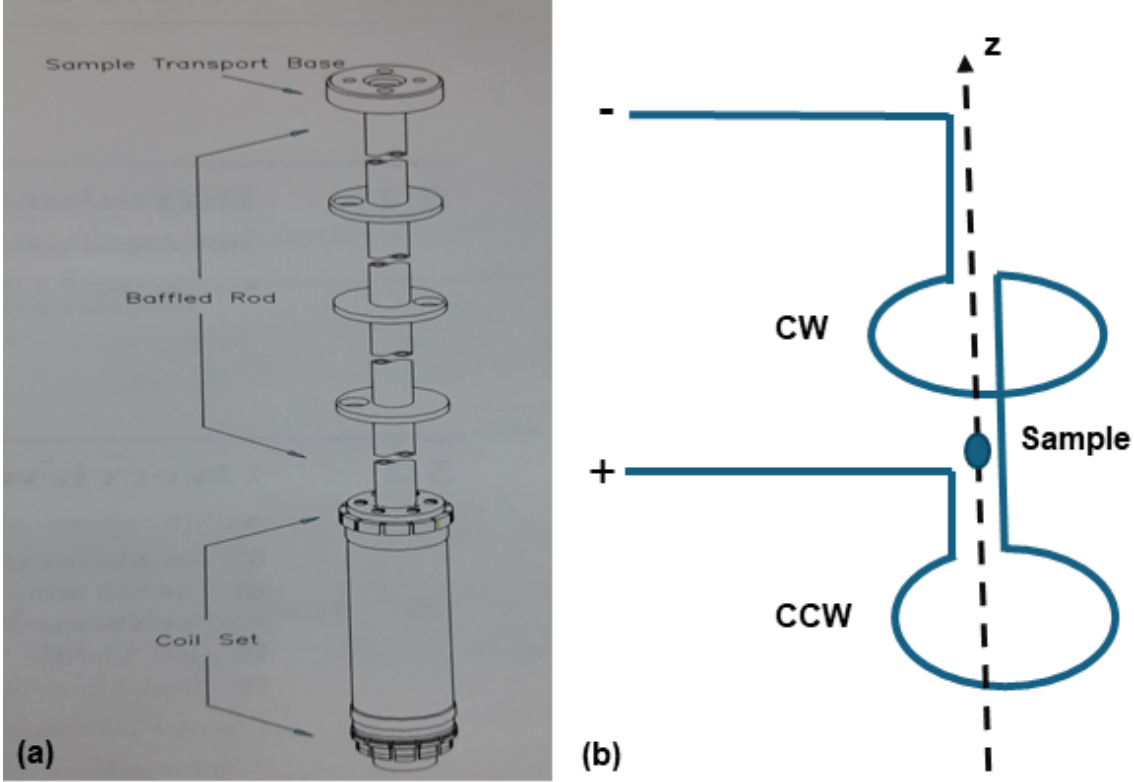


Figure 2.4: (a) ACMS insert in which sample is mounted (adapted from [12]). (b) Location of the sample during the measurement.

### 2.3.3 Heat Capacity Measurement

Heat capacity measurements are crucial for understanding the thermodynamic properties of materials and have been performed using PPMS. In a typical PPMS heat capacity measurement, a small sample is attached to a microcalorimeter, which is then placed on a temperature-controlled platform, as shown in Fig. 2.5. The sample is subjected to a controlled temperature sweep while the system measures the heat flow into or out of the sample.

The PPMS employs a thermal relaxation method to determine the heat capacity. This involves heating the sample with a small, known amount of heat and measuring the time it takes for the sample to return to thermal equilibrium, as depicted in Fig. 2.5(b). The heat capacity  $C_p$  is calculated using the relation:

$$C_p = \frac{P\tau}{\Delta T}$$

where  $P$  is the power applied,  $\tau$  is the thermal relaxation time, and  $\Delta T$  is the temperature change. The system automatically adjusts the temperature, applies the heat pulses, and

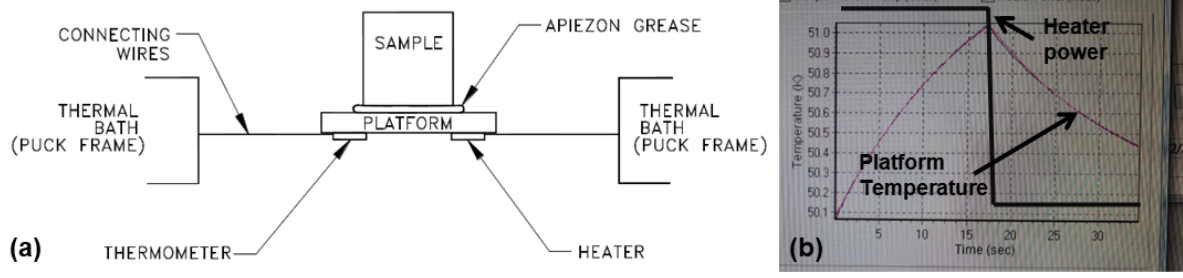


Figure 2.5: (a) Thermal connections to sample and sample Platform in PPMS heat capacity option (adapted from [14]). (b) The graph displays a plot of fit and measured temperature versus time.

records the resulting temperature changes, allowing for accurate and efficient heat capacity measurements over a wide range of temperatures.

### 2.3.4 Thermal Conductivity Measurements

Thermal conductivity measurements are essential for understanding how heat is transported through materials and have been carried out using PPMS. In a typical PPMS thermal conductivity measurement, a sample is mounted between two thermal reservoirs. One end of the sample is heated while the other end is kept at a lower temperature, creating a temperature gradient along the sample, as illustrated in Fig. 2.6(a). The thermal transport option puck used is shown in Fig. 2.6(b). The system measures the heat flow through the sample and the temperature difference between the two ends.

The thermal conductivity  $\kappa$  is determined using the relation:

$$\kappa = \frac{QL}{A\Delta T}$$

where  $Q$  is the heat flow rate,  $L$  is the length of the sample,  $A$  is the cross-sectional area, and  $\Delta T$  is the temperature difference.

The PPMS employs a steady-state or a transient method for these measurements. In the steady-state method, a constant heat flow is maintained, and the temperature difference is measured once equilibrium is reached. In the transient method, the system measures the time-dependent temperature response to a heat pulse, as depicted in Fig. 2.6(c). The PPMS thermal transport option automates the measurement process, ensuring accurate control of the temperature gradient and precise recording of the heat flow and temperature data. This capability allows for detailed studies of thermal properties, including thermal conductivity, thermal diffusivity, and the Seebeck coefficient.

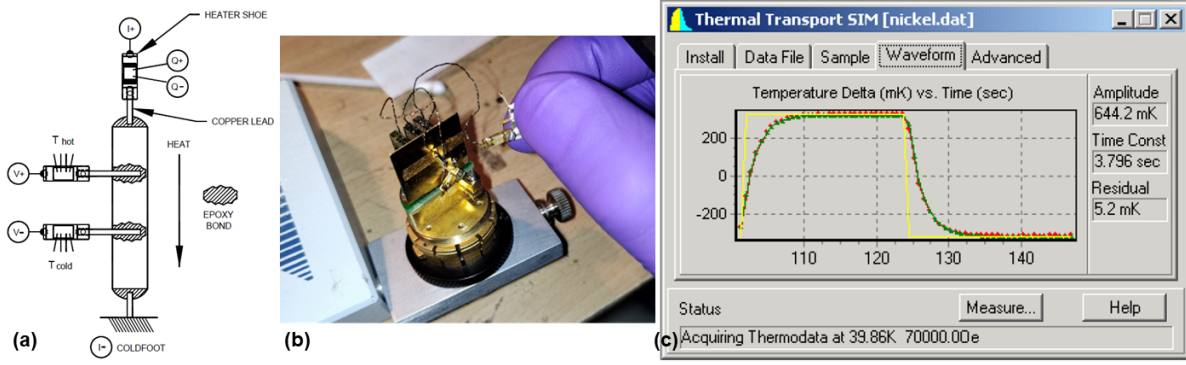


Figure 2.6: (a) Thermal connections to sample and sample platform in PPMS thermal transport option (adapted from [15]). (b) Sample being mounted on the puck. (c) The time dependence of the sample data, along with the fitted curves. The heater pulse is shown schematically as a yellow square wave (adapted from [15]).

Table 2.1: Comparison of Muons, Electrons, and Protons

Property	Muons	Electrons	Protons
Symbol	$\mu^\pm$	$e^\pm$	$p$
Charge	$\pm 1e$	$\pm 1e$	$+1e$
Rest Mass ( $\text{MeV}/c^2$ )	105.66	0.511	938.27
Mean Lifetime	$2.2 \times 10^{-6} \text{ s}$	Stable	Stable
Spin	$\frac{1}{2}$	$\frac{1}{2}$	$\frac{1}{2}$
Magnetic Moment ( $\mu_N$ )	3.183	-1.001	2.7928
Magnetic Dipole Moment	$1.001 \times 10^{-3} \mu_B$	$1\mu_B$	$2.79\mu_N$

### 2.3.5 Muon Spin Relaxation Measurements

Muons are elementary particles similar to electrons but with a much greater mass. They are unstable, with a mean lifetime of about 2.2 microseconds, and can be used as sensitive magnetic probes in condensed matter physics. A comparison of various properties of muons with elementary particles; electrons and protons, is tabulated in Table 2.1. Muons are typically produced in large accelerators, such as located in Rutherford Appleton Laboratory, UK. The  $\mu\text{SR}$  data presented in this thesis has been collected at MuSR spectrometer at RAL, UK, shown in Fig. 2.7(a).

Muon Spin Relaxation ( $\mu\text{SR}$ ) is a powerful technique used to investigate the magnetic properties of materials. In  $\mu\text{SR}$  experiments, polarized muons are implanted into a sample, and their subsequent spin behavior is monitored. The muon spin precesses in the local

magnetic field of the sample, and this precession provides detailed information about the magnetic environment.

The sequence of events for a typical  $\mu$ SR measurement is as follows:

### Production of Pions

Pions ( $\pi^\pm$ ) are typically produced in high-energy collisions, such as those involving protons in a particle accelerator or cosmic rays interacting with the atmosphere. The reaction can be represented as:

$$p + p \rightarrow p + n + \pi^+ \quad (E_p > 280 \text{ meV})$$

$$p + n \rightarrow p + p + \pi^- \quad (E_p > 280 \text{ meV})$$

$$p + p \rightarrow p + p + \pi^+ + \pi^- \quad (E_p > 600 \text{ meV})$$

$$p + n \rightarrow p + n + \pi^+ + \pi^- \quad (E_p > 600 \text{ meV})$$

### Pions Decay to Muons

Charged pions ( $\pi^+$  or  $\pi^-$ ) have spin  $S = 0$  with a mean lifetime of 26 ns and decay into muons and muon neutrinos or antineutrinos. This decay results in 100 % polarized muons due to parity violation. The decay equations are:

$$\pi^+ \rightarrow \mu^+ + \nu_\mu$$

$$\pi^- \rightarrow \mu^- + \bar{\nu}_\mu$$

### Decay of Muons into Positrons

Muons decay into positrons (for  $\mu^+$ ) or electrons (for  $\mu^-$ ) along with corresponding neutrinos. The decay equations for positive and negative muons are:

$$\mu^+ \rightarrow e^+ + \nu_e + \bar{\nu}_\mu$$

$$\mu^- \rightarrow e^- + \bar{\nu}_e + \nu_\mu$$

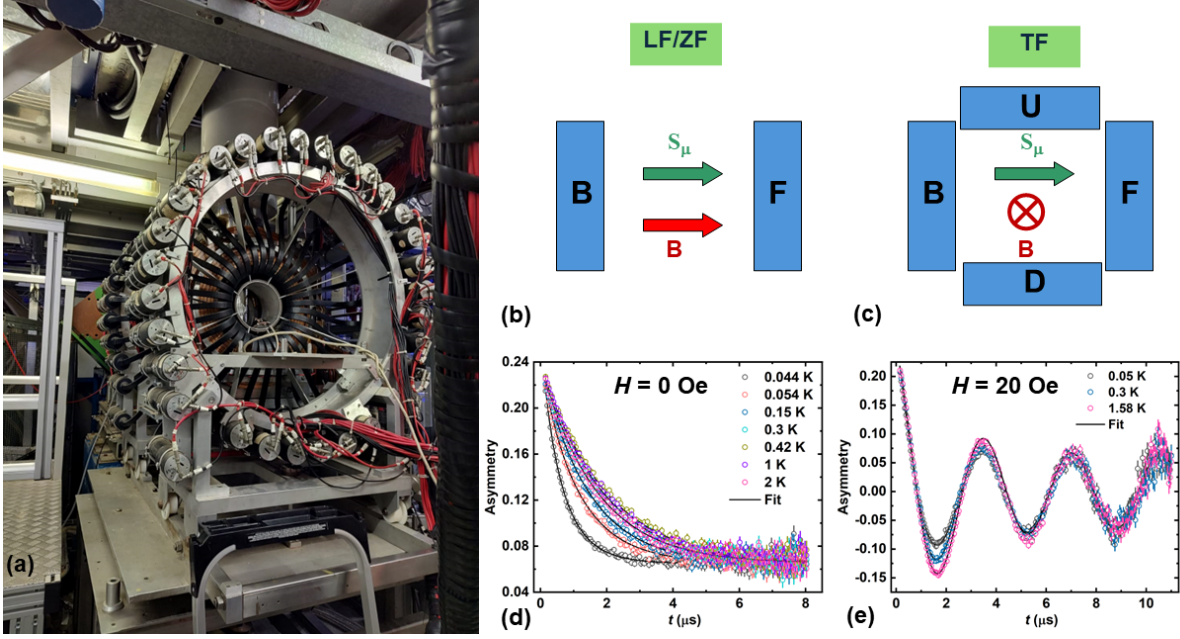


Figure 2.7: (a) MuSR spectrometer at RAL, UK. (b) Longitudinal field (LF) and Zero field (ZF) geometry of a  $\mu\text{SR}$  measurement. B and F stand for backward and forward detectors. (c) Transverse field (TF) geometry of a  $\mu\text{SR}$  measurement. U and D denoted up and down detectors. (d) Typical  $\mu\text{SR}$  spectra of a ZF measurement. (e) Typical  $\mu\text{SR}$  spectra of a TF measurement.

### Detection of Positrons (or Electrons)

The basic principle of  $\mu\text{SR}$  involves detecting the decay positrons emitted preferentially in the direction of the muon spin. By measuring the asymmetry of the positron emission as a function of time, the muon spin relaxation rate can be determined. This rate is influenced by the local magnetic fields within the sample.

There are different types of  $\mu\text{SR}$  measurements, including:

- **Zero-Field (ZF)  $\mu\text{SR}$ :** Used to study internal magnetic fields without an applied external field.
- **Longitudinal-Field (LF)  $\mu\text{SR}$ :** Involves applying a magnetic field parallel to the initial muon spin direction to study spin relaxation mechanisms and to get an estimate of the internal magnetic field. An illustration of ZF and LF geometries is shown in Fig. 2.7(b).
- **Transverse-Field (TF)  $\mu\text{SR}$ :** Involves applying a magnetic field perpendicular



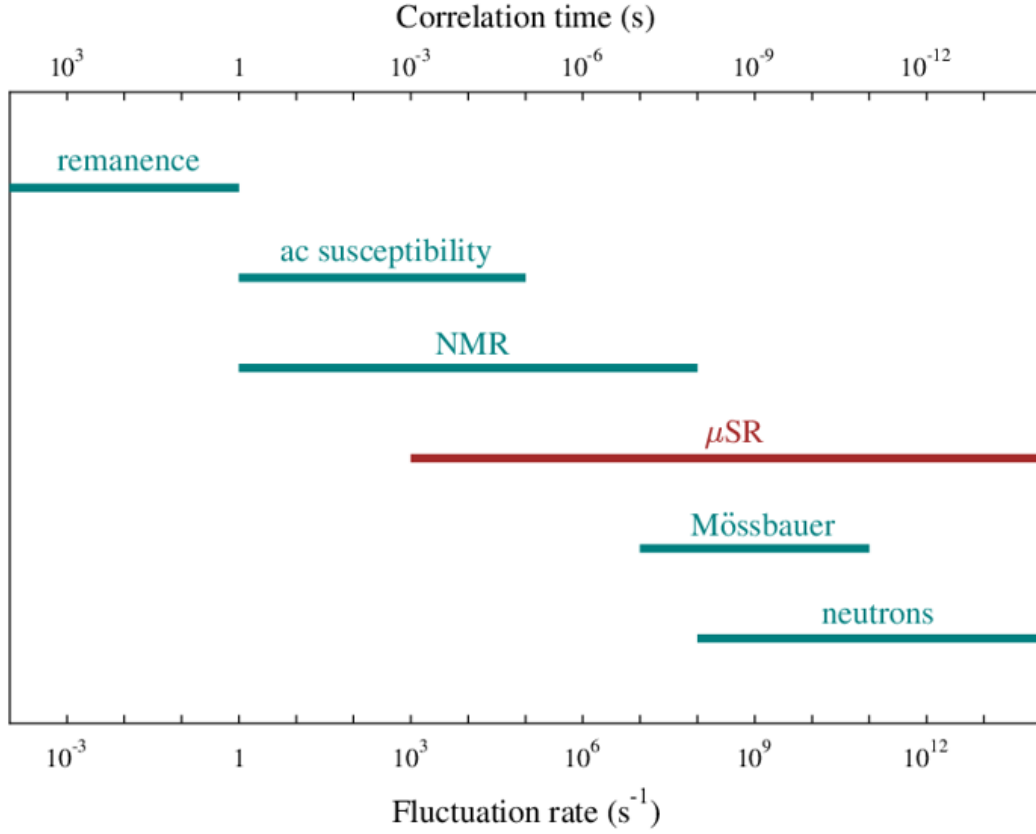


Figure 2.8: A comparison of various spectroscopic techniques, adapted from STFC website [16].

to the initial muon spin direction to study precession frequencies and line widths. This measurement can precisely unveil the magnitude of the local magnetic field. An illustration of TF geometries is shown in Fig. 2.7(c).

In a  $\mu$ SR measurement, we measure asymmetry versus time ( $A(t)$ ) which can be written as;

$$A(t) = \frac{N_F(t) - \alpha N_B(t)}{N_F(t) + \alpha N_B(t)}$$

A typical ZF and TF  $\mu$ SR spectra measured at different temperatures are shown in Fig. 2.7(d) and (e).  $\mu$ SR is particularly useful for studying magnetic order, spin dynamics, and superconductivity in various materials. It provides unique insights into the microscopic magnetic properties that are often inaccessible by other techniques. A comparison of the time scale at which different spectroscopic techniques work is shown in Fig. 2.8.  $\mu$ SR spectroscopic technique bridges the gap between other local probes such as nuclear



magnetic resonance (NMR) and inelastic neutron scattering (INS). All the  $\mu$ SR analyses reported in the thesis have been done using MANTID [17, 18].

# Bibliography

- [1] A. R. West, Solid State Chemistry and Its Applications (John Wiley & Sons, 2014).
- [2] G. Tammann, Lehrbuch der Metallkunde: Chemie und Physik der Metalle und ihrer Legierungen (1932).
- [3] R. Farla, S. Bhat, S. Sonntag, A. Chanyshev, S. Ma, T. Ishii, Z. Liu, A. Néri, N. Nishiyama, G. A. Faria *et al.*, Extreme conditions research using the large-volume press at the P61B endstation, PETRA III, J. synchrotron radiation **29**, 409 (2022).
- [4] W. H. Bragg and W. L. Bragg, The Reflexion of X-rays by Crystals, Proc. R. Soc. Lond. A. **88**, 605 (1913).
- [5] N Waesermann, Ph. D. Thesis, University of Hamburg (2012).
- [6] L. C. Chapon, P. Manuel, P. G. Radaelli, C. Benson, L. Perrott, S. Ansell, N. J. Rhodes, D. Raspino, D. Duxbury, E. Spill, and J. Norris, Wish: The new powder and single crystal magnetic diffractometer on the second target station, Neutron News **22**, 22 (2011).
- [7] H. M. Rietveld, J. Appl. Crystallogr. **2**, 65 (1969).
- [8] J. Rodríguez-Carvajal, Introduction to the program FULLPROF: refinement of crystal and magnetic structures from powder and single crystal data, (2001).
- [9] V. Petricek, M. Dušek, and L. Palatinus, Crystallographic Computing System JANA2006: General features, Z. Kristallogr. Cryst. Mater. **229**, 345 (2014).
- [10] K. Momma and F. Izumi, J. Appl. Crystallogr., VESTA: a three-dimensional visualization system for electronic and structural analysis, **41**, 653 (2008).
- [11] Magnetic Property Measurement System - MPMS 3 user's manual (Quantum Design).

- [12] Physical Property Measurement System - AC measurement system (ACMS) option - User's Manual (Quantum Design).
- [13] D. Martien, Introduction to AC susceptibility (Quantum Design) (2002).
- [14] Physical Property Measurement System - Heat capacity option - user's manual (Quantum Design).
- [15] Physical Property Measurement System - Thermal transport option - User's manual (Quantum Design).
- [16] <https://www.isis.stfc.ac.uk/>
- [17] Mantid (2013): Manipulation and Analysis Toolkit for Instrument Data.; Mantid Project.
- [18] O. Arnold, J.C. Bilheux, J.M. Borreguero, A. Buts, S.I. Campbell, L. Chapon, M. Doucet, N. Draper, R. Ferraz Leal, M.A. Gigg *et al.*, Nuclear Instruments and Methods in Physics Research Section A: Accelerators, Spectrometers, Detectors and Associated Equipment **764**, 156 (2014).

## Chapter 3

# Exploring Potential Quantum Spin Liquid State in a Quasi-One Dimensional Magnetic Chain

This chapter presents a comprehensive investigation of  $\text{NaYbTe}_2\text{O}_7$  through a range of physical property measurements. A detailed examination of its crystal structure uncovers the formation of quasi-one-dimensional magnetic chains of  $\text{Yb}^{3+}$  ions along the  $b$ -axis, with a substantial separation of approximately  $6.3 \text{ \AA}$  between these chains. This unique arrangement of Yb-ions positions  $\text{NaYbTe}_2\text{O}_7$  as an ideal candidate for exploring one-dimensional magnetism. Magnetic measurements confirm the absence of a long-range magnetic ordering down to  $0.4 \text{ K}$ ; however, they indicate the emergence of magnetic correlations below  $1 \text{ K}$ . The analysis of the inverse magnetic susceptibility corroborates that the ground state can be described as a Kramers doublet, indicating  $J_{eff} = 1/2$ . Our findings from magnetization measurements align with the results from temperature and magnetic field-dependent heat capacity measurements, both of which suggest robust magnetic correlations among  $\text{Yb}^{3+}$  ions. Moreover, heat capacity measurements reveal no long-range magnetic ordering down to  $0.285 \text{ K}$ . The assertion of these magnetic correlations is further reinforced by thermal conductivity measurements, which confirm the scattering of phonons due to magnetic excitations at low temperatures. Considering the combination of low dimensionality,  $J_{eff} = 1/2$ , the absence of magnetic ordering down to  $0.285 \text{ K}$ , and the presence of strong magnetic correlation below  $1 \text{ K}$ , we suggest that these results are indicative of a potential quantum spin liquid (QSL) state in  $\text{NaYbTe}_2\text{O}_7$ . This work has been published in [Physical Rev. B](#) and reproduced here with permission.

### 3.1 Introduction

Low dimensional quantum magnets offer a compelling platform for exploring systems governed by pronounced quantum and thermal fluctuations [1]. In particular, significant attention has been directed towards the one-dimensional (1D)  $J_1$ - $J_2$  quantum Heisenberg model, where an element of frustration is introduced through the parameter  $J_2$ . Theoretical investigations of such systems have indicated that the emergence of distinct quantum phases depends on factors like  $\alpha = J_2/J_1$ , applied magnetic fields, and axial exchange anisotropy [2–5]. This model has found experimental realization in a variety of compounds based on 3d elements, including but not limited to  $\text{Li}_2\text{CuO}_2$  [6–8],  $\text{LiCuSbO}_4$  [5],  $\text{SrCuO}_2$  [9],  $\text{LiCuVO}_4$  [10–12],  $\text{Li}_2\text{CuZrO}_4$  [13] and  $A_2\text{Cu}_2\text{Mo}_3\text{O}_{12}$  ( $A = \text{Rb}, \text{Cs}$ ) [14, 15]. Additionally, this model has been explored in a selected group of rare-earth-based compounds such as  $\text{YbAlO}_3$  [16] and  $\text{TbScO}_3$  [17]. However, the presence of large anisotropic orbital-dominated moments favors Ising or XXZ type of interactions rather than Heisenberg. Despite these assumptions, the Yb Kramers doublets exhibit distinct behavior from classical Ising spins. For example, the exchange processes among pseudospins ( $J_{eff} = 1/2$ ) within the same chain involve quantum-origin spin flip terms, challenging the notion of their classical behavior [16, 18]. The investigation on rare earth compounds has unveiled unconventional quantum phases and the presence of substantial anisotropic orbital-dominated moments, which can lead to fractional quantum excitations [18].

The strong spin-orbit coupling (SOC) combined with localized electrons in the 4f orbitals of rare earth magnets makes these materials as prime candidates for exploring strongly correlated physics. In systems characterized by an odd number of 4f electrons, the intricate interplay between the crystalline electric field and SOC assumes a central role in resolving degeneracy, ultimately leading to the formation of Kramers doublet states. This phenomenon holds significant promise for understanding and harnessing the unique electronic and magnetic behaviors exhibited by these materials. The rare earth compounds containing Yb are of particular interest as they have garnered significant attention in the pursuit of realizing QSLs owing to their  $J_{eff} = 1/2$  Kramers doublet ground state [19–21]. The low-dimensional arrangement of Yb ions, *e.g.* 1-D chain, triangular lattice, and kagome lattice, intertwined with the intricate interplay of competing exchange interactions, set the ideal backdrop for the emergence of the quantum spin liquid phenomenon. Recent developments have highlighted several Yb-based compounds, such as  $\text{YbMgGaO}_4$  [22],  $\text{NaYbO}_2$  [20], and  $\text{Ba}_3\text{Yb}_2\text{Zn}_5\text{O}_{11}$  [8], as potential candidates for hosting quantum spin liquid behavior within triangular or pyrochlore magnetic lattices. In this context, we

embark on a journey to address the fundamental question of uncovering a QSL state within a compound characterized by a quasi-one-dimensional lattice.

## 3.2 Experiment

A powder sample of  $\text{NaYbTe}_2\text{O}_7$  has been prepared by using  $\text{Na}_2\text{CO}_3$ ,  $\text{Yb}_2\text{O}_3$ , and  $\text{TeO}_2$  as starting materials. Before mixing the starting materials in a stoichiometric mixture,  $\text{Na}_2\text{CO}_3$  was preheated to 373 K to remove the moisture, and  $\text{Yb}_2\text{O}_3$  was preheated to 1173 K to remove the trapped water molecules, if any. The mixture was initially heated to 873 K at a constant ramping rate of 5 K/min to avoid sodium loss through evaporation and kept at the same temperature for 12 hrs. Finally, the mixture was pelletized and heated to 993 K for a pure phase. The synthesized sample has been characterized further on a PANalytical Empyrean Alpha I diffractometer using  $\text{Cu-K}\alpha$  single wavelength ( $\lambda = 1.54059 \text{ \AA}$ ). The magnetic properties of the compound have been explored using a magnetic properties measurement system (MPMS) of Quantum Design, USA. Further, magnetization was measured down to 0.4 K using a  $^3\text{He}$  (iHelium3, Quantum Design Japan) attachment to the MPMS. The physical properties measurement system (PPMS) of Quantum Design, USA, has been utilized to perform heat capacity, ac magnetic susceptibility, and thermal conductivity measurements. For thermal conductivity measurements, the sample was cut into a rectangular shape of the dimensions  $1.3 \times 2.9 \times 6.3 \text{ mm}^3$  and four probe measurement technique is used. The elemental mapping was performed using ZEISS Gemini scanning electron microscope (SEM). Ultra-low temperature heat capacity was measured in an Oxford Kelvinox-400MX dilution refrigerator with relaxation calorimetry. A 9.07 mg plate-like polycrystalline sample was loaded on the sample platform with Apizon-N grease to increase the thermal conductance between the sample and the platform. The two-tau model was used to analyze the data.

## 3.3 Results and Discussion

### 3.3.1 Crystal Structure

The atomic arrangement in the unit cell has been determined through Rietveld refinement of the XRD pattern using Jana software [23], and the refined pattern is shown in Fig 3.1 (a). The close match between the experimental data and the simulated pattern confirmed the phase purity and established that this compound crystallizes in the  $P2_1/n$  space

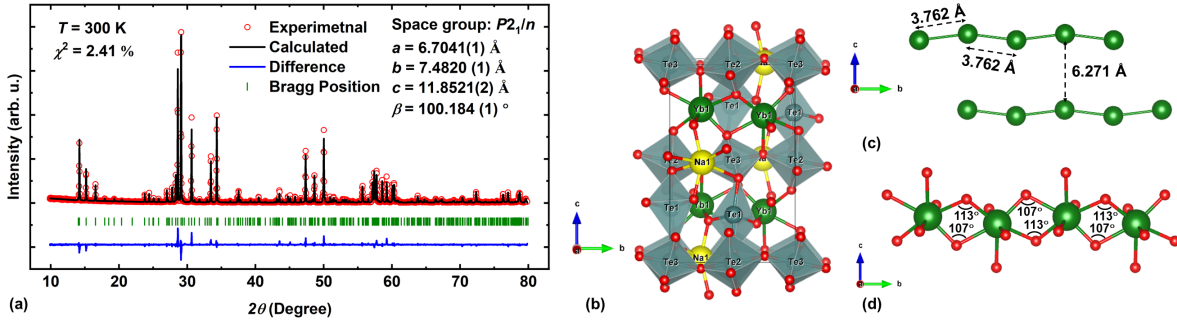


Figure 3.1: (a) Rietveld refinement of  $\text{NaYbTe}_2\text{O}_7$ . (b) The unit cell of  $\text{NaYbTe}_2\text{O}_7$  viewed along the  $a$  axis. (c) Projection of the one-dimensional Yb-chains along  $b$ -axis. (d) Possible exchange pathways between nearest magnetic ions.

group, which is isostructural with  $\text{NaYTe}_2\text{O}_7$ , having tellurium in two different oxidation states, ( $\text{Te}^{4+}$ ,  $\text{Te}^{6+}$ ) [24]. The crystal structure obtained from the Rietveld refinement is shown in Fig. 3.1 (b), and the structural parameters are given in Table 3.1. In this structure,  $\text{Te}^{6+}\text{O}_6$  octahedra and  $\text{Te}^{4+}\text{O}_4$  dispheniods form a two-dimensional layer of  $[\text{Te}_2\text{O}_7]^{4-}$  stacked along  $[1\ 0\ 1]$  direction. A close crystal structure analysis reveals that the  $\text{YbO}_7$  polyhedra share an edge through O5 and O7 to form a one-dimensional chain along the  $b$ -axis, as exhibited in Fig. 3.1 (c). Moreover, energy dispersive spectroscopy analysis reaffirmed the chemical composition of the sample as exhibited in Fig. 3.2, 3.3, and Table 3.2. The intrachain distance between  $\text{Yb}^{3+}$  ions is  $3.762$  Å compared to the interchain distance of  $6.271$  Å, indicating that the magnetic properties are dominated by intrachain exchange interactions. There are two possible pathways for superexchange interaction, one through O5 and the other through O7, featuring different bond angles ( $\text{Yb-O5-Yb} = 113.0^\circ$ ,  $\text{Yb-O7-Yb} = 107.0^\circ$ ), which change their position alternatively similar to  $\text{LiCuSbO}_4$  [5], as shown in Fig. 3.1 (d). The value of exchange parameters through these paths is sensitive to bond angle values, as reported for similar magnetic lattices [5], where a subtle change of  $2^\circ$  can influence the exchange parameters significantly, as reported earlier [25]. Further, frustration is enhanced by the anisotropic nature of the exchange interactions and may lead to a QSL state [26]. Given these compelling structural properties, further exploration of its magnetic ground state holds significant promise.

### 3.3.2 DC Magnetization

To investigate the magnetic behavior of this compound, the dc magnetic susceptibility has been measured from 300 to 0.4 K by following the zero-field-cooled (ZFC) and field-cooled

Table 3.1: Crystallographic parameters along with occupancy and isotropic displacement parameters obtained from the Rietveld refinement of the powder XRD data. Space group:  $P2_1/n$ ,  $a = 6.7041(1)$  Å,  $b = 7.4820(1)$  Å,  $c = 11.8521(2)$  Å,  $\beta = 100.184(1)^\circ$ ,  $V = 585.14(1)$  Å<sup>3</sup>,  $\chi^2 = 2.44$  %, Bragg  $R$  factor = 7.56 %,  $R_f = 5.06$  %

Atom	Wyckoff symbol	x	y	z	Occupancy	$B_{iso}(\text{\AA}^2)$
Na(1)	4e	-0.0048(43)	1.2567(39)	0.5056(19)	1.0	0.013(3)
Yb(1)	4e	0.2380(6)	0.7494(7)	0.2334(2)	1.0	0.024(4)
Te(1)	4c	0.2279(6)	0.9922(8)	0.7321(3)	1.0	0.021(5)
Te(2)	2c	0.5	1.0	0.5	1.0	0.022(5)
Te(3)	2a	0.0	1.0	1.0	1.0	0.019(6)
O(1)	4e	0.0714(53)	1.1912(49)	0.6984(29)	1.0	1.0
O(2)	4e	0.0313(42)	0.8101(39)	0.6808(20)	1.0	1.0
O(3)	4e	0.2326(39)	0.9837(54)	0.5448(22)	1.0	1.0
O(4)	4e	0.4774(62)	1.2558(64)	0.4684(27)	1.0	1.0
O(5)	4e	0.3546(45)	0.9708(51)	0.3461(22)	1.0	1.0
O(6)	4e	0.2365(42)	0.9532(41)	0.9179(22)	1.0	1.0
O(7)	4e	0.2169(44)	1.0429(49)	1.1341(24)	1.0	1.0

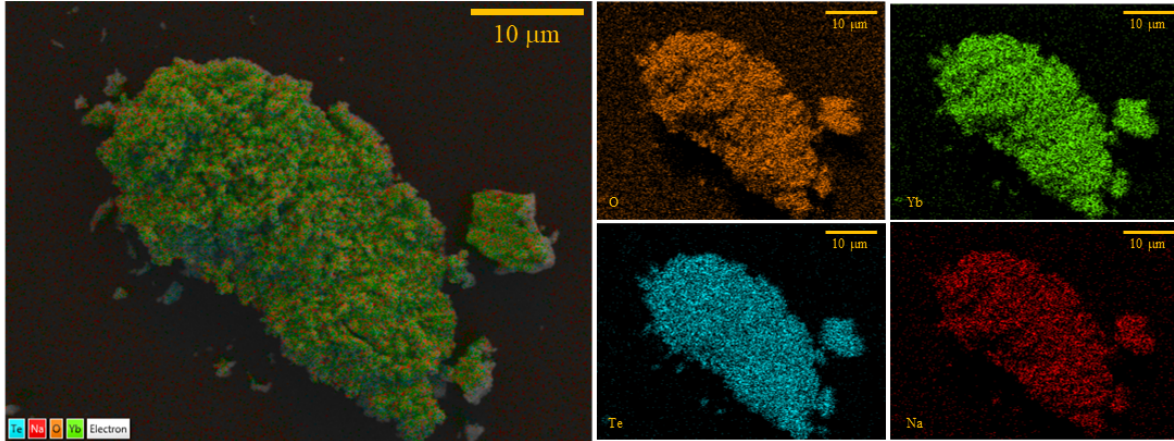


Figure 3.2: Elemental mapping of  $\text{NaYbTe}_2\text{O}_7$  sample with the help of FE-SEM. Various elements have been shown in different colors.

Table 3.2: Observed and expected weight and atomic percentage value of different elements

Element	Line Type	Weight %	Theoretical Weight %	Atomic %	Theoretical Atomic %
Na	K series	3.26	4.08	7.27	9.09
Yb	L series	32.92	30.73	9.83	9.09
Te	L series	43.48	45.31	17.60	18.18
O	K series	20.34	19.88	65.30	63.64



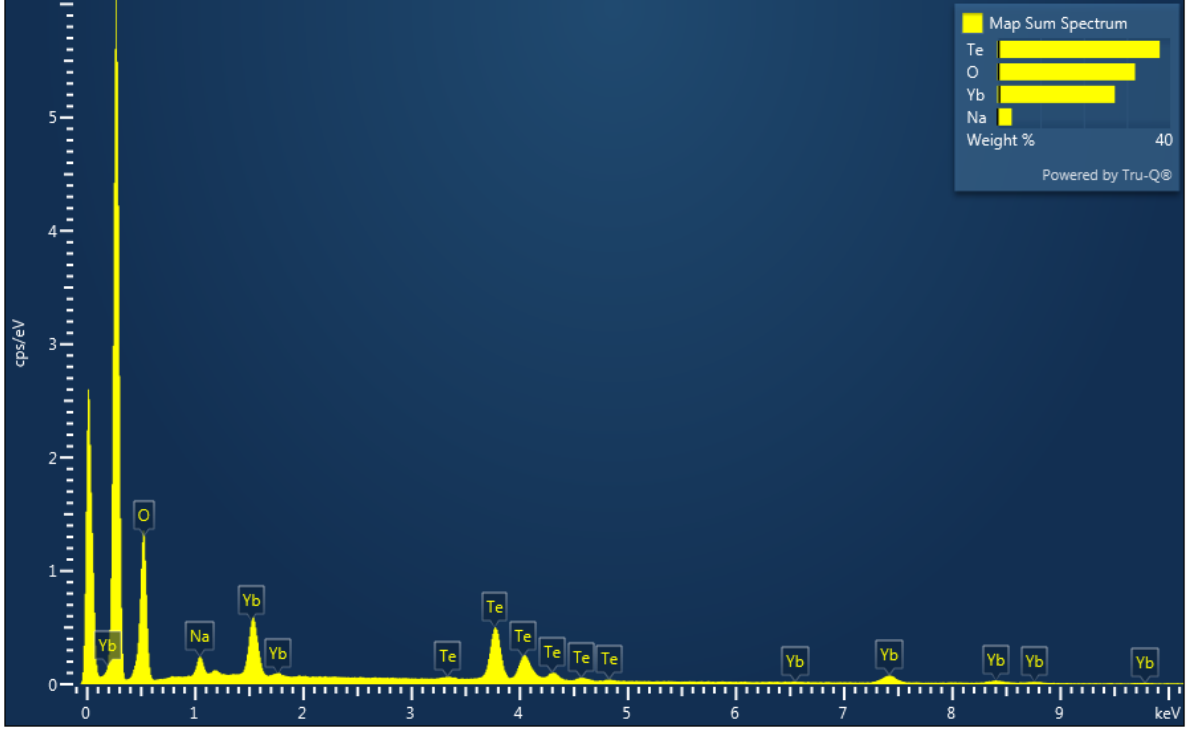


Figure 3.3: Elemental mapping spectra of the NaYbTe<sub>2</sub>O<sub>7</sub> sample.

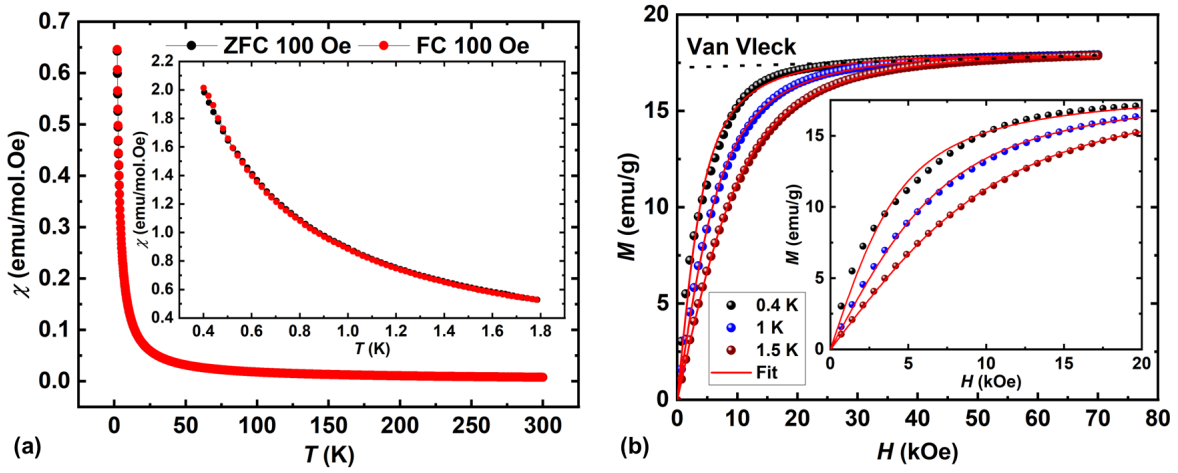


Figure 3.4: (a) Temperature dependence of dc magnetic susceptibility performed under ZFC and FC protocol down to 2 K. Inset shows the variation down to 0.4 K. (b) Isothermal magnetization curves measured at different temperatures along with the Brillouin fits represented by solid lines. The black dashed line accounts for the Van Vleck contribution. Inset shows the zoomed version of the fitting in low-field region.

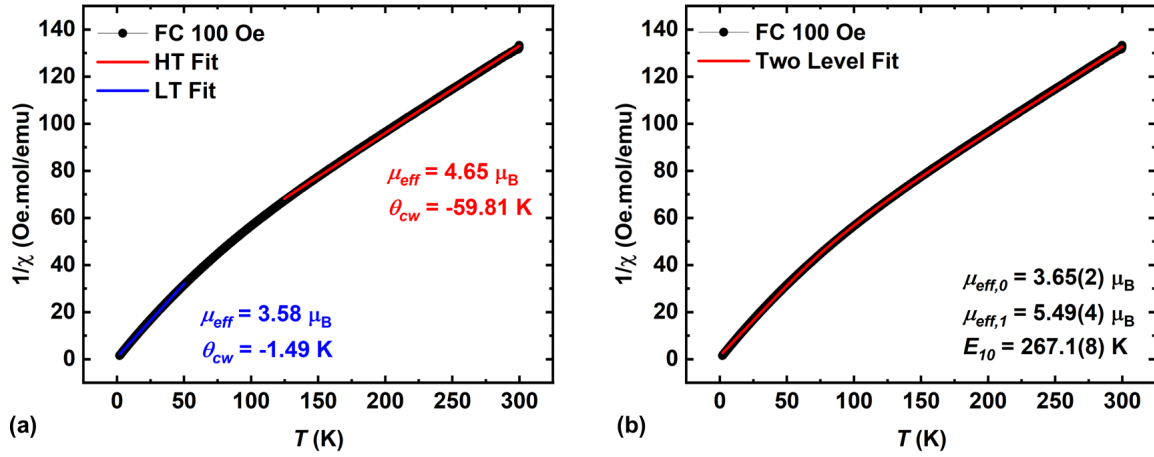


Figure 3.5: (a) Fitting of low-temperature and high-temperature linear region of the inverse susceptibility data by using the Curie-Weiss model. (b) Fitting of the inverse susceptibility data with the help of the modified Curie-Weiss model.

(FC) protocols, and the results are depicted in Fig. 3.4 (a) and its inset. It is evident from this figure that there is no long-range magnetic ordering down to 0.4 K. After removing the van Vleck contribution ( $\chi_{VV} = 6.47 \times 10^{-3}$  emu/mol-Oe, estimated from the slope of the linear fitting of isotherms at higher magnetic fields) from the inverse susceptibility data, two different linear regions have been observed, as shown in Fig. 3.5(a). Analysis of the inverse susceptibility in high-temperature (HT) region (125-300 K) gave  $\theta_{CW} = -59.81$  K and an effective paramagnetic moment ( $\mu_{eff}$ ) value of  $4.65 \mu_B/\text{f.u.}$  which is in close agreement with the theoretically expected value for  $\text{Yb}^{3+}$  ions ( $J = 7/2$ ,  $^4f_{13}$  configuration). The Curie constant can be used to calculate the Lande factor ( $g$ ) as;  $C = \frac{ng^2\mu_B^2J(J+1)}{3k_B}$ ; where  $n$  represents the number of free spins per formula unit,  $\mu_B$  is Bohr magneton and  $k_B$  is Boltzmann constant; by assuming that there is no interaction among  $\text{Yb}^{3+}$  ions at room temperature. The value of  $g$  comes out to be 1.17, which is very close to the theoretically expected value, 1.14. The fitting of the low-temperature region (2-50 K) results in a reduced value of  $\mu_{eff} \sim 3.58 \mu_B/\text{f.u.}$  and  $\theta_{CW} = -1.49$  K. Reduction of  $J$  value also results in the suppression of the  $\theta_{CW}$  values. A qualitative alignment between the observed and effective magnetic moments of  $\text{Yb}^{3+}$  ions at room temperature coupled with the reduced value of magnetic moment as the temperature is lowered indicates that  $\text{Yb}^{3+}$  ions have Kramers doublet as ground state [27–29]. The crystal electric field affects the eightfold degenerate states (for  $J = 7/2$ ) of  $\text{Yb}^{3+}$  ions and splits them into four Kramers doublet, as observed for other Yb compounds [19–21]. For the LT region ( $J_{eff} = 1/2$ ), the value of  $g$  comes out to be 4.12, which is very close

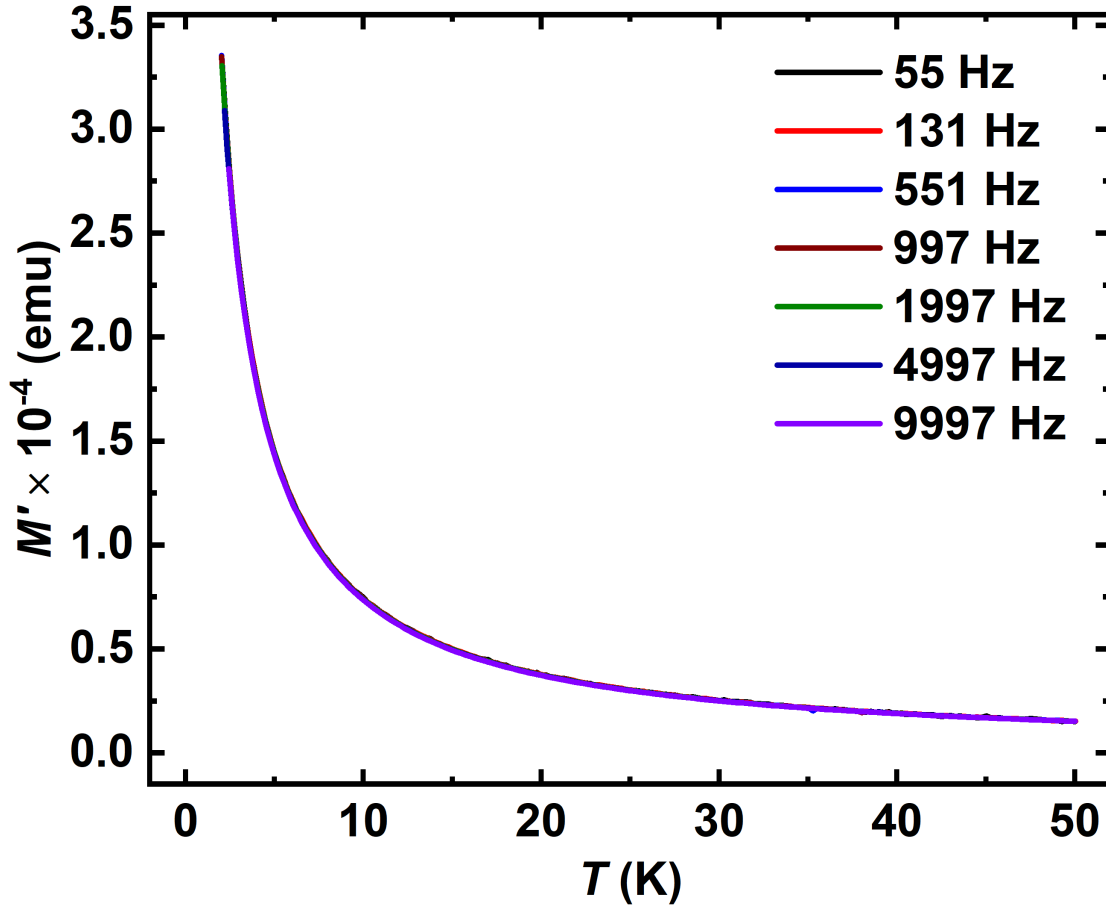


Figure 3.6: Variation of frequency-dependent ac susceptibilities with temperature.

to the  $g$  value calculated from isothermal magnetization data ( $\sim 4$ ). The Curie constant is no longer temperature independent as the higher Kramers doublets also contribute, and considering the temperature range of measurement, it is sufficient to consider only the first excited Kramers doublet. A two-level approximation of the Curie-Weiss model can be expressed as [30, 31]:

$$1/\chi = 8.(T - \theta_{CW}). \left( \frac{1 + \exp^{-\frac{E_{10}}{k_B T}}}{\mu_{eff,0}^2 + \mu_{eff,1}^2 \cdot \exp^{-\frac{E_{10}}{k_B T}}} \right) \quad (3.1)$$

where  $\mu_{eff,0}^2$  and  $\mu_{eff,1}^2$  stand for effective moments in the crystal field ground state and first excited state while  $E_{10}$  denotes the energy separation between the ground and first excited states. Figure 3.5(b) represents the fitting of the inverse susceptibility data and gives  $E_{10} \sim 267$  K, which further confirms the Kramers doublet ground state at lower temperatures.

To examine the high-field magnetism of the compound at low temperatures, we have carried out the isothermal magnetization measurements at three different temperatures, 0.4, 1, and 1.5 K, by gradually varying the magnetic field from +7 T to -7 T. Fig. 3.4 (b) depicts the variation of isothermal magnetization curves in the first quadrant. The magnetic isotherm within the paramagnetic state of a compound can be described by  $M(H) = \chi_{\nu\nu}H + gJ_{eff}N_A\mu_B B_{J_{eff}}(H)$ , where  $B_{J_{eff}}(H)$  is the Brillouin function [32]. The deviation of magnetization data from the fit below 1 K suggests the development of magnetic exchange interactions [33–35]. The slope of the high-field linear behavior of the magnetization curve at 0.4 K gives the Van Vleck contribution. After subtracting the Van Vleck contribution, the magnetization curve becomes saturated above 2 T. Furthermore, temperature-dependent ac susceptibility measurements have been carried out at the different frequencies of a small ac magnetic field ( $H_{ac} = 10$  Oe) to rule out possible glassiness. Figure 3.6 demonstrates the absence of a glassy state down to 2 K. Hence, a preliminary magnetic investigation reveals the development of exchange interactions below 1 K.

### 3.3.3 Heat Capacity

Heat capacity measurement carried out from 100 to 0.285 K in the absence of a magnetic field is shown in Fig. 3.7 (a) and (b), and fitting the data with the Debye-Einstein model is shown by the solid line. Please note that the compound is highly insulating in the measured temperature range. To access the change in magnetic entropy, removing the lattice contribution from the total heat capacity becomes necessary, which can be estimated using The Debye-Einstein model. This model considers that the sum of acoustic and phonon modes equals the total number of atoms present in the primitive cell (For  $\text{NaYbTe}_2\text{O}_7$ , it is 11). Further, the relative weights of acoustical and optical modes are taken in the ratio of 1: $n$ -1, where  $n$  is the total number of atoms. So, this compound has three acoustic modes and 30 optical phonon modes. The three acoustic modes have been described using one Debye term, and three Einstein terms have been used to describe the optical modes. To reduce the free parameters and minimize the experimental errors, several optical modes are grouped [36]. The Debye-Einstein model for this system can be expressed as follows [37, 38]:

$$C_{D-E} = \frac{9aR}{x_D^3} \int_0^{x_D} \frac{x^4 e^x}{(e^x - 1)^2} dx + 3R \sum_{i=1}^3 \frac{b_i x_{E_i}^2 e^{x_{E_i}}}{(e^{x_{E_i}} - 1)^2} \quad (3.2)$$

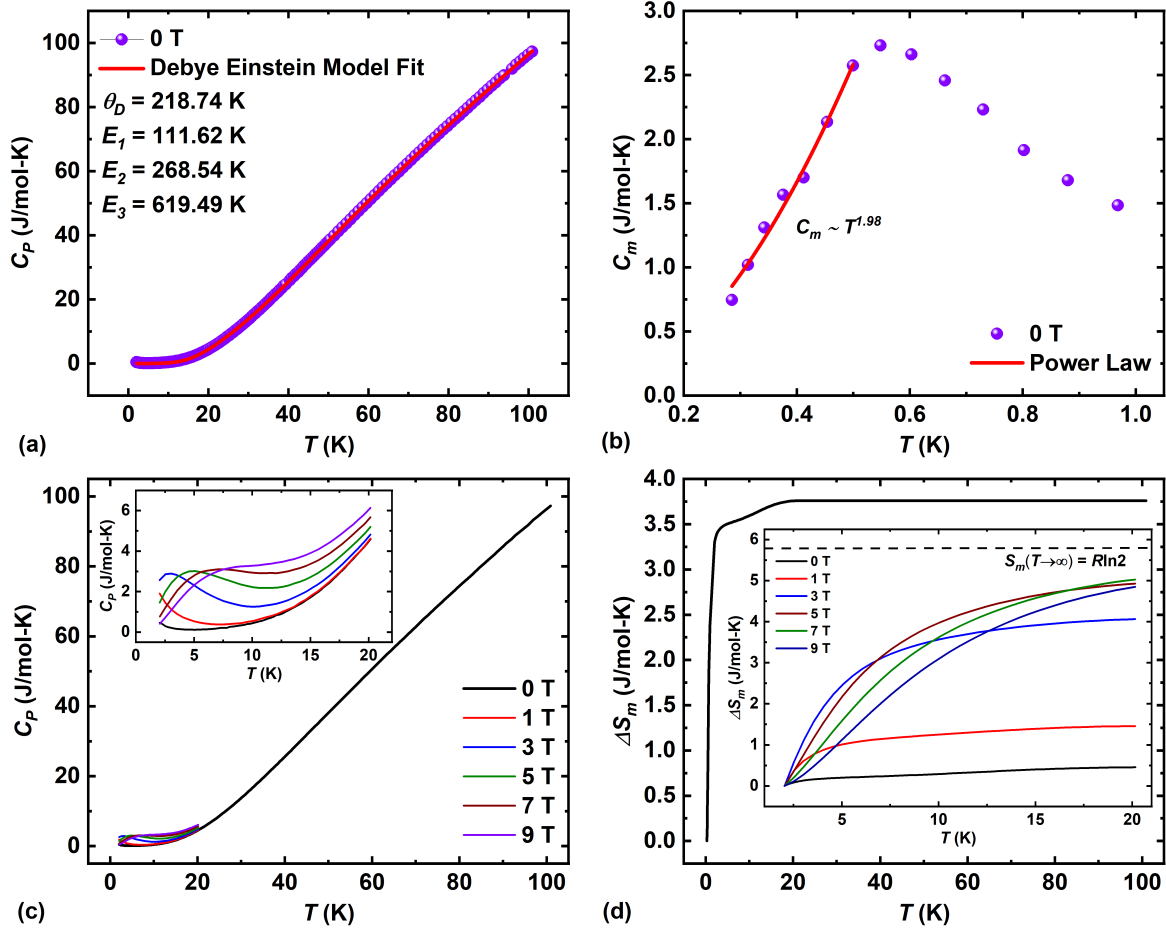


Figure 3.7: (a) Fitting of the heat capacity data measured in the absence of the magnetic field with the Debye-Einstein model. (b) Temperature dependence of heat capacity below 1 K and fitting with power law. (c) Temperature dependence of heat capacity data measured under different magnetic fields. The inset shows the variation in low-temperature regions. (d) Entropy calculated from magnetic heat capacity down to 0.285 K. Inset shows the temperature dependence of magnetic entropy calculated down to 2 K in the presence of different magnetic fields.

where  $x_{D,E} = \theta_{D,E}/T$ ;  $\theta_D$  and  $\theta_E$  are Debye and Einstein temperatures, respectively,  $R$  is the universal gas constant. The coefficients  $a$  and  $b_i$  stand for the contributions from acoustic and optical phonons, respectively. The values of these weight factors are constrained in such a way that they add up to the total number of atoms in the unit cell (In this case,  $a = 1$ ,  $b_1 = 1$ ,  $b_2 = 3$ , and  $b_3 = 6$ ). Here,  $b_1$  corresponds to Te vibrations,  $b_2$  stands for  $\text{Na}^+$  and  $\text{O}^{2-}$  motion, and  $b_3$  represents the contribution from remaining 6  $\text{O}^{2-}$  atoms. We could confine the flexible Debye-Einstein model to a physically reasonable fit using these considerations.

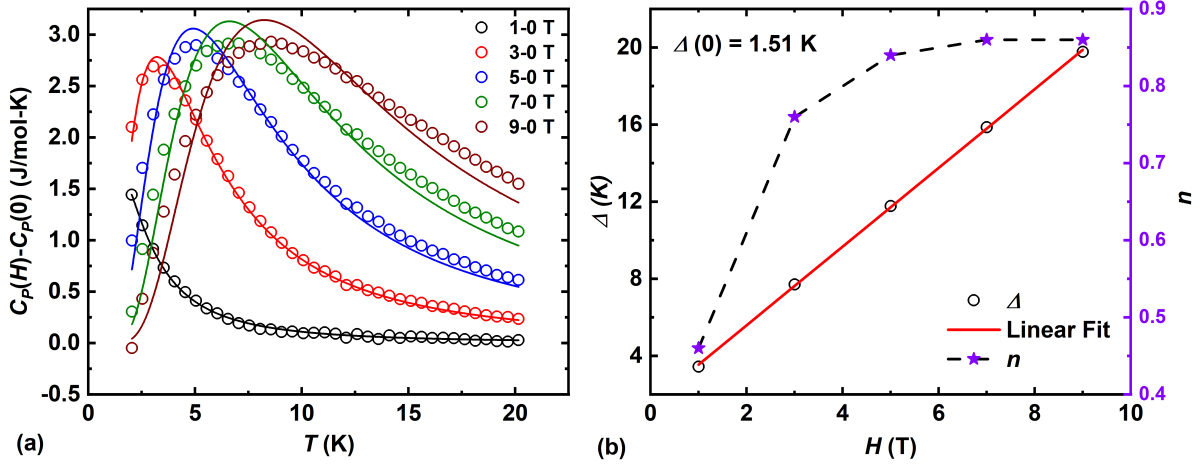


Figure 3.8: (a) Variation of Schottky contribution with temperature and its fitting with the two-level model equation. (b) Linear fitting of  $\Delta$  (left axis) values calculated from the CEF fitting and variation of  $n$  values with the magnetic fields

The absence of  $\lambda$ -like anomaly confirms that there is no long-range magnetic ordering down to 0.285 K. However, a broad peak around 0.55 K may be related to magnetic excitations or a weak splitting of degenerate Kramers doublet, which may arise due to local strain on the Yb site [39]. The magnetic contribution below 0.55 K could be fitted well with a power law ( $C_m \sim T^n$ ) with  $n \sim 2$ , as shown in Fig. 3.7 (b). A similar power law dependence has been observed for other Yb compounds and indicates the presence of a gapless ground state [20, 40, 41]. A gapped spectral function ( $C_m \sim \exp(-\Delta/T)$ ) could not fit the data, indicating that the broad anomaly is likely due to magnetic excitations. Fig. 3.7 (c) depicts that this anomaly moves towards higher temperatures with an increase in the magnetic field, which manifests the Schottky anomaly and rules out possible short-range magnetic ordering. The Schottky anomaly appears due to the splitting of ground state Kramers doublet in an applied magnetic field (Zeeman splitting), as observed for other Yb compounds [34, 42]. The magnetic entropy has been estimated by subtracting the phononic contribution, and its temperature dependence is shown in Fig. 3.7 (d). A comparison of the calculated magnetic entropy with the theoretically expected value for  $J_{eff} = 1/2$  unveils that  $\sim 35$  % of the magnetic entropy is still embedded into the system below 0.285 K. The saturation value of the magnetic entropy increases with an increase in magnetic field and approaches around  $R \ln 2$  above 5 T, as shown in the inset of Fig. 3.7 (d). A slightly lower saturation value of the magnetic entropy than  $R \ln 2$  indicates that a smaller fraction of the spins are randomly oriented.

In the presence of a magnetic field, total heat capacity can be written as  $C(T, H) =$

$C(T, 0) + C_{sch}(T, H)$ . Hence, the Schottky contribution can be probed by subtracting the zero field heat capacity from the total heat capacity measured under finite magnetic fields. Considering  $J_{eff} = 1/2$  (two-level system), Schottky anomaly can be expressed as [43–45]

$$C_{sch}(T, H) = nR \left( \frac{\Delta}{T^2} \right) \frac{\exp(\Delta/T)}{[1 + \exp(\Delta/T)]^2} \quad (3.3)$$

where  $n$  represents the number of free spins per formula unit,  $R$  is the universal gas constant, and  $\Delta$  determines the spacing between two levels.  $\Delta$  has a magnetic field dependence which can be expressed as [44–47];  $\Delta(H) = g\mu_B H_{eff}/k_B$ , where  $H_{eff} = \sqrt{H_0^2 + H_1^2}$  which implies that  $H_{eff} = H_0$  in the absence of the external magnetic field ( $H_1 = 0$ ). Figure 3.8 (a) exhibits the fitting of Schottky contribution data at different magnetic fields. We observed that the Schottky contribution for  $H > 5$  T could not be fitted well with a two-level model, and the inclusion of the third or fourth level is required. The variation of the fitted parameters with the magnetic field is shown in Fig. 3.8 (b). The intercept of the linear fit of crystal field energy gives its value at zero field,  $\Delta(0) \sim 1.51$  K. A finite value of  $\Delta(0)$  originates from the development of  $\text{Yb}^{3+} - \text{Yb}^{3+}$  exchange interactions [34, 35, 42]. In the case of  $n$ , it first increases up to 5 T and then exhibits a saturation behavior, suggesting that the energy levels are split by the magnetic field and around 86 % of the spins are excited to higher energy levels. The fraction of spins excited to higher levels in the presence of a magnetic field matches exactly with the amount of the magnetic entropy recovered ( $\sim 86$  %), as depicted in Fig. 3.7 (d). The value of Lande  $g$  factor comes out to be  $\sim 3.27$  considering the relation  $\Delta(H) = g\mu_B H_{eff}/k_B$  (taking  $\Delta(H) = 19.78$  K for  $H = 9$  T).

### 3.3.4 Thermal Conductivity

Considering the presence of Schottky anomaly in the heat capacity measurements, measuring thermal conductivity will be more helpful as it does not respond to localized entities responsible for Schottky anomaly but is only sensitive to the itinerant excitations [48]. Heat is transported mainly by acoustic phonons and magnetic contributions for low-dimensional magnetic systems [49, 50]. Figure 3.9 (a) exhibits a broad feature in  $\kappa/T$  data centered around 20 K where phonon contribution dominates the thermal conductivity. This feature has been observed for many systems [51, 52] and can be explained by the Callaway model of thermal conductivity [53], according to which a decrease in phonon population with a decrease in the temperature and an increase in phonon mean free path in a finite-sized sample can result in such feature. Figure 3.9 (b)

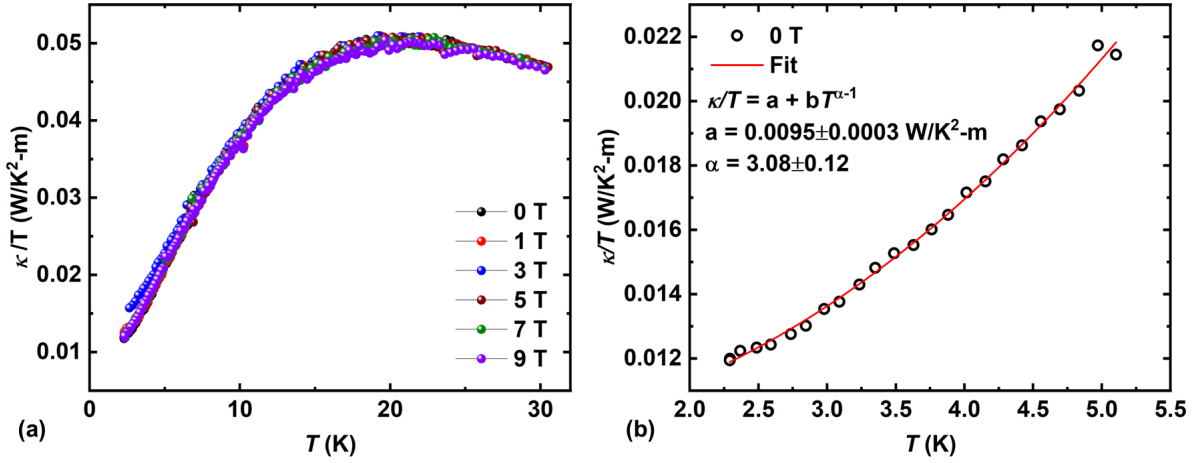


Figure 3.9: (a) Temperature dependence of the thermal conductivity divided by temperature measured under different magnetic fields. (b) Fitting of  $\kappa/T$  measured under 0 T with the equation described in the text.

Table 3.3: Magnetic field dependence of  $a$  and  $\alpha$  parameter

$H$ (T)	$a$ (W/K <sup>2</sup> -m)	$\alpha$
0	0.00958	3.0843
1	0.01052	3.1788
3	0.01167	2.6685
5	0.00898	2.7696
7	0.00748	2.4631
9	0.00786	2.5823

shows the fitting of the zero field  $\kappa/T$  data with  $\kappa/T = a + bT^{\alpha-1}$ , where the first term represents electron-like contribution (for insulators, it should be zero) and the second term is responsible for the phononic contribution. The fitting results in  $T^3$  dependence of the thermal conductivity, which confirms the diffuse scattering of the phonons and rules out the presence of the specular scattering. Further, a finite value of  $a$  under 0 T and its magnetic field dependence (as shown in Table 3.3) indicates the presence of magnetic excitations in the system. Moreover, the value of  $\alpha$  decreases with an increase in the magnetic field (all the fittings shown in Fig. 3.10), manifesting that the spins are getting ordered and contributing toward thermal resistance (although very small). The magnetic field dependence of  $\alpha$  is consistent with the magnetic entropy values, further supporting our claim of magnetic excitations.



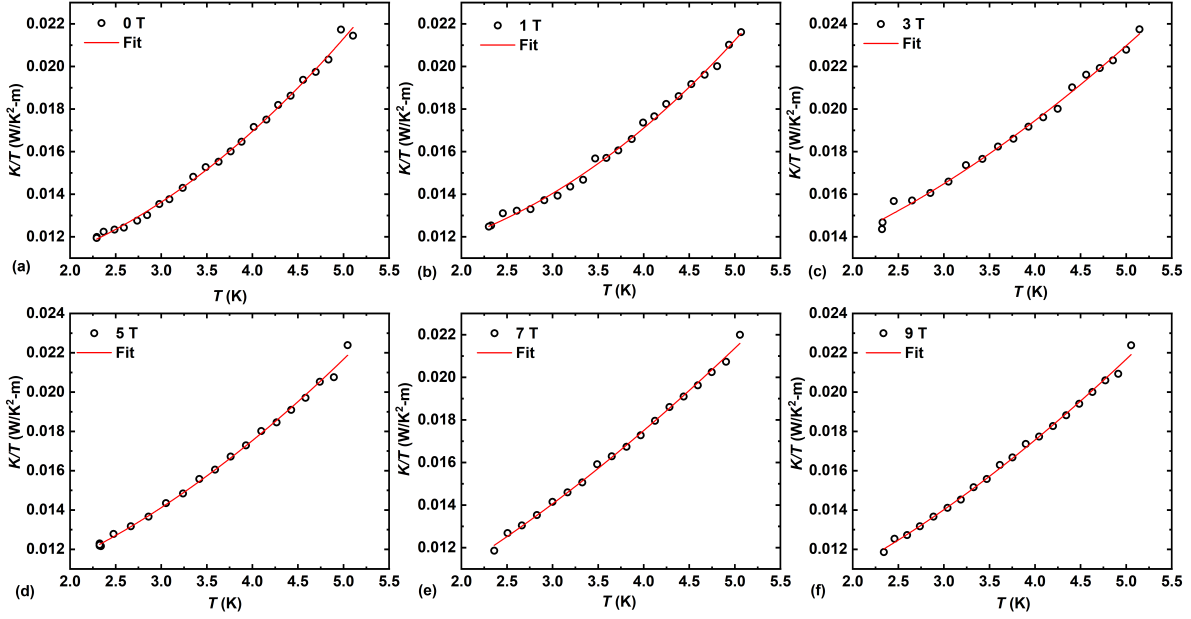


Figure 3.10: Fitting of  $\kappa/T$  versus  $T$  data measured under different magnetic fields.

### 3.4 Conclusion

In conclusion, we have undertaken a comprehensive characterization of a novel quasi-one-dimensional magnet,  $\text{NaYbTe}_2\text{O}_7$ , employing various magnetic and thermodynamic measurement techniques. This unique material features well-separated, one-dimensional zig-zag magnetic chains of  $\text{Yb}^{3+}$  ions along the  $b$ -axis, presenting an ideal platform for investigating one-dimensional magnetic properties. Our DC magnetization measurements have notably demonstrated the absence of long-range magnetic ordering down to temperatures as low as 0.4 K, despite antiferromagnetic interactions suggested by a higher  $\theta_{CW}$  value. Analyzing the low-temperature region of the inverse susceptibility has allowed us to identify the ground state as the Kramers doublet with  $J = 1/2$ , signifying the strong spin correlation evident in the slight deviation of low-temperature magnetic isotherms from the Brillouin function. Furthermore, our heat capacity measurements exhibited no lambda-like anomaly down to 0.285 K, and the magnetic field dependence of these measurements has revealed a discernible crystal electric field, reinforcing the  $\text{Yb}^{3+}$ - $\text{Yb}^{3+}$  correlations. The presence of the Schottky anomaly further confirms the Zeeman splitting, while thermal conductivity measurements have unveiled the existence of magnetic excitations in the system. Considering these collective findings, and the anisotropic and bond-sensitive nature of the exchange interactions between  $\text{Yb}^{3+}$  ions,  $\text{NaYbTe}_2\text{O}_7$  holds promise as a potential candidate for a gapless quantum spin liquid.

To delve deeper into its properties, sub-Kelvin investigations using local probes, such as  $\mu$ SR, and inelastic neutron scattering, are warranted.

# Bibliography

- [1] U. Schollwöck, J. Richter, D. J. J. Farnell, and R. F. Bishop, *Quantum Magnetism*, (Springer), 2008.
- [2] S.-L. Drechsler, J. Richter, A.A. Gippius, A. Vasiliev, A. A. Bush, A. S. Moskvina, J. Mañlek, Y. Prots, W. Schnelle, and H. Rosner, Helical ground state and weak ferromagnetism in the edge-shared chain cuprate  $\text{NaCu}_2\text{O}_2$ , *Europhys. Lett.* **73**, 83 (2006).
- [3] M. Hartel, J. Richter, D. Ihle, and S.-L. Drechsler, Thermodynamics of a one-dimensional frustrated spin-1/2 Heisenberg ferromagnet, *Phys. Rev. B* **78**, 174412 (2008).
- [4] H. T. Lu, Y. J. Wang, S. Qin, and T. Xiang, Zigzag spin chains with antiferromagnetic-ferromagnetic interactions: Transfer-matrix renormalization group study, *Phys. Rev. B* **74**, 134425 (2006).
- [5] S. E. Dutton, M. Kumar, M. Mourigal, Z. G. Soos, J.-J. Wen, C. L. Broholm, N. H. Andersen, Q. Huang, M. Zbiri, R. Toft-Petersen, and R. J. Cava, Quantum Spin Liquid in Frustrated One-Dimensional  $\text{LiCuSbO}_4$ , *Phys. Rev. Lett.* **108**, 187206 (2012).
- [6] W. E. A. Lorenz, R. O. Kuzian, S.-L. Drechsler, W.-D. Stein, N. Wizen, G. Behr, J. Mañlek, U. Nitzsche, H. Rosner, A. Hiess *et al.*, Highly dispersive spin excitations in the chain cuprate  $\text{Li}_2\text{CuO}_2$ , *Europhys. Lett.* **88**, 37002 (2009).
- [7] S. Park, Y. J. Choi, C. L. Zhang, and S.-W. Cheong, Ferroelectricity in an  $S=1/2$  Chain Cuprate, *Phys. Rev. Lett.* **98**, 057601 (2007).
- [8] S. Seki, Y. Yamasaki, M. Soda, M. Matsuura, K. Hirota, and Y. Tokura, Correlation between Spin Helicity and an Electric Polarization Vector in Quantum-Spin Chain Magnet  $\text{LiCu}_2\text{O}_2$ , *Phys. Rev. Lett.* **100**, 127201 (2008).

- 
- [9] M. Matsuda and K. Katsumata, Magnetic properties of a quasi-one-dimensional magnet with competing interactions: SrCuO<sub>2</sub>, J. Magn. Magn. Mater. **140**, 1671 (1995).
  - [10] M. Enderle, C. Mukherjee, B. Fak, R. K. Kremer, J.-M. Broto, H. Rosner, S.-L. Drechsler, J. Richter, J. Malek, A. Prokofiev *et al.*, Quantum helimagnetism of the frustrated spin- $\frac{1}{2}$  chain LiCuVO<sub>4</sub> Europhys. Lett. **70**, 237 (2005).
  - [11] M. Mourigal, M. Enderle, R. K. Kremer, J.M. Law, and B. Fak, Ferroelectricity from spin supercurrents in LiCuVO<sub>4</sub>, Phys. Rev. B **83**, 100409(R) (2011).
  - [12] M. Enderle, B. Fak, H.-J. Mikeska, R. K. Kremer, A. Prokofiev, and W. Assmus, Two-Spinon and Four-Spinon Continuum in a Frustrated Ferromagnetic Spin-1/2 Chain, Phys. Rev. Lett. **104**, 237207 (2010).
  - [13] S.-L. Drechsler, O. Volkova, A. N. Vasiliev, N. Tristan, J. Richter, M. Schmitt, H. Rosner, J. Malek, R. Klingeler, A. A. Zvyagin *et al.*, Frustrated Cuprate Route from Antiferromagnetic to Ferromagnetic Spin-1/2 Heisenberg Chains: Li<sub>2</sub>ZrCuO<sub>4</sub> as a Missing Link near the Quantum Critical Point, Phys. Rev. Lett. **98**, 077202 (2007).
  - [14] M. Hase, H. Kuroe, K. Ozawa, O. Suzuki, H. Kitazawa, G. Kido, and T. Sekine, Magnetic properties of Rb<sub>2</sub>Cu<sub>2</sub>Mo<sub>3</sub>O<sub>12</sub> including a one-dimensional spin-1/2 Heisenberg system with ferromagnetic first-nearest-neighbor and antiferromagnetic second-nearest-neighbor exchange interactions, Phys. Rev. B **70**, 104426 (2004).
  - [15] M. Hase, K. Ozawa, O. Suzuki, H. Kitazawa, G. Kido, H. Kuroe, and T. Sekine, Magnetism of A<sub>2</sub>Cu<sub>2</sub>Mo<sub>3</sub>O<sub>12</sub> (A = Rb or Cs): Model compounds of a one-dimensional spin-1/2 Heisenberg system with ferromagnetic first-nearest-neighbor and antiferromagnetic second-nearest-neighbor interactions, J. Appl. Phys. **97**, 10B303 (2005).
  - [16] L.S. Wu, S.E. Nikitin, Z. Wang, W. Zhu, C.D. Batista, A.M. Tsvelik, A.M. Samarakoon, D.A. Tennant, M. Brando, L. Vasylechko *et al.*, Tomonaga-Luttinger liquid behavior and spinon confinement in YbAlO<sub>3</sub>, Nat. comm. **10**, 698 (2019).
  - [17] N. Zhao, J. Sheng, J. Wang, H. Ge, T. Li, J. Yang, S. Wang, P. Miao, H. He, X. Tong *et al.*, Quasi-one-dimensional Ising-like antiferromagnetism in the rare-earth perovskite oxide TbScO<sub>3</sub>, Phys. Rev. Mater. **7**, 034401 (2023).

- 
- [18] L. S. Wu, W. J. Gannon, I. A. Zaliznyak, A. M. Tsvelik, M. Brockmann, J.-S. Caux, M. S. Kim, Y. Qiu, J. R. D. Copley, G. Ehlers *et al.*, 18. Orbital-exchange and fractional quantum number excitations in an f-electron metal,  $\text{Yb}_2\text{Pt}_2\text{Pb}$ , *Science* **352**, 1206 (2016).
- [19] Y. Li, D. Adroja, R. I. Bewley, D. Voneshen, A. A. Tsirlin, P. Gegenwart, and Q. Zhang, Crystalline Electric-Field Randomness in the Triangular Lattice Spin-Liquid  $\text{YbMgGaO}_4$ , *Phys. Rev. Lett.* **118**, 107202 (2017).
- [20] L. Ding, P. Manuel, S. Bachus, F. Grubler, P. Gegenwart, J. Singleton, R. D. Johnson, H. C. Walker, D. T. Adroja, A. D. Hillier *et al.*, Gapless spin-liquid state in the structurally disorder-free triangular antiferromagnet  $\text{NaYbO}_2$ , *Phys. Rev. B* **100**, 144432 (2019).
- [21] J. G. Rau, L. S. Wu, A. F. May, L. Poudel, B. Winn, V. O. Garlea, A. Huq, P. Whitfield, A. E. Taylor, M. D. Lumsden *et al.*, Anisotropic Exchange within Decoupled Tetrahedra in the Quantum Breathing Pyrochlore  $\text{Ba}_3\text{Yb}_2\text{Zn}_5\text{O}_{11}$ , *Phys. Rev. Lett.* **116**, 257204 (2016).
- [22] J. A. M. Paddison, M. Daum, Z. Dun, G. Ehlers, Y. Liu, M. B. Stone, H. Zhou, and M. Mourigal, Continuous excitations of the triangular-lattice quantum spin liquid  $\text{YbMgGaO}_4$ , *Nat. Physics* **13**, 117 (2017).
- [23] V. Petricek, M. Dušek, and L. Palatinus, Crystallographic Computing System JANA2006: General features, *Z. Kristallogr. Cryst. Mater.* **229**, 345 (2014).
- [24] H. Xia, J. Shen, Z. Zhu, Y. Lv, Q. Ma, and H. Wang,  $\text{NaYTe}_2\text{O}_7$ : A new compound with mixed valence of tellurium and large birefringence, *J. Alloys and Compd.* **816**, 152535 (2020).
- [25] J. G. Rau and M. J. P. Gingras, Frustration and anisotropic exchange in ytterbium magnets with edge-shared octahedra, *Phys. Rev. B* **98**, 054408 (2018).
- [26] Y. Li, G. Chen, W. Tong, L. Pi, J. Liu, Z. Yang, X. Wang, and Q. Zhang, 50. Rare-Earth Triangular Lattice Spin Liquid: A Single-Crystal Study of  $\text{YbMgGaO}_4$ , *Phys. Rev. Lett.* **115**, 167203 (2015).
- [27] H. W. J. Blöte, R. F. Wieringa, and W. J. Huiskamp, Heat-capacity measurements on rare-earth double oxides  $R_2M_2O_7$ , *Physica* **43**, 549 (1969).
- [28] H. B. Cao, A. Gukasov, I. Mirebeau, and P. Bonville, Anisotropic exchange in frustrated pyrochlore  $\text{Yb}_2\text{Ti}_2\text{O}_7$ , *J. Phys.: Condens. Matter* **21**, 492202 (2009).

- 
- [29] S. Guo, A. Ghasemi, C. L. Broholm, and R. J. Cava, Magnetism on ideal triangular lattices in NaBaYb(BO<sub>3</sub>)<sub>2</sub> Phys. Rev. Material **3**, 094404 (2019).
  - [30] T. Besara, M. S. Lundberg, J. Sun, D. Ramirez, L. Dong, J. B. Whalen, R. Vasquez, F. Herrera, J. R. Allen, M. W. Davidson *et al.*, Single crystal synthesis and magnetism of the BaLn<sub>2</sub>O<sub>4</sub> family (*Ln*= lanthanide), Prog. Solid State Chem. **42**, 23 (2014).
  - [31] M. Mitric, B. Antic, M. Balanda, D. Rodic, and M. L. Napijalo, An x-ray diffraction and magnetic susceptibility study of Yb<sub>x</sub>Y<sub>2-x</sub>O<sub>3</sub>, J. Phys.: Condens. Matter **9**, 4103 (1997).
  - [32] C. Kittel, *Introduction to Solid State Physics* (Wiley, Hoboken, NJ, 2005).
  - [33] R. Sibille, E. Lhotel, V. Pomjakushin, C. Baines, T. Fennell, and M. Kenzelmann, Candidate Quantum Spin Liquid in the Ce<sup>3+</sup> Pyrochlore Stannate Ce<sub>2</sub>Sn<sub>2</sub>O<sub>7</sub>, Phys. Rev. Lett. **115**, 097202 (2015).
  - [34] K. Somesh, S. S. Islam, S. Mohanty, G. Simutis, Z. Guguchia, C. Wang, J. Sichelschmidt, M. Baenitz, R. Nath, Absence of magnetic order and emergence of unconventional fluctuations in the  $J_{eff}=1/2$  triangular-lattice antiferromagnet YbBO<sub>3</sub>, Phys. Rev. B **107**, 064421 (2023).
  - [35] S. Kundu, A. Hossain, Pranava Keerthi S, R. Das, M. Baenitz, P. J. Baker, J.-C. Orain, D. C. Joshi, R. Mathieu, P. Mahadevan, S. Pujari, S. Bhattacharjee, A. V. Mahajan, and D. D. Sarma, Signatures of a Spin-1/2 Cooperative Paramagnet in the Diluted Triangular Lattice of Y<sub>2</sub>CuTiO<sub>6</sub>, Phys. Rev. Lett. **125**, 117206 (2020).
  - [36] P. Svoboda, J. Vejpravova, N.-T. Kim-Ngan, and F. Kaysel, Specific heat study of selected RNi<sub>5</sub>, J. Magn. Magn. Mater. **272-276**, 595 (2004).
  - [37] R. Kumar and A. Sundaresan, Unveiling a hidden multiferroic state under magnetic fields in BaHoFeO<sub>4</sub>, Phys. Rev. B **107**, 184420 (2023).
  - [38] R. Kumar and A. Sundaresan, Antisite disorder driven cluster glass state and colossal magnetoresistance in MnSb<sub>2</sub>Se<sub>4</sub>, Phys. Rev. B **106**, 134423 (2022).
  - [39] J. van Duijn, K. H. Kim, N. Hur, D. Adroja, M. A. Adams, Q. Z. Huang, M. Jaime, S.-W. Cheong, C. Broholm, and T. G. Perring, Inhomogeneous Level Splitting in Pr<sub>2-x</sub>Bi<sub>x</sub>Ru<sub>2</sub>O<sub>7</sub>, Phys. Rev. Lett. **94**, 177201 (2005).
  - [40] Y. Li, H. Liao, Z. Zhang, S. Li, F. Jin, L. Ling, L. Zhang, Y. Zou, L. Pi, Z. Yang, J. Wang, Z. Wu, and Q. Zhang, Gapless quantum spin liquid ground state in the

- two-dimensional spin-1/2 triangular antiferromagnet  $\text{YbMgGaO}_4$ , *Sci. Rep.* **5**, 16419 (2015).
- [41] Z. Ma, J. Wang, Z.-Y. Dong, J. Zhang, S. Li, S.-H. Zheng, Y. Yu, W. Wang, L. Che, K. Ran, S. Bao, Z. Cai, P. Cermak, A. Schneidewind, S. Yano, J. S. Gardner, X. Lu, S.-L. Yu, J.-M. Liu, S. Li, J.-X. Li, and J. Wen, Spin-Glass Ground State in a Triangular-Lattice Compound  $\text{YbZnGaO}_4$ , *Phys. Rev. Lett.* **120**, 087201 (2018).
- [42] R. Bag, M. Ennis, C. Liu, S. E. Dissanayake, Z. Shi, J. Liu, L. Balents, and S. Haravifard, Realization of quantum dipoles in triangular lattice crystal  $\text{Ba}_3\text{Yb}(\text{BO}_3)_3$ , *Phys. Rev. B* **104**, L220403 (2021).
- [43] H. M. Rosenberg, *Low Temperature Solid State Physics* Oxford University Press, Oxford, 1963.
- [44] L. Xie, T. Su, and X. Li, Magnetic field dependence of Schottky anomaly in the specific heats of stripe-ordered superconductors  $\text{La}_{1.6-x}\text{Nd}_{0.4}\text{Sr}_x\text{CuO}_4$ , *Physica C: Superconductivity* **480**, 14 (2012).
- [45] S. Mahdavifar and A. Akbari, Heat capacity of Schottky type in low-dimensional spin systems, *J. Phys.: Condens. Matter* **20**, 215213 (2008).
- [46] G. Mu, Y. Wang, L. Shan, and H.-H. Wen, Possible nodeless superconductivity in the noncentrosymmetric superconductor  $\text{Mg}_{12-\delta}\text{Ir}_{19}\text{B}_{16}$ , *Phys. Rev. B* **76**, 064527 (2007).
- [47] Y. Wang, J. Yan, L. Shan, H.-H. Wen, Y. Tanabe, T. Adachi, and Y. Koike, Weak-Coupling d-wave BCS superconductivity and unpaired electrons in overdoped  $\text{La}_{2-x}\text{Sr}_x\text{CuO}_4$  single crystals, *Phys. Rev. B* **76**, 064512 (2007).
- [48] M. Yamashita, N. Nakata, Y. Kasahara, T. Sasaki, N. Yoneyama, N. Kobayashi, S. Fujimoto, T. Shibauchi, and Y. Matsuda, Thermal-transport measurements in a quantum spin-liquid state of the frustrated triangular magnet  $\kappa$ -(BEDT-TTF) $_2\text{Cu}_2(\text{CN})_3$ , *Nat. Physics* **5**, 44 (2009).
- [49] B. C. Sales, M. D. Lumsden, S. E. Nagler, D. Mandrus, and R. Jin, Magnetic Field Enhancement of Heat Transport in the 2D Heisenberg Antiferromagnet  $\text{K}_2\text{V}_3\text{O}_8$ , *Phys. Rev. Lett.* **88**, 095901 (2002).
- [50] S. Y. Li, L. Taillefer, C. H. Wang, and X. H. Chen, Ballistic Magnon Transport and Phonon Scattering in the Antiferromagnet  $\text{Nd}_2\text{CuO}_4$ , *Phys. Rev. Lett.* **95**, 156603 (2005).

- [51] M. Yamashita, N. Nakata, Y. Senshu, M. Nagata, H. M. Yamamoto, R. Kato, T. Shibauchi, and Y. Matsuda, Highly mobile gapless excitations in a two-dimensional candidate quantum spin liquid, *Science* **328**, 1246 (2010).
- [52] P. Bourgeois-Hope, F. Laliberte, E. Lefrançois, G. Grissonnanche, S. Rene de Cotret, R. Gordon, S. Kitou, H. Sawa, H. Cui, R. Kato, L. Taillefer, and N. Doiron-Leyraud, Thermal Conductivity of the Quantum Spin Liquid Candidate  $\text{EtMe}_3\text{Sb}[\text{Pb}(\text{dmit})_2]_2$ , *Phys. Rev. X* **9**, 041051 (2019).
- [53] J. Callaway, Model for lattice thermal conductivity at low temperatures, *Phys. Rev.* **113**, 1046 (1959).



## Chapter 4

# Dynamic Magnetic Ground State in a Dimer Based Compound

## $\text{Yb}_2\text{Te}_5\text{O}_{13}$

In this chapter, we study the magnetic and thermodynamic properties of a  $\text{Yb}^{3+}$  dimer-based compound  $\text{Yb}_2\text{Te}_5\text{O}_{13}$  down to sub-Kelvin temperatures using various characterization techniques. Our magnetization measurements, conducted down to 0.4 K, reveal the absence of long-range magnetic ordering and the emergence of magnetic correlations below 1 K. Additionally, heat capacity measurements performed down to 0.37 K confirm the presence of a finite internal magnetic field of the order of 0.55 K and validate the presence of magnetic correlations with a Kramers doublet ground state ( $J_{eff} = 1/2$ ). Further insight is provided by zero field muon spin relaxation ( $\mu\text{SR}$ ) measurements, which show a gradual slowdown of  $\text{Yb}^{3+}$  spin fluctuations from 30 K to 44 mK, indicating the presence of the Orbach process mediated through crystal electric field (CEF) levels. Furthermore, longitudinal field  $\mu\text{SR}$  spectra collected at 70 mK demonstrate that the spins are dynamic even in the presence of  $H = 3200$  Oe which is significantly greater than the nuclear field. Our theoretical investigation unveils the competing exchange interaction and, hence, the origin of the dynamic state. By combining macroscopic and microscopic measurements with theoretical calculations, we propose a quantum spin liquid state within a dimer lattice of  $\text{Yb}_2\text{Te}_5\text{O}_{13}$ , presenting exciting avenues for future research in quantum magnetism.

## 4.1 Introduction

The discovery and characterization of novel states of matter have been a driving force in condensed matter physics, offering insights into the fundamental principles governing quantum systems and opening doors to potential technological applications. Among these exotic phases, quantum spin liquids (QSLs) [1–3] are particularly intriguing due to their defiance of conventional magnetic order and the emergence of exotic quantum phenomena. The study of quantum spin liquids can answer various fundamental questions in physics, ranging from the nature of quantum entanglement [4, 5] and high-temperature superconductivity [6] to the existence of fractionalized excitations [7, 8] and topological order [9]. Moreover, QSLs hold promise for applications in quantum information processing, where the robustness of their entangled states could be harnessed for fault-tolerant quantum computing. Various spin lattices, including the triangular [10], kagome [11], hyperkagome [12], pyrochlore [13], square lattices [14] and dimer lattices with frustration [15], can realize spin liquid states. Recently, rare-earth-based frustrated systems, particularly  $\text{Yb}^{3+}$  based, have been widely considered among the leading candidates for realizing novel quantum states owing to the presence of strong spin-orbit coupling (SOC) and CEF. A combination of a low-dimensional frustrated magnetic lattice and  $J_{eff} = 1/2$  ground state in Yb compounds proves to be an ideal platform to look for a quantum spin-liquid state.

## 4.2 Experimental

### 4.2.1 Single Crystal Synthesis and Refinement

The single crystals of  $\text{Yb}_2\text{Te}_5\text{O}_{13}$  were synthesized using the flux method using  $\text{TeO}_2$  as a flux. We placed  $\text{Yb}_2\text{O}_3$  and  $\text{TeO}_2$  in a platinum boat, using four times the stoichiometric amount of  $\text{TeO}_2$ . The mixture was heated to 1023 K, just above the melting point of  $\text{TeO}_2$  (1005 K), and maintained at this temperature for 24 hours. It was then slowly cooled at a rate of 0.5 K per minute to 673 K. Once such a treated mixture reached 673 K, the furnace was switched off to quench the sample. The extra flux of  $\text{TeO}_2$  was removed mechanically. We found that single crystals of  $\text{Yb}_2\text{Te}_5\text{O}_{13}$  were formed along with  $\text{TeO}_2$ , which are very small in size (less than 5 mm) and could not be used for other measurements except x-ray diffraction. A transparent single crystal was cleaned in silicone oil and mounted in a loop, as seen in Fig. 4.1. The loop was centered in a Bruker D8 venture diffractometer equipped with a Photon 100 detector and graphite

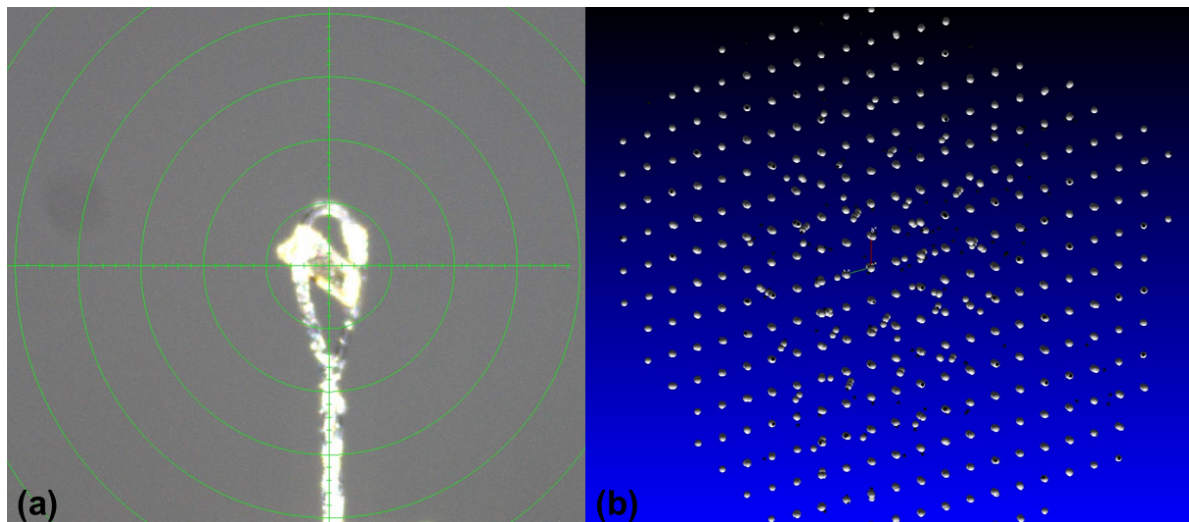


Figure 4.1: (a) A crystal centered on the sample holder of a single crystal diffractometer. (b) Reciprocal lattice observed along the  $c$ -axis.

monochromator Mo  $K\alpha$  x-ray source (wavelength = 0.71073 Å) powered with 50 kV and 1 mA. The data were collected at room temperature with a 2 s exposure per frame. The data was solved using the APEX-3 software, and multi-scan absorption was applied using the SADABS process [16]. To check the space group accuracy, XPREP software was used, and Olex-2 software was used to refine the structure using the SHELXL program [17]. All the atoms were refined anisotropically.

## 4.2.2 Polycrystalline Sample Synthesis and Refinement

A polycrystalline sample of  $\text{Yb}_2\text{Te}_5\text{O}_{13}$  was prepared through the conventional solid-state synthesis route. The respective oxides of Yb ( $\text{Yb}_2\text{O}_3$ ) and Te ( $\text{TeO}_2$ ) were mixed in a stoichiometric ratio using a mortar and pestle. The mixture was first heated to 973 K at a constant ramp rate of 5 K/min and kept at the same temperature for 24 h. Then, the product was cooled to room temperature and ground again to improve the homogeneity. In the second step, the product was pelletized and cooled down to 300 K after heating it at 973 K for 24 h. The X-ray diffraction (XRD) of the as-prepared sample was performed on a Rigaku Diffractometer using Cu-  $K\alpha_1$  and  $K\alpha_2$ . The simulated XRD pattern from the single-crystal refinement perfectly agrees with the XRD pattern of the polycrystalline sample, as shown in Fig. 4.2. The XRD pattern of the sample was analyzed using the Rietveld refinement method with the help of the FullProf Package [18], as exhibited in Fig. 4.3. The excellent agreement of theoretical simulation with the experimental data ( $\chi^2 = 2.29\%$ ) confirms the phase purity of the compound. It reveals that  $\text{Yb}_2\text{Te}_5\text{O}_{13}$

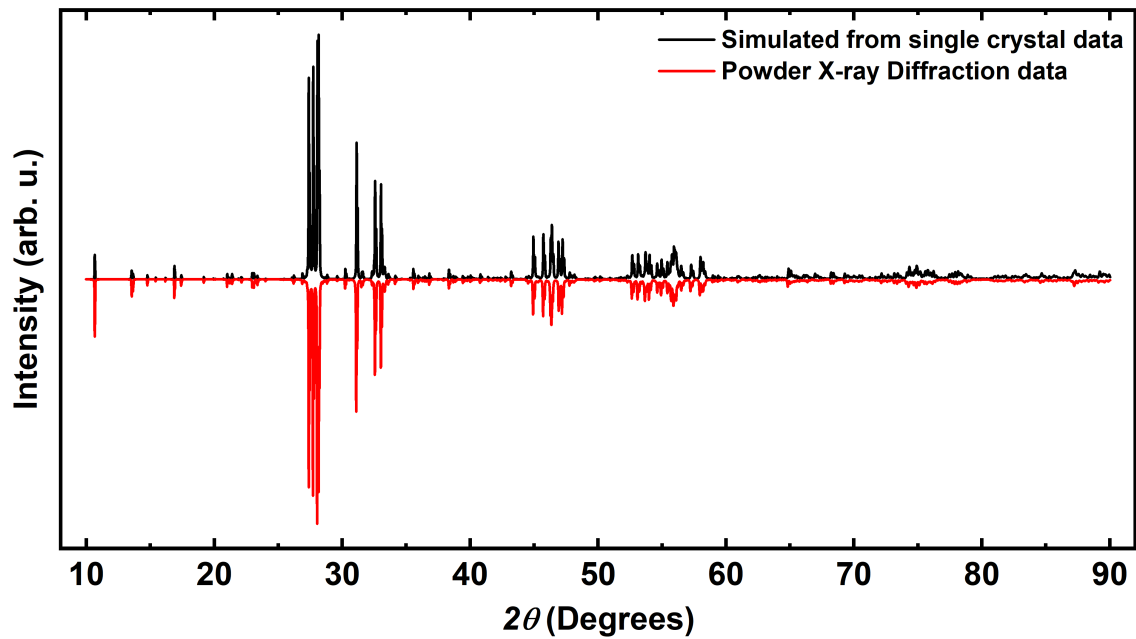


Figure 4.2: A comparison between simulated pattern from single crystal data and powder x-ray diffraction data.

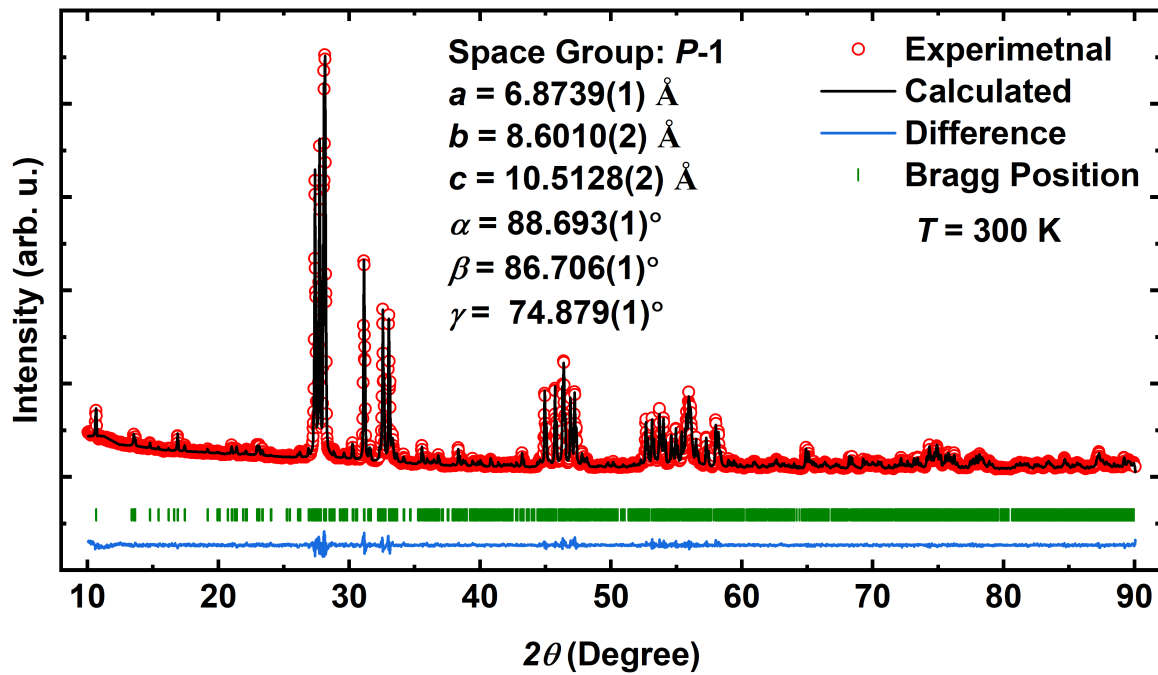


Figure 4.3: Observed and refined powder x-ray diffraction pattern of  $\text{Yb}_2\text{Te}_5\text{O}_{13}$ . Bragg positions are shown in green color and the difference between experimental and calculated intensities is represented by the bottom solid blue line.

Table 4.1: Crystallographic parameters along with occupancy and average isotropic displacement parameters obtained from the Rietveld refinement of the powder XRD data. Space group:  $P\bar{1}$ ,  $V = 599.02(1) \text{ \AA}^3$ ,  $\chi^2 = 2.29 \%$ , Bragg  $R$  factor =  $3.00 \%$ ,  $R_f = 2.07 \%$

Atom	Wyckoff symbol	x	y	z	Occupancy	$B_{iso}(\text{\AA}^2)$
Yb(1)	$2i$	0.4472(8)	0.4711(6)	0.8230(5)	1.0	0.015(3)
Yb(2)	$2i$	-0.0040(8)	0.2600(6)	0.7608(5)	1.0	0.013(3)
Te(1)	$2i$	0.4351(9)	0.9061(7)	0.3069(5)	1.0	0.019(5)
Te(2)	$2i$	0.1283(10)	0.3512(8)	0.1116(6)	1.0	0.023(5)
Te(3)	$2i$	0.2757(10)	0.3955(7)	0.4856(6)	1.0	0.020(4)
Te(4)	$2i$	0.8420(9)	0.1895(7)	0.3608(5)	1.0	0.023(4)
Te(5)	$2i$	0.7109(11)	1176(8)	0.0246(7)	1.0	0.021(4)
O(1)	$2i$	0.3373(48)	0.1864(37)	0.7816(29)	1.0	1.0
O(2)	$2i$	0.5077(76)	0.3242(47)	0.0092(37)	1.0	1.0
O(3)	$2i$	0.4196(130)	0.2444(84)	0.2839(78)	1.0	1.0
O(4)	$2i$	0.3042(56)	0.7561(37)	0.2954(33)	1.0	1.0
O(5)	$2i$	0.6470(58)	0.4705(44)	0.4148(34)	1.0	1.0
O(6)	$2i$	0.0773(64)	0.2577(48)	0.2720(43)	1.0	1.0
O(7)	$2i$	0.3469(43)	0.9987(30)	0.1136(27)	1.0	1.0
O(8)	$2i$	0.0660(51)	0.3361(33)	0.5529(31)	1.0	1.0
O(9)	$2i$	0.4523(54)	0.1658(36)	0.5201(28)	1.0	1.0
O(10)	$2i$	0.1141(52)	0.4907(36)	0.8718(32)	1.0	1.0
O(11)	$2i$	0.0449(60)	0.8118(42)	0.0373(34)	1.0	1.0
O(12)	$2i$	0.6922(75)	0.2418(49)	0.2285(42)	1.0	1.0
O(13)	$2i$	0.0369(54)	0.0202(43)	0.6608(31)	1.0	1.0

crystallizes in a triclinic space group  $P\bar{1}$  with the following lattice parameters:  $a = 6.8739(1) \text{ \AA}$ ,  $b = 8.6010(2) \text{ \AA}$ ,  $c = 10.5128(2) \text{ \AA}$ ,  $\alpha = 88.693(1)^\circ$ ,  $\beta = 86.706(1)^\circ$ ,  $\gamma = 74.879(1)^\circ$ . These parameters agree very well with the parameters obtained from the single-crystal diffraction analysis. The thermal vibrations of all the atoms are considered to be anisotropic in accordance with the *cif* file present in the Inorganic Crystal Structure Database (ICSD) (Data Code: 413668). Please note that the thermal parameters of the oxygen atoms are fixed to a reasonable value and are not refined. The refined parameters, which include crystallographic positions, thermal parameters, and occupancies of each atom, are tabulated in Table 4.1.

### 4.2.3 Characterization

The magnetic properties measurement system (MPMS), Quantum Design make, was utilized for magnetic measurements, while the physical properties measurement system (PPMS), Quantum Design make, was employed to gather heat capacity data. The

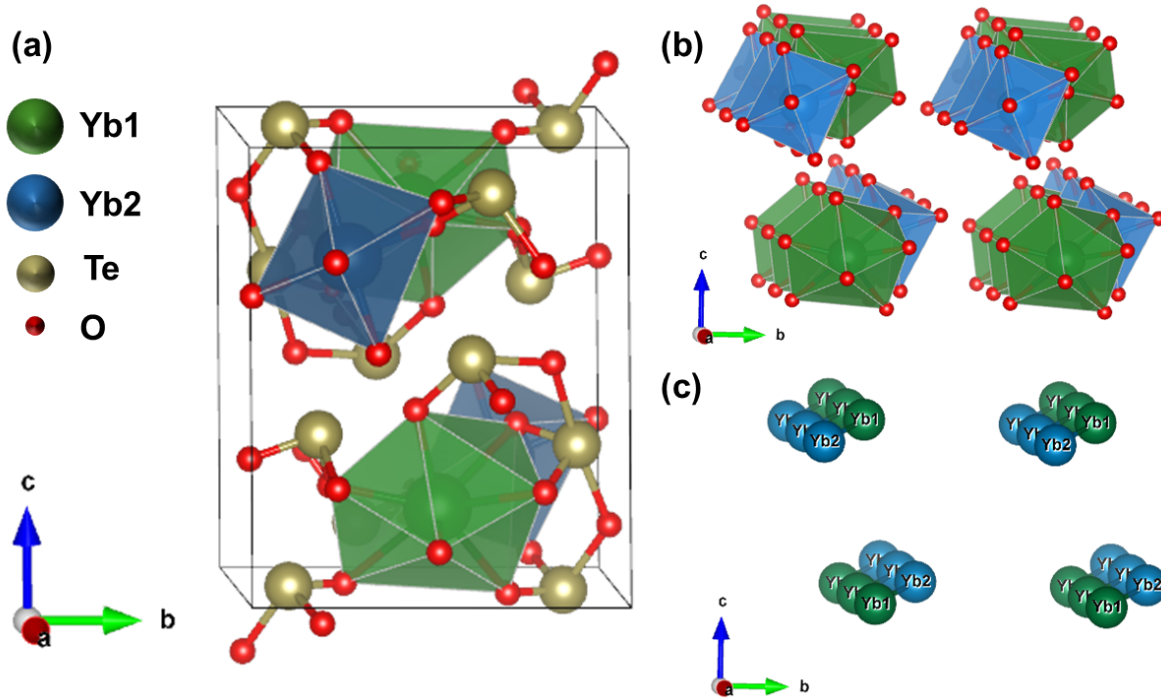


Figure 4.4: (a) Single unit cell of  $\text{Yb}_2\text{Te}_5\text{O}_{13}$ . (b) Stacking of the Yb-based two types of polyhedra in the *bc* plane. (c) Stacking of Yb1-Yb2 dimers along the *a*-axis.

low-temperature heat capacity measurements took place at the Core Lab Quantum Materials (CLQM), Helmholtz Zentrum Berlin für Materialien und Energie (HZB), Germany. Muon spectroscopy measurements were conducted at the ISIS facility, Rutherford Appleton Laboratory, UK, using the MuSR spectrometer, employing zero-field (ZF) and longitudinal-field (LF) options. The powder sample was mounted on a high-purity silver plate, which gives only a non-relaxing background signal. A dilution refrigerator was employed to achieve ultra-low measurement temperatures down to 0.044 K. Analysis of the  $\mu\text{SR}$  measurements was performed using the MANTID software [19, 20].

## 4.3 Results and Discussion

### 4.3.1 Crystal Structure

Figure 4.4(a) depicts the arrangement of all the atoms viewed along the *a* axis. A careful investigation of the crystal structure reveals that  $\text{Yb}^{3+}$  ions have two distinct Wyckoff positions with two different chemical environments. Yb1 atoms are surrounded by eight oxygen atoms in a bicapped trigonal-prismatic manner, while Yb2 atoms are

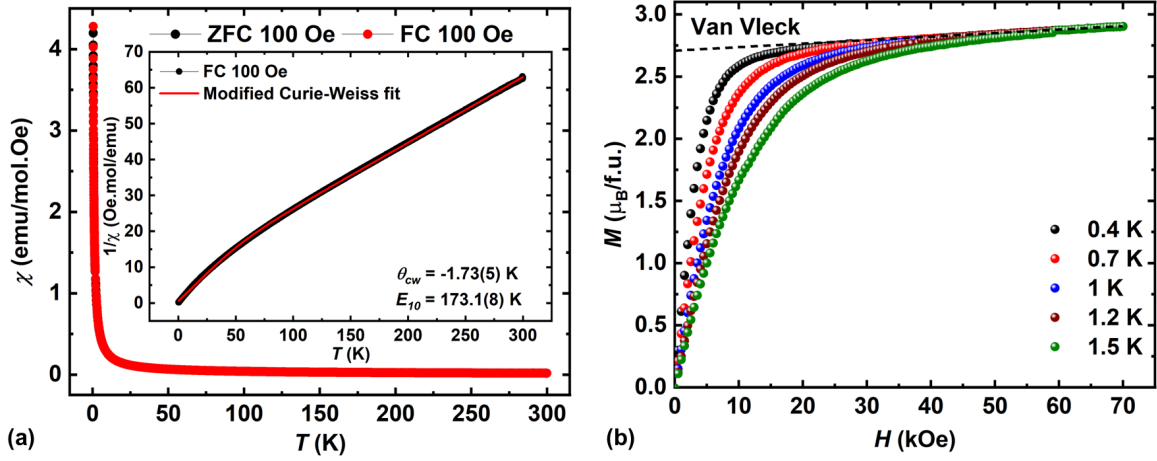


Figure 4.5: (a) Temperature dependence of dc magnetic susceptibility performed under ZFC and FC protocol down to 0.4 K. Inset shows the fitting of the inverse susceptibility data with the modified Curie-Weiss model. (b) Isothermal magnetization curves measured at different temperatures and the black dashed line account for the Van Vleck contribution.

situated in a pentagonal bipyramid environment of seven oxygen atoms, as shown in Fig. 4.4(a) and (b). The Yb atoms form a zig-zag chain along the  $a$  axis and form dimers comprising of edge-sharing  $\text{Yb}_2\text{O}_8$  and  $\text{Yb}_2\text{O}_7$  units having an intra-dimer length of 3.81 Å (see Fig. 4.4(c)). The inter-dimer distance along the  $b$  and  $c$  axis is more than 6 Å, confirming that the dimers along the  $a$ -axis are responsible for the magnetic properties of the compound. It has been established previously that competition between inter- and intra-dimer interactions can lead to a magnetically dynamic state [15]. Given these intriguing properties of  $\text{Yb}_2\text{Te}_5\text{O}_{13}$ , there is a strong motivation for its low-temperature magnetic behavior to be characterized.

### 4.3.2 DC Magnetization

The dc magnetic susceptibility measurements have been carried out down to 0.4 K, following zero-field-cooled (ZFC) and field-cooled (FC) protocols. We did not observe any magnetic anomaly, indicating the absence of magnetic long-range ordering (see Fig. 4.5(a)). The inverse susceptibility data show a deviation from the simple Curie-Weiss model below 125 K, as shown in Fig. 4.6(a), which is due to the splitting of the eightfold ground state of  $\text{Yb}^{3+}$  ( $4f^{13}$ ) ions as a result of CEF. At low temperatures, the ground state can be described as a Kramers doublet with  $J_{eff} = 1/2$ . As  $J$  is no longer temperature independent, the higher Kramers doublets can also contribute over the temperature range of the measurement (0.4-300 K). So, the inverse susceptibility data can be fitted with a



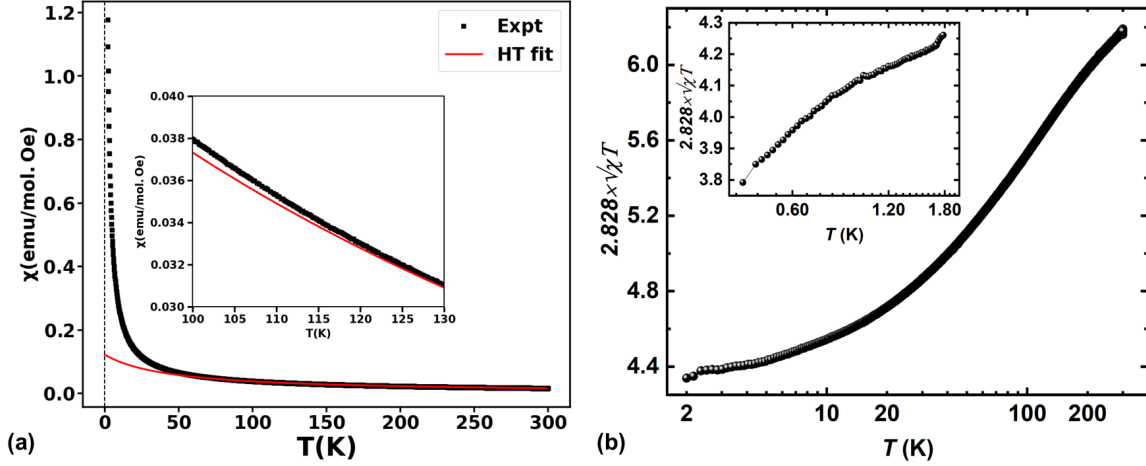


Figure 4.6: (a) The fitting of high-temperature susceptibility data with the Curie-Weiss law. Inset shows the deviation from the linear regime below 125 K (b) Variation of effective moment  $\mu_{eff} = [(3k_B/N_A\mu_B^2)\chi T]^{1/2} \sim 2.828\sqrt{\chi T}$  versus  $T$ . Inset shows the variation below 1.8 K.

two-level approximation of the Curie-Weiss model, which can be expressed as [21, 22]:

$$1/\chi = 8.(T - \theta_{CW}). \left( \frac{1 + \exp^{-\frac{E_{10}}{k_B T}}}{\mu_{eff,0}^2 + \mu_{eff,1}^2 \cdot \exp^{-\frac{E_{10}}{k_B T}}} \right) \quad (4.1)$$

where  $\theta_{CW}$  is Curie-Weiss temperature,  $\mu_{eff,0}$  and  $\mu_{eff,1}$  stand for effective moments in the crystal field ground and first excited states, respectively, and  $E_{10}$  denotes the energy difference between them. The fitting of the inverse susceptibility data, presented in the inset of Fig. 4.5(a), results in  $E_{10} = 173.1(8)$  K, further confirming the Kramers doublet ground state at lower temperatures. The  $\theta_{CW}$  is found to be  $-1.73(5)$  K, suggesting dominating antiferromagnetic interactions. Moreover, the effective moment  $\mu_{eff} = [(3k_B/N_A\mu_B^2)\chi T]^{1/2} \sim 2.828\sqrt{\chi T}$  approaches a free ion value corresponding to two  $\text{Yb}^{3+}$  ions at 300 K ( $6.36 \mu_B$ ), as shown in Fig. 4.6(b). The effective moment gradually decreases from 300 to 1.7 K and then decreases rapidly below 1.7 K, suggesting the emergence of the magnetic correlations [23].

To understand the low-temperature magnetic properties further, we have performed isothermal magnetization measurements at 0.4, 0.7, 1.0, and 1.2 K by constantly sweeping the magnetic field from +7 T to -7 T in five quadrants. Figure 4.5(b) depicts the field dependence of the isothermal magnetization curves in the first quadrant, which seem to saturate above 3 T after rapidly increasing in the low-field region. The slope of magnetization curves at higher magnetic fields corresponds to the Van Vleck contribution



produced by higher crystal electric field (CEF) levels [24]. After subtracting the Van Vleck contribution, the saturation magnetization is around  $3 \mu_B/\text{f.u.}$ , which is in agreement with the saturation magnetization values observed for other Yb-based polycrystalline compounds [24, 25].

### 4.3.3 Heat Capacity

To explore the thermodynamic properties at low temperatures, we conducted heat capacity measurements on a polycrystalline sample of  $\text{Yb}_2\text{Te}_5\text{O}_{13}$  down to 370 mK. No lambda anomaly corresponding to the main phase has been observed. A small anomaly was observed at 2.3 K, which can be attributed to a tiny amount of  $\text{Yb}_2\text{O}_3$  ( $\approx 0.5\%$ ) impurity phase which was not observed in magnetic measurements, as depicted in Fig. 4.7(a). However, the presence of this impurity phase does not affect the main phase properties. The heat capacity data have been fitted with the Debye-Einstein model to separate out the magnetic contribution (see inset of Fig. 4.7(b)).

According to this model, the total number of acoustic and phonon modes equals the total number of atoms in the primitive cell (for  $\text{Yb}_2\text{Te}_5\text{O}_{13}$ , this is 20). Here, the relative weights of acoustic and optical modes are considered  $2:(n-2)$ , where  $n$  is the total number of atoms. Consequently, there are 6 acoustic phonon branches and 54 optical phonon branches. Four Einstein terms are employed to describe the optical modes, while all six acoustic modes are grouped together and described using one Debye term. Additionally, several optical modes are combined to reduce free parameters and minimize experimental error [26]. The Debye-Einstein model for this system can be expressed as [27, 28]:

$$C_{D-E} = \frac{9aR}{x_D^3} \int_0^{x_D} \frac{x^4 e^x}{(e^x - 1)^2} dx + 3R \sum_{i=1}^4 \frac{b_i x_{E_i}^2 e^{x_{E_i}}}{(e^{x_{E_i}} - 1)^2}$$

where  $x_{D,E} = \theta_{D,E}/T$ ;  $\theta_D$  and  $\theta_E$  are the Debye and Einstein temperatures, respectively, and  $R$  is the universal gas constant. The coefficients  $a$  and  $b_i$  signify the contributions from acoustic and optical phonons, respectively. To ensure a physically meaningful model, the weight factors are adjusted such that their sum matches the total number of atoms in the unit cell. Specifically, in this context,  $a = 2$ ,  $b_1 = 1$ ,  $b_2 = 3$ ,  $b_3 = 5$ , and  $b_4 = 9$ . Each  $b_i$  value corresponds to a specific group of atomic motions:  $b_1$  for one  $\text{Te}^{4+}$  ion vibrations,  $b_2$  for three  $\text{Te}^{3+}$  motion,  $b_3$  for contributions from one  $\text{Te}^{4+}$  and four  $\text{O}^{2-}$  atoms, and  $b_4$  for the nine remaining  $\text{O}^{2-}$  atoms. By adhering to these constraints, we ensure that our Debye-Einstein model fits the system's behavior accurately.

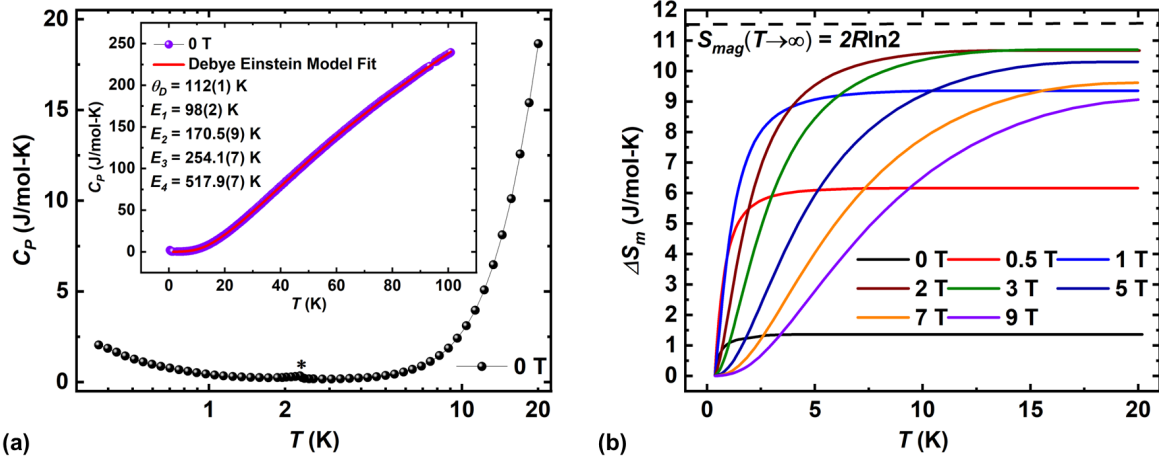


Figure 4.7: (a) Temperature dependence of the heat capacity in the absence of an applied magnetic field. The asterisk indicates an anomaly corresponding to  $\text{Yb}_2\text{O}_3$  ( $T_N = 2.3$  K). Inset: Fitting of zero field heat capacity data using the Debye-Einstein model. (b) Temperature dependence of the magnetic entropy, derived from the heat capacity data, is depicted for different magnetic fields.

The magnetic entropy, obtained by subtracting the lattice contribution, is illustrated in Fig. 4.7(b). A comparison with the entropy of a two-level system (with an effective spin  $J_{eff} = 1/2$ ) of two  $\text{Yb}^{3+}$  ions reveals that approximately 88% of the magnetic entropy embedded in the system below 360 mK. Furthermore, the temperature dependence of the magnetic entropy under various magnetic fields reveals that saturation magnetic entropy continues to rise with an increase in the applied magnetic field and attains a value of 10.75 J/mol-K for  $H \geq 2$  T, which is approximately 93 % of  $2R \ln 2$ , further corroborating the  $J_{eff} = 1/2$  ground state.

Despite the absence of long-range magnetic ordering, we observed a Schottky anomaly at low temperatures for  $H \geq 1$  T. Figure 4.8(a) illustrates the effect of the magnetic field on the anomaly observed at lower temperatures, which shifts towards higher temperatures as the applied magnetic field increases, indicating the presence of a Schottky anomaly. This anomaly arises from the splitting of the ground state Kramers doublet upon the application of an external magnetic field (known as Zeeman splitting), a phenomenon observed in other Yb compounds as well [29, 30]. The maximum in the Schottky anomaly, which corresponds to the energy at which both the levels are equally degenerate, can be used to estimate the CEF ground state magnetic moment by using the following expression [31–33]:  $\Delta = T_{max} \cdot k_B / 0.417$ . The Schottky anomaly has a maximum around 1.8 K for 2 T, which results in  $1.6 \mu_B$  per  $\text{Yb}^{3+}$  ion. This agrees well with the saturation

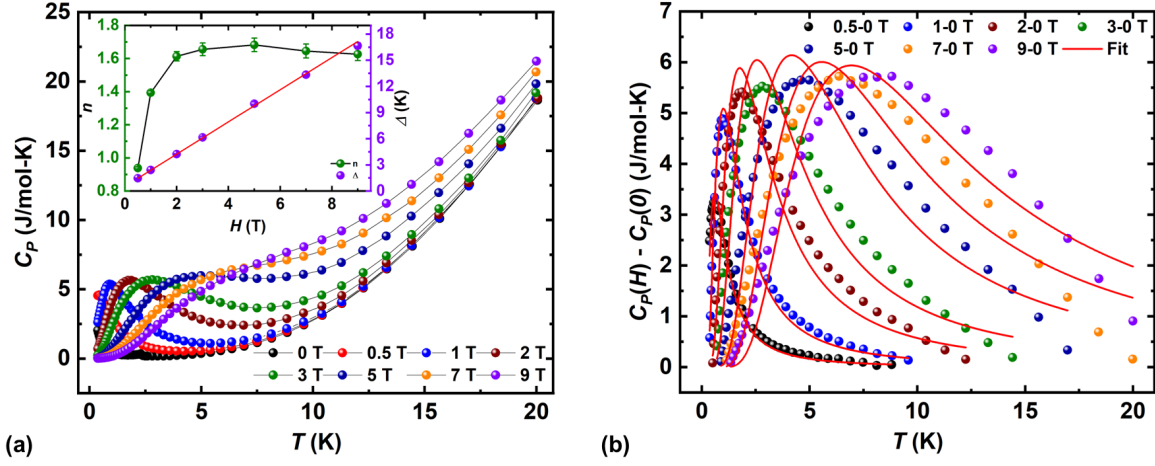


Figure 4.8: (a) Magnetic field dependence of the Schottky anomaly. Inset: Linear fitting of the  $\Delta$  values from CEF fitting (right axis) and the variation of the  $n$  values with magnetic field are presented. (b) The plot demonstrates the variation of the Schottky contribution with temperature, fitted with the two-level model equation.

magnetization per  $\text{Yb}^{3+}$  at low temperatures.

The magnetic field dependence of the total heat capacity can be expressed as  $C(T, H) = C(T, 0) + C_{\text{sch}}(T, H)$ . Consequently, the Schottky contribution at different magnetic fields can be isolated by subtracting the zero-field data from the data obtained at the respective magnetic fields. For a two-level system ( $J_{\text{eff}} = \frac{1}{2}$ ), the Schottky contribution can be written as [34–36]:

$$C_{\text{sch}}(T, H) = nR \left( \frac{\Delta}{T^2} \right) \frac{\exp(\Delta/T)}{[1 + \exp(\Delta/T)]^2} \quad (4.2)$$

where  $n$  represents the number of free spins excited to higher energy levels,  $R$  is the universal gas constant, and  $\Delta$  denotes the spacing between two energy levels. The value of  $\Delta$  has a direct relationship with the effective magnetic field experienced by the compound, given by  $\Delta(H) = \frac{g\mu_B H_{\text{eff}}}{k_B}$ , where  $H_{\text{eff}} = \sqrt{H_0^2 + H_1^2}$ , and  $H_{\text{eff}} = H_0$  when there is no external magnetic field ( $H_1 = 0$ ).

The fitting of the Schottky contribution is illustrated in Fig. 4.8(b), revealing that including more than two energy levels is necessary to obtain an accurate fit for  $H > 2$  T. The magnetic field dependence of  $\Delta$  and  $n$  is displayed in the inset of Fig. 4.8(a). The linear fitting of the  $\Delta$  variation, as depicted in the inset of Fig. 4.8(a), yields  $\Delta(0) \approx 0.55(1)$  K. A non-zero value of  $\Delta(0)$  suggests the presence of an internal magnetic field originating from  $\text{Yb}^{3+} - \text{Yb}^{3+}$  interactions. Furthermore, the number of spins excited

to higher levels ( $n$ ) stabilizes at around 1.68 beyond 5 T, as shown in the inset of Fig. 4.8(a).

#### 4.3.4 Muon Spin Relaxation Measurements

Considering the extreme sensitivity of muons to very small local magnetic fields, we have performed zero field (ZF)  $\mu\text{SR}$  measurements down to 44 mK. Representative ZF  $\mu\text{SR}$  spectra, taken at different temperatures, are shown in figure 4.9(a). The absence of oscillations, along with no loss in the initial asymmetry over the whole temperature range, confirms that there is no long-range magnetic order or freezing of the spins [37]. Moreover, the asymmetry relaxes to the same zero baseline for all the temperatures and does not recover to 1/3 of the initial asymmetry, ruling out a random distribution of static fields [38]. These observations confirm the presence of a dynamic magnetic ground state.

Initially, we used a stretched exponential function to fit the ZF spectra, which did not yield a good agreement with our data. As discussed above, Yb ions have two different chemical environments, resulting in two distinct CEFs due to different surrounding charge distributions. Since  $\mu\text{SR}$  is a local probe, muons stopping at Yb1 and Yb2 will experience different CEFs, as observed earlier [25, 39]. Thus, we used a combination of two exponential functions with a flat background term to analyze this data:

$$A(t) = A_{bg} + A_1 \exp(-\lambda_1/t) + A_2 \exp(-\lambda_2/t) \quad (4.3)$$

where  $A_{bg}$  denotes the constant background, and  $A_1$  and  $A_2$  denote the initial asymmetry of each component. The  $\lambda_1$  and  $\lambda_2$  represent muon relaxation rates for the two different sites. Note that  $A_{bg}$ ,  $A_1$ , and  $A_2$  are kept constant at 0.15, 0.07, and 0.06, respectively, during the data analysis. The values of  $A_1$  and  $A_2$  signify that the muon population implanted at both sites is almost equal [24]. The temperature evolution of both the relaxation rates is shown in Fig. 4.9(b), which precisely tracks the emergence of the correlations among  $\text{Yb}^{3+}$  spins. Although  $\lambda_1$  is one order higher than  $\lambda_2$ , both show similar temperature dependence with a plateau-like behavior at lower temperatures. Similar behavior can be seen in the case of muon diffusion, where both relaxation rates should drop at the same temperature. However,  $\lambda_2$  drops at a lower temperature compared to  $\lambda_1$ . Also,  $\text{Yb}_2\text{Te}_5\text{O}_{13}$  is an insulating oxide, and muon diffusion is not commonly observed in such systems [40]. In fact, the decrease in the  $\lambda_1$  and  $\lambda_2$  results from an Orbach process [41], which is a two-phonon scattering process mediated by an excited CEF level.

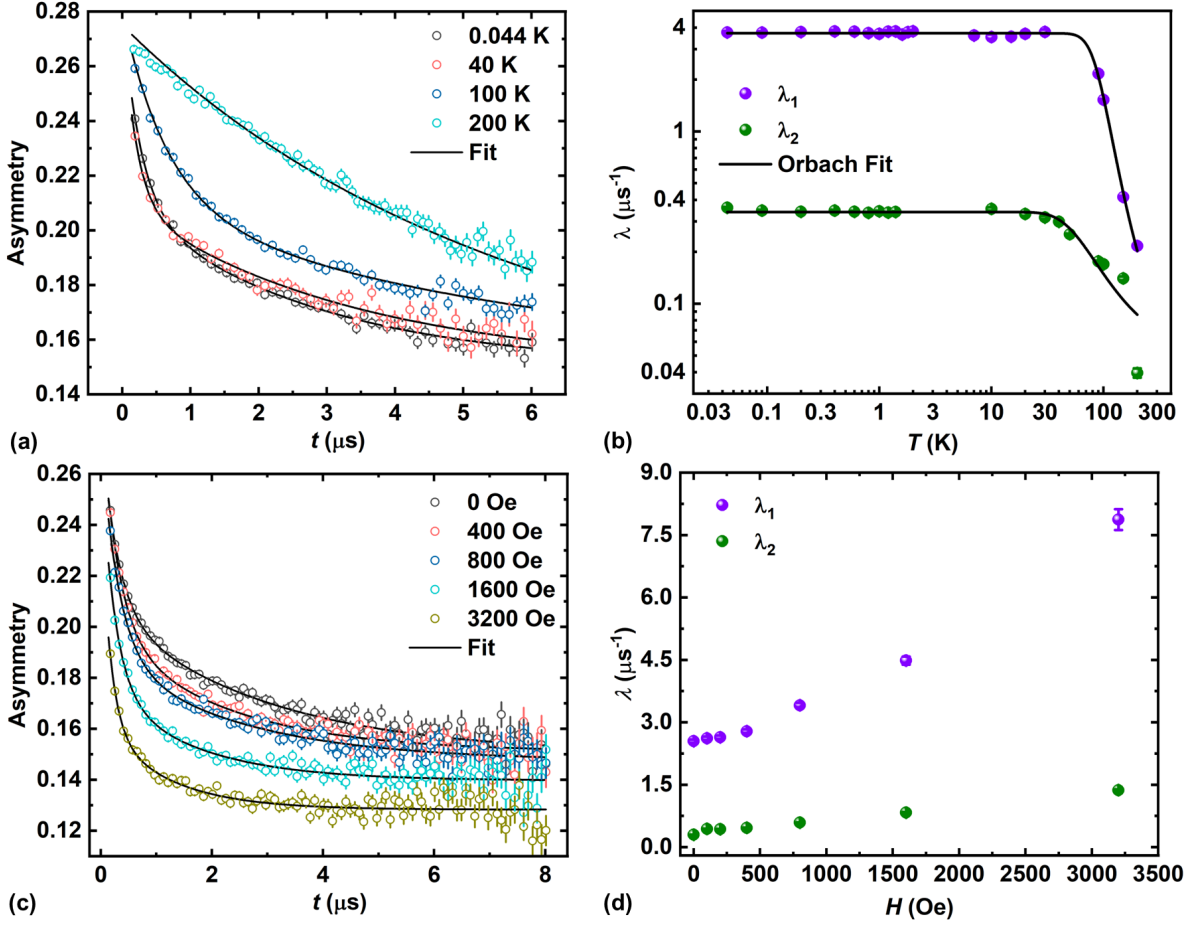


Figure 4.9: (a) Zero field muon spin relaxation data measured at different temperatures. The solid lines show fits to the data using equation 4.3. (b) The temperature dependence of the relaxation rates obtained from the asymmetry fitting. The solid line depicts their fitting with the Orbach process (equation 4.4). (c) Longitudinal Field measurements are carried out at 70 mK in the presence of the different applied fields. (d) Field dependence of both the relaxation rates.

The temperature variation of the relaxation rate can be described using the Orbach equation:

$$\lambda^{-1} = \lambda_0^{-1} + B_{me} \exp(-\Delta_{CEF}/T) \quad (4.4)$$

where  $\lambda$  stands for the relaxation rates  $\lambda_1$  and  $\lambda_2$ ,  $\lambda_0$  is the saturation value of relaxation rates at lower temperatures,  $B_{me}$  accounts for the magnetoelastic coupling of the  $\text{Yb}^{3+}$  spins with the phonon bath, and  $\Delta_{CEF}$  gives an estimation of the energy difference of the intermediate CEF levels involved in the process. Fitting of the  $\lambda_2$  variation results in the following parameters:  $\lambda_{0,2} = 2.94 \mu\text{s}$ ,  $B_{me,2} = 19.75 \mu\text{s}$  and  $\Delta_{CEF,2} = 165.21 \text{ K}$ . The value of  $\Delta_{CEF,2}$  obtained from the fit agrees very well with the value estimated from

the analysis of the inverse susceptibility data analyzed using the modified Curie-Weiss law. This agreement further reaffirms that the ground state is well separated from the higher levels and can be truly described by  $J_{eff} = 1/2$ . Further, fitting the temperature dependence of  $\lambda_1$  gives the following parameters:  $\lambda_{0,1} = 0.27 \mu\text{s}$ ,  $B_{me,1} = 59.22 \mu\text{s}$  and  $\Delta_{CEF,1} = 507.59 \text{ K}$ . The higher value of  $\Delta_{CEF,1}$  signifies that higher excited states also participate in the relaxation process at site 1. The temperature-independent behavior of  $\lambda_1$  and  $\lambda_2$  indicate the presence of a dynamic state at lower temperatures [42].

To further explore the spin dynamics, longitudinal field (LF)  $\mu\text{SR}$  measurements have been carried out at 70 mK by changing the applied fields from 0 to 3200 Oe. Representative LF  $\mu\text{SR}$  spectra, along with corresponding fits to the data using eq. 4.3, are shown in Figure 4.9(c). In an LF  $\mu\text{SR}$  measurement, the external magnetic field is applied along the initial muon spin direction. If the relaxation arises primarily from a random static internal field distribution, the application of a field that is a few times larger than the field corresponding to  $\lambda_1$  (as  $\lambda_2$  is smaller) will decouple the signal, and full asymmetry will be recovered. However, if the relaxation originates from dynamic fields, the relaxation will not be decoupled even in higher fields. The local field corresponding to  $\lambda_1$  at low temperatures can be calculated as  $B_{loc} = \lambda_1/\gamma_\mu \approx 44 \text{ Oe}$ , where  $\gamma_\mu$  is the gyromagnetic ratio for muons. The LF measurements clearly show the persistence of relaxation at least up to 3200 Oe (around 70 times higher than the  $B_{loc}$ ), confirming the dynamic nature of  $\text{Yb}^{3+}$  spins [24].

The field-dependence of the relaxation rates obtained from the LF- $\mu\text{SR}$  data fitting are presented in Figure 4.9(d). Intriguingly, both relaxation rates increase with an increase in the field, which is unusual as the magnetic field generally suppresses the dynamic relaxation rate [43, 44]. The increase in relaxation rates can be attributed to the enhancement of the density of spin excitations due to the application of the field. The increase in density of spin excitations competes with the quenching effect of the applied field. A similar behavior has previously been observed for Tb- and Yb-based compounds [25, 45].

### 4.3.5 Theoretical Calculation

Thus, milli-Kelvin magnetization, thermodynamics, and  $\mu\text{SR}$  measurements complement each other and affirm the presence of a dynamic state in  $\text{Yb}_2\text{Te}_5\text{O}_{13}$  at lower temperatures. To understand the origin of this state, we have performed a combined first principles and

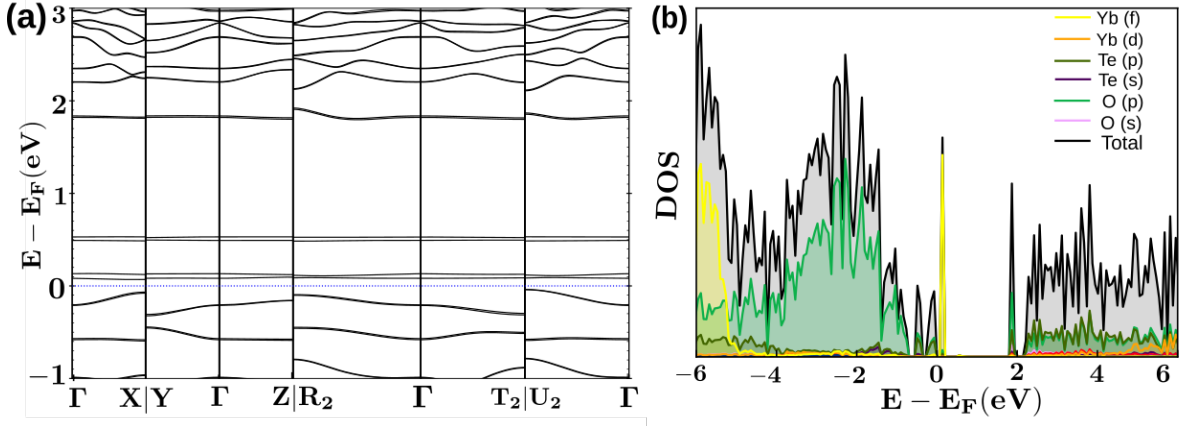


Figure 4.10: (a) The band structure and (b) the atom projected Density of States for  $\text{Yb}_2\text{Te}_5\text{O}_{13}$ . From (b), it is clear that the bands in the gap are formed by the  $f$  orbitals of Yb with significant contribution of O  $p$  and Te  $p$  orbitals near the Fermi level.

Monte Carlo simulation study.

#### 4.3.5.1 Density Functional Theory Calculations

The first principles simulation was carried out on the periodic system using the Vienna Ab Initio Simulation Package (VASP) [46–48], within the framework of the Projected Augmented Wave (PAW) [49] method, utilizing the Perdew-Burke-Ernzerhof (PBE) [50] approximation of the exchange-correlation functional. The geometry of the experimentally observed structure is optimized until the forces on all the atoms are smaller than 0.03 eV/Å. The optimized lattice parameters are given in Table 4.2. To account for the self interaction error in the highly correlated  $f$ -electrons in the system, we have included a Hubbard correction of  $U = 3$  eV for the optimization and the subsequent band structure and Density of States calculations. The band structure reveals a small band gap of about 0.1 eV, owing to the presence of a small density of Yb  $f$ -orbitals very close to the Fermi level. Apart from this slight contribution, we see a very large gap of about 1.8 eV, separating the rest of the valence band and the conduction bands. As is evident from the atom projected Density of States ( $p$ DOS), as given in Fig. 4.10, the major contributions near the Fermi level arise from Yb  $f$ -orbitals, Te  $p$  orbitals, and O  $p$  orbitals. The presence of heavy elements in the system gives rise to a large spin-orbit Coupling, which is included in all the calculations. For the calculation of band structure and the Density of States (DOS), the Brillouin Zone integration was performed on a  $\Gamma$ -centered  $7 \times 6 \times 5$  k-point grid.



Table 4.2: The optimised lattice parameters.

$a$ (Å)	$b$ (Å)	$c$ (Å)	$\alpha(^{\circ})$	$\beta(^{\circ})$	$\gamma(^{\circ})$
6.907	8.551	10.598	88.523	85.077	72.387

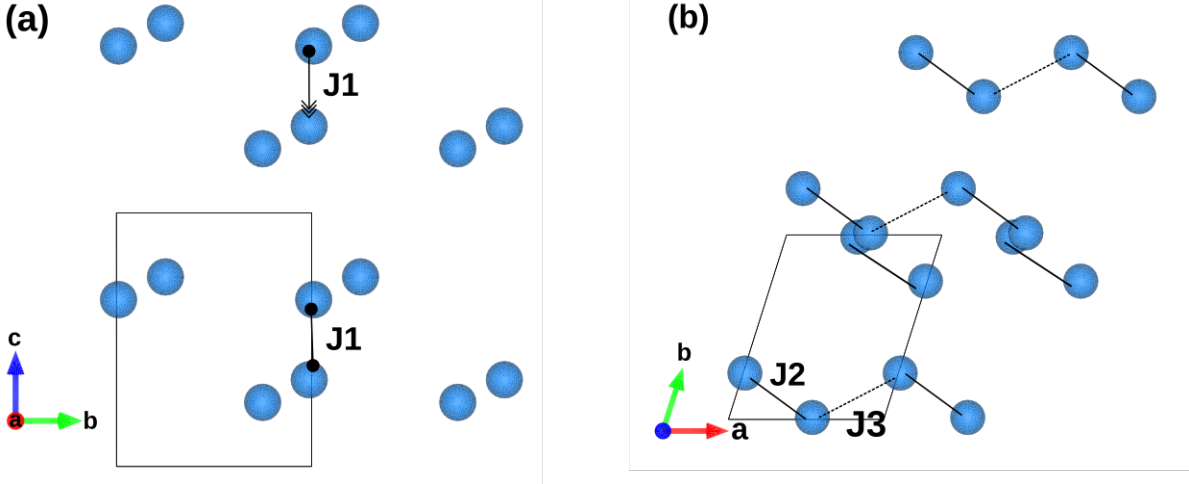


Figure 4.11: Spin exchange paths;  $J_1$  shown in (a) and  $J_2$ ,  $J_3$  are shown in (b).

Table 4.3: The nearest, next nearest, third nearest neighbor exchange couplings and the zero-field splitting parameters calculated from first principles calculations.

$J_1$ (meV)	$J_2$ (meV)	$J_3$ (meV)	$D$ (meV)	$E$ (meV)
10.8	3.9	-7.3	-0.43	-0.009

For the calculation of the magnetic exchange couplings and zero-field splitting parameters, we used the ORCA package [51]. The valence triple  $\zeta$  basis set [52] was employed for all atoms except Yb, for which a Segmented All Electron Relativistically Contracted (SARC) basis set, along with the SARC/J Coulomb fitting basis was implemented [53, 54]. The relativistic correction was applied by implementing the second-order Douglas-Kroll-Hess formalism. The nearest neighbor ( $J_1$ ), next nearest neighbor ( $J_2$ ), and the third nearest neighbor ( $J_3$ ) magnetic exchange couplings were calculated by considering isolated nearest, next nearest, and third nearest Yb pairs and calculating the difference in energy of the high spin and broken symmetry states for each pair. The zero-field splitting terms arising from the Spin-Orbit Coupling are predicted using the wave functions obtained from a Complete Active Space SCF (CASSCF) calculation.

The calculated nearest, next-nearest, and third next-nearest neighbor exchange interactions,  $J_1$ ,  $J_2$ , and  $J_3$ , (visualized in Fig. 4.11 as well as the zero-field splitting parameter,  $D$  and local anisotropic parameter,  $E$ , are given in Table 4.3.



#### 4.3.5.2 Monte Carlo Simulation

With the above coupling parameters, we constructed an effective spin Hamiltonian given by,

$$H = J_1 \sum_{\langle ij \rangle} S_i \cdot S_j + J_2 \sum_{\langle\langle ij \rangle\rangle} S_i \cdot S_j + J_3 \sum_{\langle\langle\langle ij \rangle\rangle\rangle} S_i \cdot S_j + D \sum_i S_{iz}^2 + E \sum_i (S_{ix}^2 - S_{iy}^2) \quad (4.5)$$

A Monte Carlo simulation was performed using the above equation. We have omitted the zero-field splitting terms, owing to the fact that D and E are much smaller as compared to  $J_1$ . Our simulations were performed on  $N = 2 \times 10 \times 10 \times 10$  classical spins obeying periodic boundary conditions. A single MC step involves N heat bath steps followed by ten over-relaxation steps. For each temperature, the spin configuration is initialized randomly, and the spins can orient in any direction on a three dimensional sphere. This system is used to calculate the thermodynamic quantities after a thermalization of  $5 \times 10^6$  MC steps, followed by averaging over  $2 \times 10^6$  MC steps. Our high-temperature Monte Carlo simulation reproduces the Curie-Weiss temperature observed experimentally. A detailed analysis of the static spin structure factor at various temperatures in the high-temperature region gives us an idea about the dominant interactions and the origin of frustration in the system. The static spin structure was calculated along the reciprocal vectors using the equation given below

$$S_{q_i} = \frac{1}{N_i} \sum_{kj}^{N_i} \langle \vec{S}_k \cdot \vec{S}_j \rangle e^{iq_i \cdot |r_k - r_j|} \quad (4.6)$$

where  $q_i$  corresponds to the reciprocal vector along the  $i = a, b, c$  directions and  $N_i$  the number of atoms considered in a particular direction.

#### 4.3.5.3 Origin of The Dynamic State

The paramagnetic phase observed at room temperature remains unchanged down to 125 K, where we see a deviation from the Curie-Weiss law. For temperatures above 125 K, the magnetic behavior is predominantly determined by the leading exchange coupling,  $J_1$  (10.8 meV). Since this interaction is along the  $c$ -axis, we have calculated spin structure factor  $S(q_z)$  using Eq. 4.6 and plotted its variation vs.  $q_z$ , as shown in Fig. 4.12(a). We find that the magnetic structure factor peaks at  $|q_z| = \frac{\pi}{c}$ , confirming antiferromagnetic interactions along the  $c$ -axis. However, below 125 K,  $J_2$  and  $J_3$  play a bigger role, thus

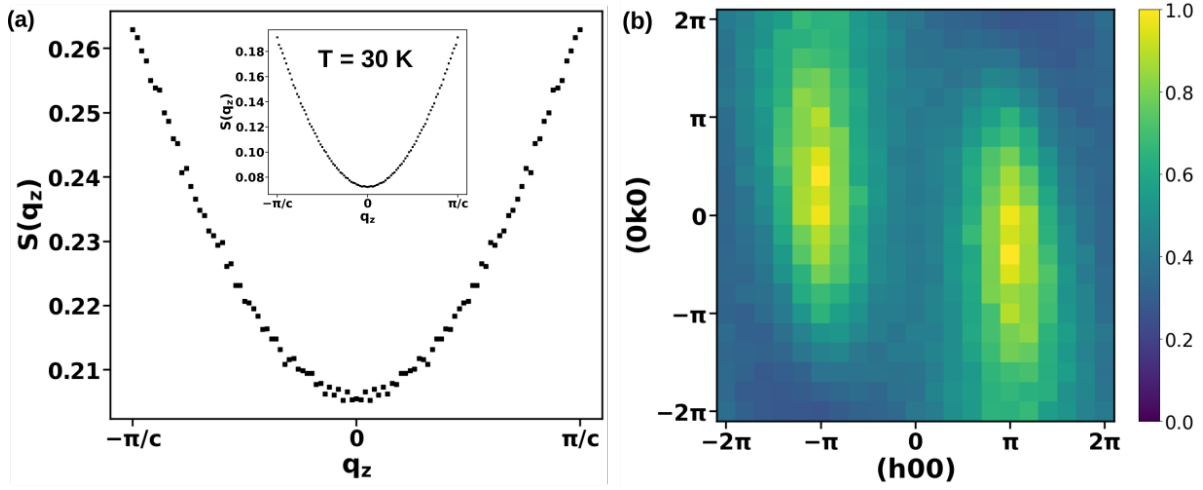


Figure 4.12: (a) The Structure Factor along the  $c$ -axis in at 100 K and 30 K(inset) (b) the static structure factor at 50 K.

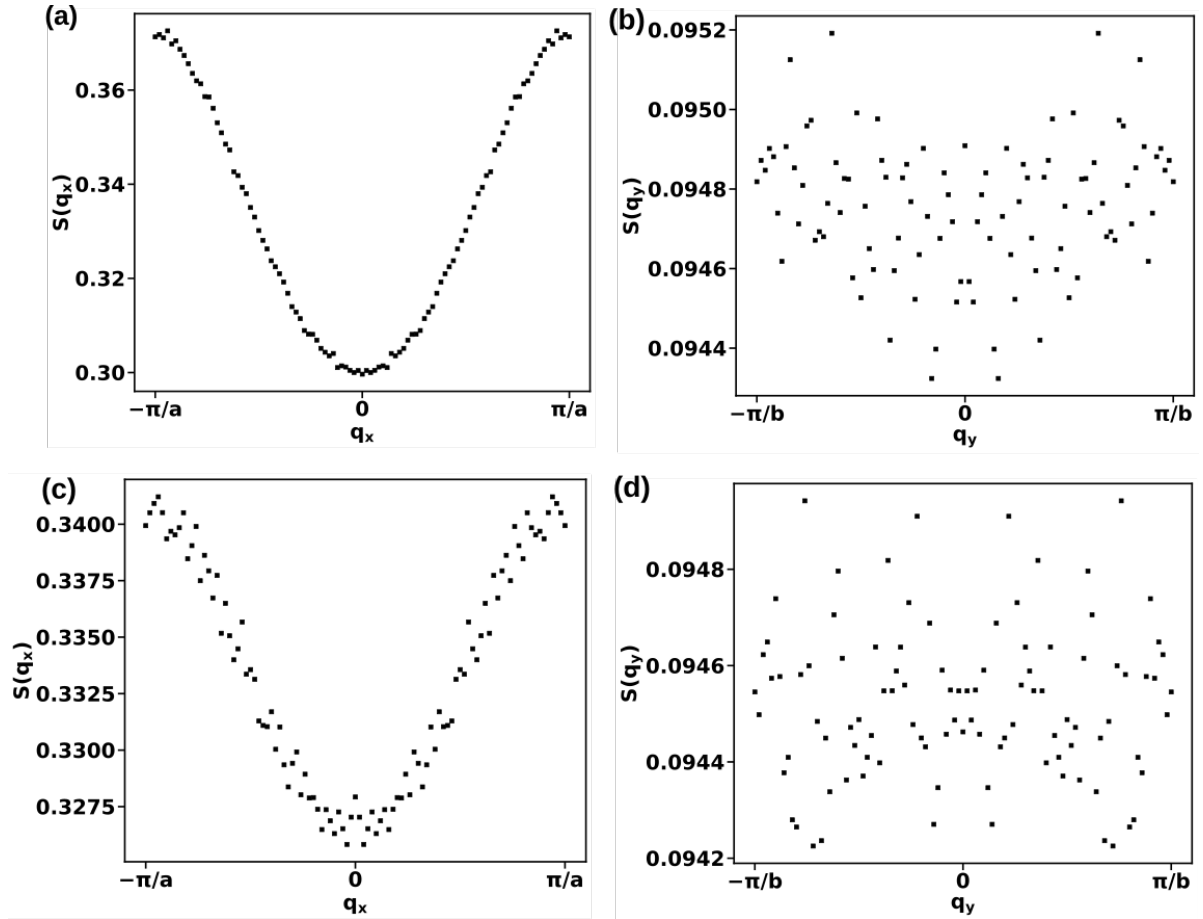


Figure 4.13: (a) and (b) depicts the  $S_{qx}$  and  $S_{qy}$  respectively at  $T = 30$  K, while (c) and (d) denote the static structure factor along  $a$ -axis and  $b$ -axis for  $T = 100$  K

making the system much more interesting. The spin structure factors along the  $a$  and  $b$  axes at  $T = 30$  and  $100$  K are plotted in Fig. 4.13, which shows a peak in  $Sq_x$  at  $\frac{\pi}{a}$  that corresponds to antiferromagnetic interactions along  $\vec{a}$ , but no prominent peak in  $Sq_y$ .

We calculated the spin-spin correlation function at various temperatures to visualize the nature of spins in the  $ab$  plane. We observe that the correlation function decays exponentially along the  $a, b$ , and  $c$  axes, with correlations existing beyond nearest neighbors along  $a$  and  $c$  but dying down relatively fast along  $b$ . The static structure factor in the  $ab$  plane shows diffuse peaks in the first Brillouin zone for  $T = 50$  K, as plotted in Fig. 4.12 (b). The diffuse peaks reveal that there is competition of exchange interactions in the  $ab$  plane owing to the spiral nature of the interaction along  $a$  and  $b$ . This phase is best described as a spiral non-trivial phase [55, 56], which exists down to a temperature close to where the susceptibility starts rising. Hence, our computational studies confirm that these competing magnetic interactions are the primary inducers of the dynamic state in  $\text{Yb}_2\text{Te}_5\text{O}_{13}$ .

## 4.4 Conclusion

In conclusion, we have performed a comprehensive study of a quantum-dimer-based compound  $\text{Yb}_2\text{Te}_5\text{O}_{13}$  using magnetization, heat capacity, and  $\mu\text{SR}$  measurements. ZF- $\mu\text{SR}$  measurements have confirmed the absence of long-range ordering down to  $44$  mK and the presence of a transition among excited CEF levels (Orbach process). Moreover, LF measurements confirm the fluctuating nature of  $\text{Yb}^{3+}$  spins in the system even up to  $3200$  Oe and reveal a field-induced enhancement of the density of spin excitations. Theoretical calculations affirm the experimental findings and reveal that competing exchange interactions are responsible for such a dynamic state. This discovery contributes to our comprehension of unusual magnetic phases and paves the way for investigating quantum spin liquids in new materials that have not been explored in this context before.

# Bibliography

- [1] L. Balents, Spin liquids in frustrated magnets, *Nature (London)* **464**, 199 (2010).
- [2] R. Moessner and A. P. Ramirez, Geometrical frustration, *Phys. Today* **59**, 24 (2006).
- [3] B. Normand, Frontiers in frustrated magnetism, *Contemp. Phys.* **50**, 533 (2009).
- [4] S. V. Isakov, M. B. Hastings, and R. G. Melko, Topological entanglement entropy of a Bose–Hubbard spin liquid, *Nat. Phys.* **7**, 772 (2011).
- [5] X.-G. Wen, Quantum orders and symmetric spin liquids, *Phys. Rev. B* **65**, 165113 (2002).
- [6] B. Keimer, S. A. Kivelson, M. R. Norman, S. Uchida, and J. Zaanen, From quantum matter to high-temperature superconductivity in copper oxides, *Nature (London)* **518**, 179 (2015).
- [7] M. J. P. Gingras and P. A. McClarty, Quantum spin ice: a search for gapless quantum spin liquids in pyrochlore magnets, *Rep. Prog. Phys.* **77**, 056501 (2014).
- [8] R. Moessner and S. L. Sondhi, Irrational charge from topological order, *Phys. Rev. Lett.* **105**, 166401 (2010).
- [9] N. Y. Yao, C. R. Laumann, A. V. Gorshkov, H. Weimer, L. Jiang, J. I. Cirac, P. Zoller, and M. D. Lukin, Topologically protected quantum state transfer in a chiral spin liquid, *Nat. Commun.* **4**, 1585 (2013).
- [10] H. D. Zhou, E. S. Choi, G. Li, L. Balicas, C. R. Wiebe, Y. Qiu, J. R. D. Copley, and J. S. Gardner, Spin liquid state in the  $S=1/2$  triangular lattice  $\text{Ba}_3\text{CuSb}_2\text{O}_9$ , *Phys. Rev. Lett.* **106**, 147204 (2011).
- [11] M. Fu, T. Imai, T.-H. Han, and Y. S. Lee, Evidence for a gapped spin-liquid ground state in a kagome Heisenberg antiferromagnet, *Science* **350**, 655 (2015).
- [12] P. Khuntia, F. Bert, P. Mendels, B. Koteswararao, A. V. Mahajan, M. Baenitz, F. C. Chou, C. Baines, A. Amato, and Y. Furukawa, Spin liquid state in the 3D

- frustrated antiferromagnet  $\text{PbCuTe}_2\text{O}_6$ : NMR and muon spin relaxation studies, *Phys. Rev. Lett.* **116**, 107203 (2016).
- [13] K. A. Ross, L. Savary, B. D. Gaulin, and L. Balents, Quantum excitations in quantum spin ice, *Phys. Rev. X* **1**, 021002 (2011).
- [14] O. Mustonen, S. Vasala, E. Sadrollahi, K. P. Schmidt, C. Baines, H. C. Walker, I. Terasaki, F. J. Litterst, E. Baggio-Saitovitch, and M. Karppinen, Spin-liquid-like state in a spin-1/2 square-lattice antiferromagnet perovskite induced by  $d^{10}$ – $d^0$  cation mixing, *Nat. comm.* **9**, 1 (2018).
- [15] I. Terasaki, T. Igarashi, T. Nagai, K. Tanabe, H. Taniguchi, T. Matsushita, N. Wada, A. Takata, T. Kida, M. Hagiwara, K. Kobayashi, H. Sagayama, R. Kumai, H. Nakao, and Y. Murakami, Absence of magnetic long range order in  $\text{Ba}_3\text{ZnRu}_2\text{O}_9$ : a spin-liquid candidate in the  $S=3/2$  dimer lattice, *J. Phys. Soc. Jpn.* **86**, 033702 (2017).
- [16] G.M. Sheldrick, Program for Empirical Absorption Correction of Area Detector Data, SADABS (1997).
- [17] G.M. Sheldrick, SHELXT-Integrated Space-Group and Crystal-Structure Determination, *Acta Crystallogr. Sect. A*, **71**, 3 (2015).
- [18] J. Rodriguez-Carvajal, FullProf: A Program for Rietveld Refinement and Pattern Matching Analysis, in Abstracts of the Satellite Meeting on Powder Diffraction of the XV Congress of the IUCr, Toulouse, France (1990), p. 127. See also, *Physica B* **192**, 55 (1993). The FullProf Suite can be freely downloaded from <https://www.ill.eu/sites/fullprof>.
- [19] Mantid (2013): Manipulation and Analysis Toolkit for Instrument Data.; Mantid Project.
- [20] O. Arnold, J.C. Bilheux, J.M. Borreguero, A. Buts, S.I. Campbell, L. Chapon, M. Doucet, N. Draper, R. Ferraz Lea, M.A. Gigg et al., Nuclear Instruments and Methods in Physics Research Section A: Accelerators, Spectrometers, Detectors and Associated Equipment **764**, 156 (2014).
- [21] T. Besara, M. S. Lundberg, J. Sun, D. Ramirez, L. Dong, J. B. Whalen, R. Vasquez, F. Herrera, J. R. Allen, M. W. Davidson *et al.*, Single crystal synthesis and magnetism of the  $\text{BaLn}_2\text{O}_4$  family (Ln= lanthanide), *Prog. Solid State Chem.* **42**, 23 (2014).

- 
- [22] M. Mitric, B. Antic, M. Balanda, D. Rodic, and M. L. Napijalo, An x-ray diffraction and magnetic susceptibility study of  $\text{Yb}_x\text{Y}_{2-x}\text{O}_3$ , J. Phys.: Condens. Matter **9**, 4103 (1997).
  - [23] R. Sibille, E. Lhotel, V. Pomjakushin, C. Baines, T. Fennell, and M. Kenzelmann, Candidate quantum spin liquid in the  $\text{Ce}^{3+}$  pyrochlore stannate  $\text{Ce}_2\text{Sn}_2\text{O}_7$ , Phys. Rev. Lett. **115**, 097202 (2015).
  - [24] L. Ding, P. Manuel, S. Bachus, F. Grussler, P. Gegenwart, J. Singleton, R. D. Johnson, H. C. Walker, D. T. Adroja, A. D. Hillier, and A. A. Tsirlin, Gapless spin-liquid state in the structurally disorder-free triangular antiferromagnet  $\text{NaYbO}_2$ , Phys. Rev. B **100**, 144432 (2019).
  - [25] C. Y. Jiang, Y. X. Yang, Y. X. Gao, Z. T. Wan, Z. H. Zhu, T. Shiroka, C. S. Chen, Q. Wu, X. Li, J. C. Jiao, K. W. Chen, Y. Bao, Z. M. Tian, and L. Shu, Spin excitations in the quantum dipolar magnet  $\text{Yb}(\text{BaBO}_3)_3$ , Phys. Rev. B **106**, 014409 (2022).
  - [26] P. Svoboda, J. Vejpravova, N.-T. Kim-Ngan, and F. Kaysel, Specific heat study of selected  $\text{RNi}_5$ , J. Magn. Magn. Mater. **272-276**, 595 (2004).
  - [27] R. Kumar and A. Sundaresan, Unveiling a hidden multiferroic state under magnetic fields in  $\text{BaHoFeO}_4$  Phys. Rev. B **107**, 184420 (2023).
  - [28] R. Kumar and A. Sundaresan, Antisite disorder driven cluster glass state and colossal magnetoresistance in  $\text{MnSb}_2\text{Se}_4$ , Phys. Rev. B **106**, 134423 (2022).
  - [29] R. Bag, M. Ennis, C. Liu, S. E. Dissanayake, Z. Shi, J. Liu, L. Balents, and S. Haravifard, Realization of quantum dipoles in triangular lattice crystal  $\text{Ba}_3\text{Yb}(\text{BO}_3)_3$  Phys. Rev. B **104**, L220403 (2021).
  - [30] K. Somesh, S. S. Islam, S. Mohanty, G. Simutis, Z. Guguchia, C. Wang, J. Sichelschmidt, M. Baenitz, and R. Nath, K. Somesh, S. S. Islam, S. Mohanty, G. Simutis, Z. Guguchia, C. Wang, J. Sichelschmidt, M. Baenitz, and R. Nath, Absence of magnetic order and emergence of unconventional fluctuations in the  $J_{eff}=1/2$  triangular-lattice antiferromagnet  $\text{YbBO}_3$ , Phys. Rev. B **107**, 064421 (2023) Phys. Rev. B **107**, 064421 (2023).
  - [31] E. S. R. Gopal, Specific Heats at Low Temperatures (Plenum Press, New York, 1966).
  - [32] R. K. Pathria, Statistical Mechanics (Elsevier, New York, 2016).

- 
- [33] K. Karlová, J. Strečka, and T. Madaras, The Schottky-type specific heat as an indicator of relative degeneracy between ground and first-excited states: The case study of regular Ising polyhedra, *Phys. B (Amsterdam)* **488**, 49 (2016).
  - [34] H. M. Rosenberg, *Low Temperature Solid State Physics* Oxford University Press, Oxford, 1963.
  - [35] L. Xie, T. Su, and X. Li, Magnetic field dependence of Schottky anomaly in the specific heats of stripe-ordered superconductors  $\text{La}_{1.6-x}\text{Nd}_{0.4}\text{Sr}_x\text{CuO}_4$ , *Physica C: Superconductivity* **480**, 14 (2012).
  - [36] S. Mahdaviifar and A. Akbari, Heat capacity of Schottky type in low-dimensional spin systems, *J. Phys.: Condens. Matter* **20**, 215213 (2008).
  - [37] X. G. Zheng, H. Kubozono, K. Nishiyama, W. Higemoto, T. Kawae, A. Koda, and C. N. Xu, Coexistence of long-range order and spin fluctuation in geometrically frustrated clinoatacamite  $\text{Cu}_2\text{Cl}(\text{OH})_3$ , *Phys. Rev. Lett.* **95**, 057201 (2005).
  - [38] Y. J. Uemura, T. Yamazaki, D. R. Harshman, M. Senba, and E. J. Ansaldo, Muon-spin relaxation in AuFe and CuMn spin glasses, *Phys. Rev. B* **31**, 546 (1985).
  - [39] J. Gaudet, D. D. Maharaj, G. Sala, E. Kermarrec, K. A. Ross, H. A. Dabkowska, A. I. Kolesnikov, G. E. Granroth, and B. D. Gaulin, Neutron spectroscopic study of crystalline electric field excitations in stoichiometric and lightly stuffed  $\text{Yb}_2\text{Ti}_2\text{O}_7$ , *Phys. Rev. B* **92**, 134420 (2015).
  - [40] P. Dalmas de Réotier, A. Yaouanc, P. C. M. Gubbens, C. T. Kaiser, C. Baines, and P. J. C. King, Absence of magnetic order in  $\text{Yb}_3\text{Ga}_5\text{O}_{12}$ : relation between phase transition and entropy in geometrically frustrated materials, *Phys. Rev. Lett.* **91**, 167201 (2003).
  - [41] R. Orbach, Spin-lattice relaxation in rare-earth salts, *Proc. Phys. Soc. London Sect. A* **264**, 458 (1961).
  - [42] Y. Cai, C. Lygouras, G. Thomas, M. N. Wilson, J. Beare, S. Sharma, C. A. Marjerrison, D. R. Yahne, K. A. Ross, Z. Gong, Y. J. Uemura, H. A. Dabkowska, and G. M. Luke,  $\mu\text{SR}$  study of the triangular Ising antiferromagnet  $\text{ErMgGaO}_4$ , *Phys. Rev. B* **101**, 094432 (2020).
  - [43] Y. Li, D. Adroja, P. K. Biswas, P. J. Baker, Q. Zhang, J. Liu, A. A. Tsirlin, P. Gegenwart, and Q. Zhang, Muon spin relaxation evidence for the U(1) quantum spin-liquid ground state in the triangular antiferromagnet  $\text{YbMgGaO}_4$ , *Phys. Rev. Lett.* **117**, 097201 (2016).

- 
- [44] A. Yaouanc and P. Dalmas de Réotier, *Muon Spin Rotation, Relaxation, and Resonance: Applications to Condensed Matter* (Oxford University Press, Oxford, 2011).
- [45] P. Dalmas de Réotier, A. Yaouanc, L. Keller, A. Cervellino, B. Roessli, C. Baines, A. Forget, C. Vaju, P. C. M. Gubbens, A. Amato, and P. J. C. King, Spin dynamics and magnetic order in magnetically frustrated  $\text{Tb}_2\text{Sn}_2\text{O}_7$  *Phys. Rev. Lett.* **96**, 127202 (2006).
- [46] G. Kresse and J. Furthmüller, Efficient Iterative Schemes for Ab Initio Total-Energy Calculations Using a Plane-Wave Basis Set, *Phys. Rev. B* **54**, 11169 (1996).
- [47] G. Kresse and J. Furthmüller, Efficiency of Ab-Initio Total Energy Calculations for Metals and Semiconductors Using a Plane-Wave Basis Set, *Comput. Mater. Sci.* **6**, 15 (1996).
- [48] G. Kresse and J. Hafner, Ab Initio Molecular Dynamics for Liquid Metals, *Phys. Rev. B* **47**, 558 (1993).
- [49] G. Kresse and D. Joubert, From Ultrasoft Pseudopotentials to the Projector Augmented-Wave Method, *Phys. Rev. B* **59**, 1758 (1999).
- [50] J. P. Perdew, K. Burke, and M. Ernzerhof, Generalized Gradient Approximation Made Simple, *Phys. Rev. Lett.* **77**, 3865 (1996).
- [51] F. Neese, F. Wennmohs, U. Becker, and C. Riplinger, The ORCA quantum chemistry program package, *J. Chem. Phys.* **152**, 224108 (2020).
- [52] F. Weigenda and R. Ahlrichs, Balanced basis sets of split valence, triple zeta valence and quadruple zeta valence quality for H to Rn: Design and assessment of accuracy, *Phys. Chem. Chem. Phys.*, **7**, 3297-3305 (2005).
- [53] D. Aravena, F. Neese, and D. A. Pantazis, Improved Segmented All-Electron Relativistically Contracted Basis Sets for the Lanthanides, *J. Chem. Theory Comput.* **12**, 3, 1148–1156 (2016).
- [54] D. A. Pantazis, F. Neese, All-Electron Scalar Relativistic Basis Sets for the Lanthanides, *J. Chem. Theory Comput.* **5**, 9, 2229–2238 (2009).
- [55] D. Bergman, J. Alicea, E. Gull, S. Trebst, and L. Balents, Order-by-disorder and spiral spin-liquid in frustrated diamond-lattice antiferromagnets, *Nature Physics*, **3**, 487–491 (2007).
- [56] S. Gao, O. Zaharko, V. Tsurkan, Y. Su, J. S. White, G. S. Tucker, B. Roessli, F. Bourdarot, R. Sibille, D. Chernyshov, T. Fennell, A. Loidl, and C. Rüegg, Spiral



spin-liquid and the emergence of a vortex-like state in  $\text{MnSc}_2\text{S}_4$  Nature Physics, **13**, 157–161 (2017).

## Chapter 5

# Quantum Spin-Liquid in a Two-Dimensional Magnetic Rhombus Lattice: An Exploration

We present the intriguing magnetic behavior of a two-dimensional Rhombus spin-lattice in  $\text{LiYbSiO}_4$ . Our magnetization measurements, extending down to 0.4 K, uncover the absence of long-range magnetic ordering alongside the emergence of magnetic correlations below 1 K. Complementing these observations, heat capacity measurements affirm the existence of a finite internal magnetic field ( $\sim 1$  K) and validate the development of magnetic correlations. Further insight is gained through zero field  $\mu\text{SR}$  measurements, revealing a gradual slowing down of  $\text{Yb}^{3+}$  spin fluctuations from 0.5 K to as low as 44 mK, indicative of magnetic correlations. Moreover, longitudinal field  $\mu\text{SR}$  measurements illustrate the persistence of correlations up to 3200 Oe. Within Hubbard  $U$ -corrected first-principles density functional theory, we determined the spin exchange ratio  $J_2/J_1 \approx 0.53$ , supporting a quantum spin-liquid state in the disorder-free compound,  $\text{LiYbSiO}_4$ , comprising magnetic rhombus lattice, which offers intriguing avenues for further exploration of quantum magnetism.

## 5.1 Introduction

The enduring theoretical anticipation of a quantum spin liquid state within spin-1/2 Heisenberg square lattice antiferromagnets, residing at the subtle boundary between Néel and columnar antiferromagnetic order-phenomena governed, respectively, by nearest-neighbor and next-nearest-neighbor interactions has persisted as a captivating yet unverified conjecture [1–5]. Previously, several efforts were made to realize such a system experimentally but did not succeed due to dominating either  $J_1$  or  $J_2$  interactions, resulting in an ordered ground state [6–20]. To date, no known compounds have exhibited this distinct state without considerable chemical disorder in a square lattice. The allure of the square lattice lies in its association with high-temperature superconductivity [21]. In the literature, most of the spin-liquid reports are focused on Cu-based materials, and little attention has been given to Yb-based compounds despite  $\text{Yb}^{3+}$  fulfilling all requisite criteria. The presence of strong spin-orbit coupling and crystal electric field can result in a Kramers doublet ground state, which can be described by effective angular momentum ( $J_{eff}$ ) = 1/2 [22–24]. Furthermore, localized  $4f$  orbitals ensure that only nearest-neighbor interactions are significant, opening the doors to realize an ideal low-dimensional magnetic lattice. Thus, if Yb atoms are arranged on a low-dimensional frustrated lattice, a novel quantum phase may follow depending on the degree of the frustration.

In this work, we report a new distorted square lattice-based compound,  $\text{LiYbSiO}_4$ , and its low-temperature physical properties, characterized using several techniques. Primary magnetization measurements reveal the emergence of magnetic correlations of the order of 1 K complemented by the specific heat measurements. The muon spin relaxation ( $\mu\text{SR}$ ) measurements confirm the presence of a dynamic state below 0.5 K, which is field-sensitive, as revealed by longitudinal  $\mu\text{SR}$  measurements. The observation of dynamic state is consistent with our theoretical estimate of the spin exchange ratio,  $J_2/J_1 = 0.53$ , as predicted for a spin-liquid state of the  $J_1$ – $J_2$  Heisenberg model on a square lattice [25].

## 5.2 Experiment

A high-quality polycrystalline sample of  $\text{LiYbSiO}_4$  has been prepared using a conventional solid-state reaction method. The carbonate of Li ( $\text{Li}_2\text{CO}_3$ ), oxide of Yb ( $\text{Yb}_2\text{O}_3$ ), and oxide of Si ( $\text{SiO}_2$ ) have been used as the raw materials. As a first step, all the starting materials are mixed together in stoichiometric amounts with 7 % molar extra  $\text{Li}_2\text{CO}_3$  and heated to 900° C and kept at the same temperature for 12 h. Extra  $\text{Li}_2\text{CO}_3$  is

taken to compensate for the loss of Li at higher temperatures due to its volatile nature. After cooling to room temperature, the mixture is pressed into a pellet and heated to 1100° C and kept at the same temperature for 24 h. As a final step, it is cooled to room temperature and used for various characterization measurements.

X-ray diffraction measurements have been performed using a PANalytical Empyrean Alpha I diffractometer using Cu-K $\alpha$  single wavelength ( $\lambda = 1.54059$  Å). Time-of-flight neutron powder diffraction (NPD) data are collected on the WISH instrument at the ISIS neutron and muon facility, UK [26]. Rietveld refinement of the XRD and NPD has been performed using the Jana 2020 software [27]. Magnetic measurements are carried out using a Quantum Design magnetic properties measurement system (MPMS). Specific heat and thermal conductivity data are collected on a Quantum Design physical properties measurement system (PPMS). For thermal conductivity measurements, the sample is cut into the shape of a rectangular bar of the following dimensions: 1.165 mm  $\times$  2.650 mm  $\times$  5.355 mm. The muon spectroscopy measurements are performed on the MuSR spectrometer at the ISIS facility using zero-field (ZF), longitudinal-field (LF), and weak transverse field (wTF) options. The powder sample was mounted on a high-purity silver plate, which gives only a nonrelaxing background signal. A dilution refrigerator has been used to achieve a temperature as low as 0.044 K. Analysis of the  $\mu$ SR measurements has been done using the MANTID software [28, 29].

## 5.3 Results and Discussion

### 5.3.1 Crystal Structure

Table 5.1: Crystallographic parameters along with occupancy and isotropic displacement parameters obtained from the Rietveld refinement of the room temperature powder XRD data. Space group:  $Pnma$ ,  $a = 10.7558(1)$  Å,  $b = 6.2530(1)$  Å,  $c = 4.9022(1)$  Å,  $V = 329.70(2)$  Å<sup>3</sup>,  $\chi^2 = 5.76$  %, Bragg  $R$  factor = 9.95 %,  $R_f = 13.87$  %.

Atom	Wyckoff symbol	x	y	z	Occupancy	$B_{iso}(\text{Å}^2)$
Li(1)	4a	0.0	0.0	0.0	1.0	1.0
Yb(1)	4c	0.2383(1)	0.25	0.0267(3)	1.0	0.0081(4)
Si(1)	4c	0.0860(6)	0.25	0.5848(12)	1.0	0.012(2)
O(1)	4c	0.0868(12)	0.25	0.2584(27)	1.0	1.0
O(2)	4c	0.0504(12)	0.75	0.2840(25)	1.0	1.0
O(3)	8d	0.1491(9)	0.0507(17)	0.7271(18)	1.0	1.0

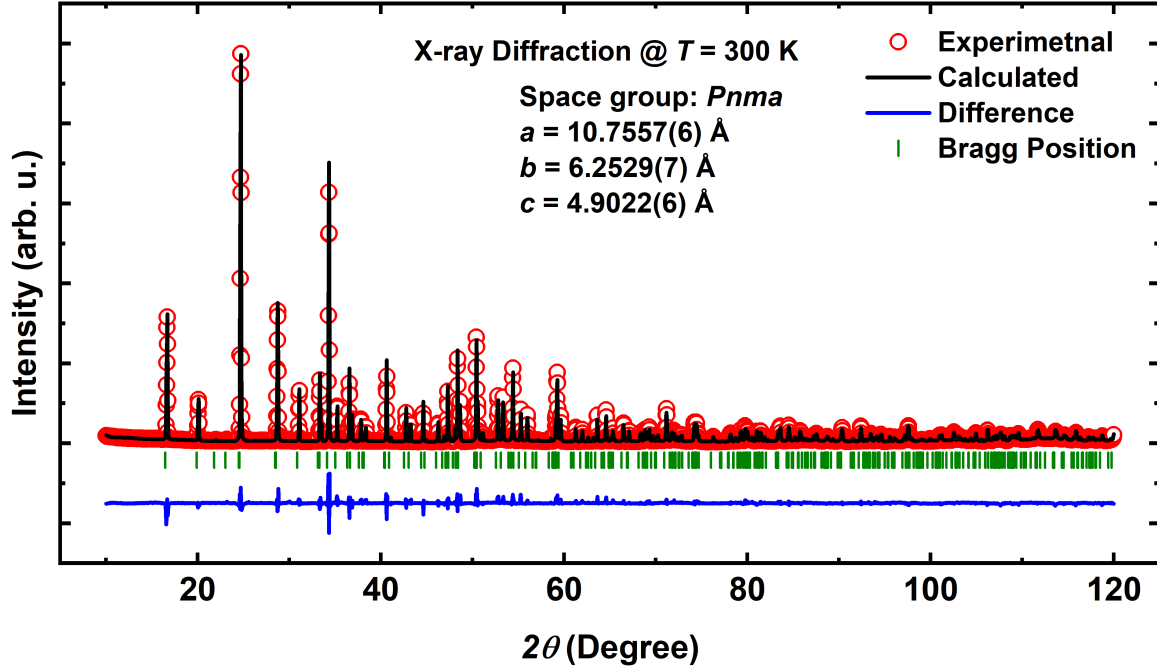


Figure 5.1: Rietveld refinement of the XRD data collected at 300 K. Experimental pattern, simulated pattern, difference, and Bragg position are shown by red open circles, black solid line, blue solid line, and green bars, respectively.

Table 5.2: Crystallographic parameters along with occupancy and isotropic displacement parameters obtained from the Rietveld refinement of the neutron diffraction data. Space group:  $Pnma$ ,  $a = 10.7166(1)$  Å,  $b = 6.2417(1)$  Å,  $c = 4.8846(1)$  Å,  $V = 326.71(1)$  Å<sup>3</sup>,  $\chi^2 = 3.92$  %, Bragg  $R$  factor = 5.39 %,  $R_f = 6.92$  %.

Atom	Wyckoff symbol	x	y	z	Occupancy	$U_{iso}(\text{\AA}^2)$
Li(1)	$4a$	0.0	0.0	0.0	1.0	0.0258(15)
Yb(1)	$4c$	0.2778(1)	0.25	0.0272(3)	1.0	0.0136(4)
Si(1)	$4c$	0.0873(6)	0.25	0.5877(2)	1.0	0.0134(8)
O(1)	$4c$	0.0970(2)	0.25	0.2576(4)	1.0	0.0214(6)
O(2)	$4c$	0.0529(2)	0.75	0.2827(3)	1.0	0.0132(6)
O(3)	$8d$	0.1606(1)	0.0463(2)	0.7303(2)	1.0	0.0145(4)

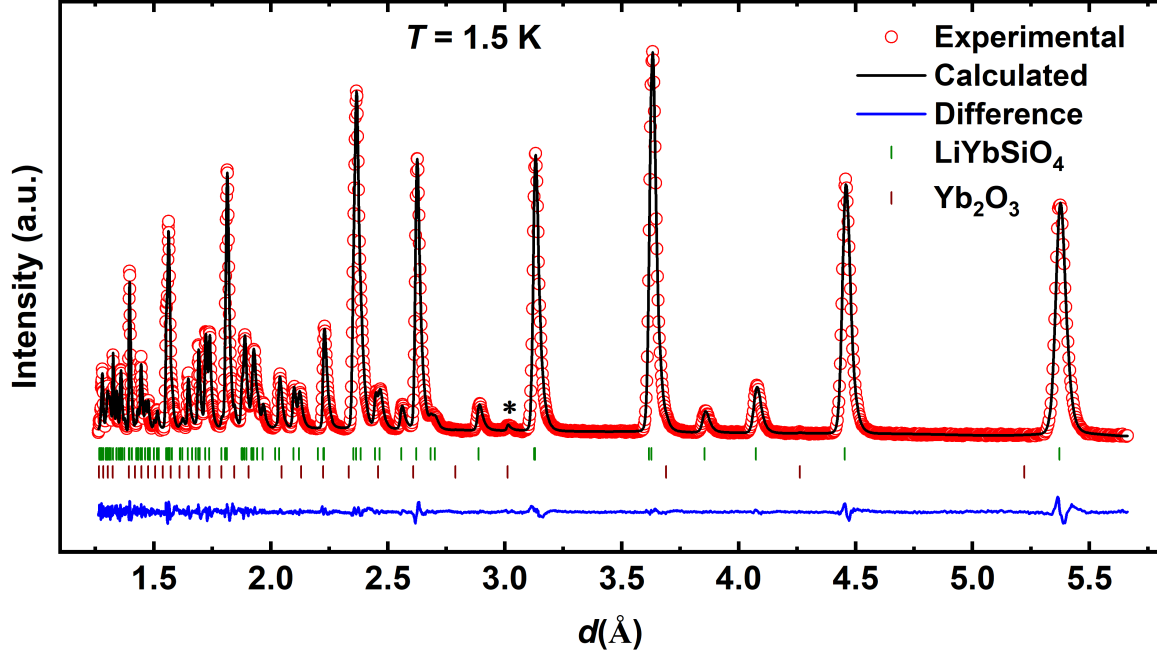


Figure 5.2: Rietveld refinement of the time of flight neutron diffraction data of  $\text{LiYbSiO}_4$ . Red open circles indicate experimental data, the black solid line represents a simulated pattern, and blue solid lines represent the difference. Green bars indicate Bragg peaks of  $\text{LiYbSiO}_4$ , while Maroon bars denote Bragg peaks of  $\text{Yb}_2\text{O}_3$ . Star indicates a small peak coming from  $\text{Yb}_2\text{O}_3$ .

Table 5.3: Crystallographic parameters along with occupancy and isotropic displacement parameters obtained from the Rietveld refinement of the neutron diffraction data. Space group:  $Pnma$ ,  $a = 10.7172(1)$  Å,  $b = 6.2420(1)$  Å,  $c = 4.8849(1)$  Å,  $V = 326.77(1)$  Å<sup>3</sup>,  $\chi^2 = 3.10$  %, Bragg  $R$  factor = 5.49 %,  $R_f = 6.94$  %.

Atom	Wyckoff symbol	x	y	z	Occupancy	$U_{iso}(\text{\AA}^2)$
Li(1)	4a	0.0	0.0	0.0	1.0	0.0216(10)
Yb(1)	4c	0.2776(0)	0.25	0.0267(1)	1.0	0.0131(3)
Si(1)	4c	0.0874(2)	0.25	0.5875(3)	1.0	0.0118(6)
O(1)	4c	0.0967(1)	0.25	0.2588(3)	1.0	0.0179(5)
O(2)	4c	0.0523(1)	0.75	0.2844(3)	1.0	0.0134(4)
O(3)	8d	0.1609(1)	0.0462(1)	0.7310(2)	1.0	0.0140(3)

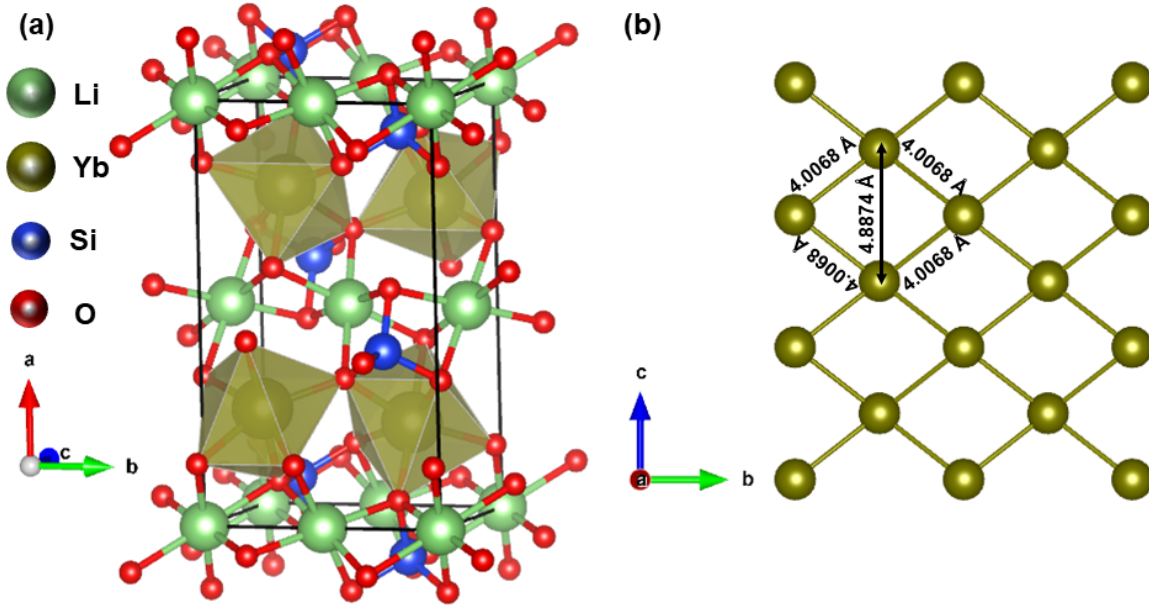


Figure 5.3: (a) Single unit cell of  $\text{LiYbSiO}_4$ . (b) Top view of the magnetic Yb sub-lattice in the  $bc$  plane.

The X-ray diffraction (XRD) and neutron powder diffraction (NPD) techniques have been employed to characterize the sample structurally at different temperatures. The simulated patterns, lattice parameters, and atomic coordinates obtained from the Rietveld refinement of the XRD and NPD data are shown in Fig. 5.1, Table 5.1, Table 5.2, Fig. 5.2, and Table 5.3.

These results reveal that  $\text{LiYbSiO}_4$  crystallizes into an orthorhombic space group ( $Pnma$ ), and there is no evidence of a structural phase transition down to 1.5 K. Analysis of the XRD and neutron data reveals the presence of a minute impurity phase of  $\text{Yb}_2\text{O}_3$  ( $\sim 1 \%$ ). Nevertheless, no magnetic peaks corresponding to  $\text{Yb}_2\text{O}_3$  ( $T_N = 2.3 \text{ K}$ ) have been observed in the NPD data. Furthermore, attempts to refine the structure by incorporating antisite disorder yielded no improvement in refinement, which confirms the absence of such disorder. The crystal structure of  $\text{LiYbSiO}_4$  consisting of well-separated planes of  $\text{Yb}^{3+}$  ions located on a rhombus sub-lattice (a distorted square lattice) in the  $bc$  plane is depicted in Fig. 5.3. The exchange interactions along the side ( $4.0068(1) \text{ \AA}$ ) and the short diagonal ( $4.8847(1) \text{ \AA}$ ) of the rhombus lattice may be comparable, suggesting that the spin sub-lattice can be effectively modeled using the  $J_1$ – $J_2$  framework. This configuration hints at a potential competition between these exchange interactions, suggesting the emergence of a novel quantum phase, as anticipated from various theoretical studies. [30–32].

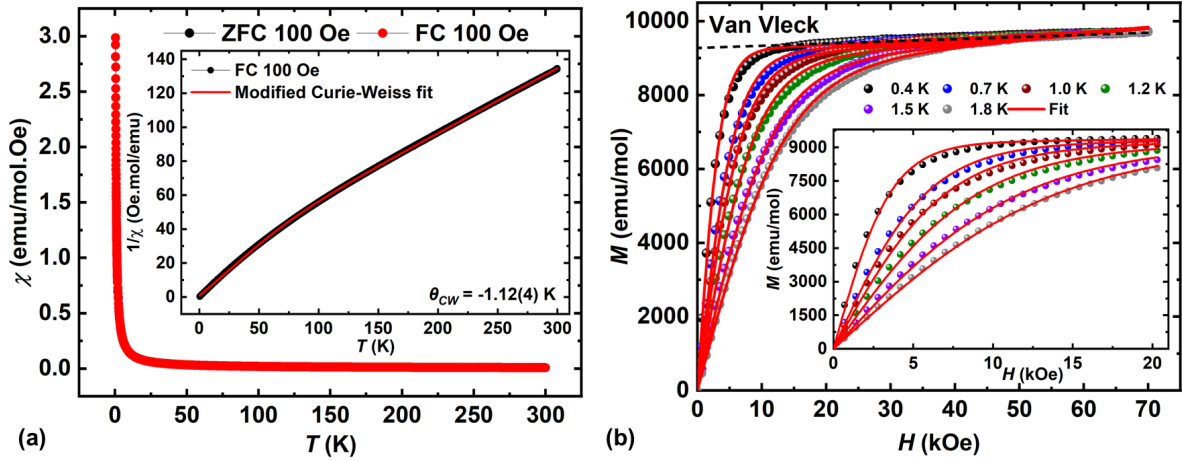


Figure 5.4: (a) Temperature dependence of dc magnetic susceptibility measured under ZFC and FC protocols down to 0.4 K. Inset shows fitting of the inverse susceptibility with the modified Curie-Weiss model. (b) Isothermal magnetization measured at different temperatures along with the Brillouin fits represented by solid lines. Black dashed line represents the Van Vleck contribution. Inset shows the zoomed version of the fitting in the low-field region.

### 5.3.2 DC Magnetization

To explore the low-temperature magnetism of the compound, zero-field-cooled (ZFC) and field-cooled (FC) dc susceptibility has been measured in zero-field-cooled (ZFC) and field-cooled (FC) modes down to 400 mK. Figure 5.4(a) depicts the temperature dependence of the dc susceptibility (Fig. 5.5(a) shows susceptibility measured with high fields), and the inset shows its low-temperature behavior. The susceptibility measurements show no evidence of any magnetic anomalies or magnetic ordering down to 400 mK. The inverse susceptibility data, after subtracting the Van Vleck contribution ( $\chi_{vv} = 6.65 \times 10^{-3}$  emu/mol, estimated from the slope of isothermal magnetization curves at higher magnetic fields), shows two linear behavior in two different temperature regions.

At higher temperatures,  $\text{Yb}^{3+}$  ions have  $J = 7/2$  ( $4f^{13}$ ) and hence an eightfold degenerate ground state. This degeneracy of  $\text{LiYbSiO}_4$  has been lifted by crystal electric field (CEF) effects, and the ground state can be described by  $J_{eff} = 1/2$ . Considering the CEF effects, the Curie constant will show a temperature dependence over the temperature range of the measurements as higher Kramers doublet will also contribute.



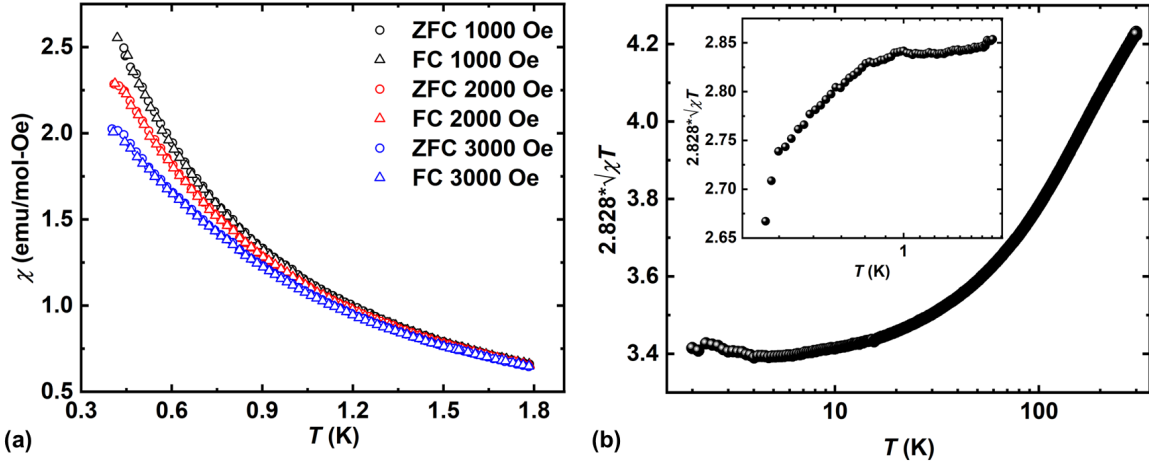


Figure 5.5: (a) Temperature dependence of the susceptibility measured in the presence of three different magnetic fields by following the ZFC and FC protocol. (b) Variation of effective moment  $\mu_{eff} = [(3k_B/N_A\mu_B^2)\chi T]^{1/2} \sim 2.828\sqrt{\chi T}$  versus  $T$ . Inset shows the variation below 8 K.

So, the Curie-Weiss model can be modified with a two-level approximation [33, 34]:

$$1/\chi = 8.(T - \theta_{CW}). \left( \frac{1 + \exp^{-\frac{E_{10}}{k_B T}}}{\mu_{eff,0}^2 + \mu_{eff,1}^2 \cdot \exp^{-\frac{E_{10}}{k_B T}}} \right) \quad (5.1)$$

where  $\mu_{eff,0}$  and  $\mu_{eff,1}$  give effective moments of the  $\text{Yb}^{3+}$  ions in the ground and the first excited states, and  $E_{10}$  represents the energy separation between these states. The result of fitting the inverse susceptibility data with the modified Curie-Weiss model (shown in the inset of Fig. 5.4(a)) gives parameters:  $\theta_{CW} = -1.12(4)$  K,  $\mu_{eff,0} = 3.62(2) \mu_B$  and  $\mu_{eff,1} = 5.34(3) \mu_B$ , and  $E_{10} = 241.4(7)$  K. The reduced value of effective moment in the ground state compared to the theoretically expected value ( $4.54 \mu_B$ ) and the separation of the ground state from the excited state confirm the ground state as a Kramers doublet with  $J_{eff} = 1/2$  [35–37]. Moreover, the effective moment  $\mu_{eff} = [(3k_B/N_A\mu_B^2)\chi T]^{1/2} \sim 2.828\sqrt{\chi T}$  attains a free ion value of around 300 K, as shown in Fig. 5.5(b). The effective moment decreases to a plateau in the temperature range of 10 to 1 K and then drops further below 1 K, suggesting the onset of magnetic correlations [38].

To understand the effect of magnetic field at low temperatures, we have performed isothermal magnetization measurements at different temperatures from 1.8 to 0.4 K. The magnetic field dependence of magnetization at various temperatures in the first quadrant is depicted in Fig. 5.4(b) (refer to Fig. 5.6(a) for the field dependence of magnetization in the units of  $\mu_B/\text{f.u.}$ ). For a paramagnetic state, the magnetic isotherms

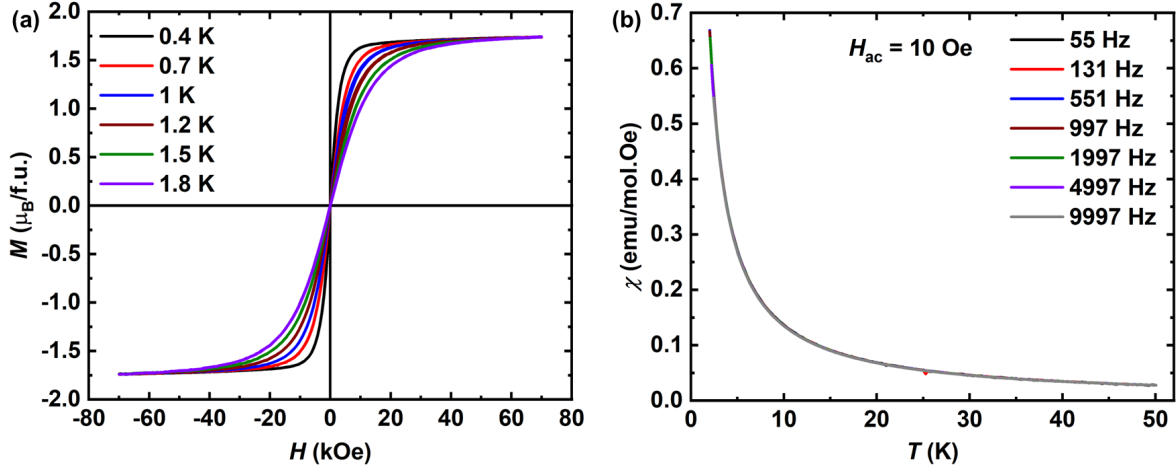


Figure 5.6: (a) Isothermal magnetization curves collected at various temperatures. (b) AC susceptibility measurements variation on applying a small ac magnetic field of 10 Oe at various frequencies.

can be modeled using  $M(H) = \chi_{\nu\nu}H + gJ_{eff}N_A\mu_B B_{J_{eff}}(H)$ , where  $B_{J_{eff}}(H)$  is the Brillouin function [39]. The solid line in Fig. 5.4(b) is its fit to the magnetization data, and its deviation from the data below 1 K, (seen in the inset of 5.4(b)), suggests the emergence of magnetic correlations [38, 40, 41]. The slope of the high-field (above 2 T) linear region of the magnetization curve at 0.4 K gives the Van-Vleck contribution, and its subtraction from the total magnetization gives a flat curve, indicating a polarized state. Furthermore, temperature-dependent ac susceptibility measurements were carried out to probe the response to a perturbation by a fixed ac magnetic field ( $H_{AC} = 10$  Oe) of different frequencies. The ac susceptibility curves overlap each other perfectly, as shown in Fig. 5.6(b) and rule out the presence of glassiness at least down to 2 K. Hence, these preliminary magnetic measurements reveal the development of magnetic correlations only below 1 K.

### 5.3.3 Heat Capacity

To probe the low-temperature thermodynamics, we have measured the temperature and magnetic field-dependent heat capacity of  $\text{LiYbSiO}_4$ . In Fig. 5.7(a), the data represents the heat capacity at zero magnetic fields, which has been fitted using the Debye-Einstein model. To calculate the change in magnetic entropy, it's necessary to subtract the lattice contribution from the total specific heat. This contribution can be estimated using the Debye-Einstein model, which assumes that the sum of acoustic and phonon modes equals the total number of atoms in the primitive cell (for  $\text{LiYbSiO}_4$ , there are 7 atoms).

Additionally, the model accounts for the relative weights of acoustic and optical modes, with the ratio being 1 to  $n-1$ , where  $n$  is the total number of atoms. For this compound, there are three acoustic modes and 18 optical phonon modes. The three acoustic modes are represented using one Debye term, while the optical modes are described using two Einstein terms. Several optical modes are grouped together to streamline the model and minimize experimental errors [42]. The Debye-Einstein model for this system can be expressed as follows [43, 44]:

$$C_{D-E} = \frac{9aR}{x_D^3} \int_0^{x_D} \frac{x^4 e^x}{(e^x - 1)^2} dx + 3R \sum_{i=1}^2 \frac{b_i x_{E_i}^2 e^{x_{E_i}}}{(e^{x_{E_i}} - 1)^2}$$

where  $x_{D,E} = \theta_{D,E}/T$ ;  $\theta_D$  and  $\theta_E$  are Debye and Einstein temperatures, respectively,  $R$  is the universal gas constant. The coefficients  $a$  and  $b_i$  represent the contributions from acoustic and optical phonons, respectively. These weight factors are constrained so that their sum equals the total number of atoms in the unit cell. For example, in this case,  $a$  equals 1,  $b_1$  equals 2, and  $b_2$  equals 4. Specifically,  $b_1$  corresponds to the vibrations of  $\text{Si}^{4+}$  and one  $\text{O}^{2-}$ , while  $b_2$  stands for the motions of  $\text{Li}^+$  and three  $\text{O}^{2-}$ . We could confine the flexible Debye-Einstein model to a physically reasonable fit by adhering to these constraints.

The magnetic entropy, calculated after subtracting the lattice contribution, is depicted in Fig. 5.7(b). A comparison with the entropy for a two-level system (with effective spin  $J_{eff} = 1/2$ ) reveals that approximately 92% of the magnetic entropy remains in the system below 2 K. The inset of Fig. 5.7(b) shows the temperature dependence of the magnetic entropy under various magnetic fields. As the magnetic field increases, the saturation magnetic entropy continues to rise, reaching a value of 5.43 J/mol-K, which is approximately 94% of  $R \ln 2$ , further complementing the  $J_{eff} = 1/2$  ground state.

Figure 5.8 illustrates the impact of the magnetic field on the anomaly observed at lower temperatures, which shifts towards higher temperatures as the applied magnetic field increases, indicating the presence of a Schottky anomaly. This anomaly arises from the splitting of the ground state Kramers doublet upon the application of an external magnetic field (known as Zeeman splitting), a phenomenon observed in other Yb compounds as well [40, 45]. The magnetic field dependence of the total heat capacity can be expressed as  $C(T, H) = C(T, 0) + C_{sch}(T, H)$ . Consequently, the Schottky contribution at different magnetic fields can be isolated by subtracting the zero-field data from the data obtained at the respective magnetic fields. For a two-level system ( $J_{eff} = 1/2$ ),

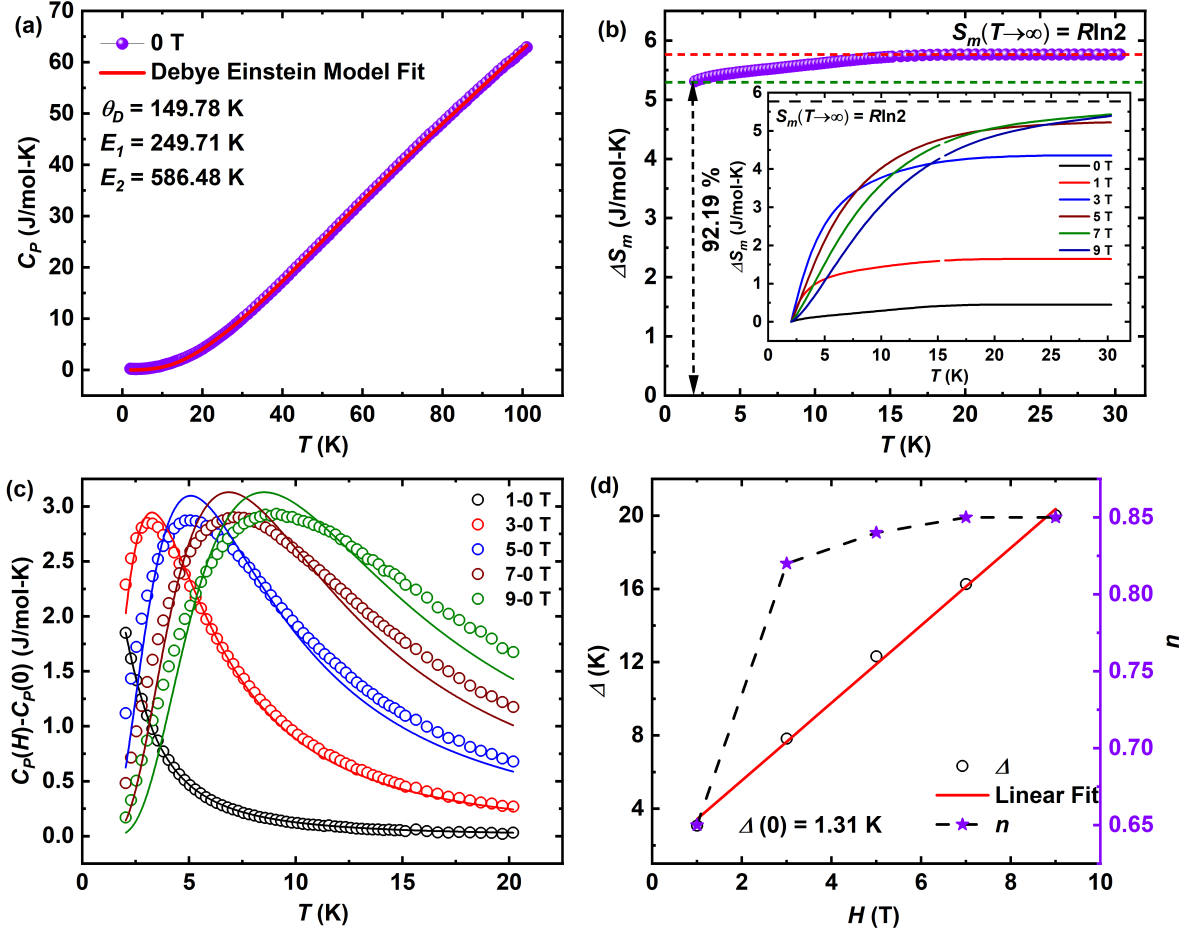


Figure 5.7: (a) Fitting of the heat capacity data measured in the absence of the magnetic field with the Debye-Einstein model. (b) Entropy calculated from magnetic heat capacity. To better observe the residual magnetic entropy, the  $S_{mag}(T)$  curve is shifted vertically so that its maxima coincide with the  $S_{mag}(T \rightarrow \infty)$ . Inset shows the temperature dependence of magnetic entropy in the presence of different magnetic fields. (c) Variation of Schottky contribution with temperature and its fitting with the two-level model equation. (d) Linear fitting of  $\Delta$  (left axis) values calculated from the CEF fitting and variation of  $n$  values with the magnetic fields.

Schottky contribution can be written as [46–48],

$$C_{sch}(T, H) = nR \left( \frac{\Delta}{T^2} \right) \frac{\exp(\Delta/T)}{[1 + \exp(\Delta/T)]^2} \quad (5.2)$$

where  $n$  denotes the fraction of spins excited to the higher levels,  $R$  is the universal gas constant, and  $\Delta$  stands for the spacing between two levels.  $\Delta$  has a linear dependence on the effective magnetic field experienced by the compound as  $\Delta(H) = g\mu_B H_{eff}/k_B$ ,

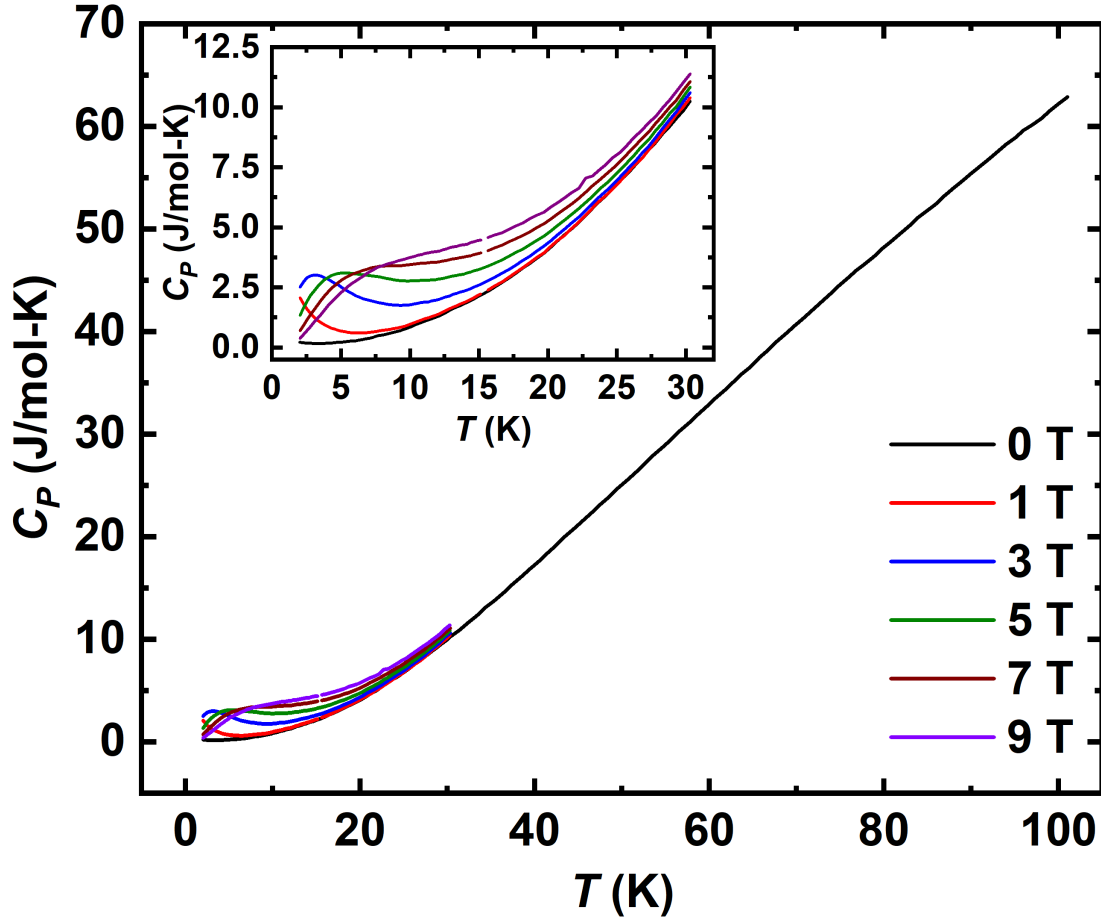


Figure 5.8: Magnetic field dependence of Specific Heat from 2 to 100 K. Inset shows the variation below 30 K.

where  $H_{eff} = \sqrt{H_0^2 + H_1^2}$  such that  $H_{eff} = H_0$  when there is no external magnetic field ( $H_1 = 0$ ). The fitting of the Schottky contribution has been shown in 5.7 (c), and the inclusion of more than two levels is required to get a proper fit for  $H > 3$  T. The magnetic field dependence of  $\Delta$  and  $n$  is shown in Fig. 5.7 (d). The linear fitting of  $\Delta$  variation results in  $\Delta(0) \sim 1.31$  K. A finite value of  $\Delta(0)$  indicates presence of an internal magnetic field originating from  $\text{Yb}^{3+} - \text{Yb}^{3+}$  interactions. The fraction of spins excited to higher levels ( $n$ ) becomes constant ( $\sim 0.85$ ) above 5 T. Thus, although no long-range magnetic ordering has been observed down to 2 K, a Schottky anomaly is observed at low temperatures for fields  $> 1$  T. Analysis of the Schottky anomaly reveals the correlations to be of the order of 1 K among  $\text{Yb}^{3+}$  spins.

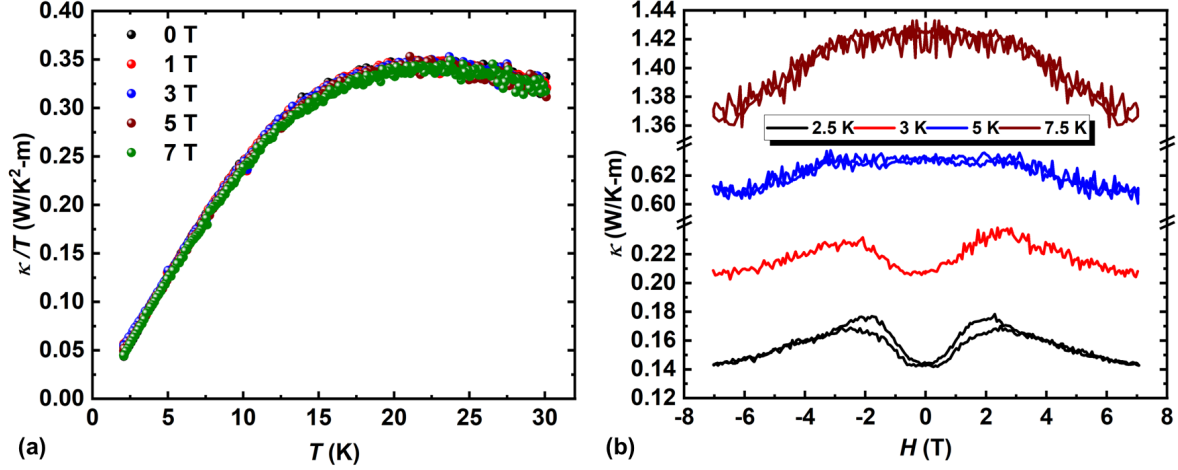


Figure 5.9: (a) Variation of thermal conductivity with temperature measured in the presence of various applied magnetic fields. (b) Magnetothermal conductivity measured at four different temperatures.

Table 5.4: Magnetic field dependence of  $a$  and  $\alpha$  parameter

$H$ (T)	$a$ ( $\text{W/K}^2\text{-m}$ )	$\alpha$
0	0.000	2.16(1)
1	0.036(2)	2.78(9)
3	0.012(6)	2.14(9)
5	0.000	2.07(1)
7	0.000	2.13(1)

### 5.3.4 Thermal Conductivity

To avoid the Schottky anomaly, thermal conductivity measurements that are not sensitive to localized entities responsible for the Schottky anomaly but rather to the itinerant excitation [49] were performed. We have carried out thermal conductivity measurements from 30 to 2.5 K with various applied fields up to 7 T, as shown in Fig. 5.9(a). We fit the field dependent  $\kappa/T$  data with  $\kappa/T = a + bT^{\alpha-1}$ , where the first term represents the electron-like contribution (for insulators, it should be zero) and the second term is responsible for the phononic contribution. The first term ( $a$ ) is found to be very small, as tabulated in Table 5.4, which means the magnetic excitations do not persist up to 2.5 K and get destroyed due to increased thermal energy. Intriguingly, we observe a broad anomaly in the isothermal thermal conductivity measurements, shown in Fig. 5.9(b), up to 3 K. These anomalies represent a transition to a polarized state for  $H > 3$  T [50], as observed in the  $M$  vs.  $H$  measurements.

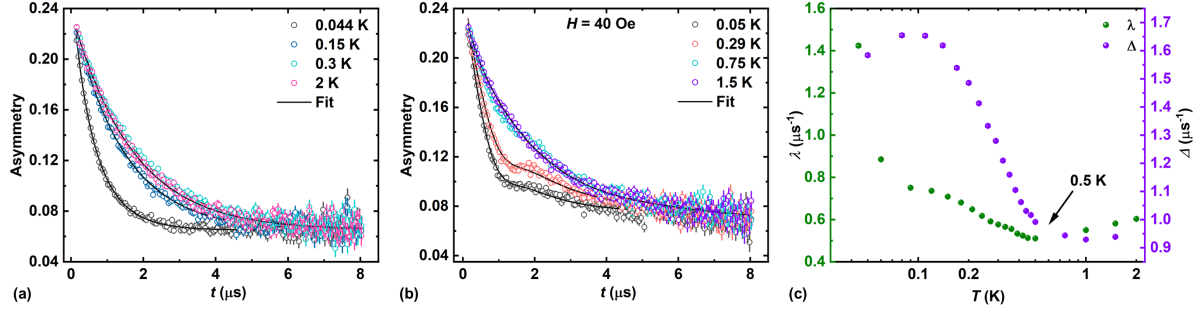


Figure 5.10: (a) Zero field  $\mu$ SR spectra collected at different temperatures. Solid lines represent fits with simple exponential function. (b) Longitudinal field  $\mu$ SR spectra collected in the presence of a 40 Oe magnetic field at various temperatures and solid lines represent their fitting with the dynamic Kubo-Toyabe function. (c) Evolution of the relaxation rate ( $\lambda$ ) (left axis) and parameter  $\Delta$  (right axis) with temperature.

### 5.3.5 Muon Spin Relaxation ( $\mu$ SR) Measurements

#### 5.3.5.1 Zero Field (ZF) $\mu$ SR Measurements

To gain further insight into the low-temperature spin-dynamics present in the compound, ZF  $\mu$ SR measurements have been performed in the temperature range of 0.044 to 2 K. Neither oscillations in the muon signal, nor loss of initial asymmetry, have been observed down to 44 mK as can be seen from the data presented in Fig. 5.10(a), which confirms the absence of static magnetism. Qualitatively, the asymmetry depolarization increases with a decrease in temperature, which indicates a broadening in the local field distribution at lower temperatures. Also, the background of these curves (asymmetry value at longer times) is significantly lower than  $1/3^{rd}$  of the initial asymmetry, which rules out the presence of magnetically frozen states such as spin glass [51].

We have used a single exponential function to analyze the ZF data, which can be written as:

$$A(t) = A_{bg} + A_1 \cdot \exp(-\lambda t) \quad (5.3)$$

where  $A_{bg}$  represents the contribution from the muons stopping in the sample holder,  $A_1$  stands for the muons stopping in the sample, and  $\lambda$  represents the muon relaxation rate.  $A_{bg}$  and  $A_1$  are kept constant at 0.065 and 0.174, respectively, during the fitting. The temperature dependence of relaxation rate ( $\lambda$ ) precisely tracks the onset of the magnetic correlations between the  $\text{Yb}^{3+}$  pseudospins. Above 0.5 K, the value of  $\lambda$  is smaller and has little temperature dependence. While below 0.5 K,  $\lambda$  starts increasing, indicating the emergence of a dynamic state. Generally, a plateau in  $\lambda$  versus  $T$  is observed at lower



temperatures for spin liquid candidates [52, 53], which is absent in this case. However, in this material, it is possible the plateau would form at a temperature lower than what could be achieved during our measurements.

### 5.3.5.2 Longitudinal Field (LF) $\mu$ SR Measurements

To explore the effect of a constant external magnetic field on the  $\text{Yb}^{3+}$ - $\text{Yb}^{3+}$  correlations, we have performed temperature-dependent longitudinal field  $\mu$ SR measurements under an applied field of 40 Oe, as depicted in Fig. 5.10(b). Application of such a small magnetic field induces an anomaly in the spectra, mimicking Kubo Toyabe behavior. We have used the dynamic Kubo Toyabe function to analyze the data, which describes the field dependence of the asymmetry as follows:

$$A(t) = A_{bg} + g_z(t) + \nu \int_0^t g_z(\tau) G_z(t - \tau) d\tau \quad (5.4)$$

where  $g_z(t)$  is the static Kubo-Toyabe function,  $A_{bg}$  is the background, and  $\nu$  is the spin fluctuating rate. During the fitting, the background is fixed at 0.065 (similar to the ZF measurements), and initial asymmetry is kept constant for individual measurements. In the presence of a finite longitudinal magnetic field,  $B_0 = \omega_0/\gamma_\mu$ ;  $g_z(t)$  has been expressed as

$$g_z(t) = A \left[ 1 - 2 \frac{\Delta^2}{\omega_0^2} (1 - \cos(\omega_0 t) e^{-\Delta^2 t^2/2}) + 2 \frac{\Delta^4}{\omega_0^4} \omega_0 \int_0^t \sin(\omega_0 \tau) e^{-\Delta^2 \tau^2/2} d\tau \right] \quad (5.5)$$

For  $B_0 = 0$ , it can further be simplified as

$$g_z(t) = A \left[ \frac{1}{3} + \frac{2}{3} (1 - \Delta^2 t^2) e^{-\Delta^2 t^2/2} \right] \quad (5.6)$$

Here,  $\Delta$  represents the width of the local field distribution.

We got the best spectra fit by fixing the field to half of the applied value, as marked by the solid lines in Fig. 5.10(b). The temperature dependence of  $\Delta$ , a fitting parameter from the dynamic Kubo-Toyabe function, which represents the local field distribution, is shown in Fig. 5.10(c). While the temperature dependence of the ZF and LF data fitting parameters ( $\lambda$  and  $\Delta$ ) have strong similarities, with a growth in the relaxation rate below 0.5K, the form of the raw data is quite distinct and unusual. The Kubo-Toyabe-like relaxation in the LF data seems to represent the formation of a disordered magnetic state in an applied field that is not present in the zero field. Spin liquids are known to be unstable with respect to magnetic ordering in applied magnetic fields [54, 55].



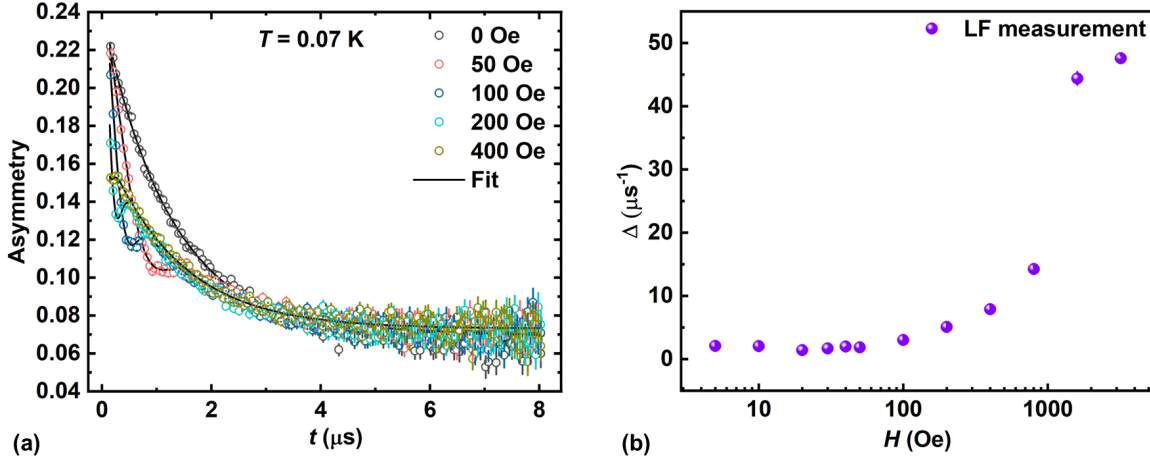


Figure 5.11: (a) Longitudinal  $\mu$ SR spectra measured at 70 mK by varying the longitudinal fields from 0 to 400 Oe. The solid lines depict fitting with the dynamic Kubo-Toyabe function. (b) Field dependence of  $\Delta$ .

To check the stability of the dynamic state in the presence of higher magnetic fields, we have carried out longitudinal field-dependent  $\mu$ SR measurements at 70 mK by applying various magnetic fields up to 3200 Oe, as shown in Fig. 5.11(a). Applying the longitudinal field can minimize the muon spin depolarization, which may arise from weaker local static fields. Weak and randomly oriented static fields are typical due to nuclear dipole moments. However, depolarization due to fast fluctuating local fields arising from atomic spins may be affected by much larger applied fields [51]. As probed in temperature-dependent LF measurements, even a small magnetic field ( $H > 40$  Oe) can induce a Kubo Toyabe anomaly in the spectra. The muon depolarization observed at shorter times becomes faster with an increase in magnetic field, and the Kubo-Toyabe anomaly becomes undetectable for  $H > 400$  Oe.

Field dependent LF  $\mu$ SR data have also been analyzed using the dynamic Kubo Toyabe function.  $\Delta$  increases rapidly above 50 Oe (refer to Fig. 5.11(b)), a similar form of the LF data has previously been observed in Pr-based pyrochlores and attributed to hyperfine-enhanced nuclear magnetism [56, 57].  $\text{Pr}^{3+}$  ions are non-Kramers ions with a non-magnetic doublet as a ground state, which split through the local distortions caused by the implanted muons, resulting in enhanced nuclear magnetic moment. However,  $\text{Yb}^{3+}$  ions have a magnetic Kramers doublet as the ground state, and muon-induced distortions should have a minimal effect. Hence, for  $\text{LiYbSiO}_4$ , growth of the  $\Delta$  parameter suggests that the disordered magnetic state is strengthening with increasing applied field, similar to the much weaker effect seen in the  $\kappa$ -(BEDT-TTF) $_2\text{Cu}_2(\text{CN})_3$  spin-liquid [58].

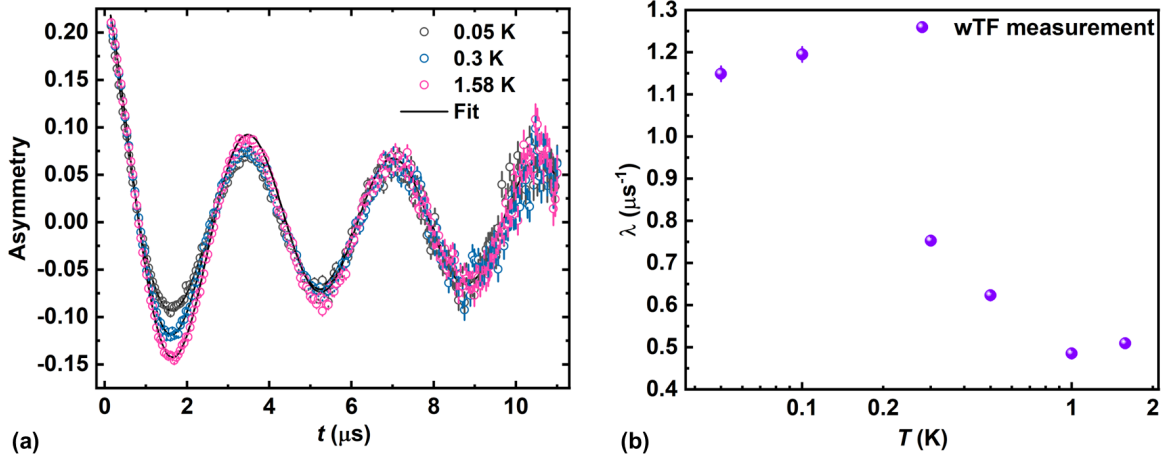


Figure 5.12: (a) Time dependence of  $\mu^+$  asymmetry in a weak transverse magnetic field 20 Oe at three different temperatures. The solid line depicts a fitting with equation 7.5. (b) Change in the relaxation rate with temperature.

### 5.3.5.3 Weak Transverse Field (WTF) $\mu\text{SR}$ Measurements

Furthermore, the weak transverse field (wTF)  $\mu\text{SR}$  measurements show direct evidence of the absence of long-range magnetic ordering. Figure 5.12(a) shows wTF measurements at different temperatures ranging from 50 mK to 1.58 K under the application of a weak transverse field of 20 Oe. The solid lines are fit to the data using a combination of two exponentially decaying oscillatory functions, as described by the following equation:

$$A(t) = A_1 \cdot e^{-\lambda_1 t} \cos(2\pi f_1 t + \phi_1) + A_2 \cdot e^{-\lambda_2 t} \cos(2\pi f_2 t + \phi_2) \quad (5.7)$$

We have taken the first exponentially decaying oscillatory function as a background to address the contribution from the sample holder.  $f_i$  represents the muon precession frequency while  $\lambda_i$  is relaxation rate,  $\phi_i$  denotes phase difference.

In this measurement, the local magnetic field experienced by muons is the sum of the applied and internal magnetic fields. For example, in a magnetically ordered system, the internal magnetic field is a few hundred Oe and significantly exceeds the applied transverse field. In the present case, the muon asymmetry oscillates at 279.5 kHz, corresponding to the expected muon precession frequency in an applied transverse field of 20 Oe (as  $\nu_{wTF} = \gamma_\mu B_{wTF}/2\pi$ , and  $\gamma_\mu/2\pi = 135.5 \text{ MHz/T}$ , hence  $\nu_{wTF} \sim 271 \text{ kHz}$ ). Thus, there is no static magnetic field in  $\text{LiYbSiO}_4$ . Moreover, the relaxation rates become constant at low temperatures and then reduce to  $0.5 \mu\text{s}^{-1}$  at higher temperatures, as depicted in Fig. 5.12(b). This behavior complements the observation of ZF and LF measurements.

### 5.3.6 Theoretical Calculation

Experimental observations here indicate the presence of a magnetically dynamic state in the temperature range of 0.4 K to 44 mK, which motivated us to determine the exchange interactions.

#### 5.3.6.1 Computation Details

The first-principles calculations in this work are based on the quantum mechanical density functional theory as implemented in the VASP [59–61]. The interaction between valence electrons and ionic cores is represented using PAW (projector augmented wave) potential [62]. The electronic exchange-correlation-energy functional is approximated by a generalized gradient approximation within a modified Perdew-Burke-Ernzerhof (PBE) parametrization [63] for solids (PBEsol) [64]. In the PAW potentials, the following valence electronic configurations are considered: Li:  $1s^2 2s^1$ , Yb:  $4f^{14} 5s^2 6s^2 5p^6$  Si:  $3s^2 3p^2$  and O:  $2s^2 2p^4$ . Note for Yb,  $f$  electrons are considered in the valence shell. To capture the localization of the electrons in the  $f$  orbitals, we have used Hubbard- $U = 3.0$  eV at the  $f$ -orbitals of Yb, using a rotationally invariant scheme as implemented in VASP [65]. The Brillouin-zone integrations are performed in a uniform gamma-centered mesh of  $3 \times 5 \times 7$  k-points. The Kohn-Sham (KS) wave functions are expanded in a plane wave basis set, which is truncated at an energy cutoff of 650 eV. The numerical solution of the KS equation is obtained iteratively until the total energy/cell is converged within  $10^{-8}$  eV/cell. To aid the convergence occupation of the electrons in the frontier states are smeared using a Gaussian function of width 0.05 eV. The structures are relaxed until the forces on each atom in all the directions are less than  $10^{-3}$  eV/Å and each component of the stress tensor is less than 0.2 GPa. We have used VESTA [66] for visualization of structure and charge density and XCrySDen [67] for visualization of the Brillouin zone, high symmetry path.

#### 5.3.6.2 Ground State Structure

We simulated  $\text{LiYbSiO}_4$  (LYSO) in an orthorhombic  $Pnma$  crystal structure, which is the structure obtained in the experiments at ambient conditions. The structure has four formula units (f.u.) per primitive unit cell. The structure is formed by layers of  $\text{SiO}_4$  tetrahedra and  $\text{LiO}_6$  octahedra stacked along the  $a$  direction. The Yb atoms are situated in the space between two such layers; see Figure 5.13. What is more interesting is that Yb atoms are forming an approximate square net network (see Figure 5.13 (c)-(d)),

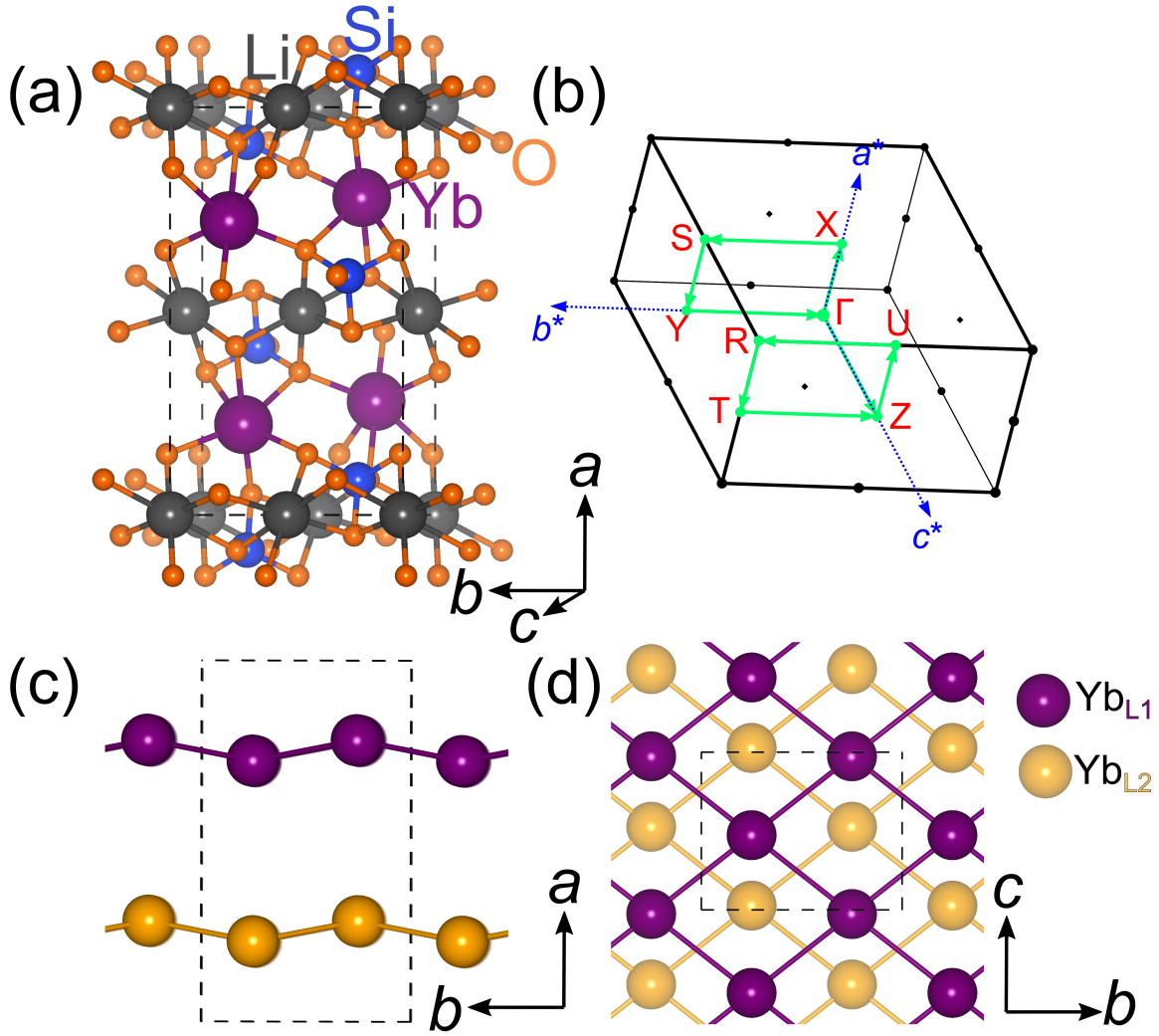


Figure 5.13: (a) Crystal structure of orthorhombic ( $Pnma$ )  $\text{LiYbSiO}_4$ , (b) shows Brillouin zone and high-symmetry path. (c) and (d) show the arrangement of Yb atoms in the structure from the side and top directions, respectively. Note that the Yb atoms form a 2D square network, stacked along  $a$  direction. Yb atoms from different layers are shown in different colors and all the other atoms are removed in (c)–(d) for clarity.

and such networks are stacked along the  $a$  direction. Our optimized (without SOC, non-spin polarized) lattice parameters are ( $a = 10.81 \text{ \AA}$ ,  $b = 6.24 \text{ \AA}$ , and  $c = 4.87 \text{ \AA}$ ) within  $\pm 0.5\%$  w.r.t. those obtained in the experiments ( $a_{\text{Expt.}} = 10.75 \text{ \AA}$ ,  $b_{\text{Expt.}} = 6.25 \text{ \AA}$ , and  $c_{\text{Expt.}} = 4.90 \text{ \AA}$ ). Calculated non-spin polarized electronic structure and orbital projected density of states reveal LYSO is a metal (see Figure 5.14 (a)–(b)); in contrast, experimentally, it is found to be an insulator. Moreover, the PDOS reveals states near Fermi energy are dominated by Yb  $4f$  and O  $2p$  orbitals. The  $4f$  electrons of Yb are

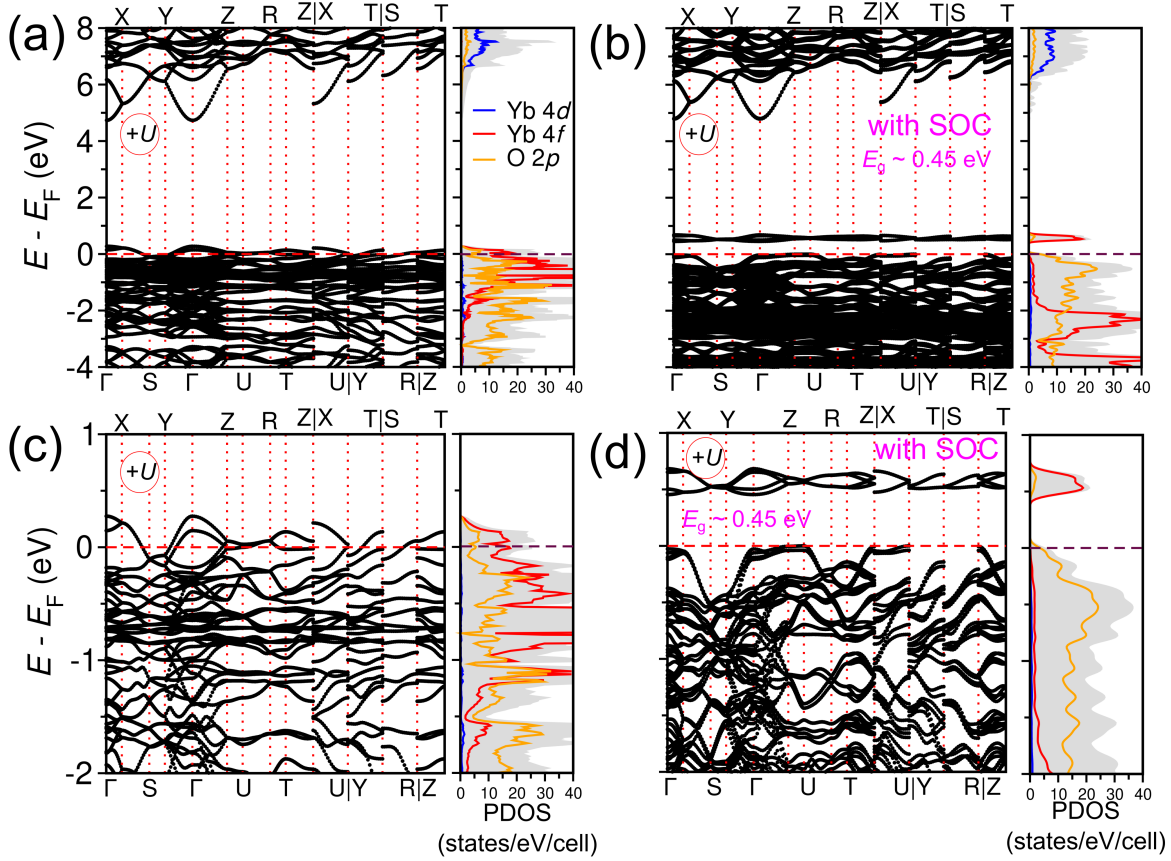


Figure 5.14: (a) The electronic structure and orbital projected density of states (PDOS) of LiYbSiO<sub>4</sub> (LYSO), which reveals LYSO is a metal. (c) shows the same in a zoomed view, which reveals that states at the Fermi level are dominated by Yb-4*f* and O-2*p* orbitals. (b) displays the same with spin-orbit coupling, which opens a band gap of 0.45 eV. The zoomed view in (d) reveals that the states near the valence band are primarily dominated by O-2*p* orbitals. In contrast, those near flat conduction bands are constituted by highly localized 4*f* orbitals of Yb atoms.

highly localized and exhibit flat bands and sharp peaks in the PDOS.

A high atomic number ( $Z$ ) of Yb indicates that spin-orbit coupling (SOC) is crucial for LYSO. Hence, we fixed the structure to the one optimized without SOC and turned on SOC to determine the electronic ground state. The calculated electronic structure and PDOS of LYSO with SOC are shown in Figure 5.14 (c)-(d), which shows a band gap opening of 0.45 eV. Furthermore, the PDOS reveals states near valence band maximum (VBM) and conduction band minimum (CBM) are dominated by O 2*p* and Yb 4*f* orbitals, respectively. Moreover, our calculation unveils that with SOC, significant forces are appearing on the atoms of LYSO; this indicates the presence of spin-optical phonon

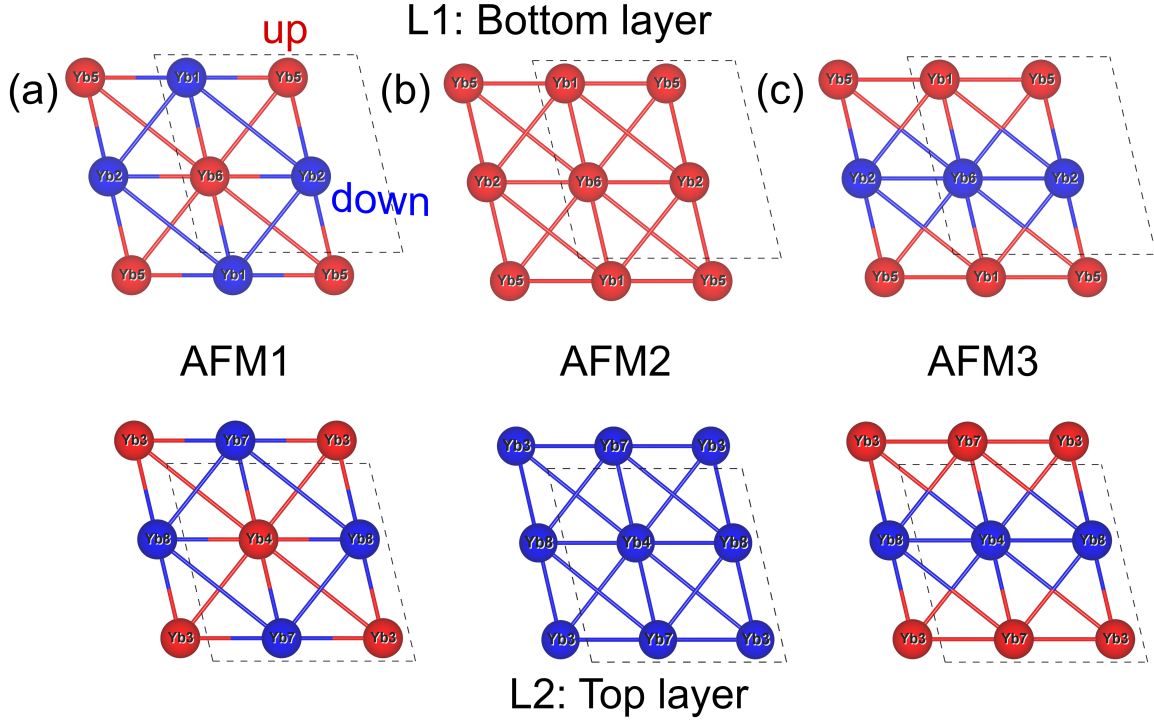


Figure 5.15: Bottom and top layers of three antiferromagnetic ordering considered for exchange coupling calculations (a) Neel antiferromagnet, (b) A-type antiferromagnet, and (c) Columnar antiferromagnet.

coupling in the material, which we have not explored in this work.

### 5.3.6.3 Magnetic Ground State and Exchange Couplings

We performed spin-polarized calculations with four different magnetic configurations. First, we consider a ferromagnetic configuration of the spins at Yb atoms and fully optimize the structure because we find significant forces on atoms in FM configuration in the self-consistent spin-polarized calculation. We find that the  $a$  and  $b$  lattice parameters diminish w.r.t. those obtained in spin-unpolarized calculations by 1% and 0.2%, respectively, but the  $c$  parameter remains unchanged. However, all the parameters remain within DFT error bar w.r.t. those of the experiments. The shrink in the lattice parameters is possibly due to change in the ionic radius of the magnetic Yb atoms. Next, we fix the structure to that obtained from optimized FM configuration and construct a  $1 \times \sqrt{2} \times \sqrt{2}$  supercell and consider various anti-ferromagnetic orders to determine magnetic exchange parameters. Note, as forces on the atoms and stress in the unit cell



Table 5.5: Table compares the relative energies of the various orders of the spins in the L1 and L2 layers of the  $1 \times \sqrt{2} \times \sqrt{2}$  supercell of LYSO. It reveals the the lowest energy configuration of spins is AFM3

Order	L1				L2				$E - E_{\text{Ref}}$ (meV/cell)
	1	2	5	6	3	4	7	8	
FM	u	u	u	u	u	u	u	u	0.00
AFM1	d	d	u	u	u	u	d	d	-30.88
AFM2	u	u	u	u	d	d	d	d	-0.19
AFM3	u	d	u	d	u	d	u	d	-31.88

remain insignificant with change in magnetic ordering, we do not perform structural relaxation (structure kept fixed to that of relaxed FM).

We consider three non-equivalent anti-ferro magnetic orders: (a) AFM1: all the in-plane spins are arranged in a Neel type of order, (b) in AFM2 configuration alternate layers of up and down spins stacked along  $a$ , (c) AFM3: in-plane, spins are forming stripes of up and down spins running along  $c$  direction; in all the cases, alternate layers of magnetic spins are stacked along  $a$  direction and shifted from each other by  $\mathbf{s} = (0, 0.25, 0.25)$ , as depicted in Fig. 5.15. The energy of all the magnetic configurations is tabulated in Table 5.5, which reveals that AFM3 is the ground state configuration of the spins. In AFM3 configuration, the magnitude of spin in each Yb atom is  $0.86 \mu_B$ , and the O atoms close to Yb atoms have spin moments  $0.02$ – $0.03 \mu_B$ . This is also reflected in the visualization of spin density in Figure 5.16.

Nevertheless, we have not considered spin-orbit coupling in the spin-polarized calculations because (a) SOC significantly increases the computation cost specifically for  $1 \times \sqrt{2} \times \sqrt{2}$  cell which contains eight f.u. (eight Yb atoms), (b) the convergence of the scf loop with SOC is very tricky; even if it converges, the electronic ground is not robust w.r.t. the algorithms used. All these indicate a separate dedicated study is required for studying the role of SOC in LYSO.

To determine the magnetic exchange couplings ( $J$ s), first, we map the low energy spectrum of the system on a Heisenberg-like Hamiltonian as follows:

$$\mathcal{H} = E_0 + J_1 \sum_{\langle ij \rangle, in} \mathbf{S}_i \cdot \mathbf{S}_j + J_2 \sum_{\langle\langle ik \rangle\rangle, in} \mathbf{S}_i \cdot \mathbf{S}_k + J_3 \sum_{\langle il \rangle, out} \mathbf{S}_i \cdot \mathbf{S}_l, \quad (5.8)$$

where  $E_0$ ,  $S$ ,  $J_1$ ,  $J_2$  and  $J_3$  represent constant energy, spin, nearest neighbor (in-plane), next nearest neighbor (in-plane), and nearest neighbor (out-of-plane) magnetic exchange

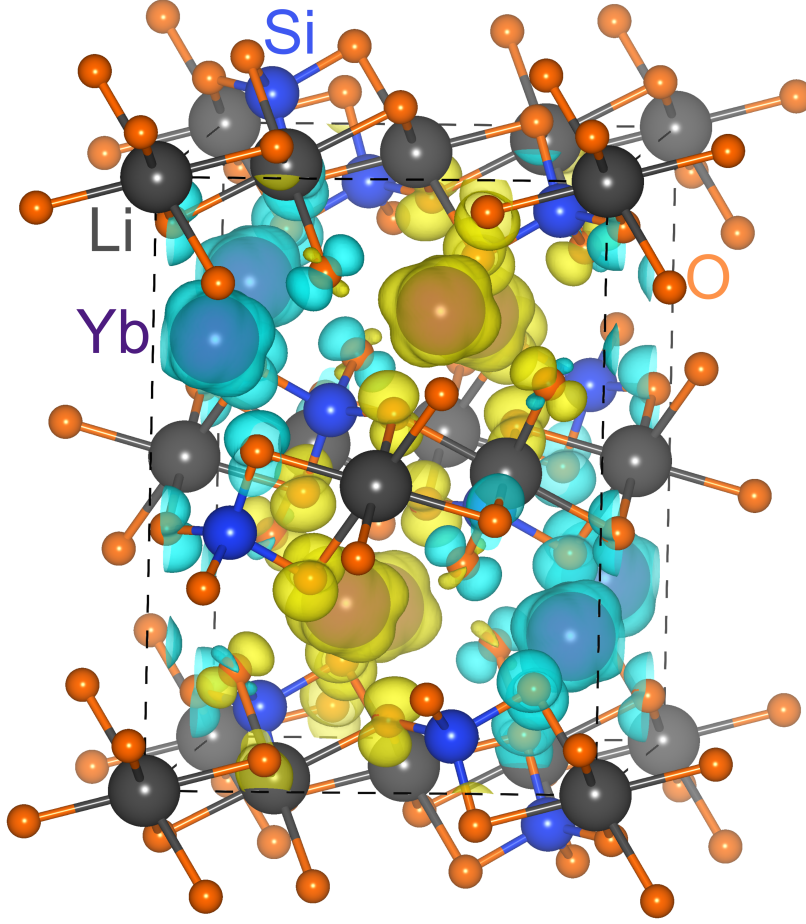


Figure 5.16: Visualization of the spin density of the AFM3 configuration of LYSO reveals that the magnetization is concentrated on Yb sites and O (nearby Yb) atoms also carry significant moment. This indicates the magnetic exchange interaction is happening through oxygen  $p$ -orbitals. The yellow color denotes positive magnetization, and cyan denotes negative.

couplings, respectively (see Fig. 5.17(a)). Next, we write energies of the magnetic configurations in terms of this model:

$$E_{\text{FM}} = E_0 + (4J_1 + 4J_2 + 8J_3)S^2 \quad (5.9a)$$

$$E_{\text{AFM1}} = E_0 + (-4J_1 + 4J_2)S^2 \quad (5.9b)$$

$$E_{\text{AFM2}} = E_0 + (4J_1 + 4J_2 - 8J_3)S^2 \quad (5.9c)$$

$$E_{\text{AFM3}} = E_0 + (-4J_2)S^2 \quad (5.9d)$$

Coefficients of the terms with exchange coupling constants  $J_i$ 's denote the number of



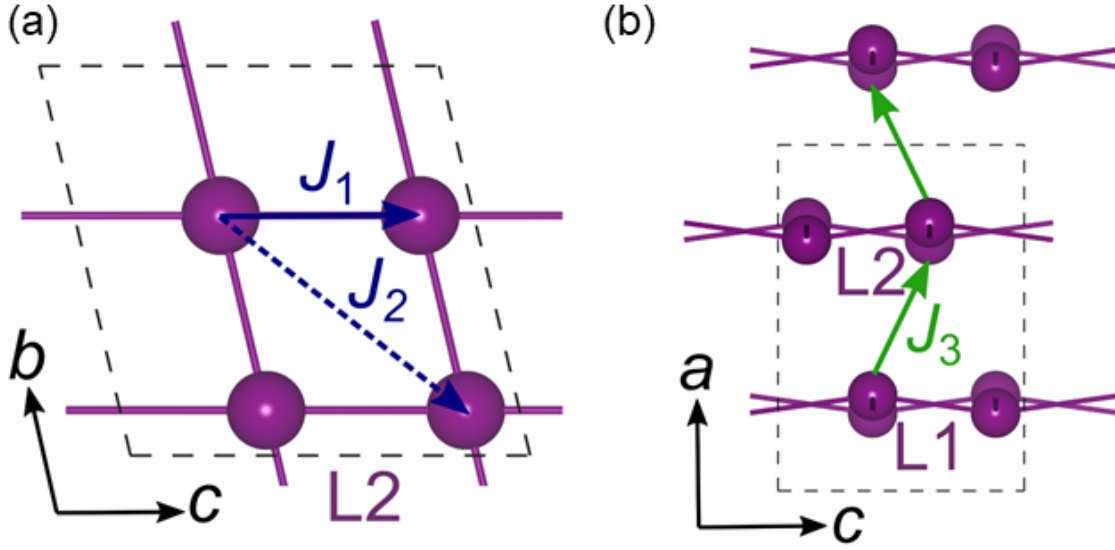


Figure 5.17: (a) Exchange interactions in the Yb atomic sub-lattice in the  $bc$  plane,  $J_1$ , and  $J_2$  representing nearest and next nearest coupling and (b) out-of-the plane exchange interaction  $J_3$  along  $a$ -axis.

coupled neighbors (as illustrated in Fig. 5.17). We solve these equations (5.9a–d) using the energies obtained using DFT and estimate values of  $J_i$ 's, which are tabulated in Table 5.6.

### 5.3.7 Origin of Dynamic State

The calculated magnetic exchange parameters are anti-ferromagnetic in nature. The out-of-plane exchange coupling ( $J_3$ ) nearly vanishes and is  $10^2$  times weaker than the in-plane  $J_1$  and  $J_2$  couplings (see Table 5.6); thus, magnetic interactions are quasi-two-dimensional in nature. Moreover, the energy difference between AFM1 (Neel) and AFM3 (Columnar) is very small (within the DFT error bar), as tabulated in Table 5.5, suggesting a degenerate ground state and frustration in spins. Furthermore, the in-plane coupling constants ( $J_1$  and  $J_2$ ) are comparable, and  $J_2/J_1$  is 0.53, which means that spins experience frustration, which is in line with the prediction made in various theoretical calculations on a square lattice [30–32].

Table 5.6: Estimated exchange couplings show that the in-plane couplings  $J_1$  and  $J_2$  are 384 and 205 times, respectively w.r.t.  $J_3$  coupling.

Exch. coupling	meV/bond
$J_1$	3.84
$J_2$	2.05
$J_3$	0.01

## 5.4 Conclusion

In conclusion, we propose  $\text{LiYbSiO}_4$  as a promising square-lattice-based quantum spin-liquid. To the best of our knowledge, it is the first disorder-free two-dimensional magnet exhibiting such properties due to competition among  $J_1$  and  $J_2$ . Magnetization and thermodynamic measurements estimate magnetic interactions of the order of 1 K. ZF  $\mu\text{SR}$  measurements complement these results and unveil the magnetic correlations emerging below 0.5 K. Application of a magnetic field drives the dynamic state to a disordered state having a broad distribution of local fields. The possibility of a local static field is conclusively ruled out by the WTF measurements. The origin of such a state lies in the competition between  $J_1$  and  $J_2$  interactions, with  $J_2/J_1 = 0.53$ , agreeing very well with the earlier predictions. Hence, a combination of macroscopic data, a sensitive local probe, and theoretical calculations indicate  $\text{LiYbSiO}_4$  as a candidate for disorder-free quantum spin liquid. These findings open up new possibilities for exploring quantum spin liquids in previously uncharted family of compounds.

# Bibliography

- [1] G. Shirane, Y. Endoh, R. J. Birgeneau, M. A. Kastner, Y. Hidaka, M. Oda, M. Suzuki, and T. Murakami, Two-dimensional antiferromagnetic quantum spin-fluid state in  $\text{La}_2\text{CuO}_4$ , Phys. Rev. Lett. **59**, 1613 (1987).
- [2] J. D. Reger and A. P. Young, Monte Carlo simulations of the spin-(1/2 Heisenberg antiferromagnet on a square lattice, Phys. Rev. B **37**, 5978 (1988).
- [3] R. J. Birgeneau, M. Greven, M. A. Kastner, Y. S. Lee, B. O. Wells, Y. Endoh, K. Yamada, and G. Shirane, Instantaneous spin correlations in  $\text{La}_2\text{CuO}_4$ , Phys. Rev. B **59**, 13788 (1999).
- [4] R. Coldea, S. M. Hayden, G. Aeppli, T. G. Perring, C. D. Frost, T. E. Mason, S.-W. Cheong, and Z. Fisk, Spin Waves and Electronic Interactions in  $\text{La}_2\text{CuO}_4$ , Phys. Rev. Lett. **86**, 5377 (2001).
- [5] C. Lacroix, P. Mendels, and F. Mila, eds., *Introduction to Frustrated Magnetism: Materials, Experiments, Theory* (Springer Series in Solid-State Sciences), 2011th ed. (Springer, 2011).
- [6] M. Greven, R. J. Birgeneau, Y. Endoh, M. A. Kastner, M. Matsuda, and G. Shirane, Neutron scattering study of the two-dimensional spin $S=1/2$  square-lattice Heisenberg antiferromagnet  $\text{Sr}_2\text{CuO}_2\text{Cl}_2$ , Z. Phys. B Condens. Matter **96**, 465 (1995).
- [7] A. Cuccoli, T. Roscilde, R. Vaia, and P. Verrucchi, Detection of XY Behavior in Weakly Anisotropic Quantum Antiferromagnets on the Square Lattice, Phys. Rev. Lett. **90**, 167205 (2003).
- [8] B. D. Piazza, M. Mourigal, N. B. Christensen, G. J. Nilsen, P. Tregenna-Piggott, T. G. Perring, M. Enderle, D. F. McMorrow, D. A. Ivanov, and H. M. Rønnow, Fractional excitations in the square-lattice quantum antiferromagnet, Nat. Phys. **11**, 62 (2015).

- 
- [9] N. Tsyrlin, F. Xiao, A. Schneidewind, P. Link, H. M. Rønnow, J. Gavilano, C. P. Landee, M. M. Turnbull, and M. Kenzelmann, Two-dimensional square-lattice  $S=1/2$  antiferromagnet  $\text{Cu}(\text{pz})_2(\text{ClO}_4)_2$ , *Phys. Rev. B* **81**, 134409 (2010).
  - [10] J. L. Manson, M. M. Conner, J. A. Schlueter, T. Lancaster, S. J. Blundell, M. L. Brooks, F. L. Pratt, T. Papageorgiou, A. D. Bianchi, J. Wosnitzae, and M.-H. Whangboo,  $J_1$ - $J_2$  square-lattice Heisenberg antiferromagnets with  $4d^1$  spins:  $\text{AMoOPO}_4$  ( $A = \text{K}, \text{Rb}$ ), *Chem. Commun.*, 4894 (2006).
  - [11] R. Melzi, S. Aldrovandi, F. Tedoldi, P. Carretta, P. Millet, and F. Mila, Magnetic and thermodynamic properties of  $\text{Li}_2\text{VSiO}_4$ : A two-dimensional  $S=1/2$  frustrated antiferromagnet on a square lattice, *Phys. Rev. B* **64**, 024409 (2001).
  - [12] H. Rosner, R. R. P. Singh, W. H. Zheng, J. Oitmaa, S.-L. Drechsler, and W. E. Pickett, Realization of a Large  $J_2$  Quasi-2D Spin-Half Heisenberg System:  $\text{Li}_2\text{VSiO}_4$ , *Phys. Rev. Lett.* **88**, 186405 (2002).
  - [13] H. Rosner, R. R. P. Singh, W. H. Zheng, J. Oitmaa, and W. E. Pickett, High-temperature expansions for the  $J_1$ - $J_2$  Heisenberg models: Applications to ab initio calculated models for  $\text{Li}_2\text{VSiO}_4$  and  $\text{Li}_2\text{VGeO}_4$ , *Phys. Rev. B* **67**, 014416 (2003).
  - [14] A. Bombardi, L. C. Chapon, I. Margiolaki, C. Mazzoli, S. Gonthier, F. Duc, and P. G. Radaelli, Magnetic order and lattice anomalies in the  $J_1$ - $J_2$  model system  $\text{VOMoO}_4$ , *Phys. Rev. B* **71**, 220406(R) (2005).
  - [15] A. A. Tsirlin, A. A. Belik, R. V. Shpanchenko, E. V. Antipov, E. Takayama-Muromachi, and H. Rosner, Frustrated spin-1/2 square lattice in the layered perovskite  $\text{PbVO}_3$ , *Phys. Rev. B* **77**, 092402 (2008).
  - [16] R. Nath, A. A. Tsirlin, H. Rosner, and C. Geibel, Magnetic properties of  $\text{BaCdVO}(\text{PO}_4)_2$ : A strongly frustrated spin-1/2 square lattice close to the quantum critical regime, *Phys. Rev. B* **78**, 064422 (2008).
  - [17] E. E. Kaul, H. Rosner, N. Shannon, R. V. Shpanchenko, and C. Geibel, Evidence for a frustrated square lattice with ferromagnetic nearest-neighbor interaction in the new compound  $\text{Pb}_2\text{VO}(\text{PO}_4)_2$ , *J. Magn. Magn. Mater.* **272-276**, 922 (2004).
  - [18] A. A. Tsirlin and H. Rosner, Extension of the spin-1/2 frustrated square lattice model: The case of layered vanadium phosphates, *Phys. Rev. B* **79**, 214417 (2009).

- 
- [19] A. A. Tsirlin, R. Nath, A. M. Abakumov, R. V. Shpanchenko, C. Geibel, and H. Rosner, Frustrated square lattice with spatial anisotropy: Crystal structure and magnetic properties of  $\text{PbZnVO}(\text{PO}_4)_2$ , *Phys. Rev. B* **81**, 174424 (2010).
- [20] H. Ishikawa, N. Nakamura, M. Yoshida, M. Takigawa, P. Babkevich, N. Qureshi, H. M. Rønnow, T. Yajima, and Z. Hiroi,  $J_1$ - $J_2$  square-lattice Heisenberg antiferromagnets with  $4d^1$  spins:  $\text{AMoOPO}_4\text{Cl}$  ( $\text{A}=\text{K,Rb}$ ), *Phys. Rev. B* **95**, 064408 (2017).
- [21] B. Keimer, S. A. Kivelson, M. R. Norman, S. Uchida, and J. Zaanen, From quantum matter to high-temperature superconductivity in copper oxides, *Nature (London)* **518**, 179 (2015).
- [22] Y. Li, D. Adroja, R. I. Bewley, D. Voneshen, A. A. Tsirlin, P. Gegenwart, and Q. Zhang, Crystalline Electric-Field Randomness in the Triangular Lattice Spin-Liquid  $\text{YbMgGaO}_4$ , *Phys. Rev. Lett.* **118**, 107202 (2017).
- [23] L. Ding, P. Manuel, S. Bachus, F. Grubler, P. Gegenwart, J. Singleton, R. D. Johnson, H. C. Walker, D. T. Adroja, A. D. Hillier *et al.*, Gapless spin-liquid state in the structurally disorder-free triangular antiferromagnet  $\text{NaYbO}_2$ , *Phys. Rev. B* **100**, 144432 (2019).
- [24] J. G. Rau, L. S. Wu, A. F. May, L. Poudel, B. Winn, V. O. Garlea, V. O. Garlea, A. Huq, P. Whitfield, A. E. Taylor, M. D. Lumsden *et al.*, Anisotropic Exchange within Decoupled Tetrahedra in the Quantum Breathing Pyrochlore  $\text{Ba}_3\text{Yb}_2\text{Zn}_5\text{O}_{11}$ , *Phys. Rev. Lett.* **116**, 257204 (2016).
- [25] W. Y. Liu, S. S. Gong, Y. B. Li, D. Poilblanc, W. Q. Chen, and Z. C. Gu, Gapless quantum spin liquid and global phase diagram of the spin-1/2  $J_1$ - $J_2$  square antiferromagnetic Heisenberg model, *Science Bulletin* **67**, 1034 (2022).
- [26] L. C. Chapon, P. Manuel, P. G. Radaelli, C. Benson, L. Perrott, S. Ansell, N. J. Rhodes, D. Raspino, D. Duxbury, E. Spill, and J. Norris, Wish: The new powder and single crystal magnetic diffractometer on the second target station, *Neutron News* **22**, 22 (2011).
- [27] V. Petricek, M. Dusek, and L. Palatinus, Crystallographic computing system JANA2006: General features, *Z. Kristallogr. – Cryst. Mater.* **229**, 345 (2014).
- [28] Mantid (2013): Manipulation and Analysis Toolkit for Instrument Data.; Mantid Project.
- [29] O. Arnold, J.C. Bilheux, J.M. Borreguero, A. Buts, S.I. Campbell, L. Chapon, M. Doucet, N. Draper, R. Ferraz Leal, M.A. Gigg *et al.*, *Nuclear Instruments and*

- Methods in Physics Research Section A: Accelerators, Spectrometers, Detectors and Associated Equipment **764**, 156 (2014).
- [30] N. Read and S. Sachdev, Valence-bond and spin-Peierls ground states of low-dimensional quantum antiferromagnets, *Phys. Rev. Lett.* **62**, 1694 (1989).
  - [31] M. E. Zhitomirsky and K. Ueda, Valence-bond crystal phase of a frustrated spin-1/2 square-lattice antiferromagnet, *Phys. Rev. B* **54**, 9007 (1996).
  - [32] S.-S. Gong, W. Zhu, D. N. Sheng, O. I. Motrunich, and M. P. A. Fisher, Plaquette Ordered Phase and Quantum Phase Diagram in the Spin-1/2  $J_1$ - $J_2$  Square Heisenberg Model, *Phys. Rev. Lett.* **113**, 027201 (2014).
  - [33] T. Besara, M. S. Lundberg, J. Sun, D. Ramirez, L. Dong, J. B. Whalen, R. Vasquez, F. Herrera, J. R. Allen, M. W. Davidson *et al.*, Single crystal synthesis and magnetism of the  $\text{BaLn}_2\text{O}_4$  family (Ln = lanthanide), *Prog. Solid State Chem.* **42**, 23 (2014).
  - [34] M. Mitric, B. Antic, M. Balanda, D. Rodic, and M. L. Napijalo, An x-ray diffraction and magnetic susceptibility study of  $\text{Yb}_x\text{Y}_{2-x}\text{O}_3$ , *J. Phys.: Condens. Matter* **9**, 4103 (1997).
  - [35] H. W. J. Blöte, R. F. Wieringa, and W. J. Huiskamp, Heat-capacity measurements on rare-earth double oxides  $\text{R}_2\text{M}_2\text{O}_7$ , *Physica* **43**, 549 (1969).
  - [36] H. B. Cao, A. Gukasov, I. Mirebeau, and P. Bonville, Anisotropic exchange in frustrated pyrochlore  $\text{Yb}_2\text{Ti}_2\text{O}_7$ , *J. Phys.: Condens. Matter* **21**, 492202 (2009).
  - [37] S. Guo, A. Ghasemi, C. L. Broholm, and R. J. Cava, Magnetism on ideal triangular lattices in  $\text{NaBaYb}(\text{BO}_3)_2$ , *Phys. Rev. Material* **3**, 094404 (2019).
  - [38] R. Sibille, E. Lhotel, V. Pomjakushin, C. Baines, T. Fennell, and M. Kenzelmann, Candidate quantum spin liquid in the  $\text{Ce}^{3+}$  pyrochlore stannate  $\text{Ce}_2\text{Sn}_2\text{O}_7$ , *Phys. Rev. Lett.* **115**, 097202 (2015).
  - [39] C. Kittel, *Introduction to Solid State Physics* (Wiley, Hoboken, NJ, 2005).
  - [40] K. Somesh, S. S. Islam, S. Mohanty, G. Simutis, Z. Guguchia, C. Wang, J. Sichelschmidt, M. Baenitz and R. Nath, Absence of magnetic order and emergence of unconventional fluctuations in the  $J_{eff}=1/2$  triangular-lattice antiferromagnet  $\text{YbBO}_3$ , *Phys. Rev. B* **107**, 064421 (2023).
  - [41] S. Kundu, A. Hossain, Pranava Keerthi S, R. Das, M. Baenitz, P. J. Baker, J.-C. Orain, D. C. Joshi, R. Mathieu, P. Mahadevan, S. Pujari, S. Bhattacharjee, A.

- V. Mahajan, and D. D. Sarma, Signatures of a Spin-1 2 Cooperative Paramagnet in the Diluted Triangular Lattice of  $\text{Y}_2\text{CuTiO}_6$ , *Phys. Rev. Lett.* **125**, 117206 (2020).
- [42] P. Svoboda, J. Vejpravova, N.-T. Kim-Ngan, and F. Kaysel, Specific heat study of selected  $\text{RNi}_5$ , *J. Magn. Magn. Mater.* **272-276**, 595 (2004).
- [43] R. Kumar and A. Sundaresan, Unveiling a hidden multiferroic state under magnetic fields in  $\text{BaHoFeO}_4$ , *Phys. Rev. B* **107**, 184420 (2023).
- [44] R. Kumar and A. Sundaresan, Antisite disorder driven cluster glass state and colossal magnetoresistance in  $\text{MnSb}_2\text{Se}_4$ , *Phys. Rev. B* **106**, 134423 (2022).
- [45] R. Bag, M. Ennis, C. Liu, S. E. Dissanayake, Z. Shi, J. Liu, L. Balents, and S. Haravifard, Realization of quantum dipoles in triangular lattice crystal  $\text{Ba}_3\text{Yb}(\text{BO}_3)_3$ , *Phys. Rev. B* **104**, L220403 (2021).
- [46] H. M. Rosenberg, *Low Temperature Solid State Physics* Oxford University Press, Oxford, 1963.
- [47] L. Xie, T. Su, and X. Li, Magnetic field dependence of Schottky anomaly in the specific heats of stripe-ordered superconductors  $\text{La}_{1.6-x}\text{Nd}_{0.4}\text{Sr}_x\text{CuO}_4$ , *Physica C: Superconductivity* **480**, 14 (2012).
- [48] S. Mahdavi-far and A. Akbari, Heat capacity of Schottky type in low-dimensional spin systems, *J. Phys.: Condens. Matter* **20**, 215213 (2008).
- [49] M. Yamashita, N. Nakata, Y. Kasahara, T. Sasaki, N. Yoneyama, N. Kobayashi, S. Fujimoto, T. Shibauchi, and Y. Matsuda, Thermal-transport measurements in a quantum spin-liquid state of the frustrated triangular magnet  $\kappa$ -(BEDT-TTF) $_2\text{Cu}_2(\text{CN})_3$ , *Nat. Physics* **5**, 44 (2009).
- [50] Y. Ishitsuka, T. Ishikawa, R. Koborinai, T. Omura, and T. Katsufuji, Comparative studies of the thermal conductivity of spinel oxides with orbital degrees of freedom, *Phys. Rev. B* **90**, 224411 (2014).
- [51] O. Mustonen, S. Vasala, E. Sadrollahi, K. P. Schmidt, C. Baines, H. C. Walker, I. Terasaki, F. J. Litterst, E. Baggio-Saitovitch, and M. Karppinen, Spin-liquid-like state in a spin-1/2 square-lattice antiferromagnet perovskite induced by  $d^{10}$ - $d^0$  cation mixing, *Nat. comm.* **9**, 1 (2018).
- [52] L. Ding, P. Manuel, S. Bachus, F. Größler, P. Gegenwart, J. Singleton, R. D. Johnson, H. C. Walker, D. T. Adroja, A. D. Hillier, and A. A. Tsirlin, Gapless spin-liquid

- state in the structurally disorder-free triangular antiferromagnet  $\text{NaYbO}_2$ , *Phys. Rev. B* **100**, 144432 (2019).
- [53] Z. Zhang, J. Li, M. Xie, W. Zhuo, D. T. Adroja, P. J. Baker, T. G. Perring, A. Zhang, F. Jin, J. Ji, X. Wang, J. Ma, and Q. Zhang, Low-energy spin dynamics of the quantum spin liquid candidate  $\text{NaYbSe}_2$ , *Phys. Rev. B* **106**, 085115 (2022).
- [54] M. Jeong, F. Bert, P. Mendels, F. Duc, J. C. Trombe, M. A. de Vries, and A. Harrison, Field-induced freezing of a quantum spin liquid on the kagome lattice, *Phys. Rev. Lett.* **107**, 237201 (2011).
- [55] J. A. M. Paddison, M. Daum, Z. Dun, G. Ehlers, Y. Liu, M. B. Stone, H. Zhou, and M. Mourigal, Continuous excitations of the triangular-lattice quantum spin liquid  $\text{YbMgGaO}_4$ , *Nat. Phys.* **13**, 117 (2017).
- [56] F. R. Foronda, F. Lang, J. S. Möller, T. Lancaster, A. T. Boothroyd, F. L. Pratt, S. R. Giblin, D. Prabhakaran, and S. J. Blundell, Anisotropic local modification of crystal field levels in Pr-based pyrochlores: A muon-induced effect modeled using density functional theory, *Phys. Rev. Lett.* **114**, 017602 (2015).
- [57] D. E. MacLaughlin, O. O. Bernal, L. Shu, J. Ishikawa, Y. Matsumoto, J.-J. Wen, M. Mourigal, C. Stock, G. Ehlers, C. L. Broholm *et al.*, Unstable spin-ice order in the stuffed metallic pyrochlore  $\text{Pr}_{2+x}\text{Ir}_{2-x}\text{O}_{7-\delta}$ , *Phys. Rev. B* **92**, 054432 (2015).
- [58] F. L. Pratt, P. J. Baker, S. J. Blundell, T. Lancaster, S. Ohira-Kawamura, C. Baines, Y. Shimizu, K. Kanoda, I. Watanabe, and G. Saito, Magnetic and non-magnetic phases of a quantum spin liquid, *Nature* **471**, 612 (2011).
- [59] G. Kresse and J. Furthmüller, Efficient Iterative Schemes for Ab Initio Total-Energy Calculations Using a Plane-Wave Basis Set, *Phys. Rev. B* **54**, 11169 (1996).
- [60] G. Kresse and J. Furthmüller, Efficiency of Ab-Initio Total Energy Calculations for Metals and Semiconductors Using a Plane-Wave Basis Set, *Comput. Mater. Sci.* **6**, 15 (1996).
- [61] G. Kresse and J. Hafner, Ab Initio Molecular Dynamics for Liquid Metals, *Phys. Rev. B* **47**, 558 (1993).
- [62] G. Kresse and D. Joubert, From Ultrasoft Pseudopotentials to the Projector Augmented-Wave Method, *Phys. Rev. B* **59**, 1758 (1999).
- [63] J. P. Perdew, K. Burke, and M. Ernzerhof, Generalized Gradient Approximation Made Simple, *Phys. Rev. Lett.* **77**, 3865 (1996).



- [64] J. P. Perdew, A. Ruzsinszky, G. I. Csonka, O. A. Vydrov, G. E. Scuseria, L. A. Constantin, X. Zhou, and K. Burke, Restoring the Density-Gradient Expansion for Exchange in Solids and Surfaces, *Phys. Rev. Lett.* **100**, 136406 (2003).
- [65] S. L. Dudarev, G. A. Botton, S. Y. Savrasov, C. J. Humphreys, and A. P. Sutton, Electron-energy-loss spectra and the structural stability of nickel oxide: An LSDA+U study, *Phys. Rev. B* **57**, 1505 (1998).
- [66] K. Momma and F. Izumi, VESTA 3 for Three-Dimensional Visualization of Crystal, Volumetric and Morphology Data, *J. Appl. Crystallogr.* **44**, 1272 (2011).
- [67] A. Kokalj, XCrySDen—a new program for displaying crystalline structures and electron densities, *J. Mol. Graphics Modelling* **17**, 176 (1999).

## Chapter 6

# Spin Frustration in a Distorted Square Lattice of NaYbZnWO<sub>6</sub> Prepared Under High Pressure

We present a comprehensive investigation of a doubly ordered perovskite NaYbZnWO<sub>6</sub>, synthesized under high-pressure and high-temperature. In this perovskite, Na<sup>+</sup> and Yb<sup>3+</sup> ions at the A-site are ordered in layers along the  $c$  axis, forming a two-dimensional distorted square lattice (kite shaped) of Yb<sup>3+</sup> ions without any antisite disorder. The magnetic susceptibility data suggest that the ground state of Yb<sup>3+</sup> is a  $J_{eff} = 1/2$  Kramers doublet. These findings, plus specific heat measurements, suggest the presence of spin frustration in NaYbZnWO<sub>6</sub>, which was confirmed by evaluating its spin exchanges using an isolated dimer approach using DFT+ $U$  and DFT+ $U$ +SOC calculations. These observations suggest that NaYbZnWO<sub>6</sub> is a promising quantum spin liquid system based on a distorted square spin lattice.

## 6.1 Introduction

The arrangement of magnetic ions in a square, triangular, kagomé, and pyrochlore lattices often leads to spin frustration, and magnets with spin frustration have actively been studied to search for novel ground states such as quantum spin liquid (QSL) and quantum spin ice [1]. The frustrated magnetism of a square lattice of Heisenberg spin  $S = 1/2$  ions is explained by the  $J_1$ - $J_2$  model, where  $J_1$  is the nearest neighbor spin exchange, and  $J_2$  the next-nearest neighbor spin exchange. Theoretical studies predict a QSL state for a square-lattice magnet when  $J_2/J_1 \approx 0.5$  [2, 3], but there has been no experimental realization of this prediction. The only square spin-lattice magnet showing the QSL state is the double perovskite Sr<sub>2</sub>Cu(Te<sub>0.5</sub>W<sub>0.5</sub>)O<sub>6</sub> but with a site disorder [4], in which the double-perovskite layers have the Cu-O...A<sup>6+</sup>...O-Cu type spin exchanges. The cause for the QSL state is two-fold; one is that this spin exchange is antiferromagnetic for A<sup>6+</sup> = W<sup>6+</sup> as found for Sr<sub>2</sub>CuWO<sub>6</sub> but is ferromagnetic for A<sup>6+</sup> = Te<sup>6+</sup> as found for Sr<sub>2</sub>CuTeO<sub>6</sub> [5]. The other is the site disorder, namely, the Te<sup>6+</sup> and W<sup>6+</sup> ions occupy the same crystallographic sites, hence leading to the spin frustration in the square spin-lattice of the Cu<sup>2+</sup> ions. It is desirable to find a magnet of the disorder-free square spin-lattice.

Rare earth magnets, characterized by strong spin-orbit coupling (SOC) and localized 4f electrons, are promising for exploring strongly correlated physics. In particular, magnets of Yb<sup>3+</sup> ions with effective  $J_{eff} = 1/2$  [6–8] have received much attention in the search for QSL states. A QSL behavior is proposed for YbMgGaO<sub>4</sub> [9] and NaYbO<sub>2</sub> [7], both of which have a trigonal spin-lattice of Yb<sup>3+</sup> ions. There is no site disorder in NaYbO<sub>2</sub> [7], so its QSL behavior reflects the genuine feature of its trigonal spin-lattice. In the case of YbMgGaO<sub>4</sub> [10], however, the Mg<sup>2+</sup> and Ga<sup>3+</sup> ions occupy the same crystallographic sites randomly, so one cannot exclude the possibility that its spin-liquid-like behavior arises from the random potential associated with the site disorder involving nonmagnetic ions.

## 6.2 Experiment

A polycrystalline sample of NaYbMgWO<sub>6</sub> has been prepared using high-pressure and high-temperature solid-state reaction method using a Hall type six-ram large volume press (mavo press LPQ6 1500–100; Max Voggenreiter GmbH, Germany) at P61B beamline at DESY, Hamburg [11]. As an initial step, the stoichiometric amount of Na<sub>2</sub>WO<sub>4</sub>, WO<sub>3</sub>, Yb<sub>2</sub>O<sub>3</sub>, and ZnO is mixed uniformly using a mortar-pestle. The experiments were

performed using standard DESY assemblies containing 14 mm MgO octahedron and 7 mm truncated edge length tungsten carbide anvils (Fujilloy TF08). The temperature in the press has been controlled by a tubular-resistive graphite heater, and Cr<sub>2</sub>O<sub>3</sub> doped MgO has been used to transmit the pressure. The pressure applied on the sample at different press loads was determined by the MgO pressure marker using the *in-situ* energy dispersive x-ray diffraction pattern (EDXRD). Similarly, the power-temperature relationship has been used to calculate the temperature values at a particular press load. During the synthesis, at first, the pressure was increased up to 9 GPa in steps, keeping the temperature constant (room temperature), and then the temperature was increased (step of 100 W which is equivalent to 100° C) while keeping the pressure exerted on the sample constant (9 GPa). During the compression and throughout heating, the reaction was monitored by in-situ EDXRD. Once the reaction is complete, the temperature was quenched to room temperature, and the pressure was gradually decreased to ambient conditions. PDIndexer software package [12, 13] has been used to analyze the EDXRD patterns.

As synthesized sample has been characterized further on a PANalytical Empyrean Alpha I diffractometer using Cu-K $\alpha_1$  single wavelength ( $\lambda = 1.54059$  Å). The magnetic properties of the compound have been explored using a magnetic properties measurement system (MPMS) of Quantum Design, USA. Further, magnetization was measured down to 0.4 K using a <sup>3</sup>He (iHelium3, Quantum Design Japan) attachment to the MPMS. The physical properties measurement system (PPMS) of Quantum Design, USA, has been utilized to perform specific heat and ac magnetic susceptibility measurements.

## 6.3 Results and Discussion

### 6.3.1 Crystal Structure

Figure 6.1(a) shows the change in energy dispersive x-ray pattern under the application of various pressures up to 9 GPa. The evolution of the pattern with increase in temperature, while keeping the pressure constant at 9 GPa, is shown in Fig. 6.1 (b). Figure 6.1(c) shows the indexed pattern using the  $P2_1$  space group. The crystal structure of NaYbZnWO<sub>6</sub> was determined by Rietveld refinement (Jana software [14]) of the XRD pattern using NaYbNiWO<sub>6</sub> as a reference [15]. A good agreement of the experimental data with the simulated pattern confirmed the phase purity of the compound, as depicted in Fig. 6.2 and established that it crystallizes into the polar  $P2_1$  space group. The refinement parameters

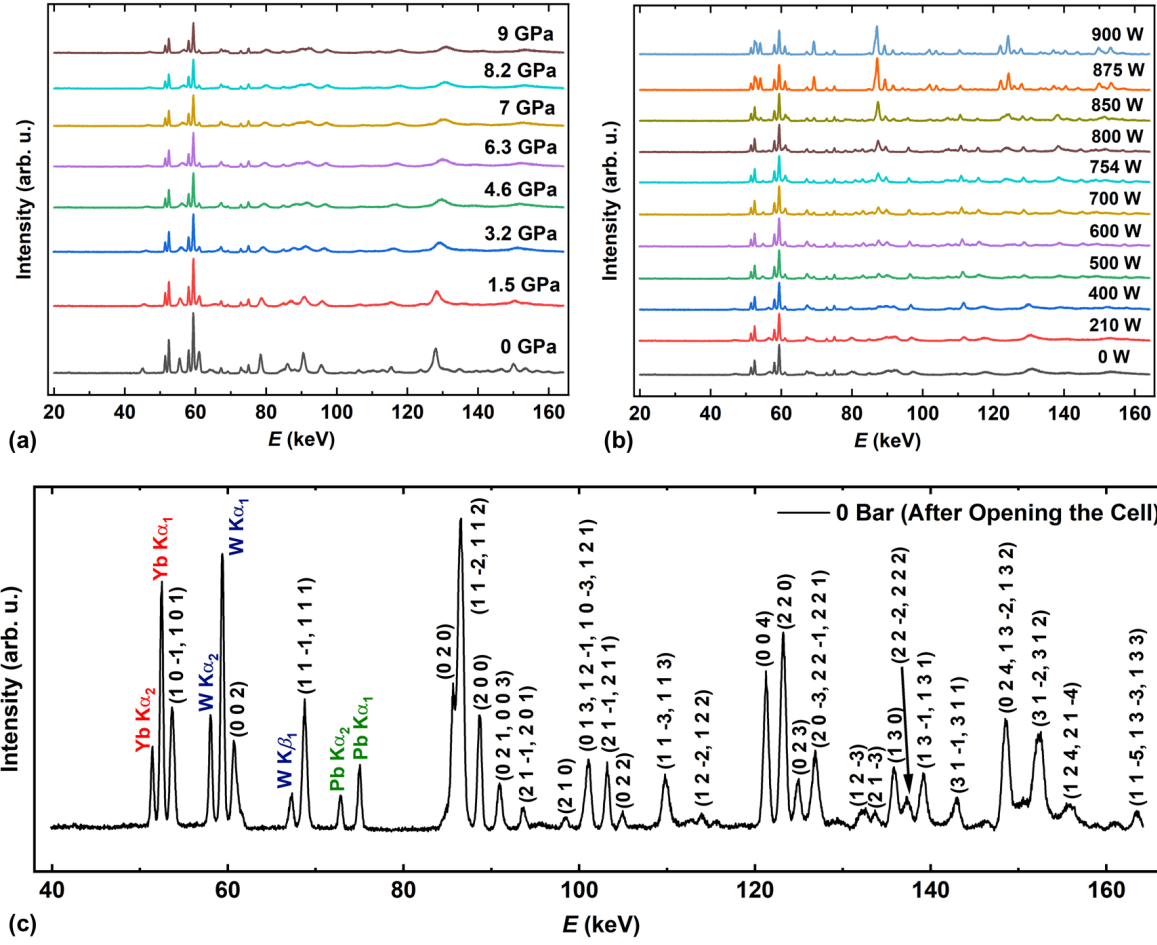


Figure 6.1: (a) Pressure-dependent evolution of energy-dispersive x-ray diffraction (EDXRD) profiles at room temperature. (b) Change in EDXRD pattern at a constant pressure of 9 GPa. (c) Indexed EDXRD profile after quenching the temperature and removing the pressure. The fluorescence peaks of Yb, W, and Pb are also indexed.

are summarized in Table 6.1. Moreover, including the antisite disorder in the refinement did not improve the fit and the reliability parameters.

NaYbZnWO<sub>6</sub> belongs to the family of doubly ordered -perovskites,  $AA'BB'O_6$ , in which the six-coordinate cations  $B$  and  $B'$  as well as the 12 coordinate cations  $A$  and  $A'$  (from the viewpoint of an ideal cubic perovskite) are ordered [16–19]. Namely, the  $BO_6$  and  $B'O_6$  octahedra alternate in all three corner-sharing directions to form the perovskite framework (Fig. 6.3(a), while the  $A$  and  $A'$  ions alternate along the  $c$ -direction so that the layers of the  $Yb^{3+}$  ions alternate with those of the  $Na^+$  ions along the  $c$ -direction (Fig. 6.3(b)). The  $Yb^{3+}$  ions, the only magnetic ions of NaYbZnWO<sub>6</sub>, form a distorted square net (Fig. 6.3(c)) in which every “square” has the shape of a kite. The adjacent

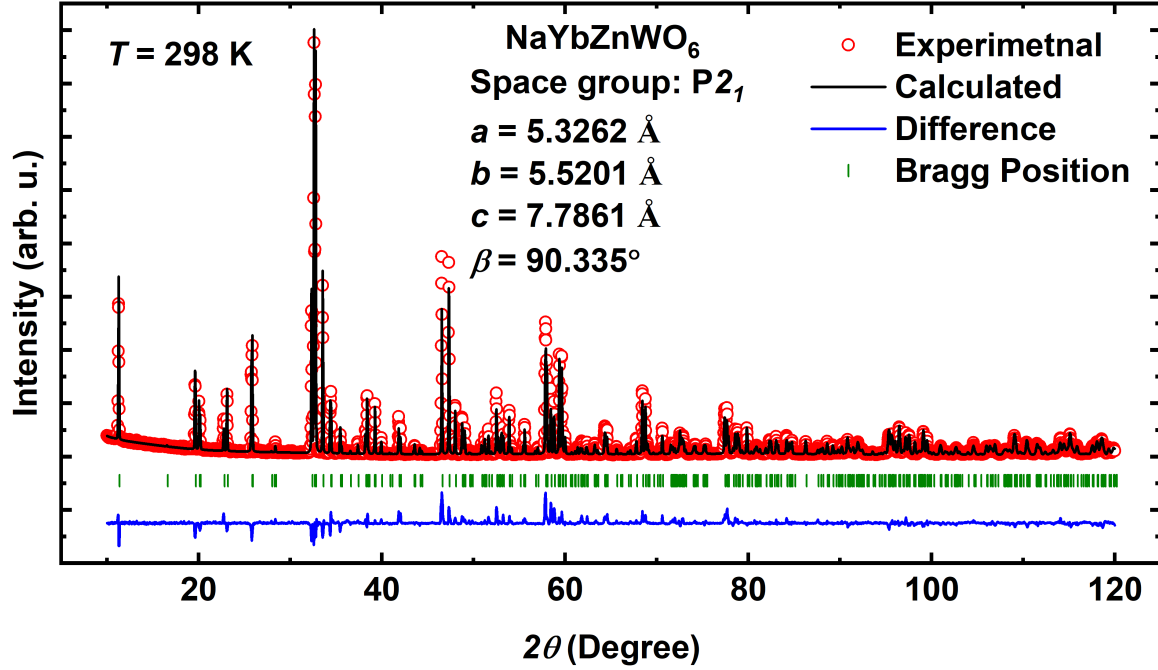


Figure 6.2: Rietveld refinement of the room temperature angle dispersive x-ray diffraction pattern. Experimental pattern, simulated pattern, difference, and Bragg positions are depicted by red open circles, black solid line, blue solid line, and green bars, respectively.

Table 6.1: Crystallographic parameters along with occupancy and isotropic displacement parameters obtained from the Rietveld refinement of the powder XRD data. Space group:  $P2_1$ ,  $V = 228.91(1) \text{ \AA}^3$ ,  $\chi^2 = 2.97 \%$ , Bragg  $R$  factor =  $7.86 \%$ ,  $R_f = 6.70 \%$ .

Atom	Wyckoff symbol	x	y	z	Occupancy	$B_{iso}(\text{\AA}^2)$
Na(1)	$2a$	0.2600(47)	0.2150(41)	0.0140(26)	1.0	0.015(4)
Yb(2)	$2a$	0.2701(6)	0.3153(2)	0.5016(4)	1.0	0.026(4)
Zn(1)	$2a$	0.7477(17)	0.2573(14)	0.2413(8)	1.0	0.025(5)
W(1)	$2a$	0.7644(6)	0.25	0.7617(3)	1.0	0.023(5)
O(1)	$2a$	0.5430(44)	0.5410(40)	0.7290(28)	1.0	1.0
O(2)	$2a$	0.5990(52)	0.5410(47)	0.7290(35)	1.0	1.0
O(3)	$2a$	-0.0930(62)	-0.0610(57)	0.1710(38)	1.0	1.0
O(4)	$2a$	-0.0990(58)	-0.0880(56)	0.8280(37)	1.0	1.0
O(5)	$2a$	0.8780(55)	0.1710(51)	0.4650(40)	1.0	1.0
O(6)	$2a$	0.6320(57)	0.1970(51)	-0.0310(40)	1.0	1.0

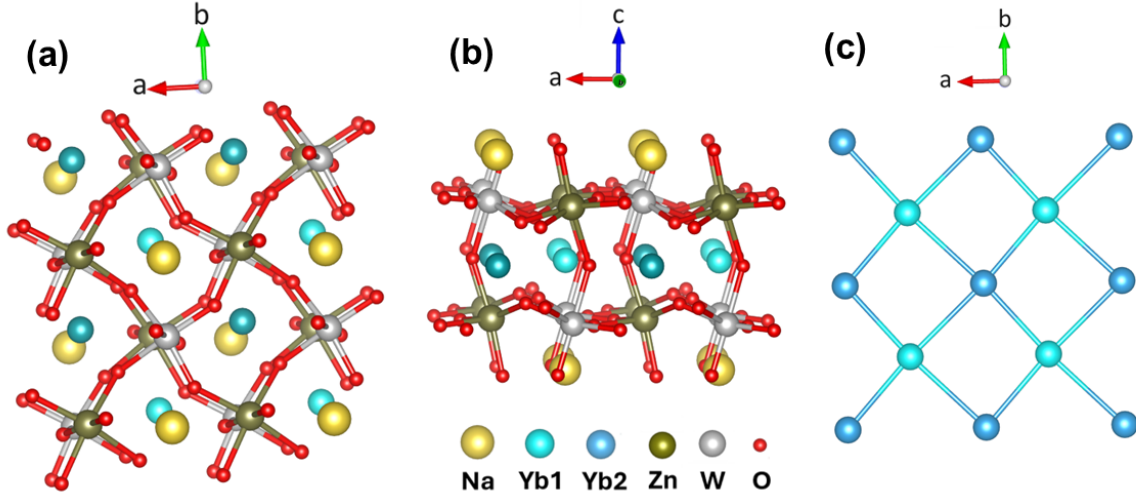


Figure 6.3: The crystal structure of  $\text{NaYbZnWO}_6$  viewed along the (a)  $c$ - and (b)  $b$ -directions. The six-coordinate  $\text{Zn}^{2+}$  and  $\text{W}^{6+}$  cations form an ordered perovskite framework, while the  $\text{Na}^+$  and  $\text{Yb}^{3+}$  cations form layers parallel to the  $ab$  plane, which alternate along the  $c$ -direction. (c) The distorted square lattice of  $\text{Yb}^{3+}$  cations.

$\text{Yb}^{3+}$  layers are separated by more than  $7 \text{ \AA}$  so  $\text{NaYbZnWO}_6$  is a two-dimensional magnet. In the following, we show that  $\text{NaYbZnWO}_6$  with no site disorder is spin frustrated in each distorted square of its spin-lattice and exhibits magnetic properties suggesting that it is a promising QSL system.

### 6.3.2 DC Magnetization

To study the low-temperature magnetic properties of  $\text{NaYbZnWO}_6$ , we measured its temperature-dependent dc magnetization down to 0.4 K by following the zero-field-cooled (ZFC) and field-cooled (FC) protocols at 100 Oe. No magnetic ordering was observed down to 0.4 K (Fig. 6.4(a)). The temperature dependence of the inverse susceptibility, after subtracting the Van Vleck contribution  $\chi_{vv} = 8.1 \times 10^{-3} \text{ emu/mol}$  (estimated from the isothermal magnetization data explained below), exhibits a linear behavior in two different temperature regions. This behavior reflects the splitting of the eightfold degenerate ground state of  $\text{Yb}^{3+}$  into four doublets as a result of the crystal electric field. Thus, the Curie-Weiss temperature ( $\theta_{CW}$ ) obtained from the fit, using the data of high-temperature region, will have a significant contribution from thermally populated crystal field split levels, overestimating the interaction strength. A thorough solution to this issue would require experimentally determining the complete crystal field scheme of the material, which can be accomplished using inelastic neutron scattering as reported

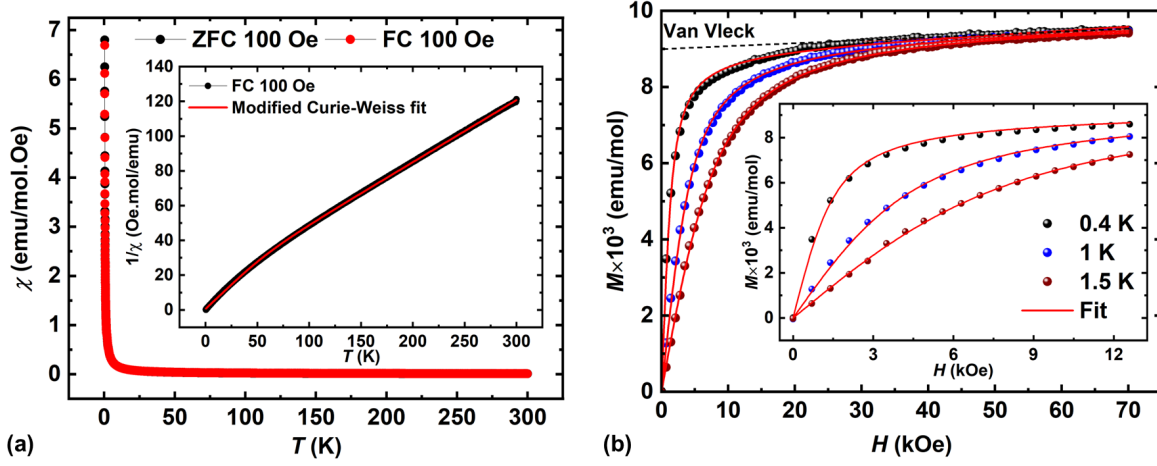


Figure 6.4: (a) Temperature dependence of dc magnetic susceptibility performed under ZFC and FC protocol down to 0.4 K. Inset shows the fitting of inverse susceptibility data with modified Curie-Weiss law. (b) Isothermal magnetization curves measured at different temperatures along with the Brillouin fits represented by solid lines. The black dashed line accounts for the Van Vleck contribution. The inset shows a zoomed-in view of the fitting at lower fields. The  $\chi^2$  values for the fitting for 0.4, 1, and 1.5 K are 0.9696, 0.9901, and 0.9972, respectively.

for other Yb compounds [6–8].

However, the impact of excited crystal field levels can be approximated using the following two-level equation [20, 21];

$$1/\chi = 8|(T - \theta_{CW})| \left( \frac{1 + \exp^{-\frac{E_{10}}{k_B T}}}{\mu_{eff,0}^2 + \mu_{eff,1}^2 \cdot \exp^{-\frac{E_{10}}{k_B T}}} \right) \quad (6.1)$$

where  $\mu_{eff,0}$  and  $\mu_{eff,1}$  are effective moments in the crystal field ground state and first excited state, respectively, while  $E_{10}$  is the energy difference between them. The fitting analysis, shown in the inset of Fig. 6.4(a), results in the following parameters:  $\theta_{CW} = -1.02(4)$  K,  $\mu_{eff,0} = 3.78(3) \mu_B$ ,  $\mu_{eff,1} = 5.49(4) \mu_B$ , and  $E_{10} = 177.6(7)$  K. The observed magnetic moment in the ground state is lower than the theoretically predicted value of  $4.54 \mu_B$  for a Yb<sup>3+</sup> ion ( $4f^{13}$ ,  $J = 7/2$ ). Additionally, the distinct energy gap between the ground state and higher energy states suggests that ground state can be described as a Kramers doublet with  $J_{eff} = 1/2$  [22–24].

To examine the magnetic behavior of NaYbZnWO<sub>6</sub> under high fields at low temperatures, we carried out magnetization measurements at different temperatures (i.e., at 0.4, 1, 1.5, and 10 K) by continuously sweeping the magnetic field from +7 to -7 T (Fig.



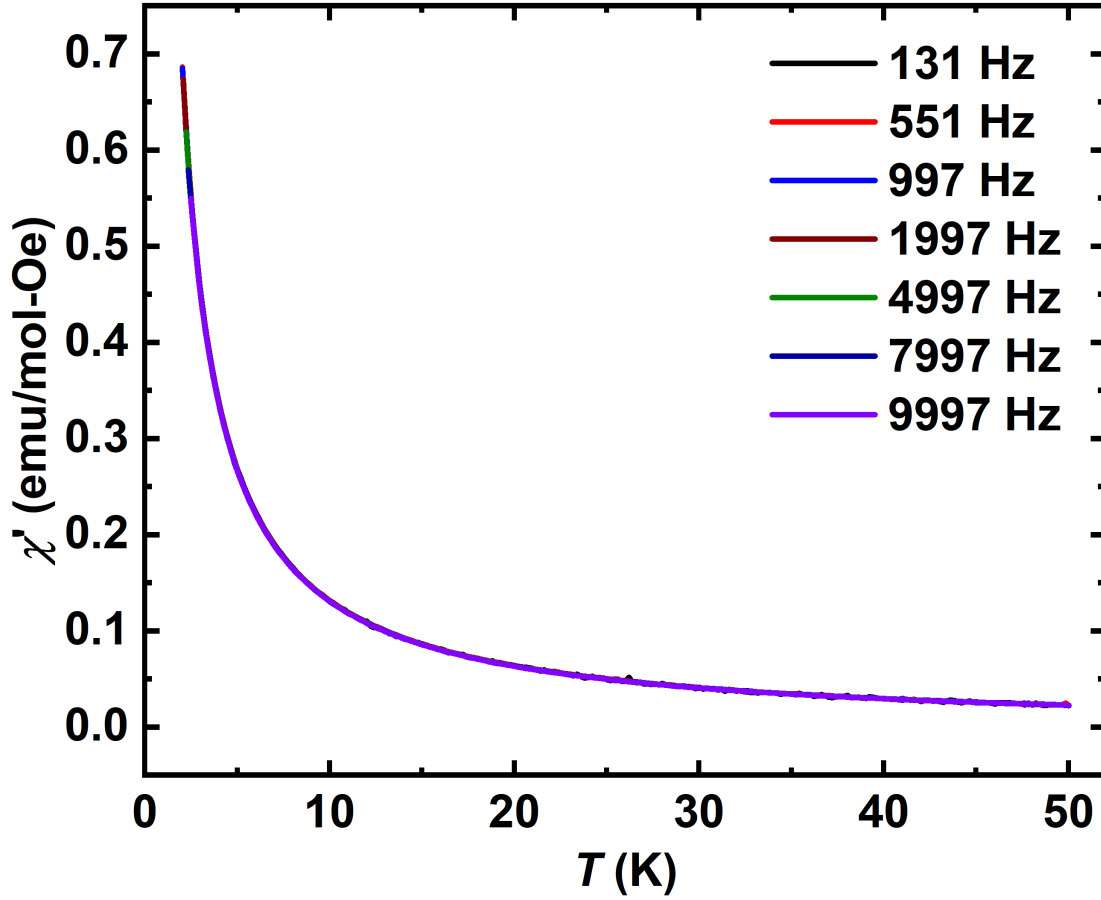


Figure 6.5: Variation of frequency-dependent ac susceptibilities with temperature.

6.4(b)). The magnetization of the paramagnetic state can be modeled by

$$M(H) = \chi_{\nu\nu}H + gJ_{eff}N_A\mu_B B_{J_{eff}}(H) \quad (6.2)$$

where  $B_{J_{eff}}(H)$  is the Brillouin function [25]. It is evident from Fig. 6.4(b) that the magnetization at  $T > 1$  K could be fitted very well, but the fit deviates significantly for  $T \leq 1$  K (depicted in the inset of 6.4(b)), suggesting that the frustrated spin exchange interactions become more important than the thermal excitations [26, 27]. To explore the possible glassiness in NaYbZnWO<sub>6</sub>, we performed temperature-dependent ac susceptibility measurements at different frequencies. As shown in Fig. 6.5, the presence of a glassy state can be ruled out.

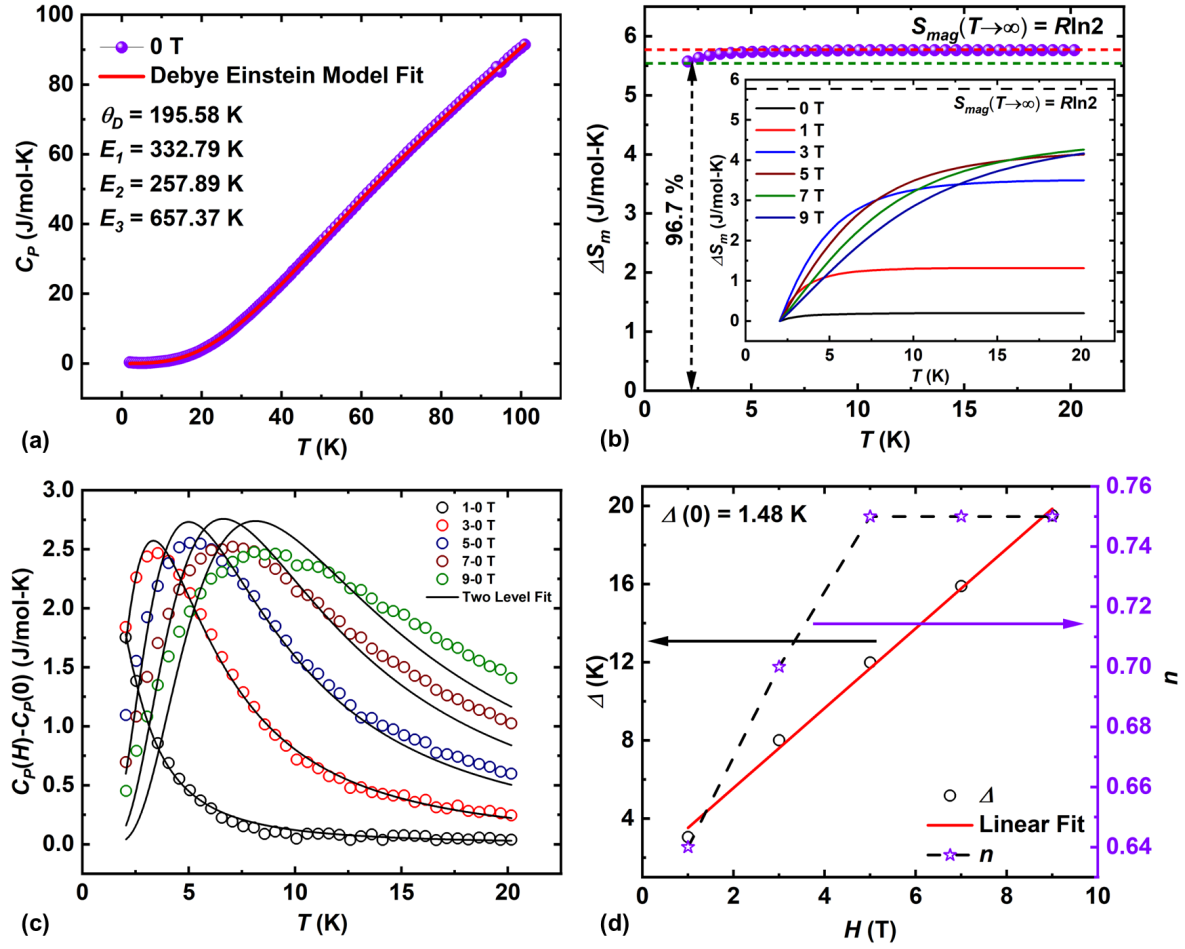


Figure 6.6: (a) Fitting of the specific heat data measured in the absence of the magnetic field with the Debye-Einstein model. (b) Entropy calculated from magnetic specific heat. To better observe the residual magnetic entropy, the  $S_{mag}(T)$  curve is shifted vertically so that its maxima coincide with the  $S_{mag}(T \rightarrow \infty)$ . Inset shows the temperature dependence of magnetic entropy in the presence of different magnetic fields. (c) Variation of Schottky contribution with temperature and its fitting with the two-level model equation. (d) Linear fitting of  $\Delta$  (left axis) values calculated from the CEF fitting and variation of  $n$  values with the magnetic fields.

### 6.3.3 Heat Capacity

Figure 6.6(a) shows the temperature dependence of the specific heat in the absence of an external magnetic field, with the solid line representing a fit using the Debye-Einstein model. To probe the entropy change associated with the variation in spin configuration, it is necessary to single out the lattice contribution from the total specific heat. The temperature dependence of the phononic contribution can be estimated by the Debye-Einstein model. According to this model, the total number of acoustic and phonon modes

sums up to the total number of atoms in the primitive cell (For NaYbZnWO<sub>6</sub>, it is 10). In this case, the relative weights of acoustical and optical modes have been considered 1: $n$ -1, where  $n$  is the total number of atoms. Hence, there are 3 acoustical phonon branches and 27 optical phonon branches. Three Einstein terms have been used to describe the optical modes, while all three acoustical modes have been grouped together and described using one Debye term. Several optical modes are also clubbed to reduce the free parameters and minimize the experimental error [28]. The Debye-Einstein model for this system can be expressed as follows [29, 30]:

$$C_{D-E} = \frac{9aR}{x_D^3} \int_0^{x_D} \frac{x^4 e^x}{(e^x - 1)^2} dx + 3R \sum_{i=1}^3 \frac{b_i x_{E_i}^2 e^{x_{E_i}}}{(e^{x_{E_i}} - 1)^2}$$

where  $x_{D,E} = \theta_{D,E}/T$ ;  $\theta_D$  and  $\theta_E$  are Debye and Einstein temperatures, respectively,  $R$  is the universal gas constant. The coefficients  $a$  and  $b_i$  represent contributions from acoustic and optical phonons, respectively. The values of weight factors are constrained in such a way that their sum equals the total number of atoms in the unit cell (In this case,  $a = 1$ ,  $b_1 = 1$ ,  $b_2 = 2$ , and  $b_3 = 6$ ). Here,  $b_1$  corresponds to W<sup>6+</sup> ion vibrations,  $b_2$  stands for Na<sup>+</sup> and Zn<sup>2+</sup> motion, and  $b_3$  represents the contribution from 6 O<sup>2-</sup> atoms. Using these considerations, we could confine the flexible Debye-Einstein model to a physically reasonable fit.

No long-range magnetic ordering was observed down to 2 K, which further supports the dc magnetization data. In the presence of magnetic fields greater than 1 T, a broad hump is observed at low temperatures, which shifts towards high temperatures with a further increase in the magnetic field (Fig. 6.7 (a)). This behavior represents the Schottky anomaly and originates from the Zeeman splitting of the ground state Kramers doublet, as reported earlier for other Yb compounds [26, 31]. The magnetic entropy calculated after subtracting the lattice part is presented in Fig. 6.6(b). Comparison with entropy for a two-level system ( $J_{eff} = 1/2$ ) reveals that approximately 97 % of the magnetic entropy still remains in the system below 2 K. The inset of Fig. 6.4(b) presents the temperature dependence of the magnetic entropy under different magnetic fields. With increasing the magnetic field, the saturation magnetic entropy keeps increasing to the value of 4.25 J/mol-K, which is  $\approx 74$  % of  $R \ln 2$ . The lower saturation value at high magnetic fields again manifests that a large fraction of spins is still disordered.

The total specific heat under higher magnetic fields can be expressed as;

$$C(T, H) = C(T, 0) + C_{sch}(T, H) \quad (6.3)$$

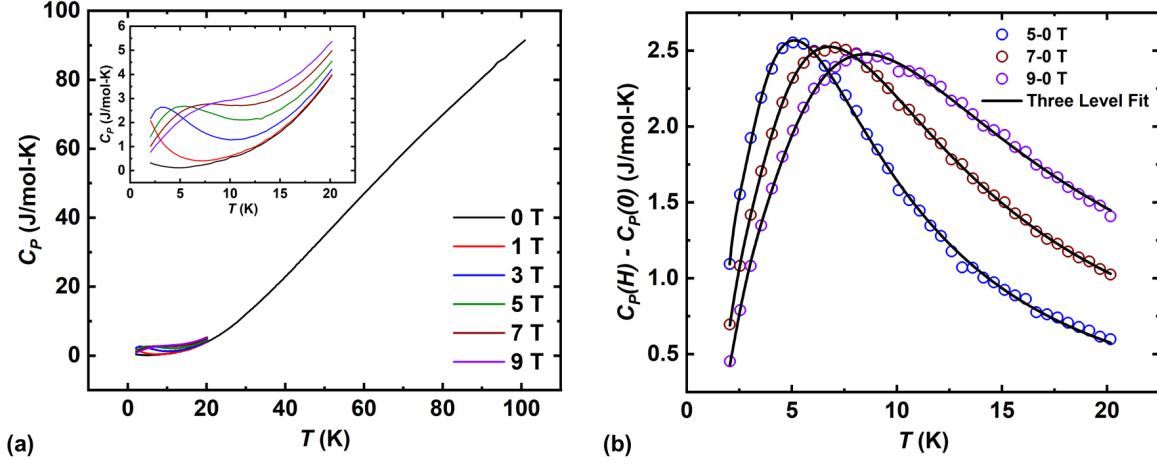


Figure 6.7: (a) Temperature dependence of specific heat data measured under different magnetic fields. The inset shows the variation in low-temperature regions. (b) Fitting of the Schottky contribution using the three-level model.

where the Schottky contribution  $C_{sch}(T, H)$  can be determined by subtracting the zero-field specific heat from the specific heat measured under high magnetic fields, as depicted in Fig. 6.6(c). For a two-level system ( $J_{eff} = 1/2$ ), the Schottky anomaly can be described by the following expression [32–34]

$$C_{sch}(T, H) = nR \left( \frac{\Delta}{T} \right)^2 \frac{\exp(\Delta/T)}{[1 + \exp(\Delta/T)]^2} \quad (6.4)$$

where  $R$  is the gas constant, and  $\Delta$  the energy separation between two levels, while  $n$  is the fraction of the lower-lying level, and hence  $1 - n$  is that of the higher-lying level of the split levels of the ground Kramers doublet state. The energy separation  $\Delta$  is large at a high magnetic field, and the thermal occupation of the higher level decreases with increasing  $\Delta$  as dictated by the Boltzmann factor. Thus, the dependence of the Schottky contribution to the specific heat on the external field and temperature can be described by Eq. 6.4 using  $n$  and  $\Delta$  as fitting parameters. The combined effect of SOC and crystal field results in a Kramers doublet ground state of Yb<sup>3+</sup> ( $m_j = \pm 1/2$ ). The magnetic field dependence of  $\Delta$  can be described as [33–36];

$$\Delta(H) = g\mu_B H_{eff}/k_B \quad (6.5)$$

where  $H_{eff} = \sqrt{H_0^2 + H_1^2}$  such that  $H_{eff} = H_0$  in the absence of the external magnetic field. The fitting analysis of the Schottky contribution using the two-level model, depicted in Fig. 6.6(c), shows that the Schottky anomaly under higher magnetic fields is not well described by the two-level model, and its adequate description requires the inclusion of

Table 6.2: Comparison of  $\Delta$  value obtained from two-level and three-level fit.

Schottky Data	$\Delta$ (K) Two-level fit	$\Delta$ (K) Three-level fit
5-0 T	11.99 $\pm$ 0.16	12.05 $\pm$ 0.07
7-0 T	15.90 $\pm$ 0.32	16.37 $\pm$ 0.11
9-0 T	19.52 $\pm$ 0.47	20.34 $\pm$ 0.27

the second excited level. Including third level results in a good agreement as shown in Fig. 6.7(b). For a three-level system, Schottky contribution can be expressed as follows [37]:

$$C = \frac{R}{T^2} \cdot \frac{g_1 g_0 \Delta_1^2 e^{\Delta_1/T} + g_2 g_0 \Delta_2^2 e^{\Delta_2/T}}{[g_0 + g_1 e^{\Delta_1/T} + g_2 e^{\Delta_2/T}]^2} + R \cdot \frac{g_1 g_2 e^{(\Delta_1 + \Delta_2)/T} \cdot (\Delta_1^2 + \Delta_2^2)}{[g_0 + g_1 e^{\Delta_1/T} + g_2 e^{\Delta_2/T}]^2} \quad (6.6)$$

Where  $R$  is the universal gas constant,  $g_0$ ,  $g_1$ , and  $g_2$  are degeneracy of ground, first excited and second excited state, respectively.  $\Delta_1$  and  $\Delta_2$  denote the energy difference between the ground and first excited state and the ground and second excited state, respectively. A comparison of  $\Delta$  value obtained from two-level and three-level models is given in Table 6.2. The  $\Delta$  values were found to be similar from both models. The dependence of the fitting parameters  $\Delta$  and  $n$  on the magnetic field is presented in Fig. 6.6(d). Since the energy gap  $\Delta$  exhibits a linear behavior, the intercept from its linear fitting results in the energy gap at zero field,  $\Delta(0) \approx 1.48$  K. The probable origin of this nonzero gap is the presence of Yb<sup>3+</sup>–Yb<sup>3+</sup> spin exchange interactions [26, 27, 31]. The value of  $n$  first increases when the field increases until 5 T and then saturates above 5 T. This behavior is reminiscent of the fact that the magnetic field splits the Kramers doublet [26, 27, 31], and a fraction of free spins ( $\sim 75$  %) is excited to higher energy levels. It should be noted that the recovered magnetic entropy is also around 75 % at higher magnetic fields.

### 6.3.4 Theoretical Calculation

The experimental observations described above strongly suggest that the distorted square lattice of NaYbZnWO<sub>6</sub> (Fig. 6.3(c)) is spin frustrated. To examine its cause, we evaluate the four spin exchanges  $J_1$ – $J_4$  describing each distorted square (Fig. 6.8(a)) using the spin Hamiltonian  $H = \sum_{j>i} J_{ij} \vec{S}_i \cdot \vec{S}_j$  where  $J_{ij} = J_1$ – $J_4$ . These spin exchanges are of the Yb–O...W<sup>6+</sup>...O–Yb type as depicted in Fig. 6.8(b). We evaluate them by performing the energy-mapping analyses [38–40] based on DFT+ $U$  calculations.

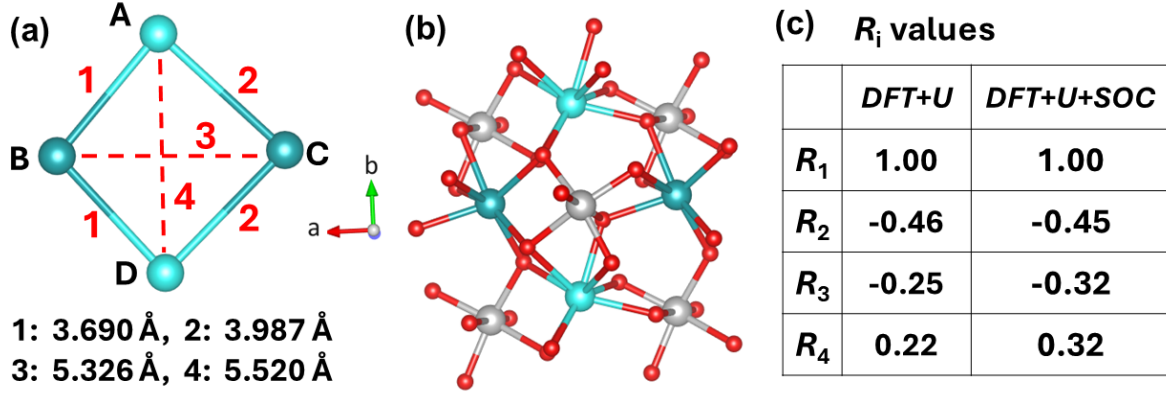


Figure 6.8: (a) Four spin exchange paths  $J_1$ – $J_4$  defined for a distorted square of four Yb<sup>3+</sup> ions in a kite arrangement. The red labels 1–4 represent the spin exchange paths  $J_1$ – $J_4$ , respectively. The black label 1–4 represents the Yb...Yb distances in the spin exchange paths  $J_1$ – $J_4$ , respectively. (b) The WO<sub>6</sub> octahedra surround a distorted square of Yb<sup>3+</sup> ions. They provide the Yb–O...W<sup>6+</sup>...O–Yb exchange paths. (c) The relative spin exchanges  $R_i = J_i/J_1$  ( $i = 1$ –4) obtained from DFT+ $U$  and DFT+ $U$ +SOC calculations.

#### 6.3.4.1 DFT Analysis

In our energy-mapping analysis based on DFT calculations, we employed the frozen core projector augmented plane wave (PAW) method [41] and the PBE exchange-correlation functional [42] encoded in the Vienna ab Initio Simulation Packages (VASP) [43]. To ensure that all broken-symmetry states of a magnet are magnetic insulating, DFT+ $U$  calculations [44] were carried out with an effective on-site repulsion  $U_{eff} = U - J = 5$  eV on Yb. The magnetic anisotropy of NaYbZnWO<sub>6</sub> was examined by DFT+ $U$ +SOC calculations [45].

#### 6.3.4.2 Optimization of the crystal structure of NaYbZnWO<sub>6</sub>

We optimized the crystal structure of NaYbZnWO<sub>6</sub> by performing DFT+ $U$  calculations for its ferromagnetic state using  $U_{eff} = 5$  eV on Yb. All atomic positions are relaxed while the space group and the cell parameters of the experimental structure are kept constant. The optimization calculations used the plane wave cutoff energy of 450 eV, a set of  $(8 \times 8 \times 4)$   $k$ -points, and the threshold of  $10^{-6}$  eV for self-consistent-field energy convergence. The fractional coordinates of the resulting crystal structure are summarized in Table 6.3.

Table 6.3: The fractional coordinates of the atoms in the optimized structure of NaYbZnWO<sub>6</sub>

Atom	Wyckoff symbol	x	y	z
Na(1)	2a	0.2600	0.2150	0.0140
Yb(2)	2a	0.2701	0.3153	0.5016
Zn(1)	2a	0.7477	0.2573	0.2413
W(1)	2a	0.7644	0.2500	0.7617
O(1)	2a	0.5698	0.5301	0.6788
O(2)	2a	0.5352	0.5572	0.3202
O(3)	2a	0.9333	0.9178	0.2190
O(4)	2a	0.9149	0.9418	0.7834
O(5)	2a	0.8695	0.2049	0.5047
O(6)	2a	0.6697	0.2856	0.9873

#### 6.3.4.3 Calculations of the spin exchange using the “isolated dimer” approach

In the usual energy-mapping analysis, the values of  $n$  spin exchanges  $J_1, J_2, \dots, J_n$  defined for a given magnet are determined as follows:

1. Define  $n+1$  ordered spin states of the magnet.
2. Calculate the energies of these states by using the spin Hamiltonian  $H = \sum_{i>j} J_{ij} \vec{S}_i \cdot \vec{S}_j$  where  $J_{ij} = J_1 - J_n$ , to have their energies  $e_1, e_2, \dots, e_n$ , and  $e_{n+1}$  written in terms of the spin exchange constants  $J_1 - J_n$ .
3. Perform DFT+ $U$  calculations for the  $n + 1$  ordered spin states to obtain their energies  $\epsilon_1, \epsilon_2, \dots, \epsilon_n$ , and  $\epsilon_{n+1}$ , which are numerical values.
4. Finally, equate the  $n$  relative energies between  $e_1, e_2, \dots, e_n$ , and  $e_{n+1}$  to those between  $\epsilon_1, \epsilon_2, \dots, \epsilon_n$ , and  $\epsilon_{n+1}$ , to find the numerical values of  $n$  spin exchanges  $J_1, J_2, \dots, J_n$ .

In our study of NaYbZnWO<sub>6</sub>, this traditional approach was not successful because our DFT+ $U$  calculations do not lead to SCF convergence for many of the ordered spin states. Thus, we employed the “isolated-dimer” approach. Namely, to evaluate  $J_1$ , for example, we choose only one  $J_1$  path in the unit cell of the NaYbZnWO<sub>6</sub> crystal and treat the two Yb<sup>3+</sup> cations associated with this path as magnetic ions, while treating all other Yb<sup>3+</sup> cations of the unit cell as nonmagnetic ions by placing their  $f$ -electrons into the core.

This can be done by using different functionals for different Yb atoms, namely, the PBE functional for the Yb representing the magnetic Yb<sup>3+</sup> cations, and Yb<sub>3</sub> functional for those representing the nonmagnetic Yb<sup>3+</sup> cations.

#### 6.3.4.4 Spin exchanges

The spin Hamiltonian for an isolated spin-dimer composed of magnetic ions of spin  $S$  is written as

$$H = J\vec{S}_1 \cdot \vec{S}_2 \quad (6.7)$$

Then, the energies of the ferromagnetic (FM) and antiferromagnetic (AFM) states of the isolated spin dimer are given by

$$E_{FM} = JS^2, E_{AFM} = -JS^2 \quad (6.8)$$

Thus we obtain,

$$J = (E_{FM} - E_{AFM})/S^2 \quad (6.9)$$

so the numerical value of  $J$  is determined once the energy difference  $E_{FM} - E_{AFM}$  is obtained by DFT+ $U$  calculations. The values of  $J_1 - J_4$  (in K) determined using the isolated dimer approach are summarized in Table 6.5.

Table 6.4: Values of the spin exchanges  $J_1 - J_4$  in K determined by DFT+ $U$  and DFT+ $U$ +SOC calculations with  $U_{eff} = 5$  eV. The numbers in the parenthesis are the relative values.

	DFT+ $U$	DFT+ $U$ +SOC
$J_1$	541(1.00)	485(1.00)
$J_2$	-248(-0.46)	-216(-0.45)
$J_3$	-135(-0.25)	-153(-0.32)
$J_4$	120(0.22)	155(0.32)

The  $J_1 - J_4$  values obtained from DFT+ $U$  calculations assumed that Yb<sup>3+</sup> is an  $S = 1/2$  ion with no orbital moment (i.e.,  $L = 0$ ) are unusually high. To examine if this is due to the neglect of spin-orbit coupling in Yb<sup>3+</sup> ions, we carried out DFT+ $U$ +SOC calculations. As summarized in Table 6.5, however, the  $J_1 - J_4$  values from the DFT+ $U$ +SOC calculations are only slightly modified in magnitude than those from the DFT+ $U$  calculations. This reflects that the local environment of each Yb<sup>3+</sup> cation has non-rotational symmetry so that the orbital moment is nearly quenched, as summarized in Table 6.5. The orbital moments of the Yb<sup>3+</sup> ions are of the order of 0.26  $\mu_B$ , which is much smaller than 3  $\mu_B$  expected for an isolated Yb<sup>3+</sup> ion. We note that the magnetic susceptibility data



at high temperatures are well explained by  $J = 7/2$ , which implies that the Yb<sup>3+</sup> ions behave as if they are isolated, perhaps due to their thermal motions. If we use  $J = 7/2$  instead of  $S = 1/2$  in Eq. 6.7, the value of  $J$  is reduced by a factor of 49. Strictly speaking, the results of DFT+ $U$ +SOC calculations are valid at 0 K because they do not include any vibrational excitations. At low temperatures, the magnetic susceptibility data are explained by  $J_{eff} = 1/2$ , implying that the Yb<sup>3+</sup> ions feel their asymmetrical environments probably because their thermal motions are quenched.

Table 6.5: Values of the spin exchanges  $J_1$ – $J_4$  in K determined by DFT+ $U$  and DFT+ $U$ +SOC calculations with  $U_{eff} = 5$  eV. The numbers in the parenthesis are the relative values.

Exchange	Moment	FM state	AFM state
$J_1$	$\mu_S$	0.923	0.937
	$\mu_L$	0.266	0.262
$J_2$	$\mu_S$	0.939	0.941
	$\mu_L$	0.263	0.265
$J_3$	$\mu_S$	0.940	0.942
	$\mu_L$	0.264	0.263
$J_4$	$\mu_S$	0.945	0.942
	$\mu_L$	0.265	0.264

### 6.3.5 Origin of Frustration

The relative values of  $R_i = J_i/J_1$  ( $i = 1$ – $4$ ) are summarized in Fig. 6.8(c), which shows that all three different spin exchange triangles ( $J_1, J_1, J_4$ ), ( $J_2, J_2, J_4$ ) and ( $J_1, J_2, J_3$ ) are spin frustrated in both DFT+ $U$  and DFT+ $U$ +SOC calculations. The 2D lattice of Yb<sup>3+</sup> ions is composed of distorted squares, ABCD (see Fig. 4(a)). Each ABCD square has four triangles: ABC, ABD, BDC, and DCA. The triangles ABC, BDC, and DCA have one AFM and two FM spin exchanges, which leads to spin frustration. The triangle ABD has three AFM spin exchanges, which is a typical case leading to spin frustration. Since all triangles of each distorted square are spin frustrated, each distorted square is spin frustrated, and hence, so is the 2D lattice. This explains why the distorted square spin-lattice of NaYbZnWO<sub>6</sub> is spin frustrated. We note that the spin exchanges  $J_3$  and  $J_4$  are weaker than  $J_1$  and  $J_2$ , but are not negligible. If each distorted square ABCD is described by using only  $J_1$  and  $J_2$ , it is not spin frustrated at all, so our experimental results are not explained by this approximation.

## 6.4 Conclusion

In conclusion, we synthesized NaYbZnWO<sub>6</sub>, a doubly ordered perovskite, via high-pressure and high-temperature methods and analyzed its crystal structure and magnetic properties. Our investigations revealed that NaYbZnWO<sub>6</sub> exhibits no site disorder, featuring well-separated layers and distinct layers of Yb<sup>3+</sup> ions arranged in a distorted square lattice. Our magnetic measurements demonstrate the absence of magnetic ordering down to ultra-low temperatures of 0.4 K, with its magnetic ground state characterized by a  $J_{eff} = 1/2$  Kramers doublet. Field-dependent heat capacity measurements indicate an internal magnetic field of approximately 1.5 K. These collective findings strongly suggest the presence of spin frustration within the distorted square lattice of Yb<sup>3+</sup> ions in NaYbZnWO<sub>6</sub>, as evidenced by the four spin exchanges of each distorted square evaluated by DFT calculations. Taken together, our results highlight NaYbZnWO<sub>6</sub>, devoid of site disorder, as a potential quantum spin liquid system based on a distorted square spin-lattice.

# Bibliography

- [1] L. Balents, Spin liquids in frustrated magnets, *Nature* **464**, 199 (2010).
- [2] G. Misguich and C. Lhuillier, *Frustrated Spin Systems*, H. T. Diep, (World Scientific), (2005).
- [3] S. S. Gong, W. Zhu, D. N. Sheng, O. I. Motrunich, M. P. A. Fisher, Plaquette Ordered Phase and Quantum Phase Diagram in the Spin 1/2  $J_1$ - $J_2$  Square Heisenberg Model, *Phys. Rev. Lett.* **113**, 027201 (2014).
- [4] O. Mustonen, S. Vasala, E. Sadrollahi, K. P. Schmidt, C. Baines, H. C. Walker, I. Terasaki, F. J. Litterst, E. Baggio-Saitovitch, and M. Karppinen, Spin-liquid-like state in a spin-1/2 square-lattice antiferromagnet perovskite induced by  $d^{10}$ - $d^0$  cation mixing, *Nat. comm.* **9**, 1 (2018).
- [5] T. Koga, N. Kurita, M. Avdeev, S. Danilkin, T. J. Sato, and H. Tanaka, Magnetic structure of the  $S=1/2$  quasi-two-dimensional square-lattice Heisenberg antiferromagnet  $\text{Sr}_2\text{CuTeO}_6$ , *Phys. Rev. B* **93**, 054426 (2016).
- [6] Y. Li, D. Adroja, R. I. Bewley, D. Voneshen, A. A. Tsirlin, P. Gegenwart, and Q. Zhang, Crystalline Electric-Field Randomness in the Triangular Lattice Spin-Liquid  $\text{YbMgGaO}_4$ , *Phys. Rev. Lett.* **118**, 107202 (2017).
- [7] L. Ding, P. Manuel, S. Bachus, F. Gr  bler, P. Gegenwart, J. Singleton, R. D. Johnson, H. C. Walker, D. T. Adroja, A. D. Hillier *et al.*, Gapless spin-liquid state in the structurally disorder-free triangular antiferromagnet  $\text{NaYbO}_2$ , *Phys. Rev. B* **100**, 144432 (2019).
- [8] J. G. Rau, L. S. Wu, A. F. May, L. Poudel, B. Winn, V. O. Garlea, V. O. Garlea, A. Huq, P. Whitfield, A. E. Taylor, M. D. Lumsden *et al.*, Anisotropic Exchange within Decoupled Tetrahedra in the Quantum Breathing Pyrochlore  $\text{Ba}_3\text{Yb}_2\text{Zn}_5\text{O}_{11}$ , *Phys. Rev. Lett.* **116**, 257204 (2016).

- 
- [9] Y. Li, G. Chen, W. Tong, L. Pi, J. Liu, Z. Yang, X. Wang, and Q. Zhang, Rare-Earth Triangular Lattice Spin Liquid: A Single-Crystal Study of  $\text{YbMgGaO}_4$ , *Phys. Rev. Lett.* **115**, 167203 (2015).
- [10] Z. Zhu, P. A. Maksimov, S. R. White, and A. L. Chernyshev, Disorder-Induced Mimicry of a Spin Liquid in  $\text{YbMgGaO}_4$ , *Phys. Rev. Lett.* **119**, 157201 (2017).
- [11] R. Farla, S. Bhat, S. Sonntag, A. Chanyshv, S. Ma, T. Ishii, Z. Liu, A. Néri, N. Nishiyama, G. A. Faria *et al.*, Extreme conditions research using the large-volume press at the P61B endstation, PETRA III, *J. synchrotron radiation* **29**, 409 (2022).
- [12] Y. Seto, Development of a Software Suite on X-ray Diffraction Experiments, *Rev. High Press. Sci. technology* **20**, 269 (2010).
- [13] Y. Seto, Yusuke, Whole Pattern Fitting for Two-Dimensional Diffraction Patterns from Polycrystalline Materials, *Rev. High Press. Sci. Technology* **22**, 144 (2012).
- [14] V. Petricek, M. Dušek, and L. Palatinus, Crystallographic Computing System JANA2006: General features, *Z. Kristallogr. Cryst. Mater.* **229**, 345 (2014).
- [15] R. Shankar PN, F. Orlandi, P. Manuel, W. Zhang, P. S. Halasyamani, and A. Sundaresan, Structural, Magnetic, and Electrical Properties of Doubly Ordered Perovskites  $\text{NaLnNiWO}_6$  ( $\text{Ln} = \text{La}, \text{Pr}, \text{Nd}, \text{Sm}, \text{Eu}, \text{Gd}, \text{and Tb}$ ), *Chem. Mater.* **32**, 5641 (2020).
- [16] P. K. Davies, H. Wu, A. Y. Borisevich, I. E. Molodetsky, and L. Farber, Crystal Chemistry of Complex Perovskites: New Cation-Ordered Dielectric Oxides, *Annu. Rev. Mater. Res.* **38**, 369 (2008).
- [17] G. King and P. M. Woodward, Cation ordering in perovskites, *J. Mat. Chem.* **20**, 5785 (2010).
- [18] S. Vasala and M. Karppinen,  $\text{A}_2\text{B}'\text{B}''\text{O}_6$  perovskites: a review, *Progress in solid state chemistry*, **43**, 1 (2015).
- [19] P. Zuo, C. V. Colin, H. Klein, P. Bordet, E. Suard, E. Elkaim, and C. Darie, Structural Study of a Doubly Ordered Perovskite Family  $\text{NaLnCoWO}_6$  ( $\text{Ln} = \text{Y}, \text{La}, \text{Pr}, \text{Nd}, \text{Sm}, \text{Eu}, \text{Gd}, \text{Tb}, \text{Dy}, \text{Ho}, \text{Er}, \text{Yb}$ ): Hybrid Improper Ferroelectricity in Nine New Members, *Inorganic Chemistry* **56**, 8478 (2017).
- [20] T. Besara, M. S. Lundberg, J. Sun, D. Ramirez, L. Dong, J. B. Whalen, R. Vasquez, F. Herrera, J. R. Allen, M. W. Davidson *et al.*, Single crystal synthesis and

- magnetism of the  $\text{BaLn}_2\text{O}_4$  family ( $\text{Ln}$  = lanthanide), *Prog. Solid State Chem.* **42**, 23 (2014).
- [21] M. Mitric, B. Antic, M. Balanda, D. Rodic, and M. L. Napijalo, An x-ray diffraction and magnetic susceptibility study of  $\text{Yb}_x\text{Y}_{2-x}\text{O}_3$ , *J. Phys.: Condens. Matter* **9**, 4103 (1997).
- [22] H. W. J. Blöte, R. F. Wieringa, and W. J. Huiskamp, Heat-capacity measurements on rare-earth double oxides  $\text{R}_2\text{M}_2\text{O}_7$ , *Physica* **43**, 549 (1969).
- [23] H. B. Cao, A. Gukasov, I. Mirebeau, and P. Bonville, Anisotropic exchange in frustrated pyrochlore  $\text{Yb}_2\text{Ti}_2\text{O}_7$ , *J. Phys.: Condens. Matter* **21**, 492202 (2009).
- [24] S. Guo, A. Ghasemi, C. L. Broholm, and R. J. Cava, Magnetism on ideal triangular lattices in  $\text{NaBaYb}(\text{BO}_3)_2$ , *Phys. Rev. Material* **3**, 094404 (2019).
- [25] C. Kittel, *Introduction to Solid State Physics* (Wiley, Hoboken, NJ, 2005).
- [26] K. Somesh, S. S. Islam, S. Mohanty, G. Simutis, Z. Guguchia, C. Wang, J. Sichelschmidt, M. Baenitz, R. Nath, Absence of magnetic order and emergence of unconventional fluctuations in the  $J_{eff}=1/2$  triangular-lattice antiferromagnet  $\text{YbBO}_3$ , *Phys. Rev. B* **107**, 064421 (2023).
- [27] S. Kundu, A. Hossain, Pranava Keerthi S, R. Das, M. Baenitz, P. J. Baker, J.-C. Orain, D. C. Joshi, R. Mathieu, P. Mahadevan, S. Pujari, S. Bhattacharjee, A. V. Mahajan, and D. D. Sarma, Signatures of a Spin-1/2 Cooperative Paramagnet in the Diluted Triangular Lattice of  $\text{Y}_2\text{CuTiO}_6$ , *Phys. Rev. Lett.* **125**, 117206 (2020).
- [28] P. Svoboda, J. Vejpravova, N.-T. Kim-Ngan, and F. Kaysel, Specific heat study of selected  $\text{RNi}_5$ , *J. Magn. Magn. Mater.* **272-276**, 595 (2004).
- [29] R. Kumar and A. Sundaresan, Unveiling a hidden multiferroic state under magnetic fields in  $\text{BaHoFeO}_4$ , *Phys. Rev. B* **107**, 184420 (2023).
- [30] R. Kumar and A. Sundaresan, Antisite disorder driven cluster glass state and colossal magnetoresistance in  $\text{MnSb}_2\text{Se}_4$ , *Phys. Rev. B* **106**, 134423 (2022).
- [31] R. Bag, M. Ennis, C. Liu, S. E. Dissanayake, Z. Shi, J. Liu, L. Balents, and S. Haravifard, Realization of quantum dipoles in triangular lattice crystal  $\text{Ba}_3\text{Yb}(\text{BO}_3)_3$ , *Phys. Rev. B* **104**, L220403 (2021).
- [32] H. M. Rosenberg, *Low Temperature Solid State Physics* Oxford University Press, Oxford, 1963.

- [33] L. Xie, T. Su, and X. Li, Magnetic field dependence of Schottky anomaly in the specific heats of stripe-ordered superconductors  $\text{La}_{1.6-x}\text{Nd}_{0.4}\text{Sr}_x\text{CuO}_4$ , *Physica C: Superconductivity* **480**, 14 (2012).
- [34] S. Mahdaviifar and A. Akbari, Heat capacity of Schottky type in low-dimensional spin systems, *J. Phys.: Condens. Matter* **20**, 215213 (2008).
- [35] G. Mu, Y. Wang, L. Shan, and H.-H. Wen, Possible nodeless superconductivity in the noncentrosymmetric superconductor  $\text{Mg}_{12-\delta}\text{Ir}_{19}\text{B}_{16}$ , *Phys. Rev. B* **76**, 064527 (2007).
- [36] Y. Wang, J. Yan, L. Shan, H.-H. Wen, Y. Tanabe, T. Adachi, and Y. Koike, Weak-coupling  $d$ -wave BCS superconductivity and unpaired electrons in overdoped  $\text{La}_{2-x}\text{Sr}_x\text{CuO}_4$ , *Phys. Rev. B* **76**, 064512 (2007).
- [37] M. Souza, R. Paupitz, A. Seridonio, and R. E. Lagos, Specific Heat Anomalies in Solids Described by a Multilevel Model, *Braz. J. Phys.* **46**, 206 (2016).
- [38] H. Xiang, C. Lee, H.-J. Koo, X. Gong, and M.-H. Whangbo, Magnetic properties and energy-mapping analysis, *Dalton Trans.* **42**, 823 (2013).
- [39] M.-H. Whangbo and H. Xiang, *Magnetic Properties from the Perspectives of Electronic Hamiltonian*, Handbook of Solid State Chemistry (Wiley Online Library) (2017).
- [40] M.-H. Whangbo, H.-J. Koo, and R. K. Kremer, Spin Exchanges between Transition Metal Ions Governed by the Ligand  $p$ -Orbitals in Their Magnetic Orbitals, *Molecules* **26**, 531 (2021).
- [41] G. Kresse and D. Joubert, From ultrasoft pseudopotentials to the projector augmented-wave method, *Phys. Rev. B* **59**, 1758 (1999).
- [42] J. P. Perdew, K. Burke, and M. Ernzerhof, Generalized gradient approximation made simple, *Phys. Rev. Lett.* **77**, 3865 (1996).
- [43] G. Kresse and J. Furthmüller, Efficiency of ab-initio total energy calculations for metals and semiconductors using a plane-wave basis set, *Comput. Mater. Sci.* **6**, 15 (1996).
- [44] S. L. Dudarev, G. A. Botton, S. Y. Savrasov, C. J. Humphreys, and A. P. Sutton, Electron-energy-loss spectra and the structural stability of nickel oxide: An LSDA+U study, *Phys. Rev. B* **57**, 1505 (1998).

- [45] J. Kuneš, P. Novák, R. Schmid, P. Blaha, and K. Schwarz, Electronic structure of fcc Th: Spin-orbit calculation with  $6p_{1/2}$  local orbital extension, Phys. Rev. B **64**, 153102 (2001).

## Chapter 7

# **Sr<sub>3</sub>CoNb<sub>2</sub>O<sub>9</sub>: A New Triangular Lattice-Based Kitaev Model Candidate**

This chapter documents an extensive study of a triangular lattice-based compound Sr<sub>3</sub>CoNb<sub>2</sub>O<sub>9</sub> using various magnetic, thermodynamic, and muon spectroscopic measurements down to sub-kelvin temperatures. In this compound, Co ions form isolated octahedra that align parallel to each other along the *b*-axis. Temperature dependence of magnetization measurements reveals a broad antiferromagnetic anomaly around 1.3 K, while field dependence of magnetization measurements unveils the presence of 1/3 and 2/3 magnetization plateau at 2.4 T and 4.1 T, respectively. Specific heat measurements reveal two magnetic transitions around 1.29 and 1.53 K, further resolving the magnetic anomaly seen in magnetization data around 1.3 K. Interestingly, zero-field  $\mu$ SR spectra collected at different temperatures from 90 mK to 20.6 K do not show any oscillation which would have indicated a long-range magnetic ordering. However, the relaxation rate ( $\lambda$ ) starts increasing below 10 K and exhibits a plateau below 1.3 K, indicating the presence of a correlated state from 10 to 1.3 K. Furthermore, this dynamic state observed below 1.3 K remains stable even in a magnetic field,  $H = 3200$  Oe, which is almost 100 times stronger than the nuclear field present (34 Oe). Our theoretical investigation reveals the presence of bond-dependent exchange interactions and frustration in the magnetic lattice. Considering the Jackelli-Khaliullin criteria, Sr<sub>3</sub>CoNb<sub>2</sub>O<sub>9</sub> is a potential Kitaev candidate as it has spin-orbit entangled  $J_{eff} = 1/2$  moments placed on a geometrically frustrated triangular lattice with Co octahedra arranged in a “parallel edge”-sharing.



## 7.1 Introduction

The concept of quantum spin liquid (QSL) was first introduced by P. W. Anderson in 1973 as a resonating valence bond state for a triangular lattice decorated with quantum spins [1]. Experimentally realizing such materials has been a difficult task. A well-established strategy to identify a QSL is to utilize geometrical frustration [2] present in triangular, kagome, pyrochlore lattices, etc. An alternate and newer approach is to use exchange frustration present in a honeycomb lattice, as proposed by Kitaev [3]. The resulting QSL can host gauge field excitations and Majorana fermions, leading to a completely new magnetism field [3]. Lately, there have been continuous efforts to realize the Kitaev model in real materials [4]. The most significant ingredient for Kitaev materials is the presence of bond-dependent exchange interactions between effective angular momentum  $J_{eff} = 1/2$  magnetic moments [5]. In 2009, Jackeli and Khaliullin envisioned a promising solution to boost the search for Kitaev candidates by studying magnetic interactions in Mott insulators with strong spin-orbit couplings [6]. They realized that the geometrical arrangement of neighboring magnetic octahedra decides the nature of the dominant exchange interactions. For a corner-sharing geometry, symmetric Heisenberg interactions will be dominating, while for an edge-sharing or “parallel edge”-sharing geometry, Kitaev-type interactions will dominate. With this motivation, we embark on realizing new Kitaev candidates.

Although the majority of attempts to realize Kitaev materials have been focused on  $4d/5d$  transition metal compounds with strong spin-orbit coupling, recent theoretical works indicate that  $\text{Co}^{2+}$  based compounds can also lead to dominating Kitaev-interactions if favorable conditions are met [7,8]. The  $\text{Co}^{2+}$  ( $3d^7$ ) ions have a  $^4F$  ( $S = 3/2$ ,  $L = 3$ ) multiplet ground state [9,10], which further splits into three orbital multiplets if  $\text{Co}^{2+}$  ions are situated in an octahedral chemical environment (cubic crystal field). The splitting leads to  $^4T_1$  as the ground state, which is further split by cubic SOC in three spin-orbit-split multiplets, and the ground state can be described by  $J_{eff} = 1/2$ . These multiplets can be further split if the CEF is not purely cubic or Co octahedra is distorted [11]. There have been some reports to search for the Kitaev interactions within the honeycomb (which is not geometrically frustrated) lattice-based  $J_{eff} = 1/2$  state of  $\text{Co}^{2+}$ , such as  $\text{Na}_3\text{CoSb}_2\text{O}_6$  [11–13],  $\text{Na}_2\text{Co}_2\text{TeO}_6$  [11,12,14] and  $\text{BaCo}_2(\text{AsO}_4)_2$  [15].

The present study focuses on how Kitaev physics will behave in geometrically frustrated systems, particularly in triangular lattice antiferromagnets (TLAFs). Recently,

$\text{CoI}_2$ , a TLAf, has been proposed by C. Kim *et al.* [16] as a Kitaev candidate and a similar proposition has been made for triangular lattice-based compound  $\text{NaRuO}_2$  by A. Razpopov *et al.* [17]. It should be noted that both compounds have Co octahedra arranged in edge-sharing geometry. However, to the best of our knowledge, we have not found any report on Kitaev candidates based on “parallel edge”-sharing geometry, which is the subject of the present work.

In this chapter, we propose  $\text{Sr}_3\text{CoNb}_2\text{O}_9$  as a Kitaev candidate, in which Co octahedra are arranged in the “parallel edge”-sharing geometry.  $\text{Sr}_3\text{CoNb}_2\text{O}_9$  exhibit two magnetic transitions, one at 1.53 K and the other at 1.29 K, along with 1/3 and 2/3 magnetization plateau. The  $\mu\text{SR}$  measurements unveil a dynamic state below 10 K, which persists down to the transition temperature (1.3 K). The presence of a dynamic state is supported by theoretical studies, which further reveal the bond-dependent nature of these interactions. Considering the presence of anisotropic exchange interaction and geometrical frustration in a triangular lattice made of  $J_{\text{eff}} = 1/2$  moments,  $\text{Sr}_3\text{CoNb}_2\text{O}_9$  is a perfect Kitaev candidate.

## 7.2 Experimental

The high-quality polycrystalline samples of  $\text{Sr}_3\text{CoNb}_2\text{O}_9$  have been prepared through conventional solid-state synthesis by using  $\text{SrCO}_3$ ,  $\text{Co}_3\text{O}_4$ ,  $\text{Nb}_2\text{O}_5$  as the starting materials. The raw materials were mixed in the stoichiometric ratio using a mortar pestle and kept in the furnace at 1173 K for 24 h. The resulting material was pelletized and treated at 1473 K for 12 h with intermittent grindings for homogeneity. To confirm the phase purity and explore the crystal structure of the compound, x-ray diffraction measurements have been carried out using a PANalytical Empyrean Alpha I diffractometer equipped with  $\text{Cu-K}\alpha_1$  single wavelength ( $\lambda = 1.54059 \text{ \AA}$ ). Magnetic measurements down to 2 K are performed using a magnetic property measurement system (MPMS3), Quantum Design, USA. The iQuantum Helium-3 refrigerator option with MPMS3 has been used to measure the magnetic properties down to 0.4 K. The physical properties such as heat capacity, AC susceptibility, and thermal conductivity have been measured using a physical properties measurement system (PPMS), Quantum Design, USA. The heat capacity measurements are done in two steps: 1. Heat capacity measurement of the Apiezon-N grease without sample. 2. Heat capacity measurement of the sample and Apiezon-N grease. Both heat capacity measurements are done using isobaric thermal

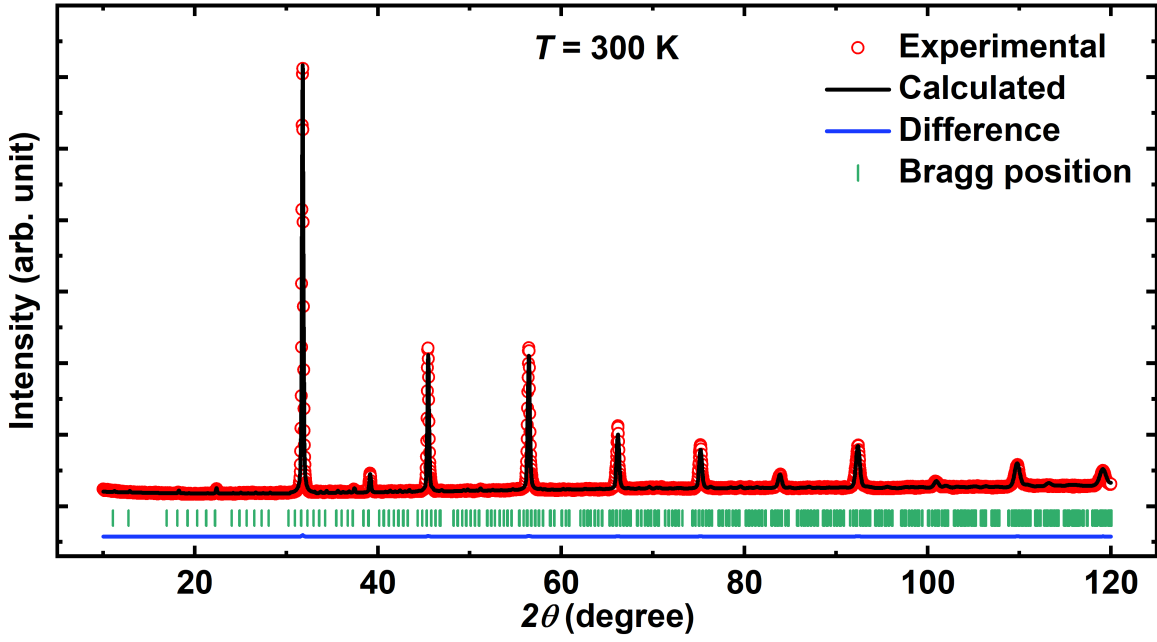


Figure 7.1: Rietveld refinement of the X-ray diffraction pattern collected at  $T = 300$  K. Experimental pattern, simulated pattern, difference, and Bragg peaks are represented by red open circles, solid black line, blue solid line, and green color, respectively.

relaxation calorimetry. For thermal transport measurements, the sample pellet was cut into a rectangular bar ( $1 \times 3 \times 7$  mm<sup>3</sup>), mounted in a standard four-probe manner on a thermal transport puck, and covered with a copper radiation shield. Muon spectroscopy measurements were conducted at the ISIS facility, Rutherford Appleton Laboratory, UK, using the MuSR spectrometer, employing zero-field (ZF), longitudinal-field (LF), and weak transverse field (WTF) options. The powder sample was mounted on a high-purity silver plate, which gives only a non-relaxing background signal. A dilution refrigerator was employed to achieve ultra-low measurement temperatures down to 0.044 K. Analysis of the  $\mu\text{SR}$  measurements was performed using the MANTID software [18, 19].

## 7.3 Results

### 7.3.1 Crystal Structure

Figure 7.1 depicts the Rietveld refinement of the x-ray diffraction pattern of  $\text{Sr}_3\text{CoNb}_2\text{O}_9$ , which is carried out using Jana 2020 software [20]. The experimental and theoretical data agree very well ( $\chi^2 = 1.87$  %) and confirm the phase purity of the compound. The

Table 7.1: Crystallographic parameters along with occupancy and isotropic displacement parameters obtained from the Rietveld refinement of the powder XRD data. Space group:  $P2_1/c$ ,  $V = 767.71(2) \text{ \AA}^3$ ,  $\chi^2 = 2.97 \%$ , Bragg  $R$  factor =  $3.6 \%$ ,  $R_f = 4.86 \%$

Atom	Wyckoff symbol	x	y	z	Occupancy	$B_{iso}(\text{\AA}^2)$
Sr(1)	$4e$	0.2434(18)	0.4905(33)	0.0828(8)	1.0	0.015(4)
Sr(2)	$4e$	0.7539(20)	-0.0072(32)	0.0836(9)	1.0	0.026(4)
Sr(3)	$4e$	0.2526(23)	-0.0088(24)	0.2488(10)	1.0	0.025(5)
Co(1)	$2a$	0.0	0.0	0.0	1.0	0.023(5)
Co(2)	$2d$	0.5	0.5	0.0	1.0	0.019(4)
Nb(1)	$4e$	0.5042(24)	0.5027(29)	0.3339(12)	1.0	0.017(3)
Nb(2)	$4e$	0.0048(21)	0.0056(26)	0.3363(11)	1.0	0.021(4)
O(1)	$4e$	1.0305(75)	0.6546(13)	0.2943(47)	1.0	1.0
O(2)	$4e$	0.4711(73)	0.8148(87)	0.2499(39)	1.0	1.0
O(3)	$4e$	0.2725(54)	0.4752(72)	0.2736(28)	1.0	1.0
O(4)	$4e$	1.0066(996)	0.7603(115)	0.9238(45)	1.0	1.0
O(5)	$4e$	-0.0014(67)	0.2665(98)	0.9340(39)	1.0	1.0
O(6)	$4e$	0.4991(71)	0.3572(89)	0.8973(35)	1.0	1.0
O(7)	$4e$	0.5650(46)	0.7747(65)	0.9575(24)	1.0	1.0
O(8)	$4e$	0.7942(54)	0.0587(70)	0.9106(28)	1.0	1.0
O(9)	$4e$	0.2738(67)	0.5243(98)	0.9304(29)	1.0	1.0

refinement revealed that the compound crystallizes into a monoclinic structure (space group:  $P2_1/c$ ) with the following lattice parameters:  $a = 9.7905 \text{ \AA}$ ,  $b = 5.6540 \text{ \AA}$ ,  $c = 16.9698 \text{ \AA}$ , and  $\beta = 125.194(11)^\circ$ . The obtained parameters agree very well with the earlier reported ones [21]. The refined parameters are summarized in Table 7.1. Figure 7.2 (a) illustrates how various ions are placed in a unit cell of  $\text{Sr}_3\text{CoNb}_2\text{O}_9$ . In the unit cell,  $\text{Co}^{2+}$  ions have two independent crystallographic positions ( $2a$ ,  $2d$ ),  $\text{Sr}^{2+}$  ions have three different sites under the same Wyckoff position ( $4e$ ), and  $\text{Nb}^{5+}$  ions have two different sites under one Wyckoff position ( $4e$ ). The crystal environment of  $\text{Co}^{2+}$  and  $\text{Nb}^{5+}$  ions is octahedral while  $\text{Sr}^{2+}$  ions are surrounded by 8 oxygen ions. The  $\text{Co}^{2+}$  ions form a layered isosceles triangular lattice, as depicted in Fig. 7.2(b) and (c). The layers are widely separated along the  $a$ -axis, and the compound can be considered a two-dimensional magnet. The  $\text{CoO}_6$  octahedra are axially elongated and may lead to in-plane anisotropy in the  $\text{CoO}_4$  plane. Interestingly, Co octahedra are isolated from each other and coordinated by  $\text{SrO}_8$  and  $\text{NbO}_6$  polyhedra, but they are perfectly parallel to each other along the  $b$  - axis, resulting in a "parallel edge"-sharing geometry.

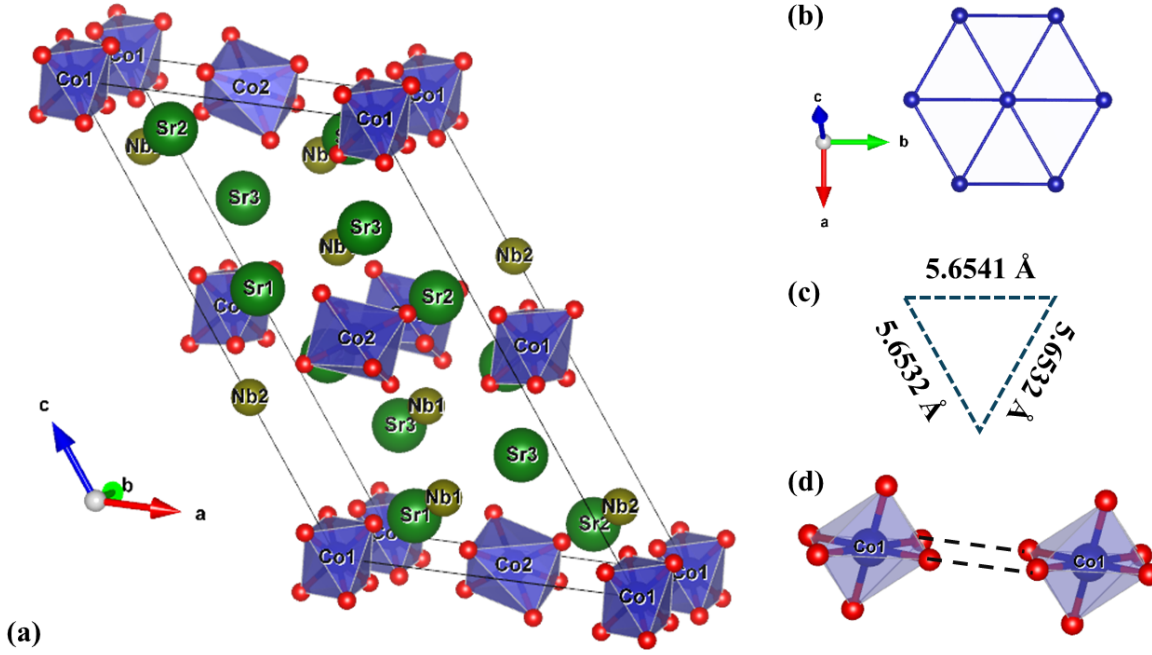


Figure 7.2: (a) Atomic arrangement of different ions in the unit cell. Co1 and Co2 octahedra are shown in blue color. (b) Top view of the magnetic lattice in the  $ab$  plane. (c) Sides of an isosceles triangle of  $\text{Co}^{2+}$  ions. (d) Co1 octahedra are perfectly parallel to each other along the  $b$  axis.

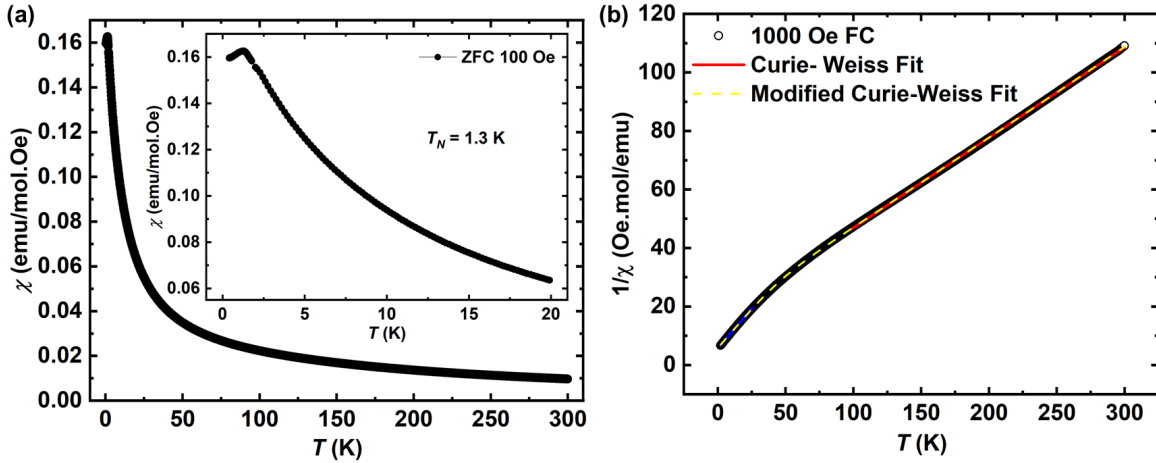


Figure 7.3: (a) Temperature dependence of dc magnetic susceptibility performed under ZFC down to 0.4 K. Inset shows zoomed version from 0.4 to 20 K. (b) Solid lines of blue and red color represent fitting of low-temperature and high-temperature linear region of the inverse susceptibility data by using the Curie-Weiss model, while yellow dotted line represents fitting of the inverse susceptibility data with the help of the modified Curie-Weiss model.

### 7.3.2 DC Magnetization

To explore the low-temperature magnetism, DC magnetization measurements have been carried out down to 0.4 K, as shown in Figure 7.3 (a). The compound undergoes a magnetic phase transition below 1.3 K, represented by a broad peak in the susceptibility data (Inset of Fig. 7.3(a)). A careful investigation of the inverse susceptibility data reveals two different linear regions, one from 100 to 300 K and the other from 2 to 40 K. Analyzing both linear regions with the Curie-Weiss model, as shown in Fig. 7.3(b), results in different parameters as follows: For the high-temperature region,  $\mu \sim 5.1 \mu_B/\text{f.u.}$ ,  $\theta_{CW} \sim -52.2$  K, degree of frustration,  $f \sim 40$  and for the low-temperature region,  $\mu \sim 3.8 \mu_B/\text{f.u.}$ ,  $\theta_{CW} \sim -10.5$  K, degree of frustration,  $f \sim 8$ . The reason behind two linear regions in the susceptibility is splitting of the ground state multiplet as a combined effect of CEF and SOC as mentioned in the section 7.1. The typical splitting of  $\text{Co}^{2+}$  ions in the presence of crystal electric field (CEF) and spin-orbit coupling (SOC) is shown in Fig. 1.13(a), and the ground state can be described by  $J_{eff} = 1/2$ . One can estimate the difference between the ground state and the first excited state by analyzing the inverse susceptibility data with the modified Curie-Weiss law [22, 23];

$$1/\chi = 8.(T - \theta_{CW}). \left( \frac{1 + \exp^{-\frac{E_{10}}{k_B T}}}{\mu_{eff,0}^2 + \mu_{eff,1}^2 \cdot \exp^{-\frac{E_{10}}{k_B T}}} \right) \quad (7.1)$$

where  $\mu_{eff,0}$  and  $\mu_{eff,1}$  stand for effective moments in the ground state and first excited state, respectively, while  $E_{10}$  gives the energy difference between the ground state and first excited state. Yellow dashed line in Fig. 7.3(b) illustrates the fitting of the inverse susceptibility data with eq. 7.1 and results in  $E_{10} \sim 149$  K. Hence, the reduced value of the effective magnetic moment of  $\text{Co}^{2+}$  ions from low-temperature fit and splitting of their electronic states due to CEF and SOC indicate that the ground state can be assigned to  $J_{eff} = 1/2$  [11, 13, 15]. Furthermore, to explore the possibility of spin freezing, AC magnetic susceptibility measurements have been performed in a temperature range of 2 – 50 K. The sample is perturbed by a small AC magnetic field of 10 Oe after cooling it down to 10 K, and its temperature-dependent response is recorded at different frequencies. Figure 7.4(a) exhibits the real part of the ac susceptibility, while Fig. 7.4(b) shows the imaginary part. Both parts do not show any dispersion and hence confirm the absence of spin freezing from 2 to 50 K [24, 25].

The isothermal magnetization measurements have been carried out at 0.4 and 0.8 K by sweeping the magnetic fields from +7 T to -7 T at a constant sweeping rate of 700 Oe/sec.

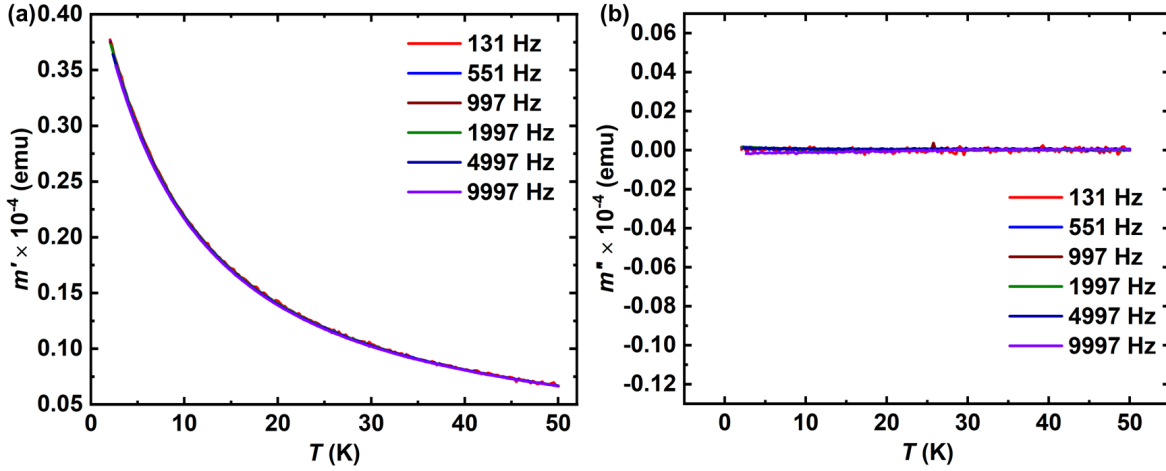


Figure 7.4: (a) Variation of the frequency-dependent real part of ac susceptibilities with temperature. (b) Temperature dependence of imaginary part of the ac susceptibilities at different frequencies.

The field dependence of the magnetization in the first quadrant is shown in Fig. 7.5 (a). The magnetization appears to increase linearly up to 6 T and then saturates. A slow increase in magnetization above 6 T can be attributed to the temperature-independent Van-Vleck magnetization originating from  $\text{Co}^{2+}$  ions in an octahedral environment. The first-order derivative of the  $M$  vs.  $H$  curves revealed the presence of anomalies around 1/3rd and 2/3rd of  $M_S$  corresponding to 2.4 T and 4.1 T, respectively. Similar anomalies in the  $dM/dH$  data have been seen previously for the Ba analog,  $\text{Ba}_3\text{CoNb}_2\text{O}_9$  [26]. The anomaly at 1/3 rd of saturation magnetization agrees very well with the previous report [21], although the 2/3 rd plateau was not reported earlier as the reported  $M$  versus  $H$  measurements were done at 1.4 K. The anomalies observed in the present case are not prominent due to the averaging effect in a polycrystalline sample [26]. The magnetization plateau can be explained by the presence of a finite energy gap in the magnetic energy spectrum of  $\text{Sr}_3\text{CoNb}_2\text{O}_9$  under an applied magnetic field [27].

### 7.3.3 Heat Capacity

The temperature dependence of the heat capacity down to 370 mK and its fitting with the Debye-Einstein model is shown in Fig. 7.6(a). The heat capacity data show two successive magnetic anomalies at 1.53 K and 1.29 K, as depicted in the inset of Fig. 7.6(b), consistent with the earlier reported values [21]. The change in magnetic entropy can be estimated by extracting the lattice contribution from the total heat capacity. The Debye-Einstein model can be used to calculate the temperature-dependent phononic



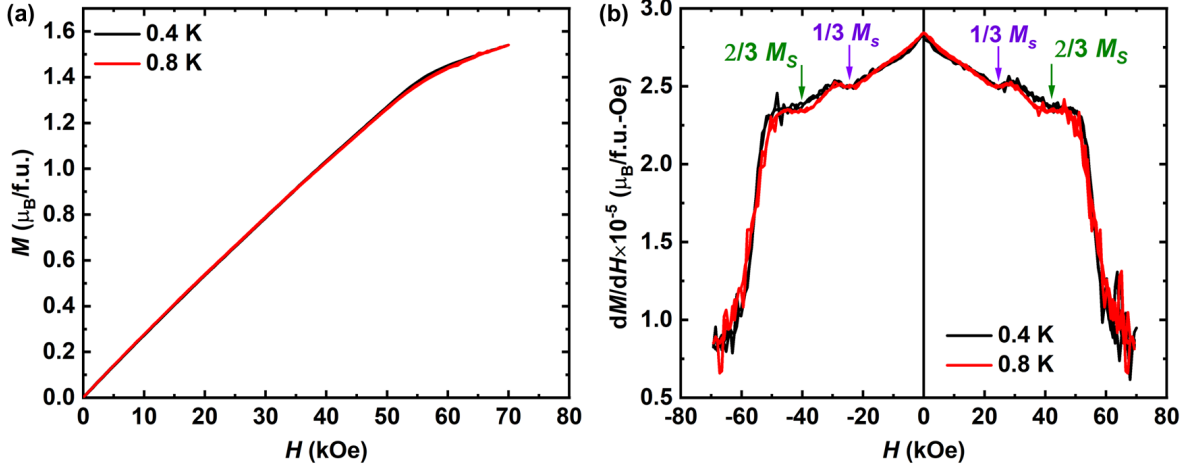


Figure 7.5: (a) Field dependence of the magnetization under isothermal conditions at 0.4 and 0.8 K. (b) First order derivative of magnetization showing anomalies at  $1/3$  and  $2/3$  of  $M_S$ .

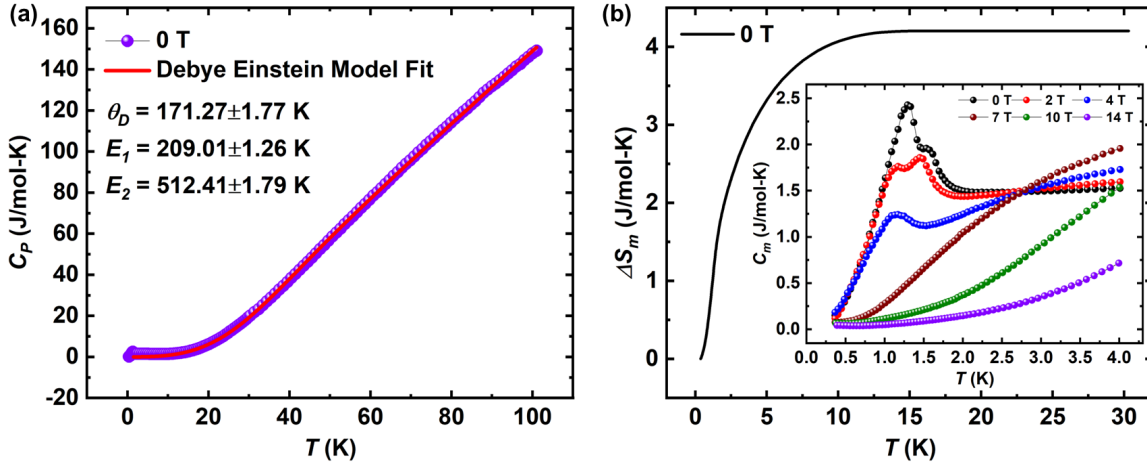


Figure 7.6: (a) Heat capacity data measured in the temperature range from 370 mK to 100 K and its fitting with the Debye-Einstein model equation 7.2. (b) Temperature dependence of the magnetic entropy calculated from magnetic heat capacity. Inset shows the variation of magnetic heat capacity calculated from the total heat capacity measured in the presence of various magnetic fields from 0 to 14 T.



contribution and assumes that the sum of optical and acoustic modes equals the total number of atoms in the primitive cell (15 in this case). We have assumed that acoustic and optical modes are in 1:  $n - 1$ , where  $n$  is the total number of atoms. For  $\text{Sr}_3\text{CoNb}_2\text{O}_9$ , we have considered six acoustic and thirty-nine optical branches corresponding to two Nb atoms and Sr, Co, and O atoms, respectively. To reduce the free parameters and consider the experimental error, all acoustical branches are grouped together and described by one Debye term. In contrast, two Einstein terms were used to describe the optical branches. So, the Debye-Einstein model for this system can be written as [24, 28]:

$$C_{D-E} = \frac{9aR}{x_D^3} \int_0^{x_D} \frac{x^4 e^x}{(e^x - 1)^2} dx + 3R \sum_{i=1}^2 \frac{b_i x_{E_i}^2 e^{x_{E_i}}}{(e^{x_{E_i}} - 1)^2} \quad (7.2)$$

where  $x_{D,E} = \theta_{D,E}/T$ ;  $\theta_D$  and  $\theta_E$  are Debye and Einstein temperatures, respectively,  $R$  is the universal gas constant. The coefficients  $a$  and  $b_i$  stand for the contributions from acoustic and optical phonons, respectively. The values of these weight factors are constrained to add up to the total number of atoms in the unit cell (In this case,  $a = 2$ ,  $b_1 = 4$ , and  $b_2 = 9$ ). Here,  $b_1$  corresponds to  $\text{Sr}^{2+}$  and  $\text{Co}^{2+}$  vibrations, and  $b_2$  stands for  $\text{O}^{2-}$  motions. Using these considerations, we could confine the flexible Debye-Einstein model to a physically reasonable fit. The fitting results in  $\theta_D \sim 171$  K,  $E_1 \sim 209$  K and  $E_2 \sim 512$  K.

The calculated magnetic entropy is shown in Fig. 7.6(b), which saturates at 4.20 J/mol-K ( $\approx 73\%$ ). The observed saturation value of the magnetic entropy reveals that  $\approx 27\%$  of the spins are still disordered below 370 mK. Further, applying the magnetic field suppresses both peaks, and they move towards lower temperatures. The 4 T heat capacity shows that both peaks are merged into a broader one, and for  $H > 5$  T, the peak becomes undetectable. Moreover, the magnetic heat capacity below 1 K could be fitted well with a power law ( $C_m \sim T^\gamma$ ), indicating the gapless nature of the magnetic excitations. The field dependence of  $\gamma$  is shown in Fig. 7.7, which first increases to  $\approx 2.7$  at 1 T and then decreases to  $\approx 1.9$  for  $H \geq 5$  T. This change in  $\gamma$  can be attributed to the 1/3 and 2/3 magnetization plateaus occurring around 2.4 T and 4.1 T, respectively.

### 7.3.4 Muon Spin Relaxation Measurements

#### 7.3.4.1 ZF $\mu\text{SR}$ Measurements

To study the spin dynamics across the antiferromagnetic transition temperature, we have carried out zero field (ZF)  $\mu\text{SR}$  measurements down to 0.09 K. Figure 7.8 (a) shows

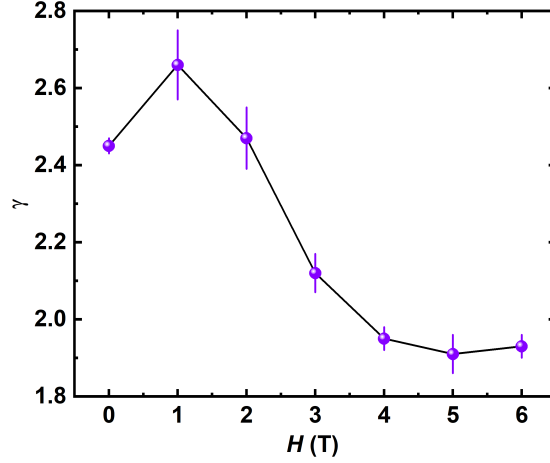


Figure 7.7: Change in the exponent of the power law with respect to the applied magnetic fields.

ZF  $\mu\text{SR}$  spectra measured at different temperatures. Although we observed long-range magnetic ordering below 1.3 K in susceptibility and heat capacity data,  $\mu\text{SR}$  spectra do not show oscillations or a loss in initial asymmetry, which would have indicated a long-range magnetic ordering. Such signatures can be seen if implanted muons are getting stopped at a site in the lattice where the effective magnetic field experienced is zero. Another reason is the presence of 27 % dynamic spins below 370 mK, as revealed by heat capacity measurements, resulting in a fast fluctuating magnetic field. Intriguingly, the ZF  $\mu\text{SR}$  measurements indicate persistent spin dynamics down to 0.09 K, as shown in Fig. 7.8(a).

Initially, we tried to fit the ZF data with a simple and stretched exponential function, which gave nonphysical results. This made us look back at the crystal structure, revealing that  $\text{Co}^{2+}$  ions have two different Wyckoff positions, which means that muons will experience two different magnetic environments [29, 30]. So, we have used a combination of two simple exponential functions to fit the ZF  $\mu\text{SR}$  spectra:

$$A(t) = A_{bg} + A_1 \cdot \exp(-\lambda_1 t) + A_2 \cdot \exp(-\lambda_2 t) \quad (7.3)$$

where  $A_{bg}$  accounts for the contribution from the muons stopping at the silver sample holder.  $A_1$  and  $A_2$  are initial asymmetries for the muons stopping at two different magnetic environments. We have kept  $A_{bg}$ ,  $A_1$ , and  $A_2$  constant to reasonable values ( $A_{bg} = 0.135$ ,  $A_1 = 0.075$ ,  $A_2 = 0.065$ ) during the fitting to avoid the covariance among the various free parameters. The fit is shown in Fig. 7.8(a) and revealed that the muons have a slightly higher preference for the fast relaxation site ( $\sim 57\%$ ).

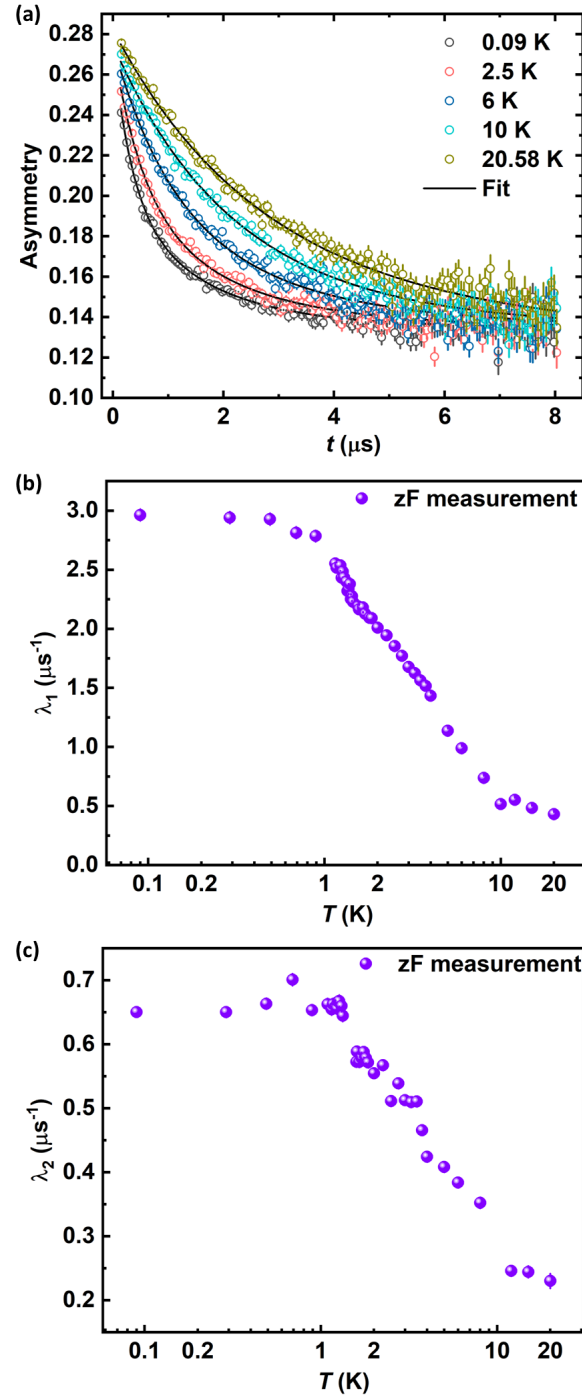


Figure 7.8: (a) Temperature dependence of the zero field MuSR measurements and solid lines represent fitting with a combination of two exponential functions. Temperature dependence of the relaxation rates,  $\lambda_1$  and  $\lambda_2$  is shown in (b) and (c), respectively.

Figure 7.8 (b) and (c) illustrates the temperature dependence of the  $\lambda_1$  and  $\lambda_2$ , respectively, which precisely tracks the onset of magnetic correlation among  $\text{Co}^{2+}$  pseudospins. Although both fast and slow relaxation rates ( $\lambda_1$  and  $\lambda_2$ ) show similar temperature dependence, but spin dynamics can be explained in terms of  $\lambda_1$  as it has larger values than  $\lambda_2$ . For an ordered system,  $\lambda$  should show a sudden change around the transition temperature [31]. However, we did not observe such dependence. It is evident from Fig. 7.8(b) that the magnetic correlations start growing below  $\sim 10$  K and become temperature-independent below 1.3 K. The variation of  $\lambda_1$  with temperature is similar to what is generally observed for spin-liquid candidates [32–34]. However, the presence of such dependence in an ordered system is rare.

#### 7.3.4.2 LF $\mu\text{SR}$ Measurements

To further understand the effect of the magnetic field on the dynamic state observed in the ZF  $\mu\text{SR}$  measurements, we have performed longitudinal field measurements in the presence of various magnetic fields up to 3200 Oe at 100 mK, as shown in Fig. 7.9 (a). The application of longitudinal fields can reduce muon spin depolarization originating from weaker local static fields. Generally, nuclear dipole moments ( $^{59}\text{Co}$  nuclei in this case) give rise to randomly oriented weak static local fields of the order of mT or less and hence can be affected by the longitudinal magnetic field of mT order [35]. However, the depolarization originating from the fast fluctuating fields of the atomic spins may require large fields. In this case, a field of 100 Oe (10 mT) results in a partial suppression of the muon depolarization. This indicates that muons stop at a site where a weak static local field from nearby nuclear spins is acting. However, the muon asymmetry could not be recovered even in the presence of a longitudinal field up to 3200 Oe (320 mT), which is characteristic of fast fluctuating local fields. Also, if we consider that the constant value of  $\lambda_1$  below 1.3 K ( $2.93 \mu\text{s}^{-1}$ ) corresponds to a static local field, the local magnetic field comes out to be 3.4 mT ( $B_{\text{loc}} = \lambda/\gamma_\mu$ , where  $\gamma_\mu$  is the gyromagnetic ratio for muons). This means a field greater than 3.4 mT should recover the total muon asymmetry [32, 33]. However, the LF data show a clear presence of relaxation in the presence of almost 100 times stronger fields, hence further complementing our assertion of dynamic  $\text{Co}^{2+}$  spins.

We have used the eq. 7.3 to analyze the field-dependent longitudinal field data. Figure 7.9(b) and (c) represent field dependence of fast ( $\lambda_1$ ) and slow ( $\lambda_2$ ) relaxation rates, and they follow the Redfield equation, further confirming fast fluctuating fields in the system. According to the Redfield theory, field dependence of the decay rate in the longitudinal

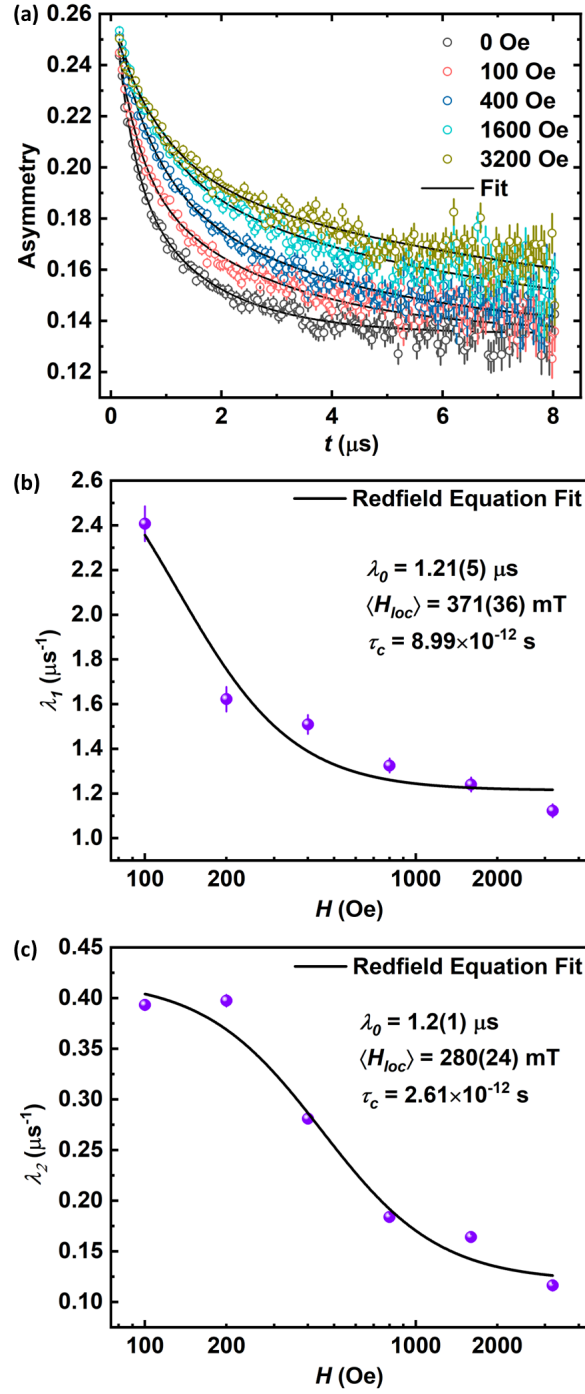


Figure 7.9: (a) Field dependence of MuSR spectra measured at 100 mK. (b) and (c) show field dependence of relaxation rates and their fitting with the Redfield equation.

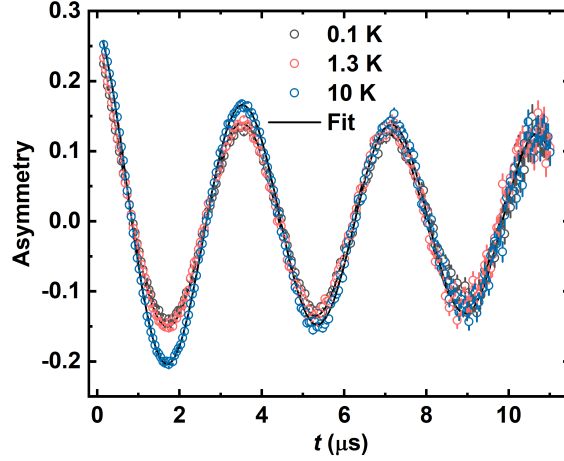


Figure 7.10:  $\mu\text{SR}$  spectra collected at three different temperatures in the presence of a weak transverse magnetic field. The solid line represents its fit with eq. 7.5.

field measurements can be written as [36];

$$\lambda = \lambda_0 + \frac{2\gamma_\mu^2 \Delta^2 \tau_C}{1 + \gamma_\mu^2 H^2 \tau_C^2} \quad (7.4)$$

where  $\lambda_0$  is the field-independent depolarization rate,  $\gamma_\mu$  denotes the muon gyromagnetic ratio,  $\Delta$  represents the time-averaged amplitude of the local dynamic field at the muon site, and  $\tau_C$  stands for the relaxation time of spin fluctuations. The fitting for fast relaxation rate results in the following parameters;  $\lambda_0 = 1.2(5) \mu\text{s}$ ,  $\Delta = 371(36) \text{ mT}$  and  $\gamma_C = 8.99 \text{ ps}$ , while for small relaxation rate, the fitting parameters are:  $\lambda_0 = 1.2(1) \mu\text{s}$ ,  $\Delta = 280(24) \text{ mT}$  and  $\gamma_C = 2.61 \text{ ps}$ . The spin correlation time observed is comparable to that observed for a spin-liquid candidate  $\text{LiCuSbO}_4$  [37].

#### 7.3.4.3 WTF $\mu\text{SR}$ Measurements

Moreover, weak transverse field (WTF)  $\mu\text{SR}$  measurements can directly rule out the presence of a static field. In this geometry, the field experienced by muons is the sum of applied and local fields at the stopping site. In magnetically ordered systems, the internal magnetic field may be of the order of several mT, and muons should see a large field compared to the applied field. We have modeled the spectra using the following equation:

$$A(t) = A_1 \cdot e^{-\lambda_1 t} \cos(2\pi f_1 t + \phi_1) + A_2 \cdot e^{-\lambda_2 t} \cos(2\pi f_2 t + \phi_2) \quad (7.5)$$

We have taken the first exponentially decaying oscillatory function as a background to address the contribution from the sample holder.  $f_i$  represents the muon precession

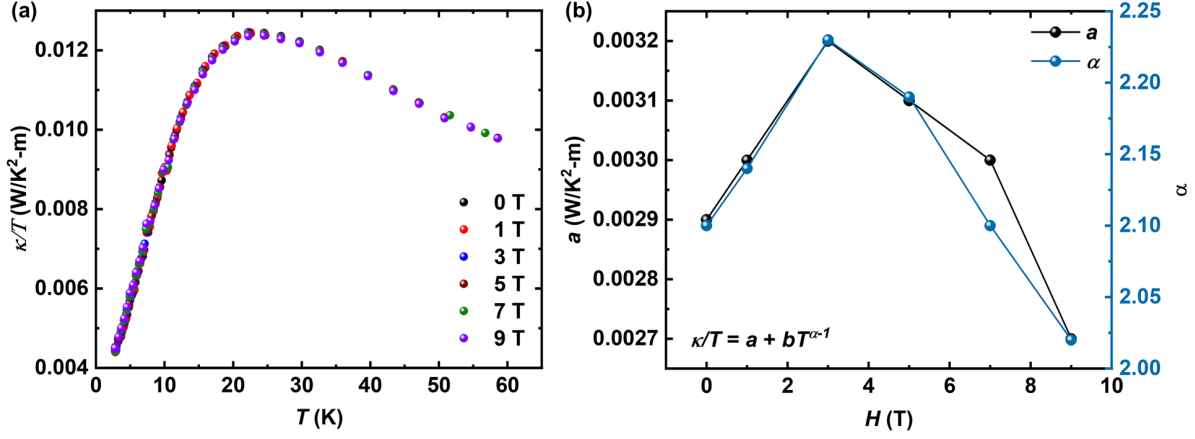


Figure 7.11: (a) Temperature dependence of thermal conductivity in the presence of different applied magnetic fields. (b) Variation of  $a$  and  $\alpha$  parameters with magnetic field.

frequency while  $\lambda_i$  is relaxation rate,  $\phi_i$  denotes phase difference. Figure 7.10 exhibits the fitting of the  $\mu\text{SR}$  data with eq. 7.5. The  $f_2$  comes out to be 279.5 kHz, expected for a muon precession in the applied 2 mT transverse field. Hence, there is no local static magnetic field in the sample.

### 7.3.5 Thermal Conductivity Measurements

Considering the presence of magnetic correlation up to  $\sim 10$  K, as unveiled by  $\mu\text{SR}$  measurements, measuring thermal transport around this temperature can be very advantageous because it does not have nuclear Schottky contribution, which may be observed in the heat capacity measurements. For low-dimensional magnetic systems, heat is transported mainly by acoustic phonons and magnetic contributions, and these measurements can be an important tool to probe the spin-mediated heat transport [38]. Figure 7.11 (a) depicts thermal conductivity measurements carried out from 60 to 2.25 K in the presence of different applied magnetic fields. Although there is no field dependence, all curves show maxima centered around 22 K, which corresponds to competition between the decrease in phonon population and an increase in phonon mean free path on decreasing the temperature [38–40].

We have fitted the low-temperature region (2.25 – 10 K) of the  $\kappa/T$  data with  $\kappa/T = a + bT^{\alpha-1}$ , where  $a$  accounts for the electron-like contribution and second term stands for the contribution from phonons. The fitting reveals  $T^3$  dependence of the thermal conductivity below 10 K, characteristic of diffuse scattering of the phonons. The finite

value of  $a$  under 0 T and its field dependence, as depicted in Fig. 7.11(b), indicate the scattering of the phonons from the magnetic correlations. There is a sudden change in the value of  $a$  and  $\alpha$  around 3 T, which can be attributed to the change in magnetic phase observed in isothermal magnetization measurements. The value of  $\alpha$  for  $H > 4$  T keeps on decreasing as more spins are getting ordered and hence contributing towards thermal resistance [25].

### 7.3.6 Energy Mapping Analysis

The experimental data suggest the presence of a dynamic state above 1.3 K, which persists up to 10 K. To understand its origin, we estimate spin exchange interactions using energy mapping analysis.

#### 7.3.6.1 DFT analysis

In our energy-mapping analysis based on DFT calculations, we employed the frozen core projector augmented plane wave (PAW) method [41] and the PBE exchange-correlation functional [42] encoded in the Vienna ab Initio Simulation Packages (VASP) [43]. To ensure that all broken-symmetry states of a magnet are magnetic insulating, DFT+ $U$  calculations [44] were carried out with an effective on-site repulsion  $U_{eff} = U - J = 4$  and 3 eV on Co.

#### 7.3.6.2 Optimization of the crystal structure

The crystal structure of  $\text{Sr}_3\text{CoNb}_2\text{O}_9$  determined from X-ray diffraction is not accurate enough for the evaluation of its spin exchange parameters by performing energy mapping analysis based on DFT+ $U$  calculations. Therefore, we first optimized the crystal structure of  $\text{Sr}_3\text{CoNb}_2\text{O}_9$  by performing DFT+ $U$  calculations for its ferromagnetic state of (a, 2b, c) supercell using  $U_{eff} = 4$  eV on Co. All atomic positions of oxygen atom are relaxed while the space group and the cell parameters of the experimental structure are kept constant. The optimization calculations used the plane wave cutoff energy of 450 eV, a set of  $(6 \times 4 \times 2)$   $k$  points, and the criterion of ionic relaxation of  $8 \times 10^{-3}$  eV/Å and threshold of  $10^{-6}$  eV for self-consistent-field energy convergence. A comparison of selected bond lengths is shown in Table 7.2



Table 7.2: Comparison of the Co-O bond distances (in Å) from the XRD and DFT calculations.

Bond	No. of Bonds	Bond Length (Å) (XRD)	Bond Length (Å) (DFT)
Co1-O4	2	1.89	2.12
Co1-O5	2	1.91	2.05
Co1-O8	2	1.76	2.08
Co2-O9	2	1.83	2.08
Co2-O7	2	1.96	2.06
Co2-O6	2	1.91	2.17

Table 7.3: Relative energies (meV/formula unit) obtained from DFT+ $U$  calculations.

State	U = 4 eV	U = 3 eV
FM	10.18	4.95
AFM1	0	0
AFM2	1.53	1.36
AFM3	1.76	1.72

### 7.3.6.3 Ordered spin states used for energy-mapping analysis

Four ordered states, shown in Fig. 7.12, have been taken for the calculation of exchange interactions. There are three different exchange paths, namely Co1...Co1 ( $J_1$ ), Co2...Co2 ( $J_2$ ), and Co1...Co2 ( $J_3$ ). The energy of the four ordered states can be written in terms of spin exchanges,  $J_i$ , as:

$$E_{\text{FM}} = (-4J_1 - 4J_2 - 16J_3)S^2 \quad (7.6a)$$

$$E_{\text{AFM1}} = (4J_1 - 4J_2)S^2 \quad (7.6b)$$

$$E_{\text{AFM2}} = (4J_1 + 4J_2)S^2 \quad (7.6c)$$

$$E_{\text{AFM3}} = (-4J_1 - 4J_2 + 16J_3)S^2 \quad (7.6d)$$

where  $S = 3/2$  for  $\text{Co}^{3+}$  ions.

Relative energy obtained using these equations is tabulated in Table 7.3.

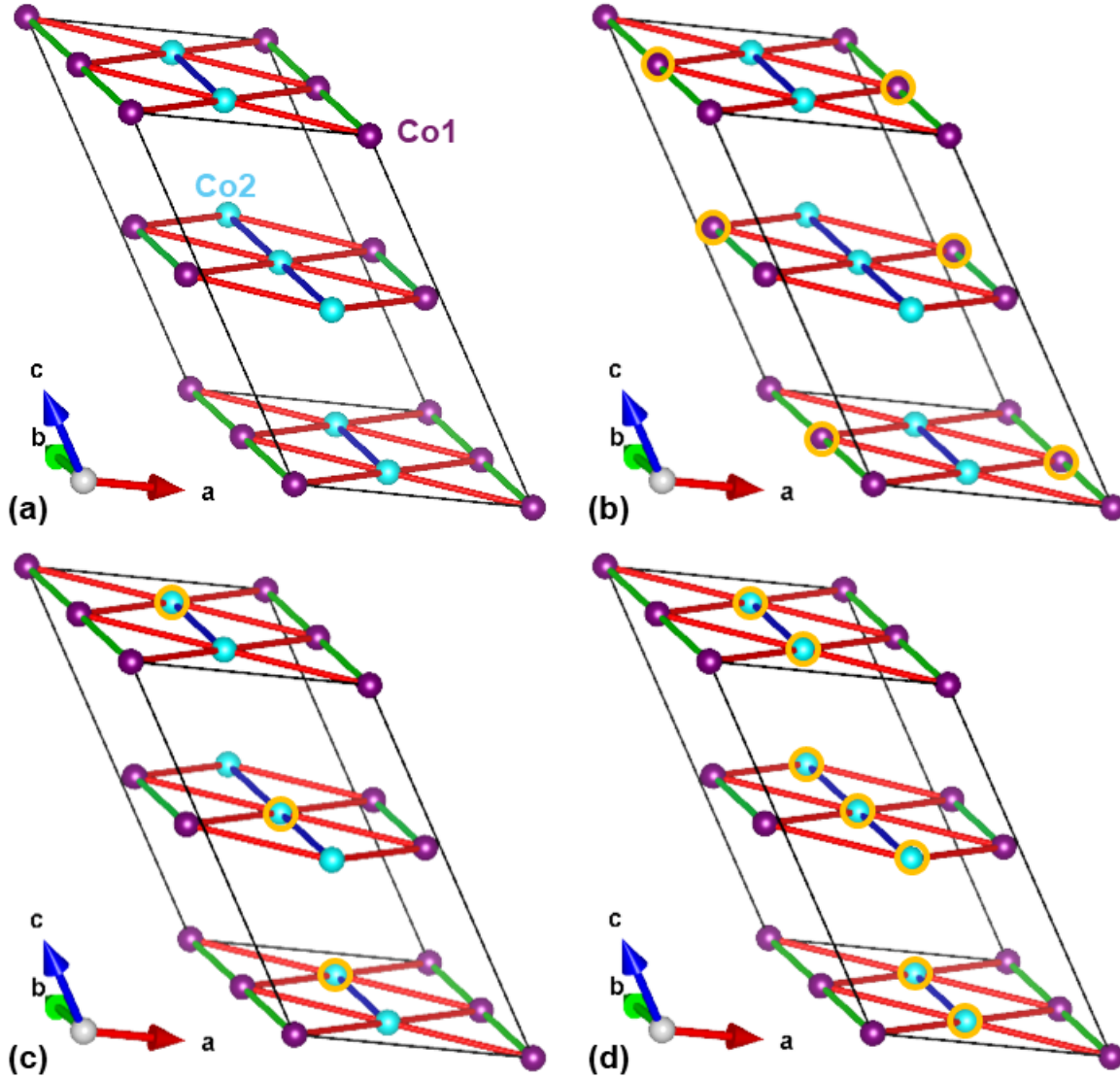


Figure 7.12: Four ordered spin states: (a) ferromagnet (FM), (b) antiferromagnet (AFM)1, (c) AFM2, and (d) AFM3 state. The orange circles indicate the down spin  $\text{Co}^{2+}$  ion sites.

From these equations,  $J_i$  can be calculated as,

$$J_3 = \frac{E(\text{AFM3}) - E(\text{FM})}{32S^2} \quad (7.7a)$$

$$J_1 = \frac{E(\text{AFM1}) - E(\text{FM})}{8S^2} - 2J_3 \quad (7.7b)$$

$$J_2 = \frac{E(\text{AFM2}) - E(\text{FM})}{8S^2} - 2J_3 \quad (7.7c)$$

The experimental data suggest the presence of a dynamic state above 1.3 K, which persists up to 10 K. To understand its origin, we estimate spin exchange interactions,  $J_1$ ,

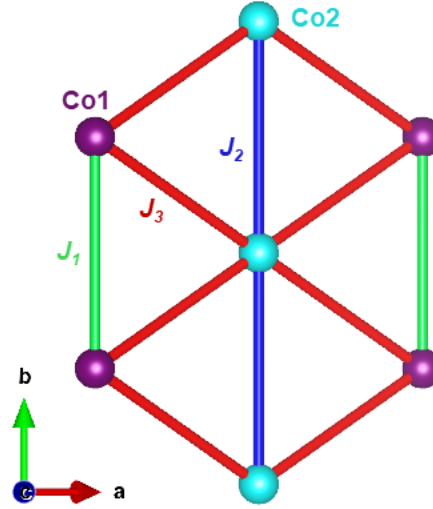


Figure 7.13: Various exchange interactions present in the triangular lattice.

Table 7.4: Values of  $J_1 - J_3$  (in K) obtained from DFT+ $U$  calculations.

	$U = 4 \text{ eV}$	$U = 3 \text{ eV}$
$J_1$	-30.76	-17.19
$J_2$	-22.87	-10.20
$J_3$	-10.86	-4.16

$J_2$ , and  $J_3$  representing Co1...Co1, Co2...Co2, and Co1...Co2 interactions, respectively, as depicted in Fig. 7.13. We have evaluated them by energy-mapping analyses [45–47] based on DFT+ $U$  calculations. The obtained values for  $J_1$ – $J_3$  are summarised in Table 7.4. Considering the  $\theta_{CW}$  obtained from the Curie-Weiss law,  $U = 3 \text{ eV}$  calculations are more appropriate for our system. Further, these values confirm the bond-dependent nature of the exchange interactions. Thus, a combination of spin-orbital entangled  $J_{eff} = 1/2$  state, “parallel edge”-sharing geometry of Co octahedra and bond-dependent exchange interactions indicates that  $\text{Sr}_3\text{CoNb}_2\text{O}_9$  is a potential Kitaev magnet.

### 7.3.7 Fundamental Question To Resolve

So far, there is no clear discussion of how magnetic anisotropy affects the magnetic structures of a Kitaev magnet. The magnetic structures observed for a trigonal layer system  $\text{CoI}_2$  made up of  $\text{CoI}_6$  octahedra [16] and that predicted for a trigonal layer made up of  $\text{IrO}_6$  octahedra show a superstructure in which the spin moment rotate in the plane parallel to the layer [48]. This can be explained by the fact that these magnetic ions have

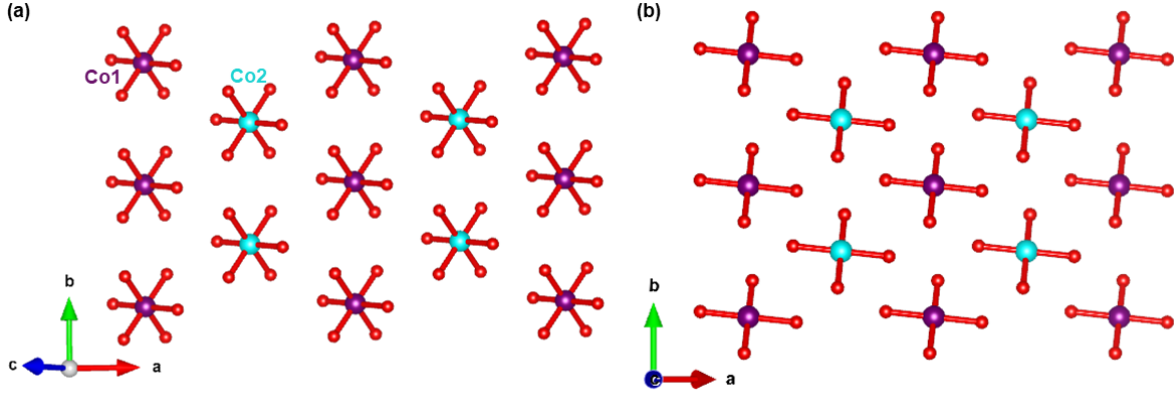


Figure 7.14: (a) Single layer of  $\text{CoO}_6$  octahedra viewed along the  $c$  direction. (b) A single layer of  $\text{CoO}_4$  square planes, which result when the elongated Co-O bonds are removed.

in-plane magnetic anisotropy and because the easy plane is parallel to the plane of the layer.  $\text{Sr}_3\text{CoNb}_2\text{O}_9$  has layers of axially-elongated  $\text{CoO}_6$  (refer to Fig. 7.14(a)), with the elongated Co-O bonds inclined to the plane of the layer. According to the selection rule for the preferred spin orientation [49], the magnetic ions of such  $\text{CoO}_6$  octahedra have an in-plane magnetic anisotropy such that the magnetic moment of each  $\text{CoO}_6$  octahedron can choose any direction in the plane of the  $\text{CoO}_4$  square planes perpendicular to the elongated Co-O bonds. Such  $\text{CoO}_4$  planes are inclined to the plane of the layer (refer to Fig. 7.14(b)). This implies that, in the magnetic superstructure of  $\text{Sr}_3\text{CoNb}_2\text{O}_9$ , when observed, the spin moments are not parallel to the layer and would rotate in the  $\text{CoO}_4$  planes inclined to the layer. Thus, neutron diffraction measurements of  $\text{Sr}_3\text{CoNb}_2\text{O}_9$  will provide a critical piece of information needed to answer how magnetic anisotropy affects the magnetic superstructures predicted by Kitaev physics.

## 7.4 Conclusion

In conclusion, we present a new Kitaev candidate,  $\text{Sr}_3\text{CoNb}_2\text{O}_9$ , which has Co octahedra arranged in a “parallel edge”-sharing geometry. Magnetization and heat capacity measurements confirm that the ground state of this compound can be described by  $J_{eff} = 1/2$  at low temperatures.  $\mu\text{SR}$  measurements revealed the presence of a dynamic magnetic state in the temperature range of  $1.3 \text{ K} \leq T \leq 10 \text{ K}$ , which remains stable even in the presence of 3200 Oe. Further, the dynamic state is indicated by thermal conductivity measurements, supporting the  $\mu\text{SR}$  results. The origin of such a state is a combination of geometrical frustration and competition between anisotropic exchange interactions,

which is confirmed by spin exchange interaction evaluation. Thus,  $\text{Sr}_3\text{CoNb}_2\text{O}_9$  have a spin-orbit entangled  $J_{eff} = 1/2$  ground state, anisotropic exchange interactions, and “parallel edge”-sharing geometry of Co octahedra, completing all the criteria to be a Kitaev material.

# Bibliography

- [1] P. W. Anderson, The resonating valence bond state in  $\text{La}_2\text{CuO}_4$  and superconductivity. *Science* **235**, 1196 (1987).
- [2] L. Balents, Spin liquids in frustrated magnets, *Nature* **464**, 199 (2010).
- [3] A. Kitaev, Anyons in an exactly solved model and beyond. *Ann. Phys.-New York* **321**, 2 (2006).
- [4] H. Takagi, T. Takayama, G. Jackeli, G. Khaliullin, and S. E. Nagler, Concept and realization of Kitaev quantum spin liquids. *Nat. Rev. Phys.* **1**, 264 (2019).
- [5] S. Trebst and C. Hickey, Kitaev Materials, *Phys. Reports* **950**, 1 (2022).
- [6] G. Jackeli and G. Khaliullin, Mott insulators in the strong spin-orbit coupling limit: From Heisenberg to a quantum compass and Kitaev models, *Phys. Rev. Lett.* **102**, 017205 (2009).
- [7] H. Liu, and G. Khaliullin, Pseudospin exchange interactions in  $d^7$  cobalt compounds: possible realization of the Kitaev model, *Phys. Rev. B* **97**, 014407 (2018).
- [8] R. Sano, Y. Kato, and Y. Motome, Kitaev-Heisenberg Hamiltonian for high-spin  $d^7$  Mott insulators, *Phys. Rev. B* **97**, 014408 (2018).
- [9] S. Sugano, Y. Tanabe, and H. Kamimura, *Multiplets of Transition-Metal Ions in Crystals* (Academic, 1970).
- [10] A. Abragam and B. Bleaney, *Electron Paramagnetic Resonance of Transition Ions* (Oxford Univ., 1986).
- [11] C. Kim, J. Jeong, G. Lin, P. Park, T. Masuda, S. Asai, S. Itoh, H.-S. Kim, H. Zhou, J. Ma, and J.-G. Park, Antiferromagnetic Kitaev interaction in  $J_{eff} = 1/2$  cobalt honeycomb materials  $\text{Na}_3\text{Co}_2\text{SbO}_6$  and  $\text{Na}_2\text{Co}_2\text{TeO}_6$ . *J. Phys. Condens. Matter* **34**, 045802 (2022).

- 
- [12] M. Songvilay, J. Robert, S. Petit, J. A. Rodriguez-Rivera, W. D. Ratcliff, F. Damay, V. Balédent, M. Jiménez-Ruiz, P. Lejay, E. Pachoud *et al.*, Kitaev interactions in the Co honeycomb antiferromagnets  $\text{Na}_3\text{Co}_2\text{SbO}_6$  and  $\text{Na}_2\text{Co}_2\text{TeO}_6$ , *Phys. Rev. B* **102**, 224429 (2020).
- [13] X. Li, Y. Gu, Y. Chen, V. Ovidiu Garlea, K. Iida, K. Kamazawa, Y. Li, G. Deng, Q. Xiao, X. Zheng *et al.*, Giant magnetic in-plane anisotropy and competing instabilities in  $\text{Na}_3\text{Co}_2\text{SbO}_6$ , *Phys. Rev. X* **12**, 041024 (2022).
- [14] W. Yao, K. Iida, K. Kamazawa and Y. Li, Excitations in the ordered and paramagnetic states of honeycomb magnet  $\text{Na}_2\text{Co}_2\text{TeO}_6$ , *Phys. Rev. Lett.* **129**, 147202 (2022).
- [15] T. Hallorana, F. Desrochersb, E. Z. Zhangb, T. Chena, L. E. Chernc, Z. Xud, B. Winnf, M. Graves-Brookf, M. B. Stonef, Alexander I. Kolesnikovf *et al.*, Geometrical frustration versus Kitaev interactions in  $\text{BaCo}_2(\text{AsO}_4)_2$ , *Proc. Natl Acad. Sci. USA* **120**, e2215509119 (2023).
- [16] C. Kim, S. Kim, P. Park, T. Kim, J. Jeong, S. Ohira-Kawamura, N. Murai, K. Nakajima, A. L. Chernyshev, M. Mourigal *et al.*, Bond-dependent anisotropy and magnon decay in cobalt-based Kitaev triangular antiferromagnet, *Nat. Phys.* **19**, 1624 (2023).
- [17] A. Razpopov, D. A. S. Kaib, S. Backes, L. Balents, S. D. Wilson, F. Ferrari, K. Riedl, and R. Valentí, A  $j_{\text{eff}} = 1/2$  Kitaev material on the triangular lattice: the case of  $\text{NaRuO}_2$ , *npj Quantum Mater* **8**, 36 (2023).
- [18] Mantid (2013): Manipulation and Analysis Toolkit for Instrument Data.; Mantid Project.
- [19] O. Arnold, J.C. Bilheux, J.M. Borreguero, A. Buts, S.I. Campbell, L. Chapon, M. Doucet, N. Draper, R. Ferraz Lea, M.A. Gigg *et al.*, Nuclear Instruments and Methods in Physics Research Section A: Accelerators, Spectrometers, Detectors and Associated Equipment **764**, 156 (2014).
- [20] V. Petricek, M. Dusek, and L. Palatinus, Crystallographic computing system JANA2006: General features, *Z. Kristallogr. – Cryst. Mater.* **229**, 345 (2014).
- [21] S. Lal, S. J. Sebastian, S. S. Islam, M. P. Saravanan, M. Uhlarz, Y. Skourski, and R. Nath, Double magnetic transitions and exotic field-induced phase in the triangular lattice antiferromagnets  $\text{Sr}_3\text{Co}(\text{Nb,Ta})_2\text{O}_9$ , *Phys. Rev. B* **108**, 014429 (2023).

- 
- [22] T. Besara, M. S. Lundberg, J. Sun, D. Ramirez, L. Dong, J. B. Whalen, R. Vasquez, F. Herrera, J. R. Allen, M. W. Davidson *et al.*, Single crystal synthesis and magnetism of the  $\text{BaLn}_2\text{O}_4$  family ( $\text{Ln} = \text{lanthanide}$ ), *Prog. Solid State Chem.* **42**, 23 (2014).
  - [23] M. Mitric, B. Antic, M. Balanda, D. Rodic, and M. L. Napijalo, An x-ray diffraction and magnetic susceptibility study of  $\text{Yb}_x\text{Y}_{2-x}\text{O}_3$ , *J. Phys.: Condens. Matter* **9**, 4103 (1997).
  - [24] R. Kumar and A. Sundaresan, Unveiling a hidden multiferroic state under magnetic fields in  $\text{BaHoFeO}_4$ , *Phys. Rev. B* **107**, 184420 (2023).
  - [25] R. Kumar, K. Nam, S.-H. Kim, K. H. Kim, and A. Sundaresan, Exploring potential quantum spin liquid state in a quasi-one-dimensional magnetic chain, *Phys. Rev. B* **109**, 224429 (2024).
  - [26] M. Lee, J. Hwang, E. S. Choi, J. Ma, C. R. Dela Cruz, M. Zhu, X. Ke, Z. L. Dun, and H. D. Zhou, Series of phase transitions and multiferroicity in the quasi-two-dimensional spin- $\frac{1}{2}$  triangular-lattice antiferromagnet  $\text{Ba}_3\text{CoNb}_2\text{O}_9$ , *Phys. Rev. B* **89**, 104420 (2014).
  - [27] H. Xiang, C. Lee, H.-J. Koo, X. Gong and M.-H. Whangbo, Magnetic properties and energy-mapping analysis, *Dalton Transactions* **42**, 823 (2013).
  - [28] R. Kumar and A. Sundaresan, Antisite disorder driven cluster glass state and colossal magnetoresistance in  $\text{MnSb}_2\text{Se}_4$ , *Phys. Rev. B* **106**, 134423 (2022).
  - [29] C. Y. Jiang, Y. X. Yang, Y. X. Gao, Z. T. Wan, Z. H. Zhu, T. Shiroka, C. S. Chen, Q. Wu, X. Li, J. C. Jiao, K. W. Chen, Y. Bao, Z. M. Tian, and L. Shu, Spin excitations in the quantum dipolar magnet  $\text{Yb}(\text{BaBO}_3)_3$ , *Phys. Rev. B* **106**, 014409 (2022).
  - [30] J. Gaudet, D. D. Maharaj, G. Sala, E. Kermarrec, K. A. Ross, H. A. Dabkowska, A. I. Kolesnikov, G. E. Granroth, and B. D. Gaulin, Neutron spectroscopic study of crystalline electric field excitations in stoichiometric and lightly stuffed  $\text{Yb}_2\text{Ti}_2\text{O}_7$ , *Phys. Rev. B* **92**, 134420 (2015).
  - [31] M. Smidman, D. T. Adroja, A. D. Hillier, L. C. Chapon, J. W. Taylor, V. K. Anand, R. P. Singh, M. R. Lees, E. A. Goremychkin, M. M. Koza, V. V. Krishnamurthy, D. M. Paul, and G. Balakrishnan, Neutron scattering and muon spin relaxation measurements of the noncentrosymmetric antiferromagnet  $\text{CeCoGe}_3$ , *Phys. Rev. B* **88**, 134416 (2013).



- 
- [32] L. Ding, P. Manuel, S. Bachus, F. Grussler, P. Gegenwart, J. Singleton, R. D. Johnson, H. C. Walker, D. T. Adroja, A. D. Hillier, and A. A. Tsirlin, Gapless spin-liquid state in the structurally disorder-free triangular antiferromagnet  $\text{NaYbO}_2$ , *Phys. Rev. B* **100**, 144432 (2019).
  - [33] A. Bhattacharyya, T. K. Bhowmik, D. T. Adroja, B. Rahaman, S. Kar, S. Das, T. Saha-Dasgupta, P. K. Biswas, T. P. Sinha, R. A. Ewings, D. D. Khalyavin, and A. M. Strydom, Dynamic spin fluctuations in the frustrated spin chain compound  $\text{Li}_3\text{Cu}_2\text{SbO}_6$ , *Phys. Rev. B* **103**, 174423 (2021).
  - [34] T. Arh, B. Sana, M. Pregelj, P. Khuntia, Z. Jaglicic, M. D. Le, P. K. Biswas, P. Manuel, L. Mangin-Thro, A. Ozarowski, and A. Zorko, The Ising triangular-lattice antiferromagnet neodymium heptatantalate as a quantum spin liquid candidate, *Nat. Mater.* **21**, 416 (2022).
  - [35] O. Mustonen, S. Vasala, E. Sadrollahi, K. P. Schmidt, C. Baines, H. C. Walker, I. Terasaki, F. J. Litterst, E. Baggio-Saitovitch, and M. Karppinen, Spin-liquid-like state in a spin-1/2 square-lattice antiferromagnet perovskite induced by  $d^{10}$ – $d^0$  cation mixing, *Nat. comm.* **9**, 1 (2018).
  - [36] Y. J. Uemura, T. Yamazaki, D. R. Harshman, M. Senba, and E. J. Ansaldo, Muon-spin relaxation in  $\text{AuFe}$  and  $\text{CuMn}$  spin glasses, *Phys. Rev. B* **31**, 546 (1985).
  - [37] M. Bosiočić, Ph. D. Thesis, University of Zagreb (2022).
  - [38] M. Yamashita, N. Nakata, Y. Senshu, M. Nagata, H. M. Yamamoto, R. Kato, T. Shibauchi, and Y. Matsuda, Highly Mobile Gapless Excitations in a Two-Dimensional Candidate Quantum Spin Liquid, *Science* **328**, 1246 (2010).
  - [39] P. Bourgeois-Hope, F. Laliberte, E. Lefrançois, G. Grissonnanche, S. Rene de Cotret, R. Gordon, S. Kitou, H. Sawa, H. Cui, R. Kato, L. Taillefer, and N. Doiron-Leyraud, Thermal Conductivity of the Quantum Spin Liquid Candidate  $\text{EtMe}_3\text{Sb}[\text{Pb}(\text{dmit})_2]_2$ , *Phys. Rev. X* **9**, 041051 (2019).
  - [40] J. Callaway, Model for lattice thermal conductivity at low temperatures, *Phys. Rev.* **113**, 1046 (1959).
  - [41] G. Kresse and D. Joubert, From ultrasoft pseudopotentials to the projector augmented-wave method, *Phys. Rev. B* **59**, 1758 (1999).
  - [42] J. P. Perdew, K. Burke, and M. Ernzerhof, Generalized gradient approximation made simple, *Phys. Rev. Lett.* **77**, 3865 (1996).

- [43] G. Kresse and J. Furthmüller, Efficiency of ab-initio total energy calculations for metals and semiconductors using a plane-wave basis set, *Comput. Mater. Sci.* **6**, 15 (1996).
- [44] S. L. Dudarev, G. A. Botton, S. Y. Savrasov, C. J. Humphreys, and A. P. Sutton, Electron-energy-loss spectra and the structural stability of nickel oxide: An LSDA+U study, *Phys. Rev. B* **57**, 1505 (1998).
- [45] H. Xiang, C. Lee, H.-J. Koo, X. Gong, and M.-H. Whangbo, Magnetic properties and energy-mapping analysis, *Dalton Trans.* **42**, 823 (2013).
- [46] M.-H. Whangbo and H. Xiang, *Magnetic Properties from the Perspectives of Electronic Hamiltonian*, Handbook of Solid State Chemistry (Wiley Online Library) (2017).
- [47] M.-H. Whangbo, H.-J. Koo, and R. K. Kremer, Spin Exchanges between Transition Metal Ions Governed by the Ligand p-Orbitals in Their Magnetic Orbitals, *Molecules* **26**, 531 (2021).
- [48] M. Becker, M. Hermanns, B. Bauer, M. Garst, and S. Trebst, Spin-orbit physics of  $j = 1/2$  Mott insulators on the triangular lattice, *Phys. Rev. B* **91**, 155135 (2015).
- [49] C. Lee, T. Park, J. H. Shim, and M. H. Whangbo, Skin-Deep Aspect of Thermopower in  $\text{Bi}_2\text{Q}_3$ ,  $\text{PbQ}$ , and  $\text{BiCuQO}$  ( $\text{Q} = \text{Se}, \text{Te}$ ): Hidden One-Dimensional Character of Their Band Edges Leading to High Thermopower, *Acc. Chem. Res.* **55**, 2811 (2022).

## Chapter 8

# Magnetic Frustration in a Hyperhoneycomb Compound $\text{NaYbW}_2\text{O}_8$

In this chapter, we explored a hyperhoneycomb lattice-based magnet,  $\text{NaYbW}_2\text{O}_8$ , featuring a scheelite structure characterized by an inherent disorder among sodium (Na) and ytterbium (Yb) sites. Through extensive magnetization measurements conducted down to 400 mK, we observed the absence of long-range magnetic ordering in the material. Further investigation using modified Curie-Weiss law indicate that the ground state can be described as a Kramers doublet with  $J_{eff} = 1/2$ . This finding was corroborated by field-dependent specific heat measurements, which suggest the presence of an internal magnetic field equivalent to 0.6 K. Moreover, muon spin relaxation ( $\mu\text{SR}$ ) measurements supported the results obtained from magnetization and heat capacity experiments while also probing the Orbach process between crystal electric field (CEF) levels. The anomalies observed in field-dependent thermal conductivity measurements complemented the magnetization and heat capacity findings, suggesting that spins are excited to the first excited level for  $H \geq 2$  T. Furthermore, the presence of dynamic magnetic state is understood by a theoretical study using Density Functional Theory (DFT) and Monte Carlo Simulations.

## 8.1 Introduction

In magnetism, frustration refers to conflicting exchange interactions that cannot be satisfied simultaneously, leading to new states of matter with exotic properties. One of the most notable outcomes of magnetic frustration is the quantum spin liquid (QSL) state, in which quantum fluctuations keep spin disordered down to 0 K [1]. The resulting QSL states are of different types, ranging from chiral spin liquids [2, 3] to  $Z_2$  topological spin liquids [4–6], which feature fractionalized excitations.

Extensive experimental and theoretical research has been conducted on QSLs in two-dimensional (2D) systems [1–9]. However, understanding how these states behave in three-dimensional (3D) systems is still largely uncharted territory. In 3D systems, the tendency to form long-range ordered magnetic states is stronger, making the disordering effect of quantum fluctuations less significant. This area remains underexplored due to the limitations of theoretical and numerical approaches in 3D, as well as the scarcity of suitable materials [10].

However, frustration is not solely a result of geometry. In quantum magnets composed of rare-earth ions, spin-orbit coupling introduces anisotropic interactions that can create quantum-disordered ground states even without the typical geometric frustration. A notable example is the honeycomb lattice, a bipartite structure, where both ferromagnetic and antiferromagnetic Heisenberg couplings result in ordered ground states. Yet, a unique set of anisotropic interactions proposed by Kitaev [11], in which neighboring spins are linked by Ising interactions along axes determined by the bond’s spatial orientation, has been found to exist in a quantum spin liquid phase. If one can experimentally realize such a system in 3D, it may be a potential 3D quantum spin liquid [12]. However, due to the difficulty in realizing 3D variants of the honeycomb lattice, material explorations have been limited to 2D layered honeycomb structure [13–22], except a few 3D iridates [23, 24].

In this chapter, we report a Yb-based hyperhoneycomb lattice compound,  $\text{NaYbW}_2\text{O}_8$ , which crystallizes into a scheelite structure. It has inherently 50% site disorder among  $\text{Na}^+$  and  $\text{Yb}^{3+}$  ions. Intriguingly, it has been proposed that inherent disorder in certain frustrated magnets can result in random exchange interactions between spins [25–30], and hence can lead to various exotic quantum phases. Despite the absence of magnetic ordering down to 0.4 K, the heat capacity measurements unveil an internal magnetic field of the order of 0.6 K. Further investigation using muon spin relaxation ( $\mu\text{SR}$ ) measurements indicate a dynamic magnetic state below 20 K. Hence, a combination of

3D spin-lattice,  $J_{eff} = 1/2$  ground state, chemical disorder, and dynamics magnetic state can lead to a randomness-driven spin-liquid-like ground state.

## 8.2 Experimental

A polycrystalline sample of  $\text{NaYbW}_2\text{O}_8$  is prepared through a conventional solid-state synthesis route using  $\text{Yb}_2\text{O}_3$ ,  $\text{WO}_3$  and  $\text{Na}_2\text{CO}_3$  as starting materials. These materials are mixed homogenously with the help of a mortar and a pestle. As a first step, the mixture was heated to 973 K at a constant ramping rate of 5 K/min and kept at the same temperature for 15 h. The first step is necessary to avoid the evaporation of Na atoms. After the heat treatment, the furnace was cooled to room temperature, and the mixture was ground again. In the second step, the mixture was pelletized and again heated to 1173 K and kept at the same temperature for 15 h. Finally, the sample is cooled back to 300 K and characterized using X-ray diffraction (XRD) on a PANalytical Empyrean Alpha I diffractometer equipped with Cu-K $\alpha$  single wavelength ( $\lambda = 1.54059$  Å). The structure analysis has been done with the help of FullProf software [31], which uses the Rietveld refinement method. Magnetic properties have been measured with the help of an MPMS, Quantum Design, USA. Heat capacity measurements have been performed with the help of a PPMS, Quantum Design, USA. The magnetic measurements down to 0.4 K are performed using an iHelium3 (Quantum Design, Japan) addition to the MPMS. The  $\mu\text{SR}$  data are collected at MuSR spectrometer by placing the sample in a cryostat at the ISIS facility, Rutherford Appleton Laboratory, United Kingdom. We have used the open-source MANTID [32] software to analyze the  $\mu\text{SR}$  data.

## 8.3 Computational Methods

The magnetic properties of  $\text{NaYbW}_2\text{O}_8$  were explored in detail employing combined Density Functional Theory (DFT) and Monte Carlo Simulations. The density functional theory calculations were carried out using the Vienna Ab-Initio Simulation Package (VASP) [33–35]. A pseudopotential based on the Projector-Augmented-Wave (PAW) [36] method is used with the exchange-correlation functional approximated using the Perdew-Burke-Ernzerhof (PBE) functional [37]. A  $\Gamma$ -centered  $4 \times 4 \times 2$  k-point grid was used for all the calculations. An on-site Hubbard  $U$  of 6 eV was assigned to the Yb  $4f$  orbitals to include their strong correlation.

The presence of inherent disorder in the lattice leads to various lattice structures as the Na and Yb can be present at the same lattice site, thereby giving rise to many lattice realizations. To simulate the experimental observations accurately, we first optimized all the possible lattice configurations. There are two Yb atoms and two Na atoms in the unit cell, which gives rise to  ${}^4C_2$  ( $= 6$ ) possible lattice configurations. Out of these six possible structures, four correspond to a particular magnetic lattice (lattice A) and the other two to another magnetic lattice (lattice B); see Fig. 8.7(a) and (b) depicting the nearest and next-nearest pairs in lattice A and B, respectively. We considered one unit cell from each kind of lattice, whose geometries were optimized until the energy between two consecutive ionic steps became less than  $10^{-5}$  eV. The optimized structures were used to calculate the exchange interactions. To calculate the exchange couplings, various collinear magnetic configurations are considered, and their energies are mapped to the  $J_1 - J_2$  Heisenberg model,

$$H = J_1 \sum_{\langle ij \rangle} \vec{S}_i \cdot \vec{S}_j + J_2 \sum_{\langle\langle ij \rangle\rangle} \vec{S}_i \cdot \vec{S}_j \quad (8.1)$$

where,  $\langle .. \rangle$  corresponds to the nearest neighbour pairs,  $\langle\langle .. \rangle\rangle$  corresponds to the next nearest neighbour pairs and  $J_1$  and  $J_2$  are the nearest and next nearest neighbor interactions respectively. The spins  $S_i$  are considered to be three-dimensional vectors in the spherical polar coordinates with  $|S_i| = 1/2$ . For this energy mapping analysis, we considered a  $1 \times 1 \times 2$  supercell for the first lattice and a  $2 \times 1 \times 1$  supercell for the second lattice. The supercells have four magnetic Yb atoms each, and we considered three different spin configurations for the mapping analysis - one ferromagnetic (FM) and two antiferromagnetic (AFM1 and AFM2). AFM1 denotes an up-up-down-down configuration, and AFM2 is an up-down-up-down configuration. Then, the ground state DFT energies for the lattice A can be written as

$$\begin{aligned} E_{FM} &= E_0 + J_1 + 3 J_2 \\ E_{AFM1} &= E_0 - J_1 + 3 J_2 \\ E_{AFM2} &= E_0 + J_2 \end{aligned} \quad (8.2)$$

and for the lattice B, these three configurations yield the following set of equations,

$$\begin{aligned} E_{FM} &= E_0 + 3 J_1 + 4 J_2 \\ E_{AFM1} &= E_0 + 3 J_1 - 4 J_2 \\ E_{AFM2} &= E_0 + J_1 \end{aligned} \quad (8.3)$$

where  $E_0$  is the DFT energy without the spin consideration.

The  $J_1$  and  $J_2$  values were obtained by solving the above system of equations and were used to simulate the magnetic properties at the zero temperature as well as the finite temperature for lattices A and B. The ground state properties were obtained by an Iterative Minimization (IM) procedure [38, 39]. The procedure is repeated for various linear system sizes  $L$ , each having  $N = 2 \times L \times L \times L$  spins. The ordering vector  $Q$ , for a given  $L$  is obtained from the peak of the equal time structure factor, which is the Fourier Transform of the spin-spin correlation function and can be calculated as:

$$S_Q = \frac{1}{N} \sum_{ij} \langle \vec{S}_i \cdot \vec{S}_j \rangle e^{iQ \cdot r_{ij}} = \langle s_Q \cdot s_{-Q} \rangle \quad (8.4)$$

where  $\langle s_Q \rangle = \frac{1}{N} \sum_i \vec{S}_i e^{iQ \cdot r_i}$ . To understand the finite temperature behavior of the system, we resorted to Monte Carlo simulations, implementing the heat-bath algorithm [40] coupled with an over-relaxation algorithm [41]. The simulations were carried out for a system size of  $L = 16$  and  $L = 10$ . Each Monte Carlo (MC) step comprises  $2 \times L \times L \times L$  heat-bath steps followed by ten over-relaxation steps. After a thermalization of  $10^6$  MC steps, the thermodynamic properties were calculated by performing  $5 \times 10^6$  MC steps.

## 8.4 Results and Discussion

### 8.4.1 Crystal Structure

Rietveld refinement of the compound results in a good agreement of experimental data with the theoretical data ( $\chi^2 = 1.56$  %), as shown in Fig. 8.1(a), and reveals that the compound crystallizes into a tetragonal space group  $I4_1/a$  with the following lattice parameters:  $a = b = 5.1749(2)$  Å,  $c = 11.1940(6)$  Å. The obtained parameters agree very well with the published crystal structure [42]. The parameters obtained from the refinement are tabulated in Table 8.1. Figure 8.1(b) exhibits the unit cell of the compound, which confirms the intrinsic substitutional disorder as observed earlier in the Sheelite-structure of  $\text{NaRE}(\text{MO}_4)_2$ , where RE = rare earth,  $M = \text{Mo}, \text{W}$  [42]. The  $\text{W}^{6+}$  ions form tetrahedra which are isolated from each other while  $\text{Na}^+/\text{Yb}^{3+}$  ions are coordinated by eight  $\text{O}^{2-}$  ions forming edge-shared polyhedra  $[(\text{Na}/\text{Yb})\text{O}_8]$ . The angle distortion index can give an estimation of the extent of deviation from an ideal tetrahedron and can be calculated as:

$$d_a = \frac{\phi_{\max} - \phi_{\min}}{\bar{\phi}} \quad (8.5)$$

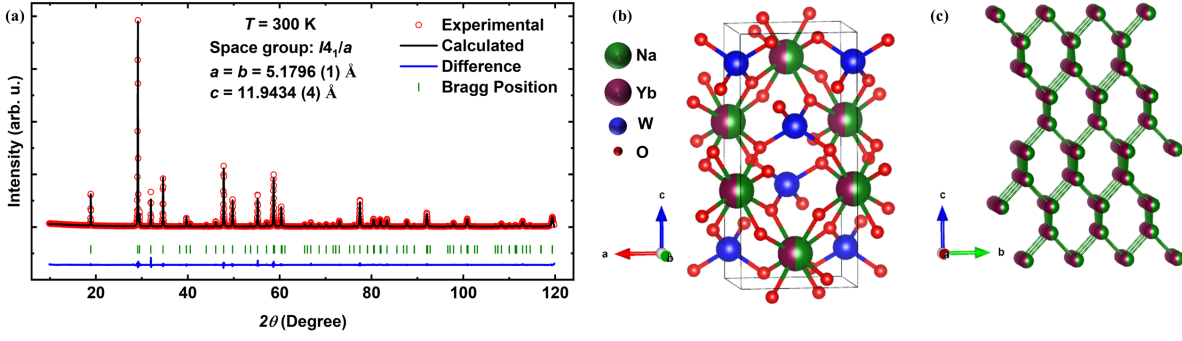


Figure 8.1: (a) Observed and refined powder x-ray diffraction pattern of  $\text{NaYbW}_2\text{O}_8$ . The Bragg positions are marked in green. The bottom solid blue line represents the difference between experimental and calculated intensities. (b) Arrangement of the atoms in the  $ac$  plane viewed along the  $b$  axis. (c) Hyper-Honeycomb magnetic lattice formed by Na/Yb ions.

where  $\phi_{max}$  and  $\phi_{min}$  are the largest and smallest angles, respectively and  $\bar{\phi}$  is mean angle. The value of  $d_a$  comes out to be 35.66 %, which is comparable to  $d_a$  values calculated for other  $I4_1/a$  systems, such as  $\text{KRuO}_4$  [43] and  $\text{KOsO}_4$  [44].

Further, a careful investigation of the structure reveals that  $\text{Yb}^{3+}$  ions form a distorted hexagon with a side of 3.8113(2) Å. It can be categorized according to the harmonic honeycomb nomenclature, which names such structures as  $^{\mathcal{H}}\langle N \rangle$  [45, 46], where  $N$  stands for a number of complete hexagonal rows present in the structure before a change of orientation happens with respect to the previous hexagon plane. Alternatively,  $N + 1$  represents the number of links before the change of orientation. In the present case, the orientation of the honeycomb changes for the very next honeycomb unit, as depicted in Fig. 8.1(c), resulting in  $N = -1$ . Thus, we propose  $^{\mathcal{H}}\langle -1 \rangle$  notation for  $\text{NaYbW}_2\text{O}_8$ . Previously,  $^{\mathcal{H}}\langle -1 \rangle$  type compounds have been studied for magnetic frustration, which originates from competition between nearest-neighbor and next-nearest neighbor interactions [47, 48]. Thus, the possibility of novel magnetic phases makes studying low-temperature magnetism of  $\text{NaYbW}_2\text{O}_8$  more appealing.

#### 8.4.2 DC magnetization

The zero-field-cooled (ZFC) and field-cooled (FC) DC susceptibility measurements performed in the temperature range of 0.4-300 K are shown in Fig. 8.2(a). The ZFC and FC curves overlap perfectly down to 0.4 K without showing any magnetic transition. The van Vleck contribution ( $\chi_{vv}$ ) to the magnetic susceptibility due to  $\text{Yb}^{3+}$  ions is calculated



Table 8.1: Atomic coordinates, occupancy and isotropic thermal parameters obtained from the Rietveld refinement, Space group:  $I4_1/a$ ,  $V = 299.75(1) \text{ \AA}^3$ ,  $\chi^2 = 1.56 \%$ ,  $R_p = 10.7 \%$ ,  $R_{wp} = 12.2 \%$

Atom	Wyckoff symbol	x	y	z	Occupancy	$B_{iso}(\text{\AA}^2)$
W	4a	0.0	0.25	0.125	0.25	0.049(8)
Yb	4b	0.5	0.75	0.75	0.125	0.023(6)
Na	4b	0.5	0.75	0.75	0.125	0.023(6)
O	16f	0.1605(28)	0.5187(20)	0.2180(11)	1.0	1.0

from the slope of magnetic isotherms at higher magnetic fields. After subtracting the value of  $\chi_{vv} = 6.92 \times 10^{-3} \text{ emu/mol-Oe}$ , the inverse susceptibility data shows two distinct linear regions: one from 100-300 K and the other from 2-25 K. The  $1/\chi$  data do not follow simple Curie-Weiss behavior due to CEF-mediated splitting of eightfold degenerate states ( $J = 7/2$ ) of  $\text{Yb}^{3+}$ . The degenerate states split in four Kramers doublet as reported for other Yb compounds [49–51].

As a result,  $J$  can no longer be considered  $7/2$  at low temperatures, and hence, the Curie constant is also no longer independent of temperature change. Hence, the modified Curie-Weiss law should be used, and Considering the temperature range of the susceptibility measurements (0.4-300 K), the contribution from the first excited Kramers doublet suffices to incorporate the CEF. A modified Curie-Weiss model with a two-level approximation can be written as [52, 53]:

$$1/\chi = 8.(T - \theta_{CW}). \left( \frac{1 + \exp^{-\frac{E_{10}}{k_B T}}}{\mu_{eff,0}^2 + \mu_{eff,1}^2 \cdot \exp^{-\frac{E_{1,0}}{k_B T}}} \right) \quad (8.6)$$

where  $E_{10}$  is the energy difference between the ground Kramers doublet and the first excited Kramers doublet,  $\mu_{eff,0}$  and  $\mu_{eff,1}$  stands for effective moments in the ground and excited state, respectively. The inset of Fig. 8.2(a) depicts the fitting of the  $1/\chi$  versus  $T$  data with the equation 8.6 and confirms that it reproduces the data nicely. The parameters obtained from the fitting are as follows:  $\theta_{CW} = -2.20(5) \text{ K}$ ,  $\mu_{eff,0} = 3.46(2) \mu_B$ ,  $\mu_{eff,1} = 5.76(3) \mu_B$ . The value of  $\theta_{CW}$  is an average of all the exchange interactions in the compound and confirms the dominance of antiferromagnetic interactions. The energy difference ( $E_{10}$ ) comes out to be  $176.9(4) \text{ K}$ , further confirming that at low temperature, the ground state can be described as a Kramers doublet with  $J_{eff} = 1/2$ .

To study the effect of high magnetic fields on the compound at very low temperatures, we have carried out isothermal magnetization measurements at 0.4, 1, and 1.5 K, as

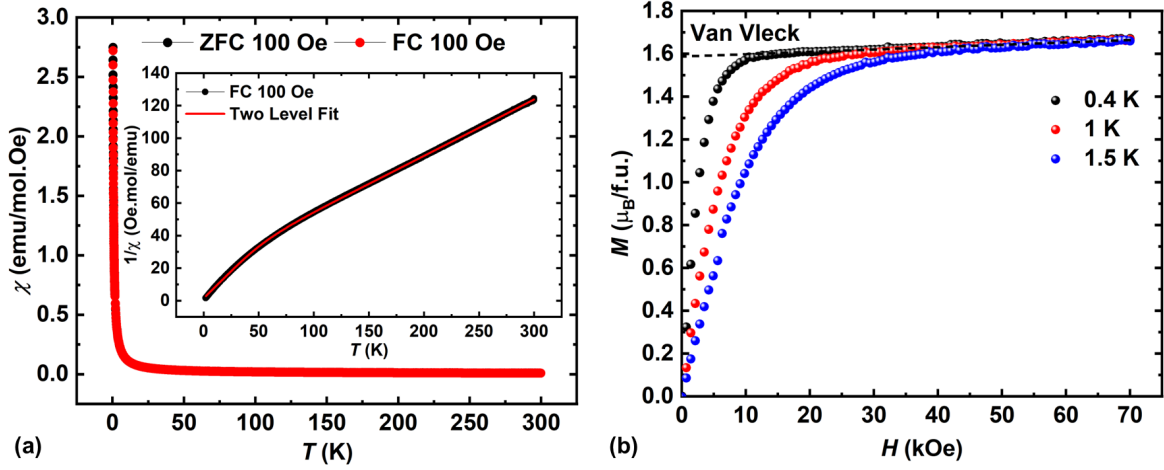


Figure 8.2: (a) Temperature dependence of the magnetic susceptibility measured under ZFC and FC protocol down to 0.4 K. Inset shows the fitting of the inverse susceptibility data with two-level Curie-Weiss model. (b) Field-dependent isothermal magnetization curves at 0.4, 1, and 1.5 K. The dashed line shows a linear fit to higher field data.

shown in Fig. 8.2(d). The magnetization curves saturate above 3 T, and the slope of the linear region ( $H > 3$  T) gives an estimation of the van Vleck contribution. The magnetization curves saturate around  $1.7 \mu_B/\text{f.u.}$ , which is a typical low-temperature saturation moment value for a  $\text{Yb}^{3+}$  ion [50, 54].

### 8.4.3 Heat Capacity

Specific heat measurements can serve as concrete evidence about the ground state of a magnetic material. For example, a  $\lambda$ -like anomaly in the heat capacity data would indicate a magnetic phase transition to an ordered state. Figure 8.3(a) shows the absence of such anomaly at least down to 2 K, which further complements the magnetization measurements. The Debye-Einstein model can be used to estimate the lattice contribution, which can be subtracted from the total heat capacity to assess the change in magnetic entropy. According to this model, the sum of acoustic and phonon modes present in a compound is equal to the total number of atoms present in the primitive cell, which is 12 for  $\text{NaYbW}_2\text{O}_8$ . Moreover, the acoustic and optical modes have a relative ratio of  $2:n-2$ , where  $n$  is the total number of atoms. Thus,  $\text{NaYbW}_2\text{O}_8$  has six acoustic modes along with thirty optical modes. Several acoustic and optical modes are clubbed together to reduce the number of free parameters, which further helps minimize the experimental error. Thus, one Debye term describes all the acoustic modes, while three Einstein terms express the optical modes. Hence, the Debye-Einstein model for  $\text{NaYbW}_2\text{O}_8$  can be

written as [55, 56]:

$$C_{D-E} = \frac{9aR}{x_D^3} \int_0^{x_D} \frac{x^4 e^x}{(e^x - 1)^2} dx + 3R \sum_{i=1}^3 \frac{b_i x_{E_i}^2 e^{x_{E_i}}}{(e^{x_{E_i}} - 1)^2} \quad (8.7)$$

where  $x_{D,E} = \theta_{D,E}/T$  such that  $\theta_D$  and  $\theta_E$  are Debye and Einstein temperatures, respectively and  $R$  is the universal gas constant. The coefficients  $a$  and  $b_i$  represent the contribution of acoustic and optic phonons, respectively. For the fitting, the values of these weight factors are constrained in such a way that they sum up to the total number of atoms in the unit cell (in the present case,  $a = 2$ ,  $b_1 = 1$ ,  $b_2 = 4$  and  $b_3 = 5$ ). The coefficient  $a$  stands for the vibration from  $W$  ions,  $b_1$  corresponds to Yb vibrations,  $b_2$  accounts for the vibrations of the  $\text{O}^{2-}$  ions of  $\text{WO}_4$  tetrahedra and  $b_3$  represents the contribution from remaining five  $\text{O}^{2-}$  ions and one  $\text{Na}^+$  ion. These considerations helped us get a physically reasonable fit even though the Debye-Einstein model is highly flexible, as depicted by the solid line in Fig. 8.3(a). The parameters obtained from the fit are as follows:  $\theta_D \sim 145$  K,  $E_1 \sim 193$  K,  $E_2 \sim 314$  K, and  $E_3 \sim 729$  K.

Figure 8.3(b) shows magnetic entropy change calculated after integrating the  $C_{mag}/T$  versus  $T$  data for zero magnetic fields. The change in magnetic entropy saturates around 5 K. The saturation value of the magnetic entropy keeps on increasing with an increase in the applied magnetic field. It saturates nearly equal to  $R \ln 2$  for the fields above 5 T, as exhibited in the inset of Fig. 8.3(b). This behavior of the saturation magnetization of the magnetic entropy further reinforces the claim of  $J_{eff} = 1/2$  ground state.

The field dependence measurements of the heat capacity exhibit the presence of a broad anomaly that moves high in temperature with an increase in the magnetic field, which is characteristic of the Schottky anomaly. On applying a magnetic field, total heat capacity can be written as  $C(T, H) = C(T, 0) + C_{sch}(T, H)$ , where  $C_{sch}$  accounts for the temperature and field dependent Schottky contribution. As mentioned earlier, Kramers doublet is the ground state, and applying a magnetic field lifts the degeneracy and opens up a gap. So, for a two-level system ( $J_{eff} = 1/2$ ), temperature and field dependence of the heat capacity can be expressed as [57–59]:

$$C_{sch}(T, H) = nR \left( \frac{\Delta}{T^2} \right) \frac{\exp(\Delta/T)}{[1 + \exp(\Delta/T)]^2} \quad (8.8)$$

where  $n$  is the concentration of the Schottky centres,  $R$  is universal gas constant, and  $\Delta$  gives the energy separation values between two levels. Figure 8.3(d) depicts the fitting of the Schottky contribution with 8.8. As shown in Fig. 8.4,  $n$  reaches a value  $\approx 1$  for  $H >$

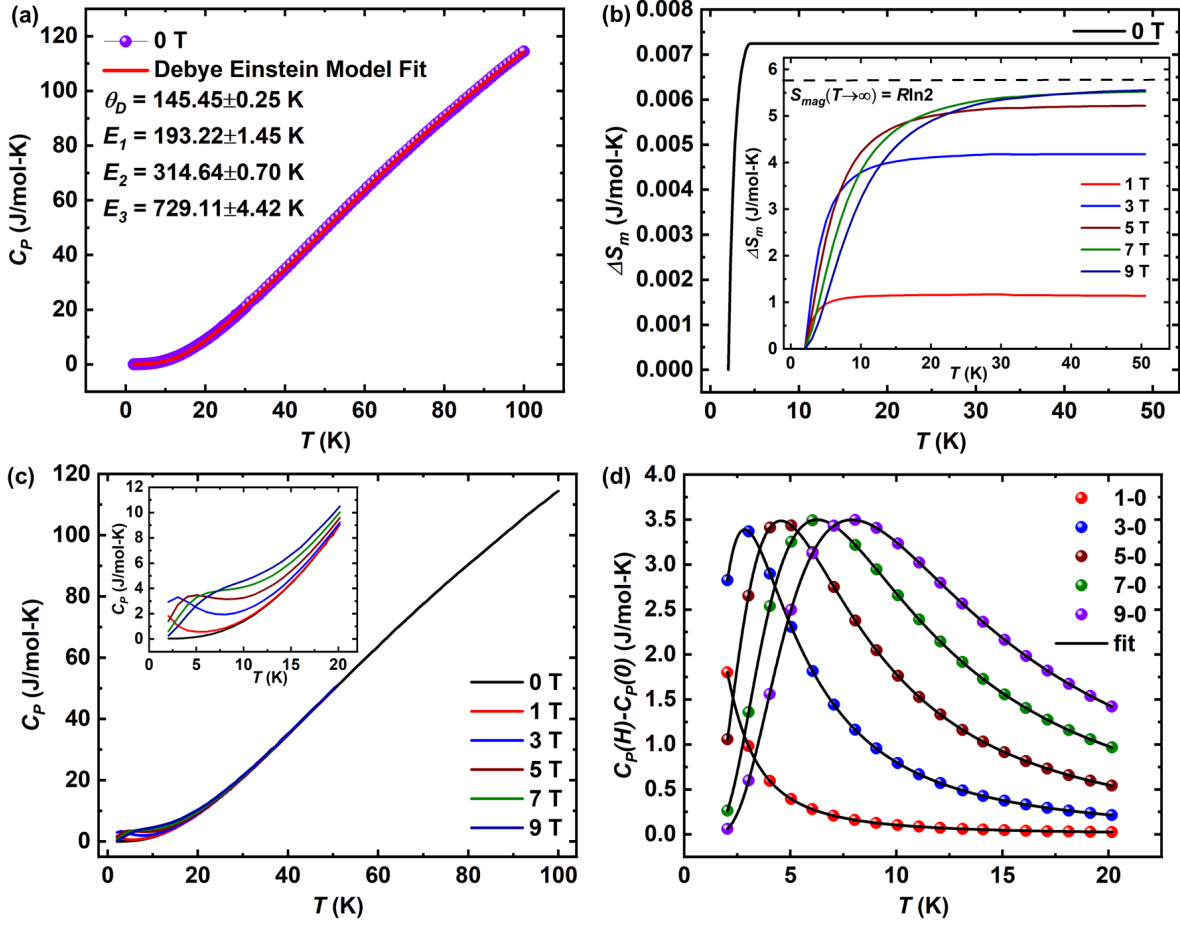


Figure 8.3: (a) Heat Capacity measured from 2 to 100 K in the absence of the magnetic field and its fitting with the Debye Einstein model. (b) Entropy calculated from magnetic heat capacity. Inset shows the temperature dependence of magnetic entropy in the presence of different magnetic fields. (c) Heat capacity measured under different magnetic fields up to 9 T, and the inset shows the variation of the heat capacity at low temperatures. (d) Temperature dependence of the Schottky contribution and its fitting with the two-level Schottky equation 8.8.

5 T, suggesting that the two levels are fully opened. The energy gap  $\Delta$  exhibits a linear dependence on the applied field due to the Zeeman splitting effect. The linear fitting of  $\Delta$ , shown in Fig. 8.4, results in a non-zero intercept ( $\Delta(0) = 0.59$  K), indicating the presence of an internal magnetic field. This finite internal magnetic field at 0 T suggests  $\text{Yb}^{3+}$ - $\text{Yb}^{3+}$  correlations [60, 61]. Thus, heat capacity measurements indicate the presence of magnetic correlations of the order of 0.6 K.

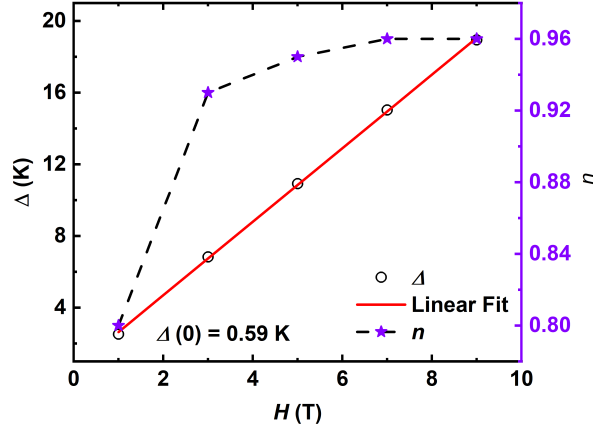


Figure 8.4: Linear fitting of  $\Delta/k_B$  (left axis) values calculated from the CEF fitting and variation of  $f$  values with the magnetic fields.

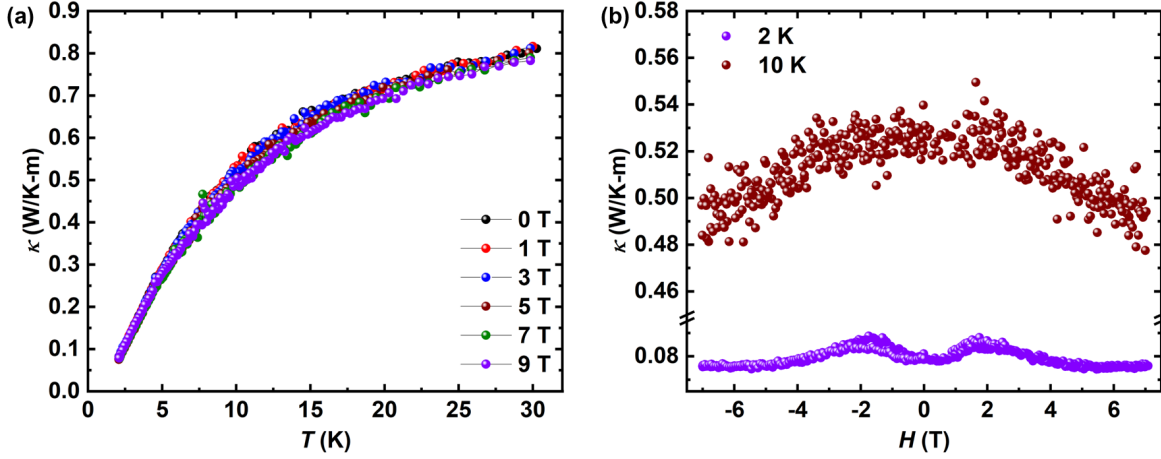


Figure 8.5: (a) Temperature dependence of thermal conductivity measured in the presence of different applied fields. (b) Change in thermal conductivity with field at two different temperatures, 2 and 10 K.

#### 8.4.4 Thermal Conductivity Measurements

To circumvent the Schottky anomaly present in the heat capacity data, we conducted thermal conductivity measurements that are immune to localized factors causing the anomaly but instead capture the itinerant excitations [62]. Figure 8.5(a) depicts the thermal conductivity variation measured from 30 to 2.25 K under different magnetic fields. We did not observe significant magnetic field dependence and tried to fit the  $\kappa/T$  data with low-temperature approximation,  $a + bT^{\alpha-1}$ , where  $a$  stands for the electron contribution to the thermal conductivity,  $b$  gives the phonon contribution. However, the fitting did not result in a finite value of  $a$ , indicating that magnetic excitations do

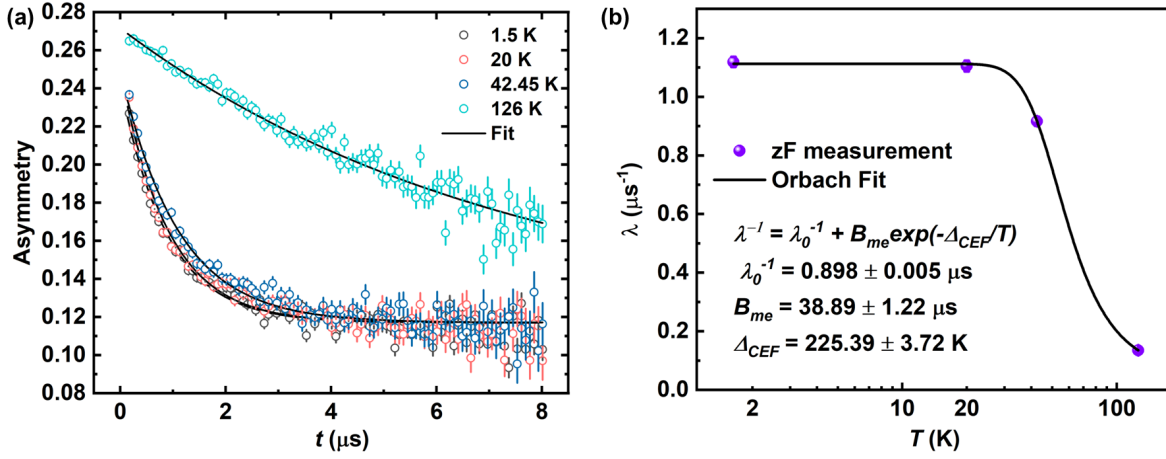


Figure 8.6: (a) Fitting of the ZF  $\mu\text{SR}$  spectra collected at various temperatures with single exponential function. (b) Temperature variation of the relaxation rate ( $\lambda$ ) and its fitting with Orbach equation.

not contribute to the thermal conductivity from 30 to 2.25 K. Furthermore, Fig. 8.5(b) illustrates magnetic field dependence of the thermal conductivity data at 2 and 10 K. At 10 K, the data do not show any significant anomaly, but 2 K data show a broad anomaly centered around 2 T. This anomaly is consistent with the heat capacity data and confirm the excitation of free spins to excited state.

#### 8.4.5 Muon Spin Relaxation Measurements

To study the local magnetism of the compound, we have carried out extremely sensitive  $\mu\text{SR}$  measurements down to 1.5 K. Figure 8.6(a) shows zero field (ZF)  $\mu\text{SR}$  measurements carried out at different temperatures up to 126 K. The absence of initial asymmetry loss and no oscillations in the spectra confirms that the compound has no long-range magnetic order or spin-freezing. Moreover, the asymmetry does not relax to 1/3 of the initial asymmetry and rules out the presence of the random distribution of static magnetic fields. We have used a single exponential muon decay function to analyze the ZF spectra, and it could reproduce the experimental data, as seen in Fig. 8.6(a). Asymmetry of a ZF spectra could be written as:

$$A(t) = A_{bg} + A_1 \exp(-\lambda/t) \quad (8.9)$$

where  $A_{bg}$  is the constant background,  $A_1$  denotes initial asymmetry and  $\lambda$  stands for the muon relaxation rate. The value of  $A_{bg}$  is kept constant at 0.117 throughout the analysis. Figure 8.6(b) exhibits the evolution of  $\lambda$  with temperature. The relaxation rate exactly

tracks the  $\text{Yb}^{3+}$  correlations. Although we have a small number of data points, a decrease in  $\lambda$  is observed above 20 K. A similar dependence can be seen in muon diffusion, but the insulating nature of  $\text{NaYbW}_2\text{O}_8$  does not support this [63]. In fact, such variation in the relaxation rate can be explained using the Orbach process, which is a two-phonon scattering process happening through an excited CEF level [64]. The Orbach equation can be expressed as:

$$\lambda^{-1} = \lambda_0^{-1} + B_{me} \exp(-\Delta_{CEF}/T) \quad (8.10)$$

where  $\lambda_0$  is the saturation value of  $\lambda$  at lower temperatures,  $B_{me}$  stands for the magnetoelectric coupling of the  $\text{Yb}^{3+}$  spins with the phonon bath, and  $\Delta_{CEF}$  gives an estimation of the energy difference of the CEF levels involved. The fitting, as shown by solid line in Fig. 8.6(b), results in the following parameters:  $\lambda_0^{-1} \approx 0.9 \mu\text{s}$ ,  $B_{me} \approx 39 \mu\text{s}$  and  $\Delta_{CEF} \approx 225$  K. The value of  $\Delta_{CEF}$  is slightly higher than the estimated from inverse susceptibility data, suggesting that higher CEF levels are also contributing to the Orbach process [65]. The temperature-independent behavior of  $\lambda$  at lower temperatures reveals the presence of a dynamic magnetic state below 20 K, as observed for other compounds [66].

#### 8.4.6 Spin Exchange Interaction Calculation

The lattice A has a nearest neighbor distance of 3.96 Å (refer to Fig. 8.7(a) and (b)), while the lattice B has a nearest neighbor distance of 5.17 Å (refer to Fig. 8.7(c) and (d)), and has lower free energy compared to the former. The obtained values for  $J_1$  and  $J_2$  are tabulated in table 8.2. In addition, we also calculated the zero-field splitting parameters, which are of the order of  $10^{-4}$  and  $10^{-6}$  respectively, and can be neglected for Monte Carlo calculations.

Table 8.2: The nearest, next nearest exchange couplings from first principles calculations for lattice A and lattice B

Lattice	$J_1$ (meV)	$J_2$ (meV)
A	-2.8	1.2
B	-0.08	0.04

For both the lattices,  $J_1$  is ferromagnetic, while  $J_2$  is antiferromagnetic and almost half of  $J_1$ . However, we see that in lattice B, the exchange interactions are one order less than in lattice A. This is because the separation among magnetic ions in lattice B is greater than that of lattice A.



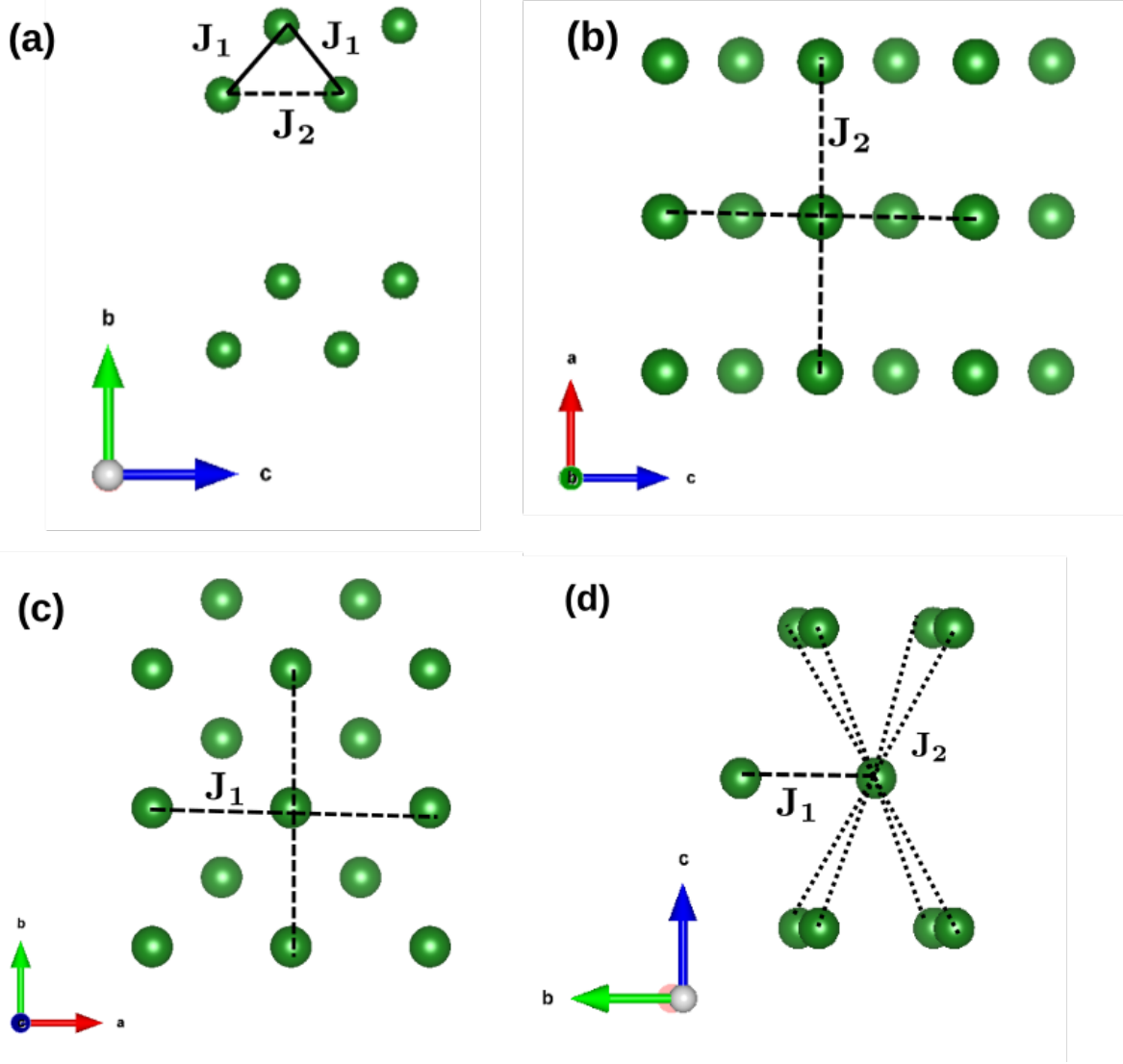


Figure 8.7: (a) and (b) shows a schematic representation of the nearest and next nearest neighbors in lattice A. (c) and (d) The nearest and next nearest pairs in lattice B. It is clear that lattice A is geometrically frustrated and that such geometric frustration is absent in lattice B. Lattice A has two nearest neighbors and four nearest neighbors as compared to lattice B, which has four nearest neighbors and eight nearest neighbors.

To identify the nature of the ground state using IM, we performed the calculations on various system sizes,  $L$ . The energy per spin for various system sizes  $L$  is plotted in Fig. 8.8. For each value of  $L$ , the equal time structure factor is calculated according to eq. 8.4. The ordering vectors, which correspond to the maxima in the structure factor, are reported in Table 8.3. To understand the quantum system at finite temperatures, we resort to Monte Carlo simulations, as described in the computational methods section.



Table 8.3: The ordering vector  $Q$  of the ground state for lattice A, in units of  $2\pi$ , obtained from the peak of the equal time structure factor obtained from Iterative Minimisation (IM).

L	$Q(2\pi)$
6	$\frac{\pm 1}{2}, \frac{\pm 1}{6}, \frac{\pm 1}{3}$
8	$\frac{\pm 1}{2}, \frac{\pm 3}{8}, \frac{\pm 3}{8}$
10	$\frac{\pm 1}{2}, \frac{\pm 3}{10}, \frac{\pm 3}{10}$
12	$\frac{\pm 1}{2}, \frac{\pm 1}{12}, \frac{\pm 1}{3}$
14	$\frac{\pm 1}{2}, 0, \frac{\pm 5}{14}$
16	$\frac{\pm 1}{2}, \frac{\pm 3}{16}, \frac{\pm 5}{16}$
18	$\frac{\pm 1}{2}, \frac{\pm 1}{3}, \frac{\pm 1}{3}$
20	$\frac{\pm 1}{2}, \frac{\pm 1}{5}, \frac{\pm 7}{20}$

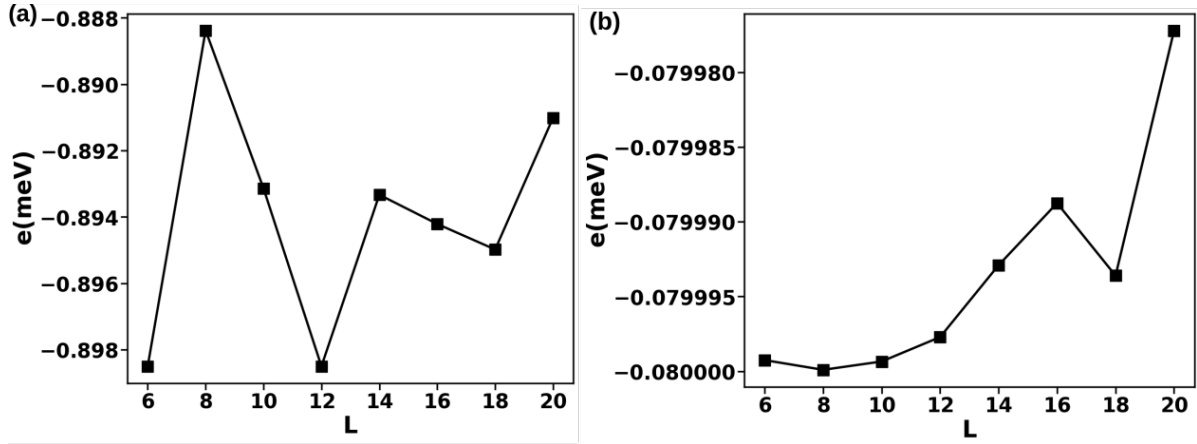


Figure 8.8: The energy per spin,  $e$ , for various linear system sizes  $L$  (a) for lattice A and (b) lattice B. The energy per spin remains almost the same for varying  $L$ .

The results at zero and finite temperatures for both the lattices are described in detail below.

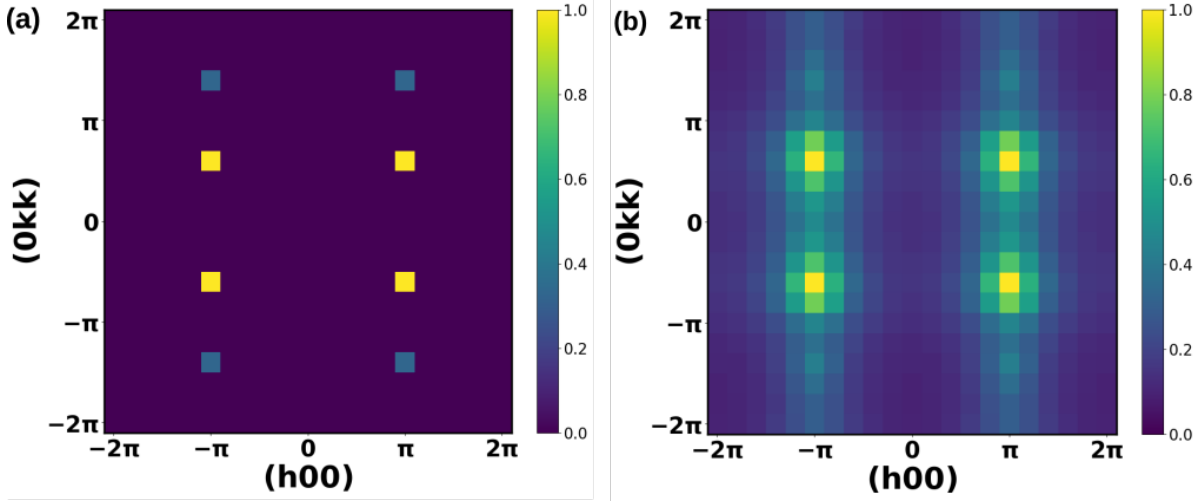


Figure 8.9: (a) The equal time structure factor of lattice A from Iterative Minimisation for  $L = 10$  at 1 K. The peaks in this case occur at  $(\frac{\pm 1}{2}, \frac{\pm 3}{10}, \frac{\pm 3}{10})$ . (b) The equal time structure factor at 5 K ( $T > T_C$ ). The peaks are diffused about the peaks in (a).

#### 8.4.6.1 Lattice A

For lattice A, the calculated energy per spin comes out to be nearly equal for  $L = 10$ ,  $L = 14$ , and  $L = 16$ , as shown in Fig. 8.8(a). Further, the ordering vector obtained from the peak of equal time structure factor varies with the system size  $L$ , indicating that the finite-size simulations cannot produce an exact magnetic ground state. This situation corresponds to an irrational ordering vector [38], which suggests an incommensurate ground state order in lattice A.

The finite temperature Monte Carlo simulations for this lattice show a magnetic transition temperature of 3 K, and the magnetic susceptibility vanishes as the  $T$  tends to zero. Experimentally, the magnetic transition has not been observed. However, by probing the temperature region just above the ordering temperature, the effect of thermal fluctuations on these classical spins can be understood. Hence, the spin structure factor calculated using this model below  $T_C$  might not reproduce the experimentally observed signatures, but for  $T > T_C$ , the thermal fluctuations can mimic the role of quantum fluctuations observed at very low temperatures [38]. The calculated equal time structure factor at 5 K, reported in figure 8.9(b), shows broad and diffused peaks, indicating a disordered magnetic phase. Such behavior is observed due to the presence of ferromagnetic and antiferromagnetic exchange interactions on a triangular lattice, leading to frustration in lattice A.

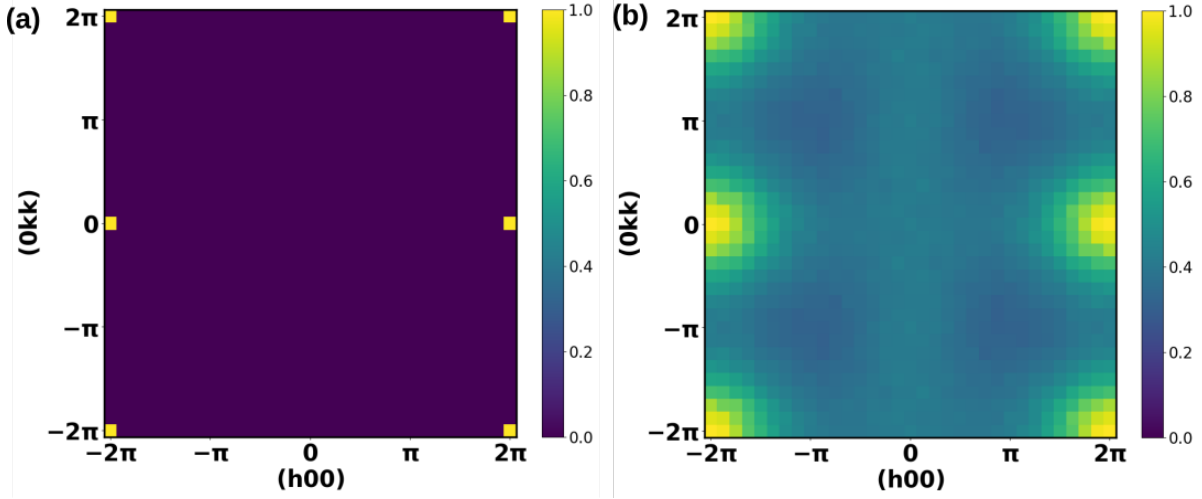


Figure 8.10: (a) The equal time structure factor of lattice B from Iterative Minimisation for  $L = 16$  at  $T = 0.1$  K (b) The equal time structure factor at 1 K ( $T > T_C$ ). The peaks are broad and diffused about the peaks in (a)

#### 8.4.6.2 lattice B

The equal time structure factor peaks at  $Q = 0$  for lattice B. The energy per spin with varying system size  $L$  is plotted in figure 8.10 (a). The very small exchange couplings lead to a much lower transition temperature ( $T_C = 0.5$  K) in this lattice. The equal time structure factor for this lattice at  $T = 1$  K is reported in figure 8.10 (b). At this temperature, which is above  $T_C$ , we see very broad diffused peaks about  $Q = 0$ . This is indicative of a “molten” state [38, 67–69], reminiscent of the dynamic magnetic state, and agrees very well with the experimental observations.

Thus, our theoretical calculations suggest the presence of a disordered state in both lattice A and lattice B. However, the origin of the disordered state is different. In lattice A, this behavior arises due to geometrical frustration, while in lattice B, it originates from the competition among exchange interactions. Considering the inherent disorder, it is highly possible that both these lattices are present in the experimental system.

## 8.5 Conclusion

We have carried out a comprehensive study of  $\text{NaYbW}_2\text{O}_8$  having an inherent antisite disorder (50 %) using various physical properties characterization techniques.  $\text{Yb}^{3+}$  ions sit on a hyperhoneycomb ( $\mathcal{H}\langle -1 \rangle$ ) lattice with sizeable antiferromagnetic interactions, and there is no magnetic phase transition down to 400 mK. The  $\text{Yb}^{3+}$ - $\text{Yb}^{3+}$  correlations

give rise to an internal magnetic field of 0.6 K magnitude, as confirmed by the analysis of the field-dependent heat capacity measurements. Further, the dynamic nature of the local fields in the systems has been confirmed by ZF  $\mu\text{SR}$  measurements. The system also shows Orbach behavior, which represents a transition mediated by an excited CEF level. The theoretical studies revealed that this state originates from a combination of geometric frustration and competition between exchange interactions. Hence,  $\text{NaYbW}_2\text{O}_8$  stands out as a candidate that provides a platform to explore the disorder-driven correlated states in the quantum magnets.

# Bibliography

- [1] L. Balents, Spin liquids in frustrated magnets, *Nature* **464**, 199 (2010).
- [2] L. Messio, B. Bernu, and C. Lhuillier, Kagome Antiferromagnet: A Chiral Topological Spin Liquid?, *Phys. Rev. Lett.* **108**, 207204 (2012).
- [3] S. Capponi, V. R. Chandra, A. Auerbach, and M. Weinstein, p6 chiral resonating valence bonds in the kagome antiferromagnet, *Phys. Rev. B* **87**, 161118 (2013).
- [4] G. Misguich, D. Serban, and V. Pasquier, Quantum Dimer Model on the Kagome Lattice: Solvable Dimer-Liquid and Ising Gauge Theory, *Phys. Rev. Lett.* **89**, 137202 (2002).
- [5] S. Yan, D. A. Huse, and S. R. White, Spin-Liquid Ground State of the  $S = 1/2$  Kagome Heisenberg Antiferromagnet, *Science* **332**, 1173 (2011).
- [6] S. Depenbrock, I. P. McCulloch, and U. Schollwöck, Nature of the Spin-Liquid Ground State of the  $S = 1/2$  Heisenberg Model on the Kagome Lattice, *Phys. Rev. Lett.* **109**, 067201 (2012).
- [7] P. Mendels, F. Bert, M. A. de Vries, A. Olariu, A. Harrison, F. Duc, J. C. Trombe, J. S. Lord, A. Amato, and C. Baines, Quantum Magnetism in the Paratacamite Family: Towards an Ideal Kagomé Lattice, *Phys. Rev. Lett.* **98**, 077204 (2007).
- [8] T.-H. Han, J. S. Helton, S. Chu, D. G. Nocera, J. A. Rodriguez-Rivera, C. Broholm, and Y. S. Lee, Fractionalized excitations in the spin-liquid state of a kagome-lattice antiferromagnet, *Nature* **492**, 406 (2012).
- [9] L. Clark, J. C. Orain, F. Bert, M. A. De Vries, F. H. Aidoudi, R. E. Morris, P. Lightfoot, J. S. Lord, M. T. F. Telling, P. Bonville *et al.*, Gapless Spin Liquid Ground State in the  $S=1/2$  Vanadium Oxyfluoride Kagome Antiferromagnet  $[\text{NH}_4]_2[\text{C}_7\text{H}_{14}\text{N}][\text{V}_7\text{O}_6\text{F}_{18}]$ , *Phys. Rev. Lett.* **110**, 207208 (2013).

- 
- [10] Y. Okamoto, M. Nohara, H. Aruga-Katori, and H. Takagi, Spin-Liquid State in the  $S = 1/2$  Hyperkagome Antiferromagnet  $\text{Na}_4\text{Ir}_3\text{O}_8$ , *Phys. Rev. Lett.* **99**, 137207 (2007).
- [11] A. Kitaev, Anyons in an exactly solved model and beyond, *Ann. Phys.* **321**, 2 (2006).
- [12] I. Kimchi, J. G. Analytis, and A. Vishwanath, Three-dimensional quantum spin liquids in models of harmonic-honeycomb iridates and phase diagram in an infinite- $D$  approximation, *Phys. Rev. B* **90**, 205126 (2014).
- [13] S. Trebst and C. Hickey, Kitaev Materials, *Phys. Rep.* **950**, 1 (2022).
- [14] G. Xiao, Z. Xia, W. Zhang, X. Yue, S. Huang, X. Zhang, F. Yang, Y. Song, M. Wei, H. Deng *et al.*, *Cryst. Growth Des.* **19**, 2658 (2019).
- [15] W. Yao and Y. Li, *Phys. Rev. B* **101**, 085120 (2020).
- [16] R. Zhong, T. Gao, N. P. Ong, and R. J. Cava, *Sci. Adv.* **6**, eaay6953 (2020).
- [17] M. Songvilay, J. Robert, S. Petit, J. A. Rodriguez-Rivera, W. D. Ratcliff, F. Damay, V. Bal´edent, M. Jim´enez-Ruiz, P. Lejay, E. Pachoud, A. Hadj-Azzem, V. Simonet, and C. Stock, *Phys. Rev. B* **102**, 224429 (2020).
- [18] C. Kim, J. Jeong, G. Lin, P. Park, T. Masuda, S. Asai, S. Itoh, H.-S. Kim, H. Zhou, J. Ma *et al.*, *J. Phys. Condens. Matter* **34**, 045802 (2021).
- [19] X. Wang, R. Sharma, P. Becker, L. Bohatý, and T. Lorenz, *Phys. Rev. Mater.* **7**, 024402 (2023).
- [20] T. Halloran, F. Desrochers, E. Z. Zhang, T. Chen, L. E. Chern, Z. Xu, B. Winn, M. Graves-Brook, M. Stone, A. I. Kolesnikov *et al.*, *Proc. Natl. Acad. Sci. U.S.A.* **120**, e2215509119 (2023).
- [21] M. J. Daum, A. Ramanathan, A. I. Kolesnikov, S. Calder, M. Mourigal, and H. S. La Pierre, *Phys. Rev. B* **103**, L121109 (2021).
- [22] H. Ishikawa, R. Kurihara, T. Yajima, D. Nishio-Hamane, Y. Shimizu, T. Sakakibara, A. Matsuo, and K. Kindo, *Phys. Rev. Mater.* **6**, 064405 (2022).
- [23] A. Biffin, R. D. Johnson, I. Kimchi, R. Morris, A. Bombardi, J. G. Analytis, A. Vishwanath, and R. Coldea, *Phys. Rev. Lett.* **113**, 197201 (2014).
- [24] T. Takayama, A. Kato, R. Dinnebier, J. Nuss, H. Kono, L. S. I. Veiga, G. Fabbri, D. Haskel, and H. Takagi, *Phys. Rev. Lett.* **114**, 077202 (2015).

- 
- [25] S.-H. Baek, H. W. Yeo, S.-H. Do, K.-Y. Choi, L. Janssen, M. Vojta, and B. Büchner, Observation of a random singlet state in a diluted Kitaev honeycomb material, *Phys. Rev. B* **102**, 094407 (2020).
  - [26] L. Liu, H. Shao, Y.-C. Lin, W. Guo, and A. W. Sandvik, Random-Singlet Phase in Disordered Two-Dimensional Quantum Magnets, *Phys. Rev. X* **8**, 041040 (2018).
  - [27] K. Kitagawa, T. Takayama, Y. Matsumoto, A. Kato, R. Takano, Y. Kishimoto, S. Bette, R. Dinnebier, G. Jackeli, and H. Takagi, A spin-orbital-entangled quantum liquid on a honeycomb lattice, *Nature* **554**, 341 (2018).
  - [28] S.-H. Do, C. H. Lee, T. Kihara, Y. S. Choi, S. Yoon, K. Kim, H. Cheong, W.-T. Chen, F. Chou, H. Nojiri, and K.-Y. Choi, Randomly Hopping Majorana Fermions in the Diluted Kitaev System  $\alpha$ -Ru<sub>0.8</sub>Ir<sub>0.2</sub>Cl<sub>3</sub>, *Phys. Rev. Lett.* **124**, 047204 (2020).
  - [29] I. Kimchi, J. P. Sheckelton, T. M. McQueen, and P. A. Lee, Scaling and data collapse from local moments in frustrated disordered quantum spin systems, *Nature Communications* **9**, 4367 (2018).
  - [30] J. Khatua, M. Gomilšek, J. C. Orain, A. M. Strydom, Z. Jagličić, C. V. Colin, S. Petit, A. Ozarowski, L. Mangin-Thro, K. Sethupathi, M. S. R. Rao, A. Zorko, and P. Khuntia, Signature of a randomness-driven spin-liquid state in a frustrated magnet, *Communications Physics* **5**, 99 (2022).
  - [31] J. Rodríguez-Carvajal, *Physica B: Condens. Matter* **192**, 55 (1993).
  - [32] O. Arnold, J.C. Bilheux, J.M. Borreguero, A. Buts, S.I. Campbell, L. Chapon, M. Doucet, N. Draper, R. F. Leal, M.A. Gigg, V.E. Lynch, A. Markvardsen, D.J. Mikkelsen, R.L. Mikkelsen, R. Miller, K. Palmen, P. Parker, G. Passos, T.G. Perring, P.F. Peterson et al., *Nucl. Instrum. Methods Phys. Res., Sect. A* **764**, 156 (2014).
  - [33] G. Kresse and J. Furthmüller, Efficient Iterative Schemes for Ab Initio Total-Energy Calculations Using a Plane-Wave Basis Set, *Phys. Rev. B* **54**, 11169 (1996).
  - [34] G. Kresse and J. Furthmüller, Efficiency of Ab-Initio Total Energy Calculations for Metals and Semiconductors Using a Plane-Wave Basis Set, *Comput. Mater. Sci.* **6**, 15 (1996).
  - [35] G. Kresse and J. Hafner, Ab Initio Molecular Dynamics for Liquid Metals, *Phys. Rev. B* **47**, 558 (1993).
  - [36] G. Kresse and D. Joubert, From Ultrasoft Pseudopotentials to the Projector Augmented-Wave Method, *Phys. Rev. B* **59**, 1758 (1999).

- 
- [37] J. P. Perdew, K. Burke, and M. Ernzerhof, Generalized Gradient Approximation Made Simple, *Phys. Rev. Lett.* **77**, 3865 (1996).
- [38] Anna Fancelli, Johannes Reuther and Bella Lake, Classical spin models of the windmill lattice and their relevance for  $\text{PbCuTe}_2\text{O}_6$ , *Phys. Rev. B* **108**, 184415 (2023).
- [39] Sophia R. Sklan and Christopher L. Henley, Nonplanar ground states of frustrated antiferromagnets on an octahedral lattice, *Phys. Rev. B* **88**, 024407 (2013).
- [40] Y. Miyatake, M. Yamamoto, J. J. Kim, M. Toyonaga and O. Nagai, On the implementation of the 'heat bath' algorithms for Monte Carlo simulations of classical Heisenberg spin systems, *J. Phys. C: Solid State Physics*, **19**, 2539 (1986).
- [41] Michael Creutz, Overrelaxation and Monte Carlo simulation, *Phys. Rev. D*, **36**, 515 (1987).
- [42] S. S. Perera and F. A. Rabuffetti, *Cryst. Eng. Comm.* **18**, 5818 (2016).
- [43] C. A. Marjerrison, C. Mauws, A. Z. Sharma, C. R. Wiebe, S. Derakhshan, C. Boyer, B. D. Gaulin, and J. E. Greedan, *Inorg. Chem.* **55**, 12897 (2016).
- [44] S. Injac, A. K. L. Yuen, B. J. Kennedy, M. Avdeev, and F. Orlandi, *Phys. Chem. Chem. Phys.* **21**, 7261 (2019).
- [45] K. A. Modic, T. E. Smidt, I. Kimchi, N. P. Breznay, A. Biffin, S. Choi, R. D. Johnson, R. Coldea, P. Watkins-Curry, G. T. McCandless, J. Y. Chan, F. Gandara, Z. Islam, A. Vishwanath, A. Shekhter, R. D. McDonald, and J. G. Analytis, Realization of a three-dimensional spin-anisotropic harmonic honeycomb iridate, *Nat. Commun.* **5**, 4203 (2014).
- [46] N. D. Kelly, L. Yuan, R. L. Pearson, E. Suard, I. P. Orench, and S. E. Dutton, *Phys. Rev. Materials* **6**, 044410 (2022).
- [47] M. M. Bordelon, J. D. Bocarsly, L. Posthuma, A. Banerjee, Q. Zhang, and S. D. Wilson, *Phys. Rev. B* **103**, 024430 (2021).
- [48] M. M. Bordelon, C. Liu, L. Posthuma, E. Kenney, M. J. Graf, N. P. Butch, A. Banerjee, S. Calder, L. Balents, and S. D. Wilson, *Phys. Rev. B* **103**, 014420 (2021).
- [49] Y. Li, D. Adroja, R. I. Bewley, D. Voneshen, A. A. Tsirlin, P. Gegenwart, and Q. Zhang, Crystalline electric-field randomness in the triangular lattice spin-liquid  $\text{YbMgGaO}_4$ , *Phys. Rev. Lett.* **118**, 107202 (2017).



- 
- [50] L. Ding, P. Manuel, S. Bachus, F. Grubler, P. Gegenwart, J. Singleton, R. D. Johnson, H. C. Walker, D. T. Adroja, A. D. Hillier *et al.*, Gapless spin-liquid state in the structurally disorder-free triangular antiferromagnet  $\text{NaYbO}_2$ , *Phys. Rev. B* **100**, 144432 (2019).
  - [51] J. G. Rau, L. S. Wu, A. F. May, L. Poudel, B. Winn, V. O. Garlea, V. O. Garlea, A. Huq, P. Whitfield, A. E. Taylor, M. D. Lumsden *et al.*, Anisotropic exchange within decoupled tetrahedra in the quantum breathing pyrochlore  $\text{Ba}_3\text{Yb}_2\text{Zn}_5\text{O}_{11}$ , *Phys. Rev. Lett.* **116**, 257204 (2016).
  - [52] T. Besara, M. S. Lundberg, J. Sun, D. Ramirez, L. Dong, J. B. Whalen, R. Vasquez, F. Herrera, J. R. Allen, M. W. Davidson *et al.*, Single crystal synthesis and magnetism of the  $\text{BaLn}_2\text{O}_4$  family ( $\text{Ln}$  = lanthanide), *Prog. Solid State Chem.* **42**, 23 (2014).
  - [53] M. Mitric, B. Antic, M. Balanda, D. Rodic, and M. L. Napijalo, An x-ray diffraction and magnetic susceptibility study of  $\text{Yb}_x\text{Y}_{2-x}\text{O}_3$ , *J. Phys.: Condens. Matter* **9**, 4103 (1997).
  - [54] R. Bag, M. Ennis, C. Liu, S. E. Dissanayake, Z. Shi, J. Liu, L. Balents, and S. Haravifard, Realization of quantum dipoles in triangular lattice crystal  $\text{Ba}_3\text{Yb}(\text{BO}_3)_3$ , *Phys. Rev. B* **104**, L220403 (2021).
  - [55] R. Kumar and A. Sundaresan, Unveiling a hidden multiferroic state under magnetic fields in  $\text{BaHoFeO}_4$ , *Phys. Rev. B* **107**, 184420 (2023).
  - [56] R. Kumar and A. Sundaresan, Antisite disorder driven cluster glass state and colossal magnetoresistance in  $\text{MnSb}_2\text{Se}_4$ , *Phys. Rev. B* **106**, 134423 (2022).
  - [57] H. M. Rosenberg, *Low Temperature Solid State Physics* (Oxford University Press, Oxford, 1963).
  - [58] L. Xie, T. Su, and X. Li, Magnetic field dependence of Schottky anomaly in the specific heats of stripe-ordered superconductors  $\text{La}_{1.6-x}\text{Nd}_{0.4}\text{Sr}_x\text{CuO}_4$ , *Physica C: Superconductivity* **480**, 14 (2012).
  - [59] S. Mahdaviifar and A. Akbari, Heat capacity of Schottky type in low-dimensional spin systems, *J. Phys.: Condens. Matter* **20**, 215213 (2008).
  - [60] S. Kundu, A. Hossain, Pranava Keerthi S, R. Das, M. Baenitz, P. J. Baker, J.-C. Orain, D. C. Joshi, R. Mathieu, P. Mahadevan, S. Pujari, S. Bhattacharjee, A. V. Mahajan, and D. D. Sarma, Signatures of a spin-1/2 cooperative paramagnet in the diluted triangular lattice of  $\text{Y}_2\text{CuTiO}_6$ , *Phys. Rev. Lett.* **125**, 117206 (2020).

- 
- [61] R. Kumar, K. Nam, S.-H. Kim, K. H. Kim, and A. Sundaresan, Exploring potential quantum spin liquid state in a quasi-one-dimensional magnetic chain, *Phys. Rev. B* **109**, 224429 (2024).
  - [62] M. Yamashita, N. Nakata, Y. Kasahara, T. Sasaki, N. Yoneyama, N. Kobayashi, S. Fujimoto, T. Shibauchi, and Y. Matsuda, Thermal-transport measurements in a quantum spin-liquid state of the frustrated triangular magnet  $\kappa$ -(BEDT-TTF)<sub>2</sub>Cu<sub>2</sub>(CN)<sub>3</sub>, *Nat. Phys.* **5**, 44 (2009).
  - [63] P. Dalmas de Réotier, A. Yaouanc, P. C. M. Gubbens, C. T. Kaiser, C. Baines, and P. J. C. King, Absence of magnetic order in Yb<sub>3</sub>Ga<sub>5</sub>O<sub>12</sub>: relation between phase transition and entropy in geometrically frustrated materials, *Phys. Rev. Lett.* **91**, 167201 (2003).
  - [64] R. Orbach, Spin-lattice relaxation in rare-earth salts, *Proc. Phys. Soc. London Sect. A* **264**, 458 (1961).
  - [65] C. Y. Jiang, Y. X. Yang, Y. X. Gao, Z. T. Wan, Z. H. Zhu, T. Shiroka, C. S. Chen, Q. Wu, X. Li, J. C. Jiao, K. W. Chen, Y. Bao, Z. M. Tian, and L. Shu, Spin excitations in the quantum dipolar magnet Yb(BaBO<sub>3</sub>)<sub>3</sub>, *Phys. Rev. B* **106**, 014409 (2022).
  - [66] Y. Cai, C. Lygouras, G. Thomas, M. N. Wilson, J. Beare, S. Sharma, C. A. Marjerrison, D. R. Yahne, K. A. Ross, Z. Gong, Y. J. Uemura, H. A. Dabkowska, and G. M. Luke,  $\mu$ SR study of the triangular Ising antiferromagnet ErMgGaO<sub>4</sub>, *Phys. Rev. B* **101**, 094432 (2020).
  - [67] Masashi Hosoi, Emily Z. Zhang, Adarsh S. Patri and Yong Baek Kim, Uncovering Footprints of Dipolar-Octupolar Quantum Spin Ice from Neutron Scattering Signatures, *Phys. Rev. Lett.* **129**, 097202 (2022).
  - [68] A. M. Samarakoon, A. Banerjee, S. S. Zhang, Y. Kamiya, S. E. Nagler, D. A. Tennant, S. H. Lee and C. D. Batista, Comprehensive study of the dynamics of a classical Kitaev spin liquid, *Phys. REv. B* **96**, 134408 (2017).
  - [69] Oliver Franke, Dumitru Călugăru, Andreas Nunnenkamp, and Johannes Knolle, Thermal spin dynamics of Kitaev magnets: Scattering continua and magnetic field induced phases within a stochastic semiclassical approach, *Phys. Rev. B* **106**, 174428 (2022)

# Summary

This thesis presents a comprehensive investigation into several novel quantum magnetic materials, emphasizing their potential to host exotic states such as quantum spin liquids (QSL) and Kitaev-like magnetic phases. The research utilizes various advanced magnetic and thermodynamic techniques, including magnetization, heat capacity, and  $\mu$ SR measurements, to explore the dynamic ground states of Yb-based compounds, characterized by frustrated magnetism, absence of long-range ordering, and spin-orbit entangled ground states.

Key findings include:

1. **NaYbTe<sub>2</sub>O<sub>7</sub>**: This quasi-one-dimensional magnet, featuring Yb<sup>3+</sup> ions arranged in zig-zag chains, shows no long-range magnetic order down to 0.4 K despite strong antiferromagnetic interactions of the order of 1 K. Low-temperature measurements suggest a Kramers doublet ground state with possible gapless quantum spin-liquid behavior, warranting further investigation through local probes and inelastic neutron scattering.
2. **Yb<sub>2</sub>Te<sub>5</sub>O<sub>13</sub>**: Characterized by dynamic Yb<sup>3+</sup> spins down to 44 mK, this compound exhibits a transition among crystal electric field (CEF) levels, known as Orbach process. Application of magnetic field enhances the density of spin excitations and competing exchange interactions contribute to its dynamic magnetic state, offering insights into unusual magnetic phases.
3. **LiYbSiO<sub>4</sub>**: This material, based on a square-lattice structure, is the first disorder-free 2D magnet proposed as a quantum spin-liquid candidate. Competing  $J_1$  and  $J_2$  interactions drive the dynamic magnetic state, which remains stable under applied fields, providing a platform for studying QSLs in two-dimensional systems.

4. **NaYbZnWO<sub>6</sub>**: This doubly ordered perovskite, synthesized under high-pressure and high-temperature conditions, shows no magnetic ordering down to 0.4 K. The distorted square lattice and absence of site disorder make it a strong candidate for exploring spin-frustration-induced quantum spin liquids.
5. **Sr<sub>3</sub>CoNb<sub>2</sub>O<sub>9</sub>**: As a potential Kitaev candidate, this compound exhibits a  $J_{eff} = 1/2$  ground state with dynamic magnetism stable between 1.3 K and 10 K. The material's geometry and anisotropic exchange interactions fulfill the criteria for Kitaev materials, highlighting its potential for further exploration.
6. **NaYbW<sub>2</sub>O<sub>8</sub>**: With inherent antisite disorder and Yb<sup>3+</sup> ions arranged on a hyper-honeycomb lattice, this compound shows no magnetic phase transition down to 0.4 K. The combination of geometric frustration and competing exchange interactions in this compound leads to a disorder-driven correlated magnetic state.

In summary, the thesis contributes to the growing field of quantum magnetism by identifying promising candidates for QSLs and other unconventional magnetic phases. It demonstrates the significance of frustrated magnetic lattices and spin-orbit coupling in stabilizing dynamic, non-ordered states, paving the way for future investigations of these phenomena in novel materials.

## About The Author



Rahul Kumar earned his master's degree in Physics from the Indian Institute of Technology, Indore. In 2019, he joined JNCASR as a Ph.D. student under the guidance of Prof. A. Sundaresan. His current research focuses on exploring quantum novel states arising from magnetic frustration.

✉ [rahulkumar@jncasr.ac.in](mailto:rahulkumar@jncasr.ac.in)

G [Rahul Kumar](#)

🐦 [@raorahul25497](#)

in [Rahul Kumar](#)

*“Frustration, although quite painful at times, is a very positive and essential part of success.”*

— Bo Bennett, Author, and Entrepreneur